CROSSOVER TO TRICRITICAL BEHAVIOR AT THE NEMATIC TO SMECTIC A TRANSITION: AN X-RAY SCATTERING STUDY

by

BENJAMIN MARK OCKO

B.A. Swarthmore College

(1978)

SUBMITTED IN PARTIAL FULFILLMENT

OF THE REQUIREMENTS FOR THE

DEGREE OF

DOCTOR OF PHILOSOPHY

at the

MASSACHUSETTS INSTITUTE OF TECHNOLOGY

February 1984

c MASSACHUSETTS INSTITUTE OF TECHNOLOGY

Signature of Author _____
Department of Physics
February, 1984

Certified by _____
Robert J. Birgeneau
Thesis Supervisor

Accepted by _____
George F. Koster
Chairman, Department Committee

MASSACHUSETTS INSTITUTE OF TECHNOLOGY

MAY 30 1984

LIBRARIES

ARCHIVES

CROSSOVER TO TRICRITICAL BEHAVIOR AT THE NEMATIC TO SMECTIC A TRANSITION: AN X-RAY SCATTERING STUDY

by

BENJAMIN MARK OCKO

Submitted to the Department of Physics on
February 9, 1984 in partial fulfillment of the
requirements for the Degree of Doctor of
Philosophy in Physics

ABSTRACT

High resolution X-ray scattering experiments, which measure the critical smectic A fluctuations in the nematic phase, have been performed in several thermotropic liquid crystal systems. The correlated region of the these fluctuations diverges at the nematic to smectic A transition, as is characteristic of second order transitions. However, reducing the nematic range by increasing the molecular chain length has several interesting consequences:

1) The correlation lengths ($\xi_{\parallel}$ and $\xi_{\perp}$) decrease.
2) The correlation length exponents $\nu_{\parallel}$, $\nu_{\perp}$ and susceptibility exponent γ decrease.
3) Eventually the latent heat becomes finite. The point at which this first occurs is referred to as the tricritical point.

1) The correlation lengths ($\xi_{\parallel}$ and $\xi_{\perp}$) decrease.
2) The correlation length exponents $\nu_{\parallel}$, $\nu_{\perp}$ and susceptibility exponent γ decrease.
3) Eventually the latent heat becomes finite. The point at which this first occurs is referred to as the tricritical point.

TABLE OF CONTENTS

		Page
	ABSTRACT	2
	LIST OF FIGURES	4
	ACKNOWLEDGEMENTS	6
Chapter 1.0	INTRODUCTION	9
1.1	Liquid Crystals	11
1.2	X-ray Scattering Theory	16
1.3	Phase Transitions	21
Chapter 2.0	THEORETICAL APPROACHES TO THE $N \rightarrow S_A$ TRANSITION	38
2.1	Mean Field and Tricritical Predictions	39
2.2	De Gennes Model	47
2.3	Anisotropic Scaling and Gauge Transformations	55
2.4	Dislocation Mediated Melting	63
Chapter 3.0	PRIOR EXPERIMENTAL RESULTS	72
Chapter 4.0	EXPERIMENTAL TECHNIQUES	82
4.1	X-ray Scattering	82
4.2	Temperature Control, Alignment, and Sample Preparation	102
Chapter 5.0	SUMMARY OF RESULTS	114
5.1	Results in 40.7 and $\overline{6}09$; The Saturated Limit	116
5.2	Results in $\bar{n}S5$ Samples	135
5.3	Results in nCB Samples	155
Chapter 6.0	CONCLUDING REMARKS	174
Appendix 1	Resolution Functions and Convolutions with S(q)	179
2	Experimental Configuration	187
3	Results in 60.8	188
4	Tables of Fitted Results	194

LIST OF FIGURES

FIGURE		Page
1.1.1	Molecular structure for $\bar{n}$S5, nO.m, and nCB materials	13
1.1.2	Schematic of mesophases	14
1.2.1	X-ray Scattering in real and reciprocal space	17
1.3.1	Phase diagram for an idealized tricritical system	31
2.1.1	Phase diagram for an idealized $N \rightarrow S_A$ transition	45
2.2.1	Nematic distortions	49
2.4.1	Smectic dislocations	64
4.1.1	X-ray spectrometer components	83
4.1.2	Single crystal Darwin profile	86
4.1.3	Spectrometer dispersion	91
4.1.4	Arms-zero profile for the Ge(111) set-up	94
4.1.5	Arms-zero profile for the Si(111) set-up	95
4.1.6	In-plane resolution for the Si(111) set-up	97
4.1.7	Vertical Resolution profile	98
4.1.8	Data acquisition and control electronics	100
4.2.1	Sketch of liquid crystal oven	103
4.2.2	Transition temperature gradient in 9CB	105
4.2.3	ANAC electromagnet	107
4.2.4	ANAC calibration curves	108
5.1.1	Smectic A q vector in 40.7	118
5.1.2	Longitudinal and transverse scans in 40.7 near T_{NA}	119
5.1.3	Nematic phase longitudinal and transverse scans in 40.7	121
5.1.4	σ_0, $\xi_{\parallel}$ and $\xi_{\perp}$ in 40.7	123
5.1.5	$\xi_{\parallel}/\xi_{\perp}$ and c in 40.7	125
5.1.6	Rocking curves above and below T_{NA} in $\bar{6}09$	128
5.1.7	Transverse scan with LFC and LPC fits in $\bar{6}09$	130
5.1.8	σ_0, $\xi_{\parallel}$, and $\xi_{\perp}$ vs. t in $\bar{6}09$	131
5.1.9	$\eta_{\perp}$ and c vs. t in $\bar{6}09$	132
5.2.1	Phase diagram for the $\bar{n}$S5 series	136
5.2.2	Layer Spacing and McMillan ratio in $\bar{n}$S5	139
5.2.3	Layering q vector in $\bar{9}$S5 and $\overline{10}$S5	140
5.2.4	Smectic integrated intensity for the $\bar{n}$S5 series	143
5.2.5	$\xi_{\parallel}$ vs. t for the $\bar{n}$S5 series	145
5.2.6	$\xi_{\perp}$ vs. t for the $\bar{n}$S5 series	146
5.2.7	σ_0 vs. t for the $\bar{n}$S5 series	147
5.2.8	c vs. t for the $\bar{n}$S5 series	148
5.2.9	$\xi_{\parallel}$ and $\xi_{\perp}$ in $\overline{10}$S5 vs. t with errors	150
5.2.10	Saturated values of $\xi_{\parallel}$ for the $\bar{n}$S5 series	154
5.3.1	Phase diagram for the nCB series	156
5.3.2	Layer spacing and McMillan ratio for the nCB series	158
5.3.3	Peak Intensity at T_{NA} in 9.20CB	160
5.3.4	Transverse and Longitudinal Scans in 9CB	161
5.3.5	$\xi_{\parallel}$ and $\xi_{\perp}$ fit with c=0.10 and c=0.25	163
5.3.6	$\xi_{\parallel}$ vs. t in 9CB	165
5.3.7	$\xi_{\perp}$ vs. t in 9CB	166
5.3.8	σ_0 vs. t in 9CB	167

5.3.9	$\xi_{\parallel}$ and $\xi_{\perp}$ in 8CB from LPC and LFC fits	171
5.3.10	$\eta_{\perp}$ and c in 8CB	172
6.0.1	$\xi_{\parallel}$, $\xi_{\perp}$, and σ in 9CB and $\overline{10}$S5	176
A3.1	Heat capacity and peak intensity in 60.8	189
A3.2	Integrated intensity at the N→S_A transition in 60.8	189
A3.3	Peak intensity at the N→I transition in 60.8	191
A4.4	Longitudinal and transverse scans in 60.8	192

ACKNOWLEDGEMENTS

First of all, I would like to thank Bob Birgeneau for his continued support and guidance as my research advisor. His enthusiasm towards physics and life have been invaluable in both my scientific and personal development.

I would like to thank my fellow graduate students and other members of my research group who have shared their ideas in countless ways. In the field of liquid crystals, my conversations and collaborations with Luz Martinez-Miranda, Refik Kortan, Kenne Evans-Lutterodt, Gabe Aeppli, and Cyrus Safinya were unparalleled. I would also like to thank Simon Mochrie, Eliot Specht, and Mark Sutton as friends and collegues. The lab has been a joint effort of many individuals; most noteably, Refik Kortan for his virtuosity with vacuum systems and Paul Heiney, Mark Sutton, Eliot Specht and Simon Mochrie for their software skills.

At MIT, I have benefited from many conversations with other researchers in the field of liquid crystals including Joel Brock, Satyen Kumar, Brent Larson, Lorraine Solomon, Sam Sprunt, Margaret Wong, Mike Fisch, Chuck Rosenblatt, Chen Chiang and Mike Meichle. I especially want to thank Carl Garland and Dave Litster for sharing their special insights into liquid crystals and as theses readers.

I have benifited greatly from my interaction with other members of the liquid crystal community. The proximity to Harvard provided numerous stimulating interactions with Jeff Collet, Larry Sorenson,

Kelby Chan and Peter Pershan. I would like to thank Dave Johnson, Tom Lubensky, John Toner, and Jan Thoen for may enlightening conversations and Mary Neubert for supplying many of the samples.

I would like to express my appreciation to my friends Rob Kwasnick and Gerry Swislow. Gerry's computer wizardry was most useful in producing many of the plots and the typesetting for this thesis.

Finally, I would like to thank my parents Lena and Richard, my sisters and brothers, and my in-laws Joe and Ramah for their continued love and support over the years. Most importantly, I would like to express my sincere appreciation to my wife Lorraine, who has shared this thesis with me in many ways.

To Lorraine

1.0 INTRODUCTION

Liquid Crystals exhibit a rich variety of phases intermediate between normal liquids and solids. X-ray scattering experiments directly probe the molecular order by measuring the Fourier transform of the instantaneous positional correlation function. Computer controlled, high resolution, triple axis spectrometers have revolutionized X-ray scattering especially in liquid crystal materials during the past decade. These advances rest on both the high resolution provided by perfect crystals and the implementation of quantitative instrumental deconvolution techniques in determining the intrinsic scattering profile. These improved techniques are extremely useful in probing subtle structural changes, especially in the neighborhood of phase transitions.

This thesis is divided into six chapters. The primary purpose of this chapter is to develop the background necessary to interpret the experiments reported here. In the first section the essential features of liquid crystals are presented. In the next section quasi-elastic x-ray scattering theory is presented. The final section of chapter one section introduces the reader to the important concepts of phase transitions, including Landau Theory, critical exponents, scaling relationships and tricritical phenomena.

The following five chapters are divided as follows. Chapter 2 builds on the phase transition section(1.3) and applies these concepts to the $N \rightarrow S_A$ phase transition. Current theoretical ideas including dislocation mediated melting and gauge transformation techniques are developed. In chapter 3 the $N \rightarrow S_A$ literature is summarized.

The experimental procedures necessary to perform and interpret x-ray scattering experiments are developed in chapter 4. Other details, such as the sample preparation, ovens and temperature control, and the magnetic alignment apparatus are also discussed. The beginning of chapter 5 provides a brief synopsis of the x-ray line-shape fitting. In section 5.1 measurements in 40.7 and 60.9, which have long nematic, ranges are presented. The remainder of this chapter pertains to experiments on families of liquid crystals (homologous series) which exhibit a cross-over from critical behavior to tricritical behavior. Section 5.2 presents the data from the $\bar{n}$S5 series which exhibits a single layer smectic whereas section 5.3 is on the nCB series which exhibits a bilayer smectic.

In the final chapter of this thesis the results of this study are summarized and new experiments are proposed to answer the remaining issues.

1.1
LIQUID CRYSTALS

The term liquid crystals signifies many different states of matter intermediate between a isotropic liquid and an crystalline solid.[1,2,3] Molecules exhibiting such states are often referred to as mesogens whereas the states themselves are referred to as mesomorphic phases. There are a plethora of possible mesomorphic phases corresponding to different degrees of order, however, only a few phases occur in most materials. There are tens of thousands of known molecules which exhibit liquid crystal behavior but all have several features in common. Firstly, the molecular geometry of mesogens is highly anisotropic, enhancing the likelihood of an aligned fluid phase rather than an isotropic fluid phase. Secondly, these materials have a rigid central core with extended aliphatic (hydrocarbon) tails. The core region is usually composed of several benzene rings bonded to each other either directly or by an intermediate linkage.

Phase transitions can be induced by several methods. The most direct method of changing the phase is by varying the temperature. Other means include modifying the pressure or mixing in another molecular component. This component may be another liquid crystal molecule as well as non-liquid crystal components such as a solvent, as in the case of lyotropic liquid crystals. The materials studied in this thesis are thermotropic liquid crystals, meaning that the phase transitions can be induced by purely thermal processes.

Perhaps the earliest observations of liquid crystal behavior were reported nearly a century ago by Reinitzer and Lehmann .[4] Fifty years later G. Friedel[5] observed mesmorphic phases that had the

characteristic x-ray diffraction pattern of a layered structure. Since these phases had properties similar to soaps he coined the word smectic from Greek. More recent experiments have established a multitude of smectic phases corresponding to different degrees of inter-layer and intra-layer ordering.

Thermotropic liquid crystals fall into two distinct subsets; nematics/cholesterics and smectics are formed by rod like molecules and discotic phases are formed by flat disk-like molecules. In this thesis the discussion will be limited to nematic and smectic mesomorphic phases. The materials studied in this thesis belong to one of three homologous liquid crystal series and are shown in figure 1.1.1. They are 4-n-pentylphenyl 4-n-alkoxybenzoate($\bar{n}$S5), 4-n-alkyl-4-cyanobiphenyl(nCB) and N-4n-(p-alkoxybenzylidene) -4-n-alkylaniline(nO.m). We have also studied 4-n-hexylphenyl 4-n-nonoxybenzoate($\bar{6}$09) in which the sulfur of the $\bar{n}$S5 series is replaced by an oxygen atom. All of these mesogens have isotropic, nematic and smectic A phases.

The nematic phase differs from the isotropic phase by the development of orientational order of the long axis of the molecules as shown in figure 1.1.2. The unit vector($\vec{n}(\vec{r})$) which describes the local alignment direction is referred to as the nematic director or sometimes just the director. Nematics are uniaxial with the optical axis along $\vec{n}(\vec{r})$. Since the index of refraction is different along $\vec{n}(\vec{r})$ and normal to $\vec{n}(\vec{r})$, nematics are birefringent. This property combined with strong thermal fluctuations of the director causes nematic to scatter light and leads to their cloudy appearance. The constituent benzene rings are highly diamagnetic enabling a magnetic field to align the director.

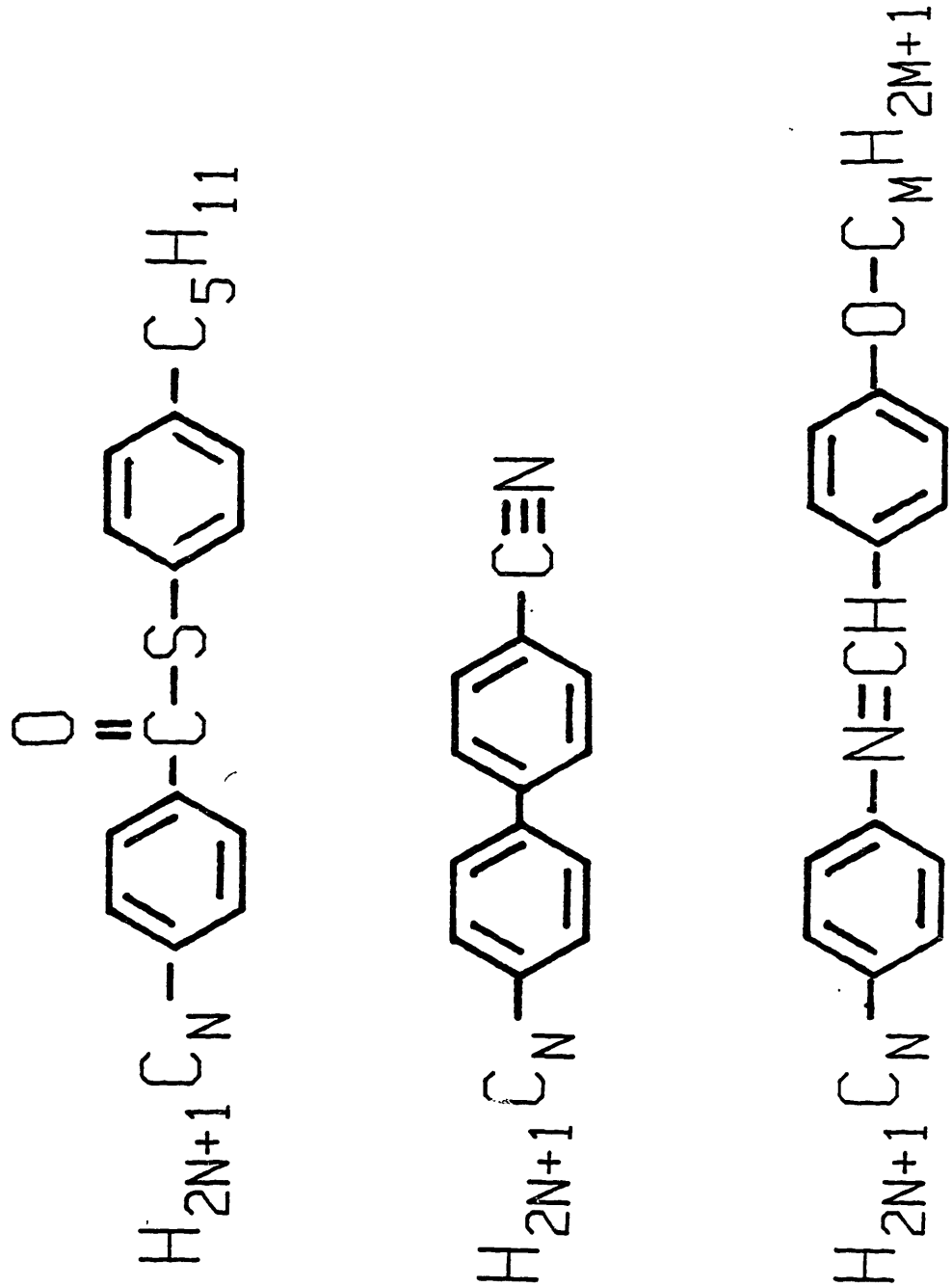

Figure 1.1.1

Molecular structure for the molecules reported in this thesis. Starting at the top, the molecules are;
1) 4-n-pentylphenyl 4-n-alkoxybenzoate(ñS5)
2) 4-n-alkyl-4-cyanobiphenyl(nCB)
3) N-4n-(p-alkoxybenzylidene) -4-n-alkylaniline(nO.m).

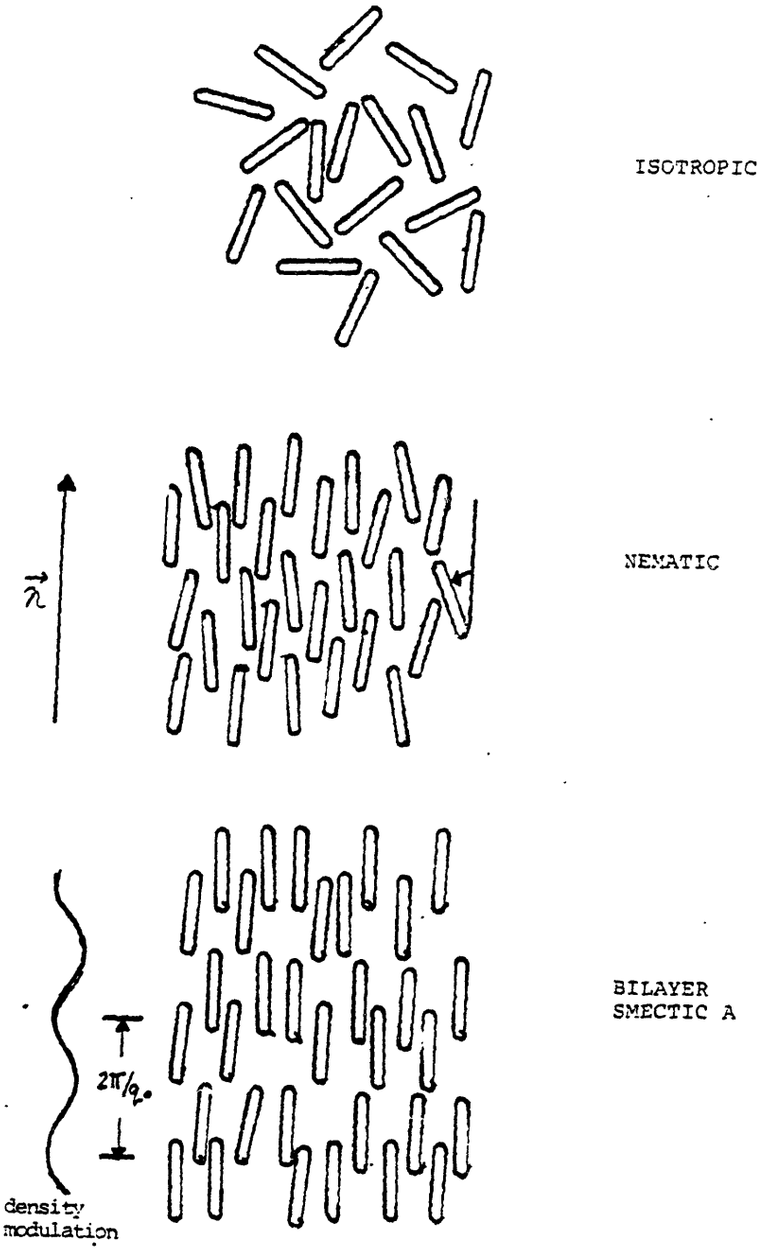

Figure 1.1.2

Physicist's conception of the isotropic, nematic and smectic phases.

The smectic A phase is the least ordered layered phase. Again, the molecules are orientationally aligned, however there is an additional degree of order corresponding to layering. This is usually expressed as a modulation of the density along the layering direction.

$$\rho = \rho_0\left[1+\frac{1}{\sqrt{2}}\,\Psi e^{i\vec{q}_0\cdot\vec{r}}+c.c.\right] + \ldots \qquad 1.1.1$$

with ρ_0 the average density, Ψ the amplitude of the modulation, and $q_0=2\pi/d$ where d is the average layer spacing. However, within the plane of the layers the molecules are fluid-like. Strongly dipolar materials, such as nCB, form bilayer smectics with a layer separation equal to about 1.3 times than length of an individual molecule. These mesogens have one aliphatic tail and a polar head group on the other end. Molecules with two aliphatic tails, such as $\bar{n}$S5 or nO.m, form single layer smectics with the layer separation approximately equal to the molecular length. Some materials with weak polar head groups exhibit both bilayer and single layer smectic ordering.

Below the smectic A phase, the smectic C phase often occurs in which the molecules tilt with respect to the layering direction but remain fluid within the plane of the layers. Lower temperature phases involve the development of various degrees of order within the plane of the layers including stacking sequences, tilt direction, bond orientational order and herringbone order. The advent of free standing x-ray scattering experiments have greatly facilitated the study of these phases.[6]

1.2
X-Ray Scattering Theory

This chapter serves as an overview of X-rays scattering as a structural probe of matter. A good review of x-ray scattering theory is provided by Warren.[7] In all scattering experiments momentum and energy are transferred between an incoming channel and an outgoing channel. For X-ray scattering an incident photon with momentum k_i and energy $E_i=\hbar k_i c$ is scattered by the sample and emerges with momentum k_f and energy $E_f=\hbar k_f c$. The momentum absorbed by the sample is $\vec{q}=\vec{k}_i-\vec{k}_f$ while the energy transferred is E_i-E_f as shown in figure 1.2.1.

For all of the problems of interest this energy difference is at least five orders of magnitude less than E_i, thus the scattering is considered as quasi-elastic in that $|k_i|\approx|k_f|$. Therefore, the momentum transferred can be expressed in terms of the incident momentum vector and the scattering angle relative to the incident angle

$$\vec{q} = 2\vec{k}_i \sin\theta \ , \qquad 1.2.1$$

where 2θ is the angular difference between the incident and outgoing photon. In reciprocal space, the magnitude of the momentum transferred is given by Eq 1.2.1, whereas the orientation of the momentum transferred in the scattering plane is given by ϕ as shown in figure 2.2.1. Bragg scattering occurs when $|\vec{q}|$ corresponds to a lattice vector of the sample.

The process of x-ray scattering can be treated classically by considering the radiation from an accelerated charge in a time varying electric field.[8] This mechanism yields the Thomson cross-section. To simplify the derivation polarization effects are ignored. Consider an

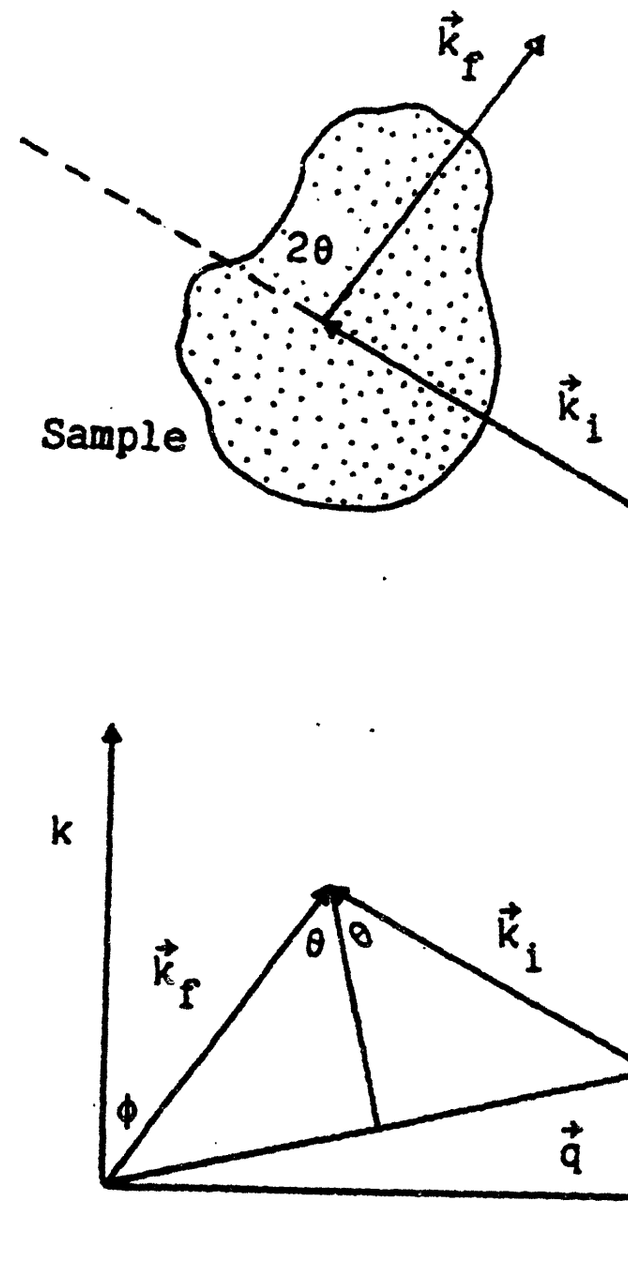

Figure 1.2.1

Top: X-ray scattering in real space.
Bottom: X-ray scattering in reciprocal space.

incident plane wave with wave vector k_i and energy $E_i = \omega_i c$.

$$E(\vec{x},t) = E_0 e^{i\vec{k}_i \times \vec{x} - i\omega_i t} \qquad 1.2.2$$

From the equation of motion for a particle of mass m and charge e,

$$\dot{v} = \frac{e}{m} E_0 \qquad 1.2.3$$

the accelerating particle radiates according to the standard form.

$$\frac{\partial P}{\partial \Omega} = \frac{e^2}{4\pi c^3} |\dot{v}|^2 \qquad 1.2.4$$

$$= \frac{c}{8\pi} E_0{}^2 \left[\frac{e^2}{mc^2}\right]^2 \qquad 1.2.5$$

If an unpolarized source is considered this result is modified by a factor of $\frac{1}{2}(1+\cos^2\theta)$. The factor $\frac{8\pi}{3}\left[\frac{e^2}{mc^2}\right]^2$ is the Thomson cross-section, σ_T. For electrons $\sigma_T = .665\times10^{-24}$ cm² whereas for protons the cross-section is more than a million times smaller since the cross-section goes as m^2. Therefore, it is only necessary to consider the scattering from electrons in the analysis of X-ray scattering experiments. A more thorough analysis would include the coherent addition of all the electrons amplitudes within an atom. Relativistic effects are minor because $E_i \ll mc^2$.

The scattering cross-section can be calculated quantum mechanically if the coupling to the electromagnetic field is included through the standard interaction Hamiltonian

$$H = \frac{\vec{A}^2}{2mc^2} + \frac{\vec{p}\cdot\vec{A}}{mc^2} \quad . \qquad 1.2.6$$

In the Born approximation the transition probability between the initial and final states is given by

$$P_{o\to\ell} = \frac{2\pi}{h}\left|\langle\psi_\ell e^{ik_f\cdot\vec{r}}|V(\vec{r})|\psi_o e^{ik_i\cdot\vec{r}}\rangle\right|^2 \delta(E_i-E_f-\hbar(\omega_i-\omega_f)) \qquad 1.2.7$$

where the probe is initially in the plane wave state $e^{i\vec{k}_i\cdot\vec{r}}$ and undergoes a transition to the final state $e^{i\vec{k}_f\cdot\vec{r}}$. For x-ray scattering the A^2 term dominates and the differential scattering cross-section reduces to

$$\frac{d^2\sigma}{d\Omega d\omega} = N\left[\frac{e^2}{mc^2}\right]^2 \left[\frac{\omega_f}{\omega_i}\right]^2 (\vec{\varepsilon}_i\cdot\vec{\varepsilon}_f)^2\, S(\vec{q},\omega) \qquad 1.2.8$$

where

$$S(\vec{q},\omega) = \frac{1}{2\pi\hbar N}\int dt\; e^{-i\omega t}\langle n(-\vec{Q},0)n(\vec{Q},t)\rangle \qquad 1.2.9$$

is the dynamic structure factor. Expressing the number operator (n) in terms of the density (ρ) and Fourier transforming yields the standard form for the dynamic structure factor

$$S(\vec{q},\omega) = \frac{1}{2\pi\hbar}\int dt d^3\vec{r}\; e^{i\vec{q}\cdot\vec{r}-i\omega t}\langle\rho(\vec{r},t)\rho(0,0)\rangle\ . \qquad 1.2.10$$

The determination of the dynamic structure factor is hindered by resolution functions which are imperfect by nature. The actual scattered intensity is proportional to the convolution of the dynamic structure factor and the resolution function

$$I(\vec{q},\omega) \propto \int d^3q' d\omega'\; R(\vec{q}-\vec{q}',\omega-\omega')\; S(\vec{q},\omega)\ . \qquad 1.2.11$$

In turn, the resolution function depends on the three components of momentum and energy transferred to the sample. It is adequate to assume that the resolution function is separable in terms of its four components

$$R(\vec{q},\omega) = R_x(q_x)R_y(q_y)R_z(q_z)R_\omega(\omega)\ . \qquad 1.2.12$$

It is convenient to normalize each element of the resolution function such that it has unit volume. If the resolution is perfect, i.e. a delta function, then $I(\vec{q}) \propto S(\vec{q})$. Equivalently, if $S(\vec{q})$ is a delta function then the scattered intensity has the same functional form as the resolution function. For all practical purposes the energy resolution function of the spectrometer, $R_\omega(\omega)$, is always much broader than the energy width of $S(\vec{q},\omega)$. Therefore, the spectrometer integrates over all energies of $S(\vec{q},\omega)$. From Eq 1.2.11 and 1.2.12 we have

$$I(\vec{q}) \;\alpha\; \int d^3q' \; R(\vec{q}-\vec{q}') \; S(\vec{q}) \qquad 1.2.13$$

where

$$S(\vec{q}) = \int d\omega \; e^{i\omega t} S(\vec{q},\omega) \qquad 1.2.14$$

is the instantaneous structure factor. In summary, x-ray scattering measures the Fourier transform of the electron-electron density distribution function convoluted with the appropriate instrumental resolution function. The actual form of the resolution function depends on the spectrometer set-up. Resolution functions for particular spectrometer configurations will be discussed in chapter 4.

1.3
Phase Transitions

Statistical mechanics is the study of many particles and their collective behavior. Equilibrium is achieved when the free energy of a system is minimized. A phase transition occurs when the state of the system must change to achieve equilibrium. This is extremely difficult to calculate exactly since the energies and degeneracies of all the states of the system must be summed over to determine the precise phase behavior. However there are many techniques which ignore these details but provide excellent approximations to the physical behavior. These theories provide a universal framework for the study of phase transitions. Some of the basic principles and results are summarized in this section. In the next chapter those techniques which relate to the nematic to smectic A transition are presented.

A) Mean Field Theory

All phase transitions can be described by an "order parameter" which is zero in the disordered phase and finite in the ordered phase[9,10] The free energy can be expanded in powers of the order parameter taking into account the appropriate symmetries. In many instances, such as the ferromagnet to paramagnet transition where the magnetization m is the order parameter, inversion symmetry only permits even terms. Therefore, the free energy density can be expressed as

$$f(m) = \sum_{n=0}^{n=\infty} \frac{a_n}{n} m^{2n} \qquad 1.3.1$$

where fluctuations have been ignored (mean field limit). Furthermore, close to the phase transition m is small, therefore the series can be

truncated after the first positive term. First consider the case where the a_4 term is positive, the free energy density is given by

$$f(m) = a_0 + \frac{a_2}{2} m^2 + \frac{a_4}{4} m^4 . \qquad 1.3.2$$

If a_2 is positive then the free energy density is a minimum when m=0, however if a_2 is negative then the free energy density is minimized when $m=(-a_2/a_4)^{1/2}$. Transitions of this kind are second order since the order parameter is continuous at the transition. At the phase transition the a_2 term must vanish, therefore, to lowest order in temperature

$$a_2 = a'_2 t \qquad 1.3.3$$

where the reduced temperature t is defined as

$$t = \frac{T-T_C}{T_C} . \qquad 1.3.4$$

The critical exponent β describes how the order parameter changes with temperature below the transition, i.e.

$$m(t) \propto |t|^{\beta} . \qquad 1.3.5$$

In the mean field limit, the magnetization is always zero on the high temperature side. If this model is extended to incorporate a linear coupling between an applied field and the magnetization, then the susceptibility

$$\chi = \partial m/\partial h \propto t^{-\gamma} \qquad 1.3.6$$

Within the context of this model the heat capacity undergoes a jump at the transition.

The second case occurs when the coefficient of the fourth order term a_4 is less than zero. In this case it is essential to include a positive coefficient of the sixth order term in a Landau expansion so that the free energy has a bounded minimum. This implies a first order rather than a second order transition since the order parameter is discontinuous at the transition. For a first order transition the equilibrium times can be very long since there is always a metastable state at zero magnetization.

The third and final case considered occurs when the coefficient of the fourth order term a_4 is exactly zero. The transition is referred to as tricritical. Again the first step is to expand the free energy in terms of a power series

$$f(m) = a_0 + \frac{a_2}{2} m^2 + \frac{a_6}{6} m^6 \qquad 1.3.7$$

stopping at the first positive coefficient. Minimizing the free energy with respect to the magnetization yields,

$$\beta = 1/4 \qquad 1.3.8$$

and

$$\gamma = 1 \ . \qquad 1.3.9$$

In addition to the jump in the heat capacity, there is a power law divergence for $T<T_c$ given by

$$C \propto t^{-\alpha} \ ; \quad \alpha = 1/2 \ . \qquad 1.3.10$$

Tricritical theory, beyond Landau theory, will be developed in the latter part of this chapter.

B) Harmonic Approximation

In most real systems gradient terms must be included in a free energy expansion. For the ferromagnet discussed above, including the lowest order gradient term permitted by symmetry considerations, the following form for the free energy is found.

$$F(m) = \int d^3\vec{x} \left[a_0 + \frac{a_2}{2} m(\vec{x})^2 + \frac{a_4}{4} m(\vec{x})^4 + c(\nabla m(x))^2\right] \qquad 1.3.11$$

This is known as the harmonic approximation. Note that the free energy density has been integrated over all space to account for the spatial variations of the magnetization. The magnetization can be expanded in terms of the average value which is spatially independent $m_0 = \langle m(\vec{r})\rangle$, and a spatially varying term $\delta m(\vec{r})$

$$m(\vec{r}) = m_0 + \delta m(\vec{r}) \ . \qquad 1.3.12$$

Just as before the average value of the magnetization on the high temperature side is zero. Keeping terms to order $(\delta m(\vec{r}))^2$, Fourier transforming and applying the equipartition theorem yields

$$F = \sum_{\{\vec{k}\}} V\langle \delta m(\vec{k})\delta m(-\vec{k})\rangle \left[a_2 + c_2 k^2\right] \qquad 1.3.13$$

where,

$$\langle \delta m(\vec{k})\delta m(-\vec{k})\rangle = \frac{K_B T}{V(a_2 + c_2 k^2)} \qquad 1.3.14$$

is the structure factor for magnetic fluctuations. If the system is translationally invariant, the Fourier transform of the structure factor defines the correlation function. For a Lorentzian profile in three dimensions the correlations fall off as

$$G(\vec{r}) \propto \langle m(\vec{r})m(\vec{0})\rangle = \frac{K_B T}{4\pi} \frac{e^{-r/\xi}}{r} \qquad 1.3.15$$

where

$$\xi = \sqrt{\frac{c_2}{a_2}} \qquad 1.3.16$$

is the correlation length which is the coherence length of fluctuations. It is useful to define the critical exponent ν which describes the divergence of the correlation length

$$\xi \propto t^{-\nu} \qquad 1.3.17$$

where ν is .5 in the mean field approximation. On the ordered side of the transition it is useful to define the large $|\vec{q}|$ limit of the structure factor by the exponent η,[11]

$$S(q) \propto q^{-2+\eta} , \qquad 1.3.18$$

where η is zero in Ornstein-Zernike limit.

A system which does not exhibit long range order is below its lower critical dimension. For instance, in many <u>two</u> dimensional systems such as continuous symmetry magnets the correlation function falls of algebraically; therefore the lower critical dimensionality is two. The smectic A phase is unusual since its lower critical dimensionality is three.

Mean field theory is applicable if the Ginzburg criterion is satisfied.[12,13] Below the transition, this condition is met if the fluctuations of the order parameter averaged over a correlation volume are less than the order parameter itself. The spatial dimension of the system where this occurs is the upper critical dimension. For instance, the Ginzburg criterion is satisfied for $d \gtrsim 4$ in the harmonic approximation. At an isotropic tricritical point the upper critical dimension is three. Below the upper critical dimensionality more

sophisticated methods must be employed to calculate the critical behavior. Such techniques include renormalization group methods and various series expansion methods.

C) Scaling and Renormalization Group

Inherent in the renormalization group approach is the concept of scaling. Scaling asserts that the long wavelength fluctuations are responsible for all of the singular behavior at the phase transition.[9,10] Accordingly, if the scale of the system changes by a factor ℓ, the singular part of the free energy should obey the homogeneity relation given by

$$G(\ell^{a_t} t, \ell^{a_H} H) = \ell G(t,H) \ . \qquad 1.3.19$$

Embedded in the scaling hypothesis is the assumption that there is only one relevant length scale. All other divergent quantities must scale as a power of ξ. From the scaling hypothesis the following scaling relationships emerge

$$2\beta = \nu(d-2+\eta) \qquad 1.3.20$$

$$\gamma = \nu(2-\eta) \qquad 1.3.21$$

$$2-\alpha = d\nu \qquad 1.3.22$$

where d is the dimensionality of the system. The final relationship, known as hyperscaling, provides a direct link between the dimensionality of the system and the critical exponents. In the next chapter extensions to the scaling hypothesis will be made to incorporate more than one diverging length scale.

Perhaps the most important contribution to the theory of critical phenomena is the renormalization group technique introduced by Wilson.[14] By starting at an atomic scale and moving to successively larger scales the effects of thermal fluctuations can be integrated out. At each step recursion relations for the coefficients of the free energy can be calculated as a function of the dimensionality. These techniques provide a prescription for calculating the critical exponents when mean field theory is inadequate.

D) Tricritical Phenomena

Tricritical behavior occurs when a line of second order transitions crosses over continuously to a line of first order transitions. At an ordinary critical point there is an ordering field and the temperature field, however, a nonordering field which drives the fourth order coefficient of the Landau expansion to zero must be considered at a tricritical point.[12,15] Unlike an ordinary critical point where only the ordering density fluctuates, at a tricritical point both the ordering and nonordering densities fluctuate.[16]

In the vicinity of the tricritical point it is necessary to introduce an additional scaling parameter, the crossover exponent ϕ, which relates how the critical behavior scales in different field directions. The crossover exponent determines the shapes of the critical line and the crossover lines to tricritical behavior. A crossover exponent of two is expected from mean field theory[12] and from renormalization group calculations.[17] These calculations are in good agreement with experiments on He_3-He_4 mixtures[18] mixtures and on metamagnets.[19] Renormalization group calculations also predict

logarithmic corrections to simple power law behavior, though current experiments have not been able to distinguish these effects.

Within the formalism of tricritical scaling it is necessary to introduce three pairs of conjugate variables. As might be expected, a rather diverse set of notation has been employed by different authors to maintain compatibility with ordinary critical theory and various real systems. For the purpose of this discussion we will follow the notation set forth by Griffith[20] where the three conjugate variables are: entropy density s and temperature T, ordering density M and ordering field H, and nonordering density Ψ and nonordering field ζ. To aid the reader familiar with a different notation Table 1.3.1 is provided. For instance, in systems exhibiting metamagnet-antiferromagnet transitions the ordering field and density are given by the staggered magnetic field and the staggered magnetization respectively, whereas the nonordering field and density are just the internal magnetic field and the ordinary magnetization. Likewise, for He^3-He^4 mixtures the nonordering field is the chemical potential difference between the two species $\mu_3 - \mu_4$ and the concentration of He^3 is the conjugate density. The ordering density is the superfluid order parameter Ψ, though the conjugate field is not experimentally accessible. This is also the case for the $N \rightarrow S_A$ tricritical point as developed in section 2.1.

In developing a Landau theory from microscopic interactions the coefficients of the order parameters must be functions of the field variables H and T. At $H=H_t$ the coefficient of the fourth order term in the expansion goes to zero. Furthermore, at the tricritical point $T=T_t$ the coefficient of the second order term is also zero. Consequently, the point (H_t,T_t) divides the first order line from the second order

NOTATION/SYSTEM	Griffiths	Riedel	He^3-He^4	Magnets	$N \to S_A$
Ordering Field	H	h	?	H_s	?
Ordering Density	M	m	ψ	M_s	ψ
Nonordering Field	ζ	g	$\mu_3-\mu_4$	H	n
Nonordering Density	ψ	n	x_3	M	δS

Table 1.3.1

Comparison between different notations useful in describing tricritical phenomena.

line thereby providing the link to Landau theory.

If the nonodering field is considered, the tricritical point is the intersection of three lines of second order transitions. The line of interest is in the H,T plane as shown in figure 1.3.1 whereas the other two lines do not lie in this plane. More importantly, for most real systems the field ζ is not physically accessible. Therefore, tricritical phenomena out of (H,T) plane will not be considered. In describing tricritical phenomena it is necessary to define three sets of exponents corresponding to the

1) First order
2) Second order
3) Tricritical

regions. For the second order region with $\zeta=0$ and H held fixed the critical exponents are given by α, β, γ, ... for $T>T_t$ and by α', β', γ', ... for $T<T_c$. According to the Pippard relations[21] the same exponents should apply if T is held fixed and H varied, ie.

$$\langle\Psi\rangle \propto (H-H_c)^{\beta} \qquad 1.3.23$$

where H_c is the critical field. Since the critical exponents are the same for both directions all linear paths which cross the λ line should provide the same exponents.

The critical exponents in the tricritical region are not the same as those along the λ line. A subscript t is used to denote the tricritical exponents. Once again, a prime indicates which side of the phase boundary the exponent represents. For instance, if $H<H_c$, $T=T_t$ and $\zeta=0$

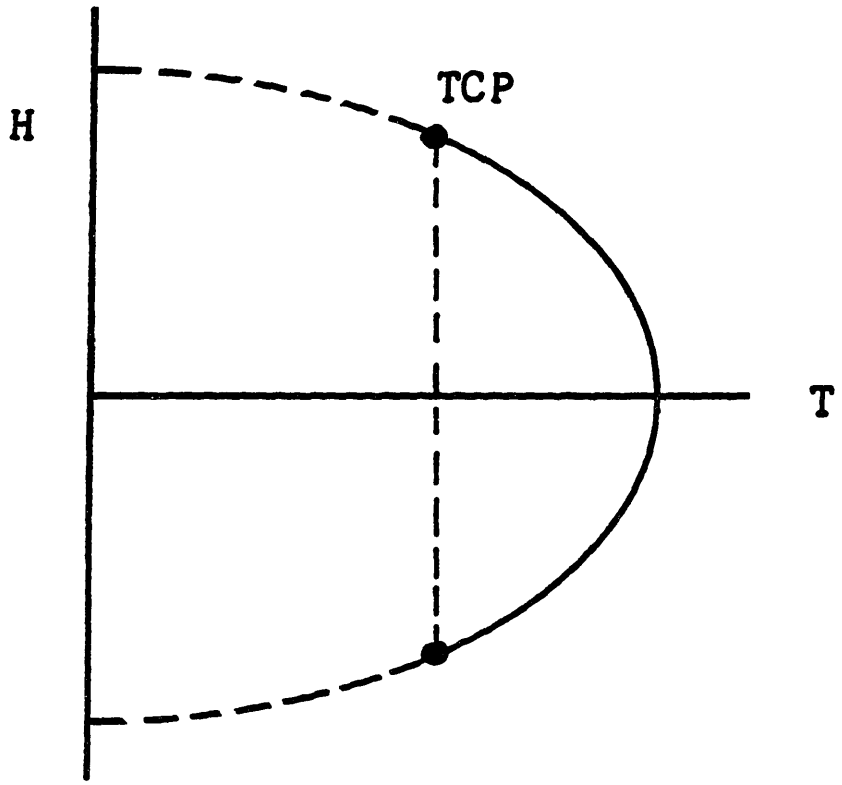

Figure 1.3.1

Phase diagram for an idealized tricritical system in the H and T plane. The tricritical point is the intersection of a first order line (dashed) and a second order line (solid). For instance, the nonordering field H corresponds to the internal magnetic field in metamagnets, the chemical potential difference $\mu_3-\mu_4$ in helium mixtures and pressure in NH_4Cl.

$$\langle\Psi\rangle \propto (H_t - H)^{\beta_t'} , \qquad 1.3.24$$

is the analogue of Eq 1.3.5.

Along the first order line the subscript u is used to denote the critical indices. The discontinuity of the magnetization is

$$\Delta M \propto (T_t - T)^{\beta_u} . \qquad 1.3.25$$

The indices with a u subscript describe the behavior of the nonordering density whereas the tricritical exponents refer to the ordering density. Far from the critical point the system should be described by one length scale, therefore one expects that

$$\xi_u = \xi_t . \qquad 1.3.26$$

The validity of this hypothesis must be reexamined for liquid crystal systems where two lengths scales are required.

Scaling at a tricritical point requires an additional exponent, the crossover exponent ϕ, since there is an additional field. The best choice for a coordinate system for tricritical scaling is not where H, ζ and T are all orthogonal. A more suitable choice is a coordinate system defined by

$$g = H - H_1(T) \qquad 1.3.27$$

$$\lambda = T - T_t \qquad 1.3.28$$

where $H_1(T)$ is the line which passes through the tricritical point lying tangent to the first and second order transition lines. This choice is not unique; however, different coordinate systems should not modify the result.

The singular part of the free energy in this new coordinate system should scale as

$$F_s(\ell^{\phi}\lambda, \ell g, \ell^{\Delta t}\zeta) = \ell^{2-\alpha t}\, F_s(\lambda, g, \zeta) \qquad 1.3.29$$

where phi is the crossover exponent. Likewise, the correlation function scales as

$$\Gamma(\ell\lambda, \ell^{\phi}g, \ell^{\phi\Delta t}\zeta; \ell^{-\nu t}\vec{r}) = \ell^{\phi\nu t\,(d-2-\eta t)}\Gamma(\lambda, g, \zeta; \vec{r}) \qquad 1.3.30$$

where ℓ is the size of the length rescaling and Δ is the gap exponent. By assuming continuity of the free energy and the correlation function scaling relationships on both sides of the tricritical point the following relationships emerge:

$$\alpha_u = 2-\phi(2-\alpha_t) \qquad 1.3.31$$

$$\beta_u = \phi(1-\alpha_t) \qquad 1.3.32$$

$$\nu_u = \phi\nu_t \qquad 1.3.33$$

as well as some additional relations among the various exponents. These relationships provide a test for tricritical scaling.

The renormalization group technique has been applied to tricritical behavior by Riedel and Wegner[17] and by Nelson and Fisher.[22] Despite the competition between the two densities they find that the tricritical point is mean field/Gaussian for $d \geq 3$, albeit logarithmic corrections for $d=3$. This is rather unusual since the upper critical dimensionality for an ordinary critical point is four!

Logarithmic corrections raised to a fractional power were first predicted by Wegner and Riedel[23] but were thought to be benign because the fractional power is small. Using higher order diagrams, Stephen et al. [24] found that the logarithmic corrections are non-universal since

they depend on the size of the sixth order term in Landau theory. More recently, Fisher and Sarbach[25] have examined tricritical behavior in the multi-component limit where $n \to \infty$. Again, the amplitude of the corrections are non-universal. Although experiments do agree with $\phi = 2$, they do not agree well with several of the other Gaussian tricritical predictions. For example, α_t is should be 1/2 though Shang and Salamon measure .65 in $FeCl_2$.[26] The same authors find agreement with the predicted value by adding logarithmic corrections. The discrepancy for β_u^- in $FeCl_2$ as measured by Birgeneau et al.[27] is even greater than the discrepancy for α_t. The origin of these deviations away from Gaussian behavior may be due to random-field effects rather than logarithmic corrections.[28]

REFERENCES

1. P.G. de Gennes, The Physics of Liquid Crystal (Clarendon, Oxford, 1974)

2. S. Chandrasekhar, Liquid Crystals (Cambridge University Press,Cambridge,1977)

3. J.D. Litster and R.B. Birgeneau, Physics Today, May 1982, and other articles contained within.

4. F. Reinitzer, Montash Chem.,9,421(1888); O. Lehmann, Z. Krist.,18,464(1890)

5. G. Friedel, Anns. Phys. 18,273 (1922)

6. D.E. Moncton and R. Pindak, Phys. Rev. Lett.,43,701(1979)

7. B.E. Warren, X-Ray Diffraction,(Clarendon Press, Oxford), 1971

8. See for example J.D. Jackson, Classical Electrodynamics (John Wiley, New York, 1975)

9. S.K. Ma; Modern Theory of Critical Phenomena; Benjamin; Reading,Mass.(1976)

10. H.E. Stanley, Introduction to Phase Transitions and Critical Phenomena; Oxford University Press, N.Y. and Oxford(1971)

11. M.E. Fisher; Journal of Mathematical Physics,5,944 (1964)

12. R. Bausch, Z. Physik 254 ,81(1972).

13. J. ALs-Nielsen and R.J. Birgeneau, Am. J. Phys. 45 ,554(1977)

14. K.G. Wilson, Phys. Rev. B 4 ,3174(1971) and Phys. Rev. B 4 ,3184(1971)
An excellent review of the renormalization group is found in K.G. Wilson, Rev. of Mod. Phys., 55 ,583(1983)

15. R.B. Griffiths and J.C. Wheeler, Phys. Rev. A 2 , 1047(1970)

16. E.K. Riedel, Phys. Rev. Lett. 28 , 675(1972)

17. E.K. Riedel and F.J. Wegner, Phys. Rev. Lett. 29 ,349(1972) and Phys. Rev. B 9 ,294(1974)

18. E.K. Riedel, H. Meyer, and R.P. Behringer, J. Low Temp. Phys. 22 ,369 (1976), and references cited therein.

19. N. Giordano, Phys. Rev. B 14 ,2927(1976)

20. R.B. Griffiths, Phys. Rev. B 7 ,545(1973)

21. A.B. Pippard, Elements of Classical Thermodynamics (Cambridge U.P., Cambridge, England, 1957), Chapter 9

22. David Nelson and Michael Fisher, Phys Rev. B 11 ,1030(1975)

23. F.J. Wegner and E.K. Riedel, Phys. Rev. B 7 ,2481(1973).

24. M.J. Stephen, E. Abrahams, and J.P. Straley, Phys. Rev. B 12 ,256(1975)

25. M.E. Fisher and S. Sarbach, Phys. Rev. Lett., 41 ,1127(1978) and S. Sarbach and M.E. Fisher, Phys. Rev. B 18 ,2350(1978)

26. H.T. Shang and M.B. Salamon, Phys. Rev. B 22 ,4401(1980).

27. R.J. Birgeneau, G. Shirane, M. Blume, and W.C. Koehler, Phys. Rev. Lett. 33 ,1098(1974)

28. R.J. Birgeneau and A.N. Berker, Phys. Rev. B 26 ,3751(1982)

2.0
Theoretical Approaches to the $N \rightarrow S_A$ Transition

Many new theoretical ideas have been proposed to understand the $N \rightarrow S_A$ transition, and at the same time experimental techniques have been improved. This chapter serves to review these theoretical concepts for the reader. Unfortunately, these new theories do not adequately explain the old experimental results (chapter 3) nor do they address many of the new results presented here (chapter 5).

This chapter is arranged into four sections. The first section presents a mean-field approach and an analogy to tricritical phenomena. In the next section the De Gennes theory of the $N \rightarrow S_A$ transition is reviewed. Gauge transformation techniques which predict anisotropic critical behavior are presented in the third section. In the final section the $N \rightarrow S_A$ transition will be discussed in the language of dislocation mediated melting.

2.1
Mean Field and Tricritical Predictions for the $N \rightarrow S_A$ Transition

Prior to the development of the DeGennes free energy for the $N \rightarrow S_A$, mean-field theory provided the best theoretical framework for the understanding of this problem. Mean field theory, which calculates the order parameters self consistently, was developed independently by McMillan[1] and Kobayashi.[2] Although this theory does not provide an adequate description of the critical behavior, it is useful in constructing the proper phase diagram. Furthermore, mean-field theory correctly predicts a crossover from a transition with zero latent heat to a first order transition with finite latent heat as the nematic range is shortened. However, the predicted crossover point is incorrect.

The starting point of all self-consistent mean-field calculations is to describe the potential in terms of both a global order parameter and the local order. Then, the average value of the order parameter is determined self consistently from the partition function. It is useful to review the self-consistent calculations of Maier and Saupe[3] for the nematic to isotropic transition since the McMillan theory for the nematic to smectic A transition is an extension of this important earlier work.

If the nematogens are assumed to be simple rods, then the states $\vec{n}(\vec{r})$ and $-\vec{n}(\vec{r})$ are indistinguishable. Therefore, the order parameter should not depend on the sign of the director. Thus, the nematic order parameter is composed of a traceless tensor and a scalar contribution. The scalar part is defined to be

$$S(T) = \langle \tfrac{3}{2}\cos^2\theta - \tfrac{1}{2} \rangle \qquad 2.1.1$$

where θ is the angle between the optical axis and the local director $\vec{n}(\vec{r})$. Maier and Saupe pointed out that the simplest form of the potential must be proportional to $\cos^2\theta$. In the mean-field approximation the potential close to the N→I transition is written as

$$V_{NI}(\cos^2\theta) = -V_0(\tfrac{3}{2}\cos^2\theta-\tfrac{1}{2})S(T) \qquad 2.1.2$$

where the temperature scale is set by V_0. The molecular distribution function is given by

$$p(\cos^2\theta) = p_0\, e^{\frac{V_0 S(T)}{k_B T}\langle\frac{3}{2}\cos^2\theta-\frac{1}{2}\rangle} \qquad 2.1.3$$

where p_0 is the appropriate normalization factor. Using Eq 2.1.3 S(T) is calculated self-consistently by

$$S(T) = \int_{-1}^{1} p(\cos^2\theta)\ \langle\tfrac{3}{2}\cos^2\theta-\tfrac{1}{2}\rangle\ d(\cos(\theta)) \qquad 2.1.4$$

Above the critical temperature $S(T>Tc)=0$. At the critical point, however, $S(T=Tc)=0.44$. As the temperature is decreased further, the nematic order parameter slowly increases. These basic features of the Maier-Saupe model have been confirmed by NMR measurements[4] though other features such as the first order region do not agree.

McMillan[1] has extended the Maier-Saupe theory to include a short range anisotropic interaction.

$$V_{NA} = -V_0[S(T)+\sigma\,\alpha\cos(\vec{q}_0\cdot\vec{r})](\tfrac{3}{2}\cos^2\theta-\tfrac{1}{2})\ . \qquad 2.1.5$$

The coefficient α is a measure of the smectic condensation energy and depends on chain length. The order parameter σ describing the smectic density wave is given by

$$\sigma = \langle \cos(\vec{q}_0 \cdot \vec{r}) \; (\tfrac{3}{2}\cos^2\theta - \tfrac{1}{2}) \rangle \qquad 2.1.6$$

where $\vec{q}_0$ is the momentum vector. This provides two self-consistentcy equations for the two order parameters. Three possible phases exist: an isotropic phase with $\sigma = S = 0$, a nematic phase with $\sigma = 0$, $S \neq 0$ and a smectic phase with $\sigma \neq 0$, $S \neq 0$.

The solutions are found by minimizing the free energy while maintaining the self-consistent condition on the two order parameters. The nematic to isotropic transition temperature does not depend on α whereas T_{NA}/T_{NI} does. Within the context of this model, if $T_{NA}/T_{NI} < 0.88$ the $N \rightarrow S_A$ transition has no latent heat and both the nematic and smectic order parameters are continuous at the transition. However, if $T_{NA}/T_{NI} > 0.88$ there is a finite latent heat and the nematic and smectic order parameters are discontinuous at the transition. Although these general features agree with experimental results the crossover point between first and second order is found to occur at a much larger T_{NA}/T_{NI}.

In summary, McMillan predicts a crossover from second order to first order behavior with increasing chain length though there are no predictions for the critical exponents. However, within the context of mean-field theory $\gamma = 1$; $\nu_{\parallel} = \nu_{\perp} = .5$ is expected.

The coupling between the nematic and smectic order parameters can be incorporated into a Landau Theory without fluctuations as described by DeGennes. This is analogous to the Rodbell Bean effect[5] in magnetism where the magnetization and density couple strongly to drive the transition first order if the crystal is very compressible. In the

liquid crystal case the smectic ordering enhances the nematic ordering if the nematic ordering is unsaturated, thereby causing a first order transition. The ideas which follow do not include fluctuation effects.

Ordering in the nematic phase is described by the Maier-Saupe order parameter $S_0(T)$, Eq 2.1.1, where the subscript denotes the equilibrium value without any smectic ordering. The smectic order parameter is the strength of the density modulation,

$$\rho = \rho_0\left[1+\frac{1}{\sqrt{2}}\Psi e^{i\vec{q}_0\cdot\vec{r}}+c.c.\right] + \ldots \qquad 2.1.7$$

where $\vec{q}_0$ is the wave vector of the layer spacing. If the nematic order parameter is at its equilibrium value, the free energy close to the $N\rightarrow S_A$ transition can be expanded in terms of Ψ alone

$$F_S = a_0 + \frac{a_2}{2}|\Psi|^2 + \frac{a_4}{4}|\Psi|^4 . \qquad 2.1.8$$

The coupling between Ψ and $S(T)$ must be incorporated to lowest order in the free energy. Since the coupling increases $S(T)$ from the equilibrium value $S_0(T)$ in the absence of coupling (i.e. absence of smectic layers), the lowest order additional correction term is

$$F_C = -C|\Psi|^2\delta S \qquad 2.1.9$$

where

$$\delta S = S - S_0(T). \qquad 2.1.10$$

Finally, in the absence of smectic fluctuations, the free energy minimum must correspond to $\delta S = 0$, therefore the final form of the free energy is

$$F_{NA} = F_S - C|\Psi|^2\delta S + \frac{1}{2\chi}\delta S^2 . \qquad 2.1.11$$

Here χ is a measure of how susceptible the nematic order parameter is to

an induced change from its equilibrium value. Minimizing Eq 2.1.11 with respect to δS gives

$$\delta S = \chi C|\Psi|^2 \qquad 2.1.12$$

which is the jump in the nematic order parameter at the transition. From Eq 2.1.12 and Eq 2.1.11 a new free energy is obtained in terms of of Ψ alone:

$$F_{NA} = a_0 + \frac{a_2}{2}|\Psi|^2 + \frac{a_4'}{4}|\Psi|^4 \qquad 2.1.13$$

where the coefficient of the fourth order term is:

$$a_4' = a_4 - 2C^2\chi. \qquad 2.1.14$$

For long nematic ranges the nematic order parameter is reasonably well saturated at the $N \rightarrow S_A$ transition, therefore, the susceptibility must be small for δS to be small. As the nematic range decreases the susceptibility must increase. Eventually the susceptibility becomes large enough to change the sign of the fourth order term from positive to negative, thus the order of the transition changes from second order to first order. For nematic ranges where the fourth order term is small tricritical behavior should occur.

Although the above analysis only includes a coupling between the nematic and smectic order parameters other couplings can have the same effect. Other possible order parameters which might couple to Ψ include higher harmonics of the density modulation as discussed by Meyer and Lubensky[6] , higher harmonics of the nematic order parameter, pressure[7] , and impurities. Experiments on materials where there is a strong coupling between the single layer order parameter and the bilayer order parameter are currently under progress at Harvard.[8]

If tricritical behavior occurs rather than ordinary critical behavior, a nonordering field and the conjugate density must be considered in addition to the ordering field and density. For the $N \rightarrow S_A$ transition, following the notation set forth in section 1.3, the smectic order parameter ψ is the ordering field however, as is the case for helium mixture the nonordering field is not physically accessible. Alben[9] has pointed out that the chain length acts as a nonordering field since a crossover from first to second order can be induced by varying the chain. Unlike tricritical points in metamagnets where the internal field is impossible to measure or in helium mixtures where the chemical potential can not be varied independently, the nonordering field can be continuously adjusted by mixing a compound with a first order transition with a compound with a second order transition.

Brisbin et al.[10] point out that δS acts as a nonordering density. Thus, the $N \rightarrow S_A$ tricritical point should be characterized by fluctuations in ψ and in δS. The field conjugate to δS must tend to align the nematic director such as a strong electric or magnetic field. Alignment may also be accomplished by varying the chain length; the chain length acts as the nonordering field and δS acts as the conjugate density.

There are several important differences between an ordinary tricritical phase diagram such as in helium mixtures or in magnets as shown in figure 1.3.1 and the $N \rightarrow S_A$ analogy which is shown in figure 2.1.1. Unlike an ordinary tricritical phase diagram where the λ line occurs for temperatures above the tricritical point, the second order line is reversed with the first order line for the $N \rightarrow S_A$ problem. The identification of δS as the nonordering density and the chain length as

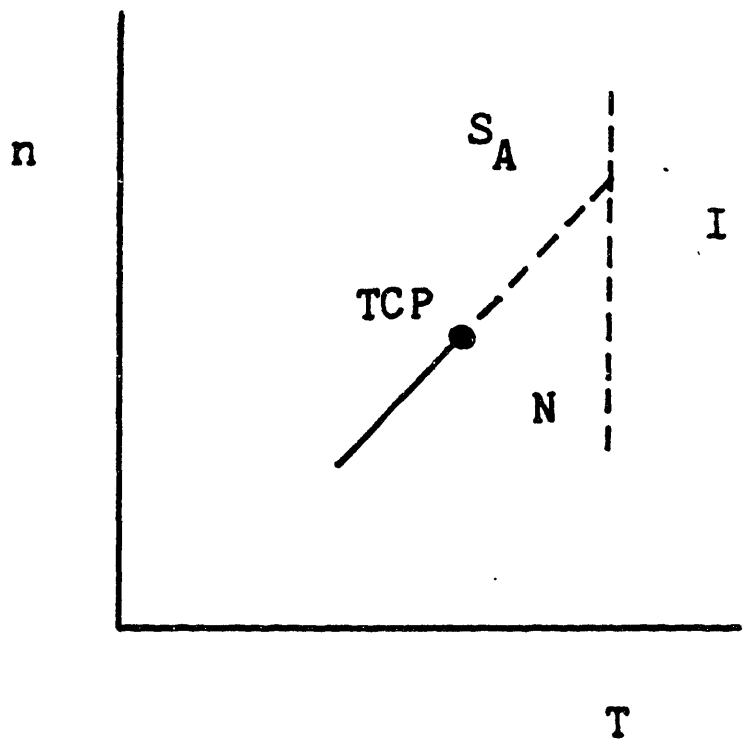

Figure 2.1.1

Phase diagram of the $N \rightarrow S_A$ problem in terms of the nonordering field (n) and the temperature (T).

the nonordering field raises several interesting issues. Compared with metamagnets, where there is a competition between ferromagnetic and antiferromagnetic order, the liquid crystal case is opposite. In the liquid crystal problem, increasing S tends to enhance the smectic ordering, whereas increasing the ordinary magnetization decreases the antiferromagnetic magnetization. This difference may be essential in developing an understanding of the $N \rightarrow S_A$ tricritical point.

The coexistence behavior is also rather different from an ordinary tricritical point. On the first order side of the tricritical point two phases with different densities should coexist. Presumably, regions with different values of δS will phase separate into macroscopic regions. Unlike helium mixtures where a meniscus forms between the two regions, the density difference between these two liquid crystal phases is too small and the viscosity too large for this to occur. Impurities may also influence the phase separation, however these effects are poorly understood in the vicinity of a tricritical point. Observations of the coexistence behavior may be impaired since a macroscopic probe such as light scattering is only capable of measuring the average δS and not the difference between the two coexisting phases.

If there is only one relevant length scale the ordering density correlation length , i.e. the smectic correlation length, scales as the nonordering correlation length then the tricritical scaling relationship $\nu_u = \phi \nu_t$ should apply. Unfortunately the δS correlation length can not be measured with x-rays nor is it obvious what probe would be suitable. Furthermore, there is no a priori reason why one length scale should provide an adequate description of the $N \rightarrow S_A$ problem (see section 2.3).

2.2
DE GENNES MODEL

In this section the De Gennes free energy for the $N \rightarrow S_A$ transition is developed.[11] Prior to this point of the analysis, fluctuations of the nematic and smectic order parameters, S(T) and Ψ, have been ignored. To incorporate spatial variations a phenomenological free energy is developed which includes the lowest order elastic energies. In many respects the smectic A free energy is analogous to the charged superfluid. An important difference which will emerge is that the smectic A phase does not have true long range order.

In the McMillan model, as presented in the previous section, the $N \rightarrow S_A$ critical exponents should be mean-field, $\nu_\perp = \nu_{\parallel} = \nu = 0.5$; $\gamma = 1.0$. However, in the De Gennes analogy the $N \rightarrow S_A$ problem is in the n=2, D=3 universality class with $\nu_\perp = \nu_{\parallel} = \nu = 2/3$; $\gamma = 1.32$. This analogy ignores the inherent anisotropies of the $N \rightarrow S_A$ free energy which are responsible for the observed anisotropic behavior with $\nu_\perp \neq \nu_{\parallel}$. Anisotropic behavior is predicted by a dislocation mediated melting model and gauge-transformation techniques. Both theories build on the De Gennes free energy and will be discussed in subsequent sections.

The deformations of the director in the nematic phase can be described by a continuum theory in terms of simple elastic constants. This theory is only valid in the limit that the distortions are slow on a molecular scale, that is, $\nabla\vec{n}(\vec{r}) \ll 1/d$. The free energy must be even in terms of $\vec{n}(\vec{r})$ as discussed in section 1.1. Furthermore there can be no terms linear in $\nabla\vec{n}(\vec{r})$. To order $[\nabla\vec{n}(\vec{r})]^2$ the distortion free energy is expressed in terms of three elastic constants, K_1, K_2, and K_3 as developed by Oseen and Frank.[12]

$$F_N(K_i) = \tfrac{1}{2}\int d^3x[K_1(\nabla\cdot\vec{n}(\vec{r}))^2+K_2(\vec{n}(\vec{r})\cdot\nabla\times\vec{n}(\vec{r}))^2+K_3(\vec{n}\times(\nabla\times\vec{n}(\vec{r})))^2] \quad 2.2.1$$

These distortions correspond to <u>splay</u> , <u>bend</u> , and <u>twist</u> as shown in figure 2.2.1. Far from either the $N\rightarrow S_A$ or $N\rightarrow I$ transitions, the elastic constants are $\approx 10^{-7}$ dynes. In the following analysis the average value of the director, $\vec{n}_0=\langle\vec{n}(\vec{r})\rangle$, is assigned to the parallel ($\parallel$) direction. Transverse to $\vec{n}_0$ is the $\perp$ direction. To lowest order, the deviations of the director are transverse to $\vec{n}_0$, and given by

$$\delta\vec{n}(\vec{r}) = \vec{n}(\vec{r})-\vec{n}_0 \quad 2.2.2$$

where,

$$\delta\vec{n}\cdot\vec{n}_0=0. \quad 2.2.3$$

In the smectic A phase uniform rotations of the layers and the molecules must leave the free energy unchanged. Including terms through order $|\delta n|^2$ and $|\nabla\Psi|^2$, where Ψ is defined by Eq 2.2.7, yields the De Gennes free energy

$$F_D = \int d^3x[a|\Psi|^2 + C_{\parallel}|\nabla_{\parallel}\Psi|^2 + C_{\perp}|(\nabla_{\perp} - iq_0\delta n)\Psi|^2 + \tfrac{1}{2}b|\Psi|^4] \quad 2.2.4$$

The total free energy must also include the contribution from Eq 2.2.1. Molecules are kept parallel to the layers through the $C_{\perp}$ term which vanishes at the $S_A\rightarrow S_C$ transition. Higher order terms are required to preserve global rotational invariance; however, these terms are believed to be irrelevant close to the $N\rightarrow S_A$ transition and are ignored in future analysis.[13] The transition proceeds, in the normal Landau sense, when the coefficient of $|\Psi|^2$ goes to zero.

$$a = a'\left[\frac{T - T_{NA}}{T_{NA}}\right] = a't \quad 2.2.5$$

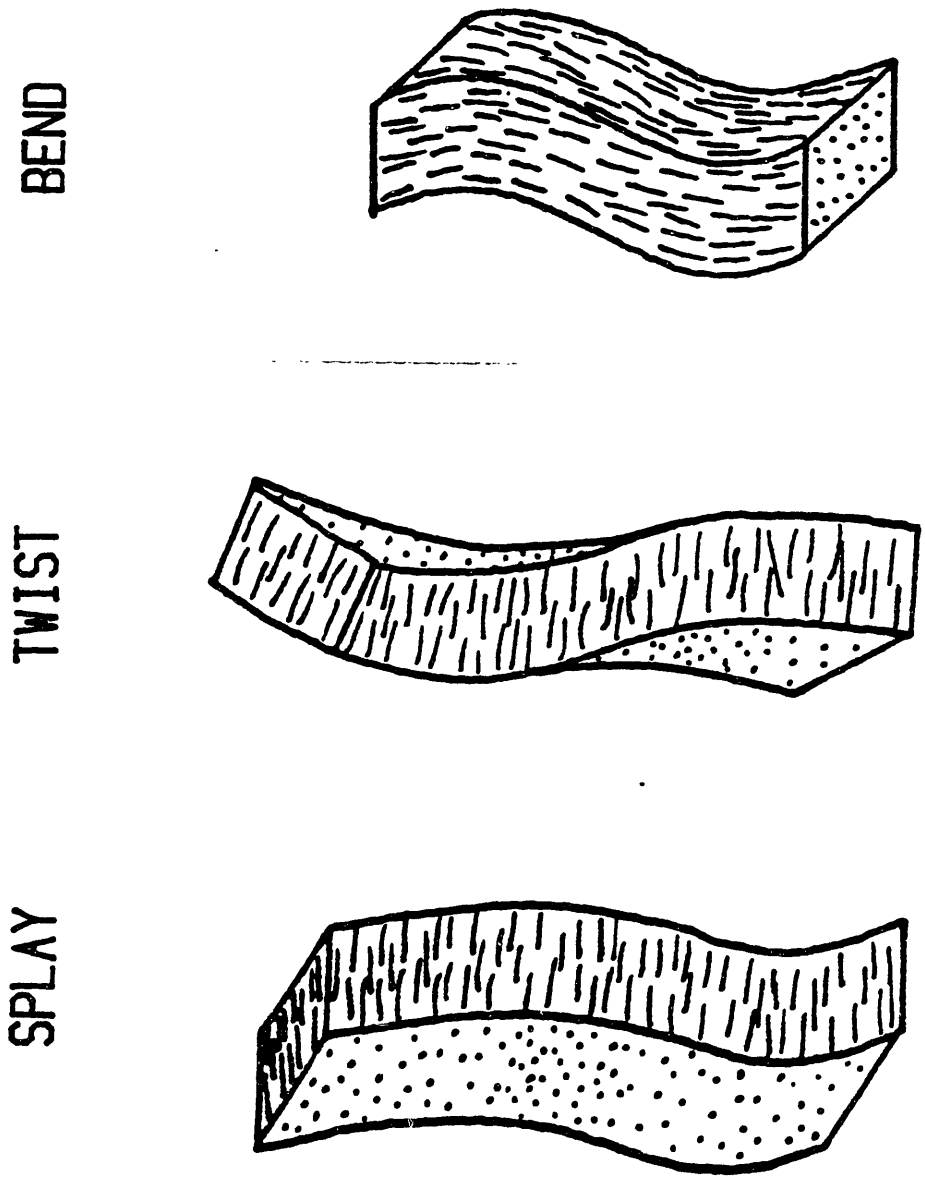

Figure 2.2.1 The three types of nematic distortions. Each type of deformation is obtained by distorting a slab of an aligned nematic.

Summing the nematic free energy, Eq 2.2.1, and the smectic free energy, Eq 2.2.3 produces the total free energy

$$F_{NA} = F_D + F_N(K_i) \quad . \quad . \qquad 2.2.6$$

All configurations are summed over in calculating the partition function,

$$Z = \int D\Psi D\delta n e^{-F_{NA}/kT} \quad .; \qquad 2.2.7$$

In practice, the variables of integration are always in q space.

In the smectic A phase, the smectic order parameter, Ψ, is described in terms of a magnitude and a phase

$$\Psi(\vec{x}) = |\Psi| e^{iq_0 u(\vec{x})} . \quad . \qquad 2.2.8$$

The phase, $q_0 u(\vec{x})$, reflects the displacement, $u(\vec{x})$ from equilibrium. Substituting Eq 2.2.8 into Eq 2.2.6 provides the smectic A free energy in terms $u(\vec{r})$,

$$F_A = 1/2 \int d^3x \, [B(\nabla_{\parallel} u)^2 + D(\nabla_{\perp} u - \delta n)^2] + F_N(K_i). \qquad 2.2.9$$

The elastic constants for the layer displacements along and transverse to the layering direction are given by

$$B = 2C_{\parallel} q_0^2 |\Psi|^2 \qquad 2.2.10$$

and

$$D = 2C_{\perp} q_0^2 |\Psi|^2. \qquad 2.2.11$$

There are many theoretical predictions which originate from the De Gennes free energy. These include the divergence of the bend and twist elastic constants on the nematic side of the transition and the lack of true long-range order in the smectic phase.

In the smectic phase, the line Integral, $\frac{1}{d}\int\vec{n}(\vec{r})\cdot d\vec{l}$, counts the number of layers. Thus, the closed loop integral must be zero in a <u>dislocation free sample</u>, therefore $\vec{\nabla}\times\vec{n}(\vec{r})=0$ in the bulk. Bend and splay distortions must correspond to dislocations! The energy associated with breaking layers is much greater in the smectic phase, therefore an enhancement of these elastic constants is expected from the development of the smectic density wave.

The enhancement of K_2 and K_3 in the nematic phase are analogous to fluctuation diamagnetism in superconductors. Just as the magnetic field is expelled from the superconductor, K_2 and K_3 are expelled at the $N\rightarrow S_A$ transition. The size of the dislocation free smectic corresponds to the smectic correlation lengths in the nematic, $\xi_\perp$ and ξ_{11}. Following Schmid's analysis for fluctuation diamagnetism[14] one finds,

$$K_2 = K_2^{\,0} + \delta K_2, \qquad 2.2.12$$

and,

$$K_3 = K_3^{\,0} + \delta K_3, \qquad 2.2.13$$

where the elastic constant enhancements are related to the correlation lengths via,

$$\delta K_2 \propto \frac{\xi_\perp^{\,2}}{\xi_{11}} \qquad 2.2.14$$

and,

$$\delta K_3 \propto \xi_{11} \ . \qquad 2.2.15$$

These relations provide a direct link between the correlation lengths as measured by x-rays and the elastic constants determined by light scattering measurements. The exact behavior of δK_2 and δK_3 depends on

the precise behavior of the correlation lengths. If the correlation lengths are isotropic both elastic constants should diverge at the same rate. However, anisotropic behavior would be manifested by different rates of divergence. In contrast to these relations, Eq 2.2.14 and Eq 2.2.15, Lubensky has shown that the correlation lengths observed by x-rays may not be the same correlation length as those characterizing the divergence of the elastic constants.[15] This is a consequence divergent phase fluctuations and will be discussed in the following section.

In the smectic A phase, the molecules would prefer to be normal to the layers. This is satisfied when $\vec{n}(\vec{r})=\vec{\nabla}_{\perp}u$ which eliminates the D term in the free energy.This assumption is only valid on length scales smaller than $\lambda=\sqrt{\frac{K_1}{D}}$. Furthermore, in a dislocation free smectic A phase bend and twist distortions are expelled from the bulk and only splay distortions are permitted. Thus, in the smectic A phase the free energy, Eq 2.2.9, reduces to

$$F_{LP} = 1/2 \int d^3x \left[B(\nabla_{\parallel}u)^2 + K_1(\nabla_{\perp}^2u)^2\right] \qquad 2.2.16$$

which is often referred to as the Landau-Peierls free energy.[16]

Fourier transforming Eq 2.2.16 and applying the equipartition theorem yields the spectrum for fluctuations of the layer displacement in q space

$$\langle|u(q)|^2\rangle = \frac{k_BT}{Bq_{\parallel}^2 + K_1q_{\perp}^4} . \qquad 2.2.17$$

Transforming to real space gives the mean squared layer displacement

$$\langle u^2(r)\rangle = \frac{V}{(2\pi)^3} \int d^3q \, \langle|u(q)|^2\rangle \qquad 2.2.18$$

$$= \frac{V}{(2\pi)^3} \int \frac{dq_{\parallel} d^2q_{\perp}}{Bq_{\parallel}^2 + K_1 q_{\perp}^4} \qquad 2.2.19$$

$$= \frac{K_B T \pi}{(2\pi)^3 \lambda B} \int \frac{dq_{\parallel} q'}{q_{\parallel}^2 + q'^2} \qquad 2.2.20$$

where $q'^2 = \frac{K_1}{B} q_{\perp}^4 = \lambda^2 q_{\perp}^4$. From Eq 2.2.20 is clear that the mean squared displacements for the Sm A phase are isomorphic to the two-dimensional system. Integrating Eq 2.2.20 provides the standard result that the correlation function diverges logarithmically with the sample size[17,18,19]

$$\langle |u(q)|^2 \rangle = \frac{K_B T}{4\pi\lambda B} \ln(L/d) \quad . \quad . \qquad 2.2.21$$

This, of course, comes about because of the lack of a $q_{\perp}^2$ term in the free energy.

The correlation function is defined as

$$G(r) = \langle \Psi(r) \Psi^*(r) \rangle \qquad 2.2.22$$

where all spatial dependence is contained in the phase of Ψ. Therefore, the correlation function can be rewritten as

$$G(r) = |\psi|^2 \langle e^{iq_0[u(r)-u(0)]} \rangle . \qquad 2.2.23$$

It is important to emphasize that on the nematic side, where $\langle\psi\rangle=0$, Ψ is spatially dependent as well as the phase. The harmonic nature of the fluctuations permits further simplification of the correlation function

$$G(r) = |\psi|^2 \, e^{-\frac{1}{2} q_0^2 \langle u^2 \rangle} \quad . \qquad 2.2.24$$

This assumption may not be valid in the nematic phase where fluctuations are always large. Substituting Eq 2.2.17 into Eq 2.2.24 yields

$$G(r)=|\psi|^2 e^{\frac{1}{2}q_0^2\int\frac{d^3q}{(2\pi)^3}\frac{1}{Bq_{\parallel}^2+K_1q_{\perp}^4}(1-e^{i\vec{q}\cdot\vec{r}})} \quad . \qquad 2.2.25$$

At large distances, Caille reports that the correlation function should go as

$$G(r) \propto r_{\parallel}^{-\eta} \; ; \quad r_{\perp} = 0 \qquad 2.2.26$$

and

$$G(r) \propto r_{\perp}^{-2\eta} \; ; \quad r_{\parallel} = 0 \qquad 2.2.27$$

where

$$\eta = \frac{q_0^2 K_B T}{8\pi\sqrt{K_1 B}} \quad . \qquad 2.2.28$$

This is the standard result along the layering direction although in the plane of the layers there is an additional factor of 2. Note that there is only one η for both directions and this η depends only on fundamental elastic constants, K_1 and B corresponding to splay and layer compression. Fourier transforming yields the structure factor for the smectic A phase

$$S(q) \propto |q_{\parallel}-q_0|^{-2+\eta} \qquad 2.2.29$$

$$S(q) \propto |q_{\perp}|^{-4+2\eta}. \qquad 2.2.30$$

It is important to emphasize that the structure factor diverges when $\eta=2$ and that this occurs somewhere below the transition when B is sufficiently large. This behavior is certainly unphysical because the susceptibility is predicted to diverge not only at T_{NA} but also at an additional temperature somewhere below the transition. There is nothing inherent in the De Gennes model to prevent this from occurring.

2.3
Anisotropic Scaling and Gauge Transformations

The scaling hypothesis asserts that all intrinsic properties associated with the phase transition scale with the correlation length. Though there may be several correlation lengths in different directions due to anisotropic interactions they are related by a fixed scale factor. The $N \rightarrow S_A$ problem is unusual since it appears that more than one length scale is necessary to describe the critical behavior. In other words, the correlation length along the layering direction and transverse to the layering direction appear to develop at different rates with reduced temperature. Anisotropic critical behavior is also expected for directed percolation[20] and possibly for (3 x 1) structures adsorbed on uniaxial surfaces.[21]

Following the analysis of Lubensky and Chen[22] we now develop the theory of anisotropic scaling at the $N \rightarrow S_A$ transition. The starting point is to introduce two correlation length exponents via

$$\xi_{\parallel} \propto |t|^{-\nu_{\parallel}} \quad \text{and} \quad \xi_{\perp} \propto |t|^{-\nu_{\perp}} . \qquad 2.3.1$$

For isotropic scaling $\nu_{\parallel}=\nu_{\perp}$, otherwise, a dimensionless representation of the anisotropy is given by

$$\mu = \frac{\nu_{\parallel}}{\nu_{\perp}} - 1 \qquad 2.3.2$$

If the elastic constant K_1 remains constant at the transition, it must appear explicitly in the scaling relationships. This provides the following homogeneity relationships,

$$G(q_{11},q_{\perp},t,K_1) = b^{2-\eta_{\perp}}G(b^{(1+\mu)}q_{11},bq_{\perp},b^{1/\nu_{\perp}}t,b^{-\tau}K_1) \qquad 2.3.3$$

$$D_{ij}(q_{11},q_{\perp},t,K_1) = b^{2-\eta_n}D_{ij}(b^{(1+\mu)}q_{11},b^{q_{\perp}},b^{1/\nu_{\perp}}t,b^{-\tau}K_1) \qquad 2.3.4$$

$$f(t,K_1) = b^{-(1+\mu)},b^{-(d-1)}f(b^{1/\nu_{\perp}}t,b^{-\tau}K_1) \qquad 2.3.5$$

where b corresponds to the length rescaling. It can be shown that $\tau = \eta_n$.

From these homogeneous relations a number of new scaling relationships are found. The isotropic scaling relationships between γ, ν, ξ transform to

$$\gamma = (2-\eta_{11})\xi_{11} = (2-\eta_{\perp})\xi_{\perp} \ . \qquad 2.3.6$$

If $\eta_{11} \neq \eta_{\perp}$ then the scattering in different directions should have different line-shapes. The hyperscaling relationship Eq 1.3.22 must be modified to

$$2-\alpha = \nu_{11}+2\nu_{\perp} \qquad 2.3.7$$

in three dimensions. These homogeneous relations also predict the scaling form of the elastic constants for K_2 and K_3 in agreement with the Schmid analogy to superconductivity and relationships for B and D which are

$$\delta K_2 \propto \xi_{11} \qquad 2.3.8$$

$$\delta K_3 \propto \frac{\xi_{\perp}^{2}}{\xi_{11}} \qquad 2.3.9$$

$$B \propto \frac{\xi_{11}}{\xi_{\perp}^{2}} \qquad 2.3.10$$

$$D \propto \frac{1}{\xi_{11}} \ . \qquad 2.3.11$$

in three dimensions.

When the renormalization group is applied to the De Gennes free energy, the following recursion relationship for K_1 is obtained[22]

$$\frac{\partial K_1}{\partial \ell} = -(\varepsilon-\mu)K_1 \qquad 2.3.12$$

Furthermore, at the fixed point K_1 must not depend on the scale, therefore, at least one of the following conditions must be satisfied for K_1^* which is the renormalized K_1.

$$1)\quad K_1^* = 0 \qquad 2.3.13$$

$$2)\quad K_1^* = \infty \qquad 2.3.14$$

$$3)\quad \varepsilon = \mu \qquad 2.3.15$$

If $K_1^*=0$ then the De Gennes free energy reduces to the superconductor free energy with $\nu_{\parallel}=\nu_{\perp}$. For all $K_1^* \neq 0$ and $\neq \infty$ the last case must be satisfied. Anisotropic scaling clearly predicts that for non-zero K_1 $\nu_{\parallel} =2\nu_{\perp}$. An important consequence of this and Eq 2.3.8 and Eq 2.3.10 is that the elastic constants B and K_2 do not depend on temperature.

De Gennes has pointed out the analogy between the superconductor phase of a metal and the smectic A phase.[23] The director and the smectic order parameter couple in the liquid crystal case in the same manner that the electromagnetic vector potential and the superconductor order parameter couple. However, there are several important differences between the superconductor and the smectic A phase. Due to the lack of the $q_{\perp}^2$ term in the free energy, in contrast to the superconductor, the smectic A phase does not have true long range order. Halperin and Lubensky[24] have proposed a gauge transformation which restores long range order in the smectic phase. In analogy with the superconductor this is often referred to as the superconductor (S.C.)

gauge. Calculations of the order parameter are performed in the S.C. gauge and then transformed back into the physical gauge.

The free energy of the smectic phase Eq 2.2.4 can be modified such that the elastic constants C_{11} and $C_{\perp}$ are equal by scaling the lengths. This yields the smectic A contribution to the free energy

$$F_A\{\Psi,\delta n\} = \int d^3x[a|\Psi|^2 + C_0|(\nabla - iq_0\delta n)\Psi|^2 + \frac{1}{2}b|\Psi|^4 \qquad 2.3.16$$

where the total free energy must also include the nematic contribution. The free energy of the superconductor[25] is given by

$$F_{SC} = F_A\{\Psi,\vec{A}\} + \frac{1}{2}K\int d^3x\ [\vec{A}\cdot(\nabla\times\vec{A})^2 + \vec{A}\times(\nabla\times\vec{A})^2] \qquad 2.3.17$$

where the additional terms are analogous to K_2 and K_3 in the liquid crystal problem. Fundamentally, the difference between the smectic and the superconductor results from the splay elastic energy term which is missing from the superconductor.

It is this term, $\frac{1}{2}K_1(\nabla\cdot n)^2$ in the free energy that breaks the gauge invariance for the smectic phase. Consider a gauge transformation of the form

$$\Psi = \Psi' e^{iq_0L} \qquad 2.3.18$$

$$\vec{A} = \delta\vec{n} + \nabla L \qquad 2.3.19$$

$$u = u' - L \qquad 2.3.20$$

where L=0 produces the familiar liquid crystal (L.C.) gauge with $\delta\vec{n}\cdot\vec{n}=0$. This L.C. gauge is mathematically troublesome since the K_2 and K_3 terms increase with respect to K_1 as the transition is approached thus making renormalization group calculations impossible.

In the superconductor gauge where $\nabla \cdot A = 0$ the phase fluctuations which prevented long range order in the S.C. gauge are at a minimum. There is a continuum of gauges between the S.C. and the L.C. gauges which produces intermediate phase fluctuations.

Unlike the superconductor problem, the free energy and order parameters are not gauge invariant. Correlation functions in different gauges are related via the transformation

$$G(\vec{r}) = \langle \Psi'(\vec{r})\Psi'^{*}(0)e^{-iq_0 L(\vec{r})-L(0)}\rangle \qquad 2.3.21$$

$$= G_{SC}(\vec{r})\langle e^{-iq_0 L(\vec{r})-L(0)}\rangle \qquad 2.3.22$$

$$= G_{SC}(\vec{r})e^{-R(\vec{r})} \qquad 2.3.23$$

In the limit that the phase and magnitude decouple the second step becomes an equality. Application of the renormalization group is still a formidable task and it is unclear how relevant the results are in three dimensions. Recently this problem has been overcome by using a 1/N expansion which is well behaved in all dimensions between 2 and 4.[26] However the calculation is only exact in the limit of large N, where there are 2N degrees of freedom. The $N \rightarrow S_A$ problem corresponds to N=1 and not the large N limit but some features of the 1/N expansion are independent of N. For instance, the thermodynamic properties such as the specific heat and the corresponding critical exponent α are independent of the choice of the gauge.

Using the S.C. gauge Halperin, Lubensky and Ma[27] found that to first order in an ε expansion the $N \rightarrow S_A$ transition should always be first order. They predicted a first order region greater than 0.01 °C. Furthermore, by increasing the number of components of the order parameter ($N >= 365.9$) a crossover to a second order transition occurs.

Recently Dasgupta and Halperin have shown that in three dimensions the $N \to S_A$ and superconductor transitions should be inverted XY like, that is, the critical behavior is XY like but the temperature axis is reversed.[28] Consequently the heat capacity amplitude should be reversed. For a normal XY transition the heat capacity amplitude ratio A'/A, that is the ratio of the amplitude below T_C to that above, should be 0.9.[29] However for the $N \to S_A$ and superconductor transitions, which should be inverted XY like, the ratio should be 1.11. Due to the inherent anisotropy in the correlation lengths, heat capacity might be the best means of identifying the universality class. A comparison with heat capacity results is forthcoming in chapter 3.

Recently, Lubensky and coworkers have investigated isotropic scaling in a continuum of gauges between the S.C. and L.C. gauges. The process of gauge transforming back to the physical (L.C.) gauge always introduces anisotropy in the critical exponents. It is important to emphasize that even though anisotropy exists in the physical gauge, the fixed point is still isotropic in the non-physical gauge. Accordingly, the x-ray correlation lengths are not fundamental, rather, the correlation lengths in the superconductor gauge are. Transforming back into the physical gauge yields the correlation lengths as measured by x-rays. The inverse correlation lengths in the two gauges are related by additive constants $\ell_\perp$ and $\ell_{\parallel}$

$$\xi_{\parallel}^{x-1} = \xi_{\parallel}^{-1} + \ell_{\parallel}^{-1} \qquad 2.3.24$$

$$\xi_{\perp}^{x-1} = \xi_{\perp}^{-1} + \ell_{\perp}^{-1} \qquad 2.3.25$$

Close to the transition where the correlation lengths are large the behavior is dominated by $\ell_{\parallel}$ and $\ell_\perp$. These are given by

$$\ell_{11}^{-1} = \frac{q_0 K_B T}{8\pi K_3} S^{-2}\left[1-S^2\frac{K_1}{K_3}\right]^2\left[\ln\left[S^{-2}\frac{K_3}{K_1}\right]-1+S^2\frac{K_1}{K_3}\right] \qquad 2.3.26$$

and,

$$\ell_{\perp}^{-1} = \frac{q_0{}^2 K_B T}{8\pi\sqrt{K_1 K_3}}\left[1+\frac{1}{2}S\left[\frac{K_1}{K_3}\right]^2\right]\left[1+S\sqrt{\frac{K_1}{K_3}}\right]^{-2} . \qquad 2.3.27$$

At small length scales (large reduced temperatures) the x-ray correlation lengths are identical. Thus, if the 3D inverted XY classification is correct, then, the x-ray correlation lengths should diverge with $\nu_{11}=\nu_{\perp}=\nu_{XY}$. However, as the transition is approached, $\ell_{\perp}$ starts to effect $\xi_{\perp}$ at $K_3 \simeq K_1 S^2$. This has the effect of reducing $\nu_{\perp}$ in the X-ray gauge to $\nu_{XY}/2$ close to the transition. For typical values of the elastic constants this crossover occurs at a reduced temperature between 10^{-4} and 10^{-3} which is in the middle of the experimentally observable region. Eventually ξ_{11} undergoes a crossover, Eq 2.3.24, and the x-ray correlation lengths diverge with respect to each other at a rate given by

$$\xi_{11}^{x} \sim \frac{(\xi_{\perp}^{x})^2}{\ln \xi_{\perp}^{x}} \qquad 2.3.28$$

asymptotically close to the transition. According to the theory, the bend and twist elastic constants should exhibit identical behavior with $\delta K_2 \propto \delta K_3 \propto t^{-\nu_{XY}}$. In closing, for the isotropic fixed point ξ_{11}^{x}, K_2, and K_3 diverge with an exponent ν_{XY} whereas $\xi_{\perp}^{x}$ diverges at a slower rate. The anisotropy in $\xi_{\perp}^{x}$ is only a result of the transformation back to the physical world.

Halsey and Nelson[30] have considered a new class of $N \rightarrow S_A$ transitions in which the nematic fluctuations are confined to an axis rather than a plane. Unlike the anisotropic fixed point where $\nu_{\parallel}=2\nu_{\perp}$ they conclude that $\nu_{\parallel}=3/2\nu_{\perp}$. Therefore, by reducing the phase space for fluctuations the anisotropy of the phase transition is reduced. This finding supports the notion that the degree of anisotropy is connected with the coupling of the nematic and smectic order parameters.

2.4
Dislocation Mediated Melting

Kosterlitz and Thouless[31] found that the unbinding of bound dislocations may provide a mechanism for melting in two dimensions. Helfrich[32] investigated the possibility that dislocations may drive the $N \rightarrow S_A$ transition. Unlike the two dimensional problem, the $N \rightarrow S_A$ transition is characterized by a divergence in the size of unbound dislocations. Nelson and Toner[33] have shown that a smectic A with a finite density of dislocation loops behaves like a nematic with elastic constants K_2 and K_3 related to the dislocation core energies. As the transition is approached the dislocation loops increase in size anisotropically because of the peculiar elasticity of smectic dislocations. As a result, the mean distance between dislocations which acts as the correlation length must also grow in an anisotropic manner with $\nu_{\parallel} = 2\nu_{\perp}$.

In the high temperature expansion of an arbitrary spin 1/2 model the partition function is formed by counting the graphs of loops.[32] which inverts the high and low temperature axis. These loops must be closed to have non-zero weight. For the smectic A phase, the loops correspond to dislocations loops where the sign of the spin is the direction of the Burgers vector.

There are two basic types of dislocations which can occur in a smectic A crystal. Dislocation lines normal to the layering direction are edge dislocations whereas dislocation lines parallel to the layering direction are screw dislocations. Segments of both screw and edge dislocations are shown in figure 2.4.1. Of course, any real dislocation loop can be composed of both edge and screw dislocations.

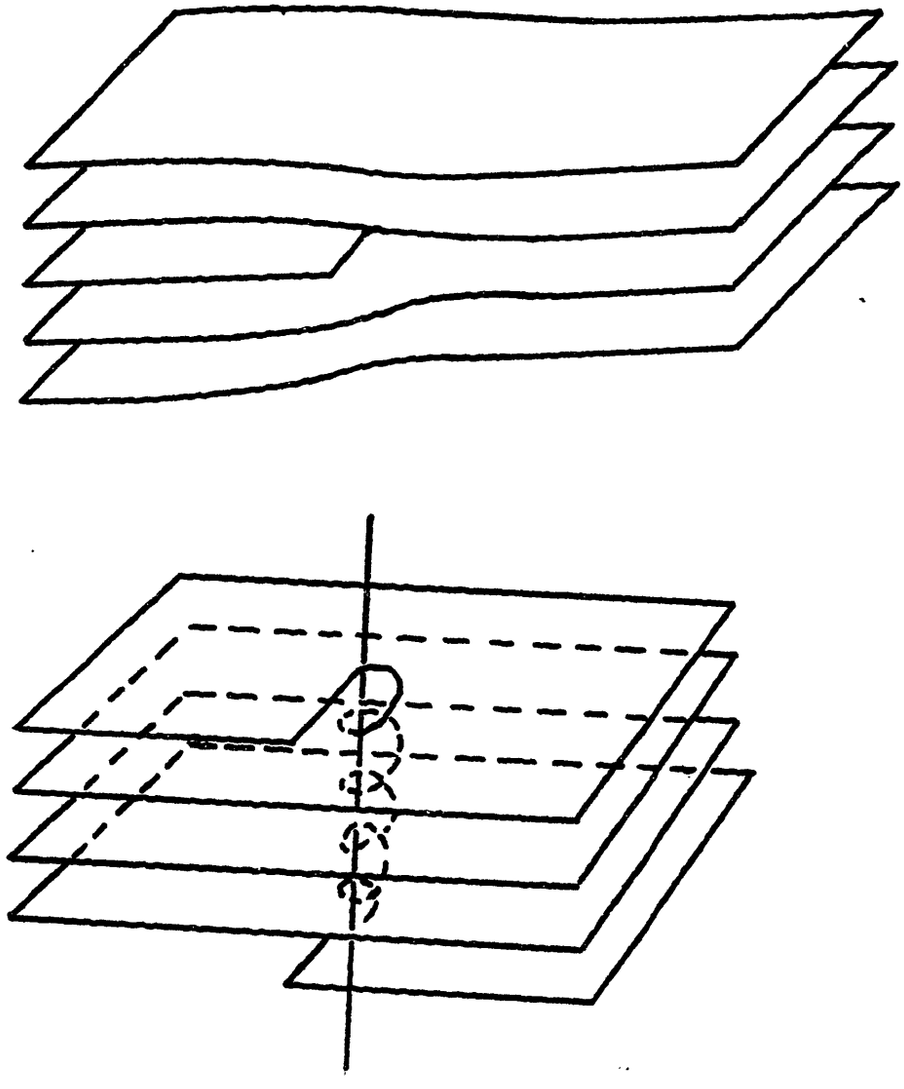

Figure 2.4.1

Top: Edge dislocation in a smectic A crystal
Bottom: Screw dislocation in a smectic A crystal

The self energies per unit length for edge and screw dislocations have been calculated by Kleman and coworkers[34] and are given by,

$$W_{s,edge} = \frac{Kd^2}{\lambda r_{c,edge}} \qquad 2.4.1$$

$$W_{s,screw} = \frac{Bd^4}{128\pi^3 r^2_{c,screw}} \qquad 2.4.2$$

where d is the molecular size and r_c is the core radius for the two types of dislocations. In normal solids the elastic energies diverge slower, often logarithmically with the size of the strain field. The strain field of two interacting edge dislocations with one field at the origin and the other at (x,z) is

$$W_{1,edge} = \pm \frac{sd^2}{4\pi\lambda \left[\frac{\pi}{\lambda|z|}\right]^{\frac{1}{2}}} e^{\left[-\frac{x^2}{4\lambda|z|}\right]} \qquad 2.4.3$$

per unit length. The region of maximum strain generated by these two dislocations is bounded by the two parabolae given by

$$z = \pm \frac{x^2}{4\lambda} \qquad 2.4.4$$

Strain fields from screw dislocations need not be considered since they fall off much slower then edge dislocations.

A transition to a state where infinite loops grow[32] is suggested by Helfrich. Entropic considerations promote large loops whereas the core energy favors smaller loops. The free energy for a loop of length N is approximated by

$$F = N[E_c - K_B T \ln(n)] \qquad 2.4.5$$

where E_c is the core energy and n is the coordination number. If the

core energy is temperature independent then the free energy can be expressed as

$$F = N \frac{T_c - T}{T_c} K_B T_c \ln(n). \qquad 2.4.6$$

Since free energy should be of the order of $K_B T$ the maximum chain length is approximated by

$$N_{max} = \frac{T_c}{T_c - T} . \qquad 2.4.7$$

Thus, at the transition the size of the dislocation loops diverge.

In summary, Helfrich concludes that the $N \rightarrow S_A$ transition may be driven by the divergence of the size of dislocation loops. The strain field generated by these loops is parabolic in nature. It is this parabolic elasticity which is the foundation for the predictions of Nelson and Toner including the relationship $\nu_{\parallel} = 2\nu_{\perp}$.

Nelson and Toner have included the dislocation contribution to the free energy of the smectic phase. By including a dislocation density to the smectic free energy given by

$$F_S(q_{\parallel}, q_{\perp}) \propto B q_{\parallel}^2 + K_1 q_{\perp}^4 . \qquad 2.4.8$$

the free energy can be expressed in terms of K_1 and B, and the core energies for edge and screw dislocations, E_e and E_s. The displacement of the layers has the usual thermal fluctuation component plus an additional term arising from dislocations. A smectic with dislocations has the same functional form as the nematic where the Frank elastic constants take the form

$$K_2 = 2E_s \qquad 2.4.9$$

$$K_3 = 2E_e \ . \qquad 2.4.10$$

If the correlation lengths reflect the distance between dislocations then it is reasonable to assume the elastic constants should scale as

$$K_2 \propto \frac{\xi_\perp^{\ 2}}{\xi_{11}} \qquad 2.4.11$$

and

$$K_3 \propto \frac{\xi_\perp \xi_{11}}{\xi_\perp} \propto \xi_{11} \ . \qquad 2.4.12$$

This is exactly the same result as the anisotropic prediction of Chen and Lubensky.

For an edge dislocation, the phase difference between the smectic order parameters on opposite sides of the region of maximum stress defined by Eq 2.4.4 is 180°. Since this region is parabolic the cross-sectional area contained is $(zr_\perp) \propto r_\perp^3/\lambda$. The probability of dephasing is unity when the product of the decorrelated area and the dislocation density is one. This condition necessitates that ξ_{11} scale as $\xi_\perp^{\ 2}$, in agreement with the anisotropic fixed point of Chen and Lubensky.

Toner has also carried out a renormalization group calculation which assumes that dislocation loops are the sole excitation responsible for the $N \rightarrow S_A$ transition.[35] He predicts an inverted XY transition with critical exponents $\nu_{11}=6/5\nu_{XY}$ and $\nu_\perp=4/5\nu_{XY}$. These results have not been confirmed by the dislocation loop calculation of Grinstein and Toner.[36]

Grinstein and Toner[36] have proposed a global picture of the Nematic-Smectic A-Smectic C phase diagram based on the dislocation loop theory. A new phase, N', which has long-range tilt but short-range positional order emerges from the analysis. This phase, which might separate the Smectic C and nematic phase, is the analogue of the hexatic phase in two dimensions. Within the context of this model the Sm A to Sm C and the N to N' transitions are in the isotropic XY universality class whereas the Sm A to N and the Sm C to N' are inverted XY like. No specific predictions for the critical behavior for the correlation lengths are calculated for this model although the crossover form of Lubensky may apply.

REFERENCES

1. W.L. McMillan, Phys Rev. A 4 ,1238(1971)

2. K.K. Kobayashi, Phys Lett. 31A , 125(1970), J. Phys. Soc. Japan ,101(1970)

3. W. Maier and A. Saupe, Z. Naturf. A13 ,564(1968)

4. A. Saupe, Angewandte Chemie, 7 ,97(1968)

5. C.P. Bean and D. Rodbell, Phys. Rev. 126 ,104(1962).

6. R.B. Meyer and T.C. Lubensky, Phys. Rev. A 24 ,2307(1976)

7. P.H. Keyes, H.T. Weston and W.B. Daniels, Phys. Rev. Lett. 628(1973).

8. K. Chan, L.B. Sorensen, and P.S. Pershan, Private communication.

9. R. Alben, Solid State Commun., 13 ,1783(1973).

10. D. Brisbin, R. DeHoff, T.E. Lockhart, and D.L. Johnson, Phys. Rev. Lett. 43 ,1171(1979)

11. De Gennes, P.G., Solid State Commun.,10,753(1972)

12. Oseen, C.W. Trans Faraday Soc. 29, 883 (1933); Frank, F.C. Discuss. Faraday Soc. 25, 19 (1958)

13. G. Grinstein and Robert A. Pelcovitz, PRL, 1981,47,856

14. A. Schmid, Phys. Rev., 180,527(1969).

15. T.C. Lubensky, J. Chemie Phys. (Paris) 80 ,31(1983)

16. D.L. Landau and E.M. Lifshitz, Statistical Physics (Addison Wesley, Reading, Mass.) 1969

17. A. Caille, C.R. Acad. Sci. 274B ,891 (1972).

18. L. Gunther, Y. Imry, and J. Lajzerowicz, Phys. Rev. A 22 , 1733(1980)

19. J. Als-Nielsen, J.D. Litster, R.J. Birgeneau, M. Kaplan and C.R. Safinya, A. Lindegaard-Andersen and S. Mathiesen, Phys. Rev. B 22 ,312(1980)

20. S. Redner and P.R. Mueller, Phys. Rev. B 26 ,5293(1982); W.G. Kinzel, Annals of the Israeli Physical Society, edited by G. Deutscher, R. Zallen, and J. Adler(Adam Higler, Bristol, 1982); S. Redner, ibid.

21. W. Kinzel, Phys. Rev. Lett. 51 ,996(1983).

22. T.C. Lubensky and Jing-Huei Chen, Phys. Rev. B, 17 ,366(1978)

23. P.G. De Gennes, Solid State Commun., 10 ,753(1972)

24. B.I. Halperin and T.C. Lubensky, Solid State Commun. , 14 ,997(1973)

25. P.G. De Gennes, Superconductivity of Metals and Alloys (W.A. Benjamin, N.Y.) 1966.

26. S.G. Dunn and T.C. Lubensky, J. Phys. (Paris) , 42 , 1201(1981)

27. B.I. Halperin, T.C. Lubensky and S. Ma, Phys. Rev. Lett., 32 ,292(1974)

28. Chandan Dasgupta and B.I. Halperin, Phys. Rev. Lett., 47 1556(1981)

29. D. Stauffer, M. Ferer, and M. Wortis, Phys. Rev. Lett., 29 ,345(1972)

30. Thomas C. Halsey and David R. Nelson, Phys. Rev. A, 26 ,2840(1982)

31. J.M. Kosterlitz and D.J. Thouless, J. Phys. C 6 ,1181(1973)

32. W. Helfrich, J. Phys.(Paris) 39 ,1199(1978)

33. David R. Nelson and John Toner, Phys. Rev. B 24 ,363(1981)

34. M. Kleman and C.E. Williams, J. Physique Lett. 35 L-49(1974), M. Kleman, Philos. Mag 34 ,79(1976)

35. J. Toner, Phys. Rev. B 26 ,462(1982)

36. Grinstein and Toner(in press)

3.0
PRIOR EXPERIMENTAL RESULTS

The $N \rightarrow S_A$ transition has been studied extensively via heat capacity, light scattering, and x-ray experiments and the critical exponents α, γ, ν... have been obtained. Some early measurements were consistent with mean-field behavior, whereas others supported 3D XY behavior. More recent experiments are not entirely consistent with either 3D XY or mean-field behavior although the critical exponents in a particular material may support one of the two critical behaviors. Recent experiments indicate that the transition is usually second order to within a few millidegrees Centigrade; earlier experiments were unable to rule out first order behavior. Though much progress has been made in developing a better understanding of the $N \rightarrow S_A$ transition many important issues remain unresolved. Before presenting my results, a cursory summary of prior experimental results is presented.

Due to the inherent anisotropy of the $N \rightarrow S_A$ problem, heat capacity measurements provide the most unambiguous determination of the universality class. Heat capacity measurements have been performed on many liquid crystal systems including the bilayer materials 4-n-octyloxy-4-cyanobiphenyl (8OCB)[1] ,4-n-octyl(1-4-cyanobiphenyl) (8CB)[2] and homologs of 8CB including 9CB and 10CB mixtures.[3] Measurements have also been carried out on the single layer smectic materials 4-n-pentylphenyl-4-n-octyloxybenzoate ($\overline{8}$S5) and homologs $\overline{9}$S5 and $\overline{10}$S5[4] and members of the N-(4-n-p-alkoxybenzylidene)-4-n-alkyaniline family, 40.8[5] , 40.7[6,7] , and 60.8.[8] Johnson and coworkers heat capacity measurements on 8OCB[1] found the transition to be slightly first order, presumably because of an impurity induced two phase region. If the

points close to the transition were ignored, they were able to show that $\alpha=0$, consistent with 3D XY behavior. More recent measurements by Garland et. al, LeGrange and Mochel, and Hatta and Ikushima[1] did not reveal a two phase region and strongly suggested $\alpha=0.15\pm0.05$ rather than the 3D XY value. Heat capacity measurements in 40.8 showed that α is the same as for 8OCB, but measurements for α in 8CB gave 0.31. These experiments do not support the 3D XY universality class.

Brisbin et al. [4] found that for the $\overline{n}$S5 series α depends on the nematic range with $\alpha=0$ for $\overline{8}$S5 which has a 23°C range ($T_{NA}/T_{NI}=0.936$) and with $\alpha=0.45$ for $\overline{10}$S5 which has a 5.5°C range ($T_{NA}/T_{NI}=0.985$). They made the important observation that these varying exponents might be connected with a crossover from 3D XY behavior to tricritical behavior with decreasing nematic range. Due to phase separation, however, the data could only be analyzed for $t > 10^{-4}$. Measurements in 40.7 [6] ($T_{NA}/T_{NI}=0.926$), which extend closer to T_{NA}, also support the 3D XY value for α. However, the ratio of the heat capacity amplitude above T_{NA} to the amplitude below $A/A'=1.035$ does not agree with the inverted 3D XY prediction (see section 2.3). In mixtures of the bilayer materials 7CB and 8CB, Thoen et al. also report consistency with the 3D XY value of α. These measurements suggest that 3D XY behavior occurs for large nematic ranges, tricritical behavior for short nematic ranges and crossover behavior for intermediate ranges. The crossover temperatures, given by the McMillan number T_{NA}/T_{NI}, are not universal numbers for different systems.

Most of the calorimetric measurements have used an ac-calorimeter because of its superior sensitivity at second order transitions but this technique is unreliable for first order

transitions. Recently Thoen et al. [3] have measured the heat capacity for several nCB materials and mixtures using an adiabatic scanning calorimeter. This technique is ideal for $N \rightarrow S_A$ tricritical region since it is capable of separating the latent heat from the pretransitional fluctuations. Furthermore, the sample can be mixed to prevent impurity gradients from occurring. They conclude that 9CB (T_{NA}/T_{NI}=.994) is still second order but very near the tricritical point with α=0.50. As the nematic range is shortened by mixing 10CB with 9CB the latent heat steadily increases from zero. The heat capacity ratio, A'/A, is still close to unity, whereas it is predicted to be 3.56.[9]

Heat capacity measurements on the λ transition in helium[10] are of particular relevance to the $N \rightarrow S_A$ transition because both are predicted to be in the 3D XY universality class, therefore, they should exhibit the same critical behavior. Recent measurements by Lipa and Chui[10] report that $\alpha = -0.0127 \pm 0.0026$ and $A/A' = 1.058 \pm 0.004$. Furthermore, these measurements confirm renormalization group predictions for the 3D XY model of $\alpha = -0.007 \pm 0.006$ and $A/A' \simeq 1.03$.[11]

According to the hypothesis of two-scale universality (section 1.3), the free energy per correlated volume should have the same constant value, independent of temperature, for all systems belonging to the same universality class.[12] For the $N \rightarrow S_A$ transition this leads to

$$C^p_{Crit} t^2 \xi_{\parallel} \xi_{\perp}^2 = \text{constant} \qquad 3.0.1$$

and the anisotropic scaling relation

$$\nu_{\parallel} + 2\nu_{\perp} = 2 - \alpha \ . \qquad 3.0.2$$

For all materials in which there are both detailed heat capacity and correlation length data, Garland and coworkers[7] have shown that Eq 3.0.2

is satisfied within the combined uncertainties. Lubensky argues that if the anisotropy of the x-ray exponents results from the lack of long range order in the smectic phase (section 2.3), the relevant relationship is $3\nu_{\parallel}=2-\alpha$, however, experimental results do not support this prediction. In a comparative study of 8OCB and 4O.8, which have have the same critical exponents, Birgeneau et al. found that both materials have a universal constant. There is as yet no evidence that this constant remains universal for materials with different critical exponents.

Light scattering probes the long wavelength thermal fluctuations of the nematic director. From the DeGennes free energy (section 2.2) and the equipartition theorem the dispersion relations for these fluctuations can be derived. By choosing a suitable coordinate system, two independent modes for the fluctuations in the nematic phase are obtained

$$\langle|\delta n_{\alpha}(q)|^2\rangle \propto \frac{K_B T}{K_{\alpha} q_{\perp}^2 + K_3 q_{\parallel}^2}; \quad \alpha=1,2 \qquad 3.0.3$$

where α denotes the mode. In the smectic phase, the smectic elastic constants B and D modify this result. Since the director fluctuations correspond to dielectric fluctuations the scattered intensity is directly proportional to this expression.

According to the analogy with fluctuation diamagnetism (section 2.2) the divergent part of the elastic constants δK_3 and δK_2 should scale as $\xi_{\parallel}$ and $\xi_{\perp}^2/\xi_{\parallel}$ respectively. However, to analyze the light scattering data close to the transition, Jahnig and Brochard[13] have included the crossover effect from hydrodynamic to non-hydrodynamic behavior. Using their results, in principle, the correlations lengths

corresponding to the smectic fluctuations $\xi_{\parallel}$ and $\xi_{\perp}$ can extracted from the measured intensity. In practice, the K_2 behavior is difficult to obtain due to the divergence of K_3 as is obvious from Eq 3.0.3 when $q_{\parallel} \neq 0$. Lubensky predicts that if the transition is isotropic then $\delta K_2 \propto \delta K_3 \propto \xi \propto \xi_{\parallel}$ whereas $\xi_{\perp}$ as measured by x-rays should not be proportional to $\xi_{\parallel}$ (section 2.3). Nelson and Toner predict that $\xi_{\parallel} \propto \xi_{\perp}^2$ (section 2.4) if the transition is mediated by dislocations, implying that K_2 and B are finite at the transition. To distinguish between the two theories reliable measurements of K_2 and B would be extremely valuable. The critical behavior of the elastic constants can also be obtained from Fredericks transition measurements.

There have been numerous measurements of K_3 in a variety of materials, however, there is little consensus as to the exact critical dependence of the elastic constants. The early experiments did not consider the crossover to non-hydrodynamic behavior close to the transition, therefore, these measurements did not obtain the true critical behavior near the transition. For CBOOA, Chu and McMillan[14] reported mean-field behavior for K_2 whereas Cladis[15] found that the exponent for K_3 varied between 0.5 and 1.0. More recent measurements by Litster and coworkers[16] have included these crossover effects in the analysis and suggest that K_3 is proportional to $\xi_{\parallel}$ as measured by x-rays for 8OCB[16], 8CB[16], 40.8[17] and 40.7[7]. On the smectic side, both B and D enter into the dispersion relations, hence, they can be obtained from light scattering data. The value of B, obtained in this manner, vanishs with an exponent 0.30 ± 0.05 for 8OCB whereas D vanishes as 0.50 ± 0.03 [16]. The exponent for B in 8OCB has been confirmed by Fisch et al.[18] who measure B directly through a surface scattering scattering

technique, however the absolute magnitudes differ. The critical exponent corresponding to B is not consistent with any of the theories of the transition presented in chapter 2. Solomon and Litster[19] find that the mode 1 light scattering data, which give B when $K_3 q_{\parallel}^2$ is small, go to zero at a temperature which is approximately 0.050°C higher than the transition temperature extracted from the mode 2 data. This is because the K_3 term contributes on both sides of the transition thereby complicating their determination of B.

In the early 1970's McMillan pioneered the use of x-ray scattering as a probe of the smectic fluctuations in the nematic phase. For p-cyanobenyzylidene-amino-p-n-octyloxybenzene (CBAOB)[20] which has a 25°C nematic range, he found that the scattering could be modeled by an anisotropic Lorentzian modified by a $q_{\perp}^{2.5}$ rather than the usual $q_{\perp}^2$ term. The correlation lengths $\xi_{\parallel}$ and $\xi_{\perp}$ diverged anisotropically with $\nu_{\parallel}$=.79 and $\nu_{\perp}$=0.60 respectively and γ=1.49. These measurements did not confirm either the predictions of mean-field theory or the 3D XY model.

Over the past several years x-ray measurements have been performed on a number of materials at M.I.T. with much better instrumental and temperature resolution than those of McMillan. The measurements on CBOOA[21] , 8CB[22] and 8OCB[22] confirmed the predictions of the 3D XY model for the susceptibility and for $\xi_{\parallel}$, however, $\xi_{\perp}$ diverged at a somewhat slower rate. Although a Lorentzian was adequate to describe the longitudinal scans, these studies found that a fourth order term was necessary to describe the transverse scattering.

Recently, Safinya and coworker have conducted a detailed study of the $N \rightarrow S_A$ transition near the nematic-smectic A-smectic C multicritical point in mixtures of $\overline{8}S5$ and $\overline{7}S5$. For pure $\overline{8}S5$ they found

that both γ and $\nu_{\parallel}$ were greater than the values predicted by the 3D XY model by 15-20% although $\nu_{\perp}$ agreed with the predictions of this model. It was suggested that this behavior was related to the nearby smectic C phase, however, the measurements to presented in the next chapter strongly suggest that these larger exponents are related to the longer nematic range in $\overline{8}S5$ compared to that in 8CB and 8OCB. It is interesting to note that McMillan's original measurements on CBAOB, which has a comparable range to $\overline{8}S5$, gave critical exponents which are close to those in $\overline{8}S5$.

The phase diagram of 8OCB and 6OCB mixtures is unusual in that the nematic phase is reentrant upon cooling. Pershan and Prost[23] have postulated that the parabolic shape of the reentrant phase diagram results from an optimal density for the formation of the smectic phase. X-ray measurement by Kortan et al.[24] have shown that the effective correlation length critical exponents increase as the nose of the phase diagram is approached. This behavior has been modeled with a Landau-Ginzburg free energy expansion which incorporates the shape of the phase diagram into the second order term of the expansion. One consequence is that the effective critical exponents double at the critical endpoint, however, the critical exponents $\nu_{\parallel}$=0.76, $\nu_{\perp}$=0.62, and γ=1.49 have been extrapolated for the case where the density is only weakly temperature dependent. At all concentrations the critical behavior in the reentrant nematic phase is nearly identical to the behavior in the high temperature nematic.

REFERENCES

1. C.W. Garland, G.B. Kasting and K.J. Lushington, Phys. Rev. Lett. 43 ,1420(1979); D.L. Johnson, C.F. Hayes, R.J. DeHoff and C.A. Schantz, Phys. Rev. B 18 ,4902(1978); J.D. LeGrange and J.M. Mochel, Phys. Rev. A 23 ,3215(1981); I. Hatta and A. J. Ikushima, Japanese Journal of Applied Physics, 20 ,1995(1981).

2. G.B. Kasting, C.W. Garland and K.J. Lushington, J. Phys(Paris) 41 ,1200(1980). J. Thoen, H. Marynissen, and W. Van Dael, Mol Cryst. Liquid Cryst. 97 ,149(1983) and J. Thoen, H. Marynissen, and W. Van Dael, Phys. Rev. A 26 , 2886(1982).

3. J. Thoen, H. Marynissen, and W. Van Dael, Phys. Rev. Lett., 52 , 204 (1984).

4. D. Brisbin, R. Dehoff, T.E. Lockhart, and D.L. Johsnon, Phys. Rev. Lett. 43 ,1171(1979).

5. K.J. Lushington, G.B. Kasting, and C.W. Garland, J. Phys. Lett.(Paris) 41 , L-419(1980) and R.J. Birgeneau, C.W. Garland, G.B. Kasting, and B.M.Ocko, Phys. Rev. A 24 ,2624(1981);

6. E. Bloemen and C.W. Garland, J. Phys. (Paris) 42 ,1299(1981).

7. C.W. Garland, M. Meichle, B.M. Ocko, A.R. Kortan, C.R. Safinya, L.J. Yu, J.D. Litster, and R.J. Birgeneau, Phys. Rev. A 27 ,3234(1983).

8. C. Chiang and C.W. Garland, Private communication.

9. E.E. Gorodetskii and V.M. Zaprudskii, Sov. Phys. JETP 45 ,1209(1977).

10. G. Ahlers, Phys. Rev. A 3 ,696(1971); J.A. Lipa and T.C.P. Chui, Phys. Rev. Lett. 51 , 2291(1983).

11. J.C. LeGuillou and J. Zinn-Justin, Phys. Rev. B 21 ,3976(1980); E. Brezin, J.C. LeGuillou, and J. Zinn-Justin, Phys. Rev. Lett. 47A ,285(1974).

12. D. Stauffer, M. Ferer, and M. Wortis, Phys. Rev. Lett. 29 ,345(1972); P.C. Hohenberg, A. Aharony, B.I. Halperin, E.D. Siggia, Phys. Rev. B 13 ,2986(1976).

13. F. Jahnig and F. Brochard, J. Phys.(Paris) 35 ,301(1974).

14. K.C. Chu and W.L. McMillan, Phys. Rev. A 11 ,1059(1974).

15. P.E. Cladis, Phys. Rev. Lett. A 48 ,179(1974).

16. R. Schaetzing and J.D Litster, "Advances in Liquid Crystals" vol. 4 (Academic Press, 1979) and references therein; ,1657(1979); J.D. Litster, J. Als-Nielson, R.J. Birgeneau, S.S. Dana, D. Davidov, F. Garcia-Golding, M. Kaplan, C.R. Safinya and R. Schaetzing, J. Phys. (Paris), 40 , C3-339(1979).

17. H. von Kanel and J.D. Litster, Phys. Rev. A 23 ,3251(1981).

18. M.R. Fisch, L.B. Sorenson and P.S. Pershan, Phys. Rev. Lett. 47 ,43(1981).

19. L. Solomon, private communication.

20. W.L. McMillan, Phys. Rev. A 7 ,1419(1973).

21. J. Als-Nielsen, R.J. Birgeneau, M. Kaplan, J.D. Litster, and C.R. Safinya, Phys. Rev. Lett. 39 ,352(1977).

22. M. Kaplan, Ph.D. Thesis, MIT (1980).

23. P.S. Pershan and J. Prost, J. Phys. Lett. (Paris) 40 L27(1979).

24. A.R. Kortan, H.V. Kanel, R.J. Birgeneau, and J.D. Litster, Phys. Rev. Lett. 47 ,1206(1981) and J. Phys. (Paris) in press.

4.0 EXPERIMENTAL TECHNIQUES

4.1 X-RAY SCATTERING

In all scattering experiments the goal is to measure a particular aspect of the structure factor $S(\vec{q},\omega)$ where $\vec{q}$ is the momentum transferred to the sample and ω is the energy transferred($\omega=E/\hbar$). Spectrometers measure the convolution of the "real" scattering profile with the instrumental resolution as discussed in section 1.2. An "ideal spectrometer" would have perfect resolution, however, even if this were possible it would be useless since x-ray sources are never perfectly collimated. This "ideal spectrometer" raises the issue that a compromise must be struck between resolution and signal. This compromise must be made on an individual basis for each experiment.

The width of the smectic structure factor in the nematic phase is inversely proportional to the smectic correlation length in the nematic phase. Hence, the resolution of the spectrometer provides a cutoff for the largest resolvable correlation length. Previous $N \rightarrow S_A$ measurements have shown that correlation length can grow continuously to a micron, therefore the spectrometer resolution must be $\sim 10^{-4} A^{-1}$ to resolve such large lengths. To achieve such high resolution with appreciable count rates triple-axis spectrometers were used. An excellent review of the set-up is found in theses by Kaplan[1] and by Safinya.[2] An identical set-up is used for these measurements and is sketched in figure 4.1.1. The "spectrometer" refers to the entire x-ray scattering apparatus. It includes the x-ray source, monochromator, analyzer, rotation stages, detection electronics and control electronics. Before describing the triple-axis set-up in detail I will

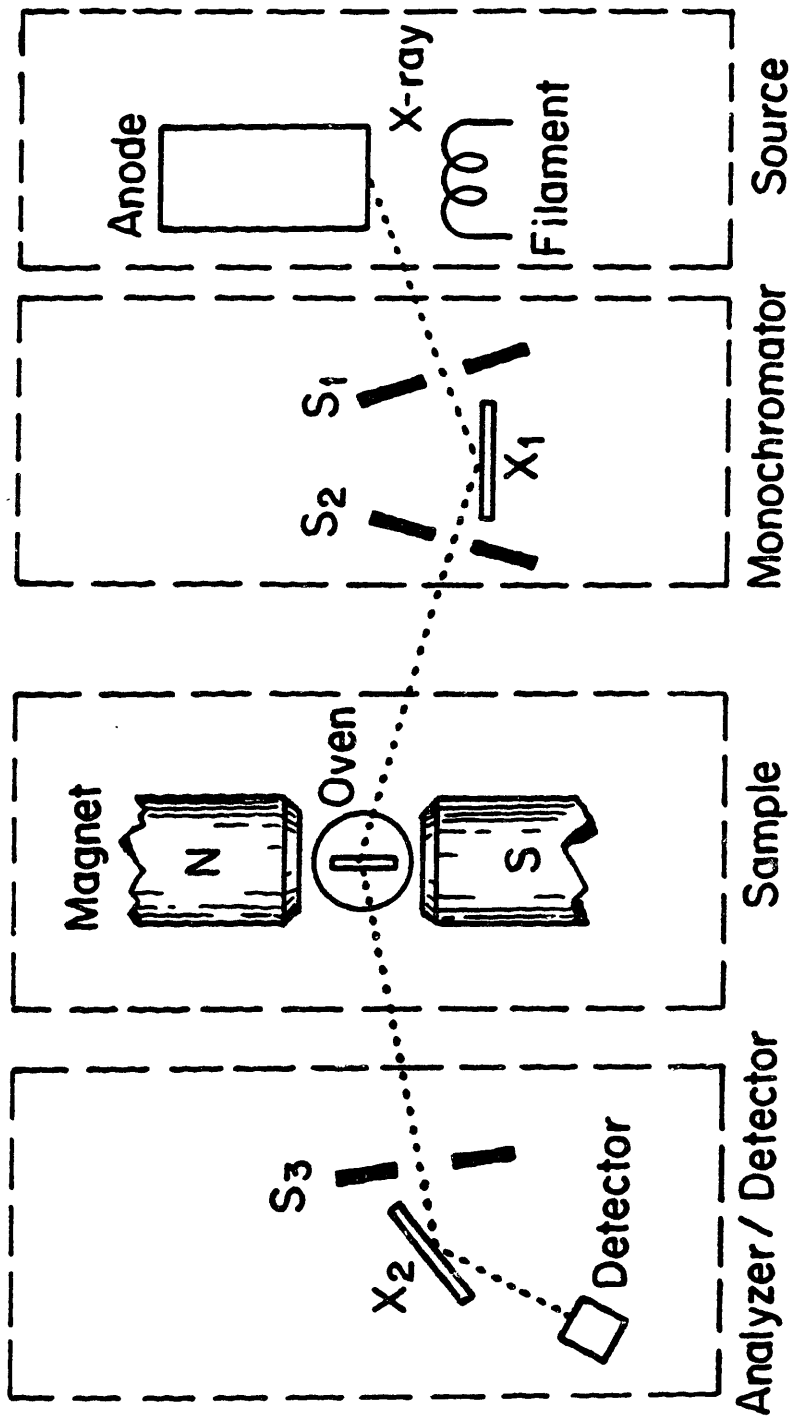

Figure 4.1.1

X-ray spectrometer components in the scattering plane. Slits S1, S2, and S3 are horizontal slits, X1 and X2 are either Si(111) or Ge(111) perfect crystals.

review some of the individual components.

A) X-RAY SOURCES

Since Wilhelm Roentgen first produced x-rays in 1895 using a gas discharge tube considerable progress has been made in devising better x-ray sources. Present day tube sources, as developed by Coolidge, utilize a hot filament to produce an electron beam that bombards a metal target. This gives rise to bremsstrahlung radiation as well as the characteristic radiation from the target which is usually copper, molybdenum, iron, cobalt or gold. It is also possible to excite these characteristic lines using atomic beams from accelerators. Radiation produced from radioactive isotopes such as Fe_{55} do not provide adequate intensity for scattering experiments. Recent advances allow the dipole radiation from synchrotron sources to be collimated to produce photon fluxes many orders of magnitude more intense than conventional sources. Unlike the visible counterpart, the development of x-ray lasers is still on the drawing board.

The majority of the experiments in this thesis utilize a Rigaku Rotaflex RU-200 as an x-ray source (preliminary experiments used a General Electric XRD-5 tube source). A hot filament at a large negative potential provides electrons that are focused on the anode. At full power the electron current is 200 ma across a 40 kilovolt potential and is focused onto a 0.5 by 10.0 mm^2 spot on the anode. By rotating the anode at 3000 R.P.M. the heat is spread over the anode surface and removed by circulating cooling water in the interior.

The copper K_α lines were used for all of these measurements since they are more intense than the other intrinsic copper lines. An initial valence state with a vacancy in the 1s level with a final state vacancy in the 2p shell gives rise to the K_α lines. There are two lines resulting from the $2p_{\frac{3}{2}}$ and the $2p_{\frac{1}{2}}$ final states corresponding to $K_{\alpha 1}$ and $K_{\alpha 2}$ with energies 8048 ev. (λ=1.54056Å) and 8027 ev. (λ=1.54439Å) respectively. The $K_{\alpha 1}$ line is more than twice as intense as the $K_{\alpha 2}$ line. The finite lifetime of the initial and final states yield a Lorentzian energy distribution where these widths are 2.66 ev and 3.77 ev for $K_{\alpha 1}$ and $K_{\alpha 2}$.[3] Additionally, there is a 1% background due to bremmstrahlung.

B) Bragg Reflection

The x-rays emitted from a rotating anode target have no collimation and are polychromatic. Bragg reflection from single crystals provide collimation and improve the monochromaticity of the x-ray beam. Reflection from a crystal occurs when the the incident beam satisfies the Bragg condition ($\tau=2k_0\sin\theta$). This happens when the scattered wavefronts are in phase though the scattering amplitude diminishes as the incident wave is reflected back. Effectively, only a finite number of scattering centers contribute to the Bragg reflection. As a result, the reflected beam has a finite angular width (Darwin width) rather than the characteristics of a delta function. Figure 4.1.2 shows the calculated angular dependence assuming no absorption. Though the function is flat topped the wings are Lorentzian (q^2) in profile.

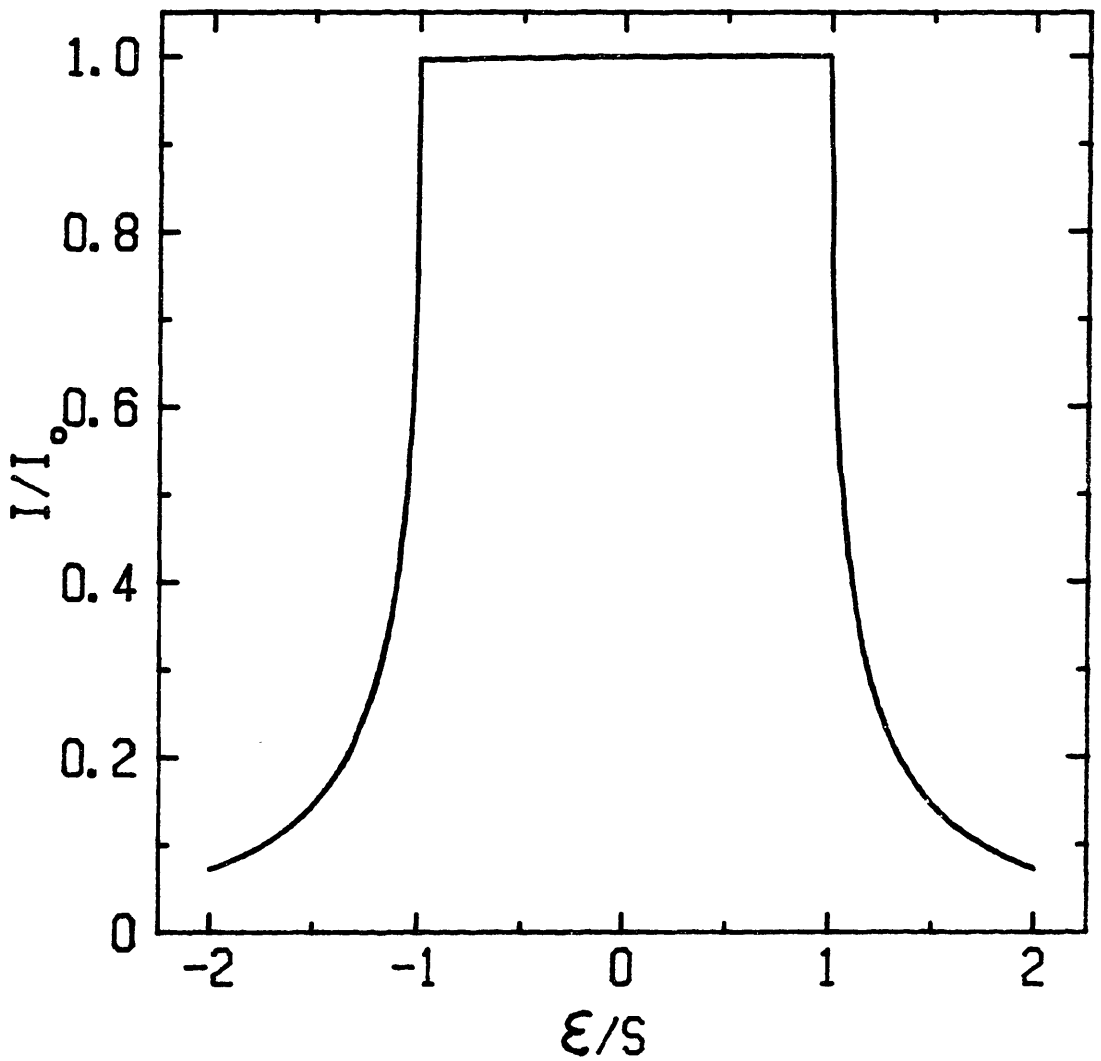

Figure 4.1.2

Plot of I/I_0 as a function of ε/s where the angle ε is the deviation from the Bragg angle $Theta_0$. Between $\pm\varepsilon/s$ the reflected intensity is unity. It is assumed that absorption processes are negligible and that the incoming beam is monochromatic with perfect collimation.

The penetration depth depends on the scattering cross-section of the crystal lattice and on the incident and reflected angles. Higher order reflections always have smaller Darwin widths because the beam enters the crystal at a steeper angle. Asymmetrically cutting the crystal (i.e. not along an hkl plane) also modifies these angles, therefore, the Darwin width can be changed in this manner. Another useful technique is to cut a channel into a single crystal so that if the Bragg condition is satisfied for the first bounce it will also be satisfied for successive reflections. Although these channel cut crystals have the same Darwin widths as their single crystal counterparts, each additional bounce reduces the wings of the distribution function by a factor of q^2. This feature is extremely useful since real scattering profiles often have q^2 tails making it difficult to resolve the profile from the instrumental resolution.

Perfect crystals perform two distinct and essential features in x-ray set-ups. For a well collimated polychromatic source a single crystal acts a monochromator since only a narrow range of incident photon energies are reflected. Likewise, for an uncollimated monochromatic source a single crystal acts as an analyzer since rays will be reflected for only a small range of the crystal orientation. In either case, the distribution of reflected rays is given by the intrinsic Darwin profile.

C) Triple Axis Spectrometers

Triple axis spectrometers were used for all the measurements reported in this thesis and the essential elements are drawn in figure 4.1.1 and detailed below. It is important to note that the spectrometer

described in this thesis only has two axes, hence, the scattering profile can only be measured in a plane. The in-plane elements of the spectrometer are presented first followed by a discussion of the vertical component which is out of the scattering plane.

A small fraction of the total radiation emitted from the rotating anode leaves the machine vacuum through two 1 cm Be windows on either side of the anode. The beam is controlled by an on/off electromagnetic shutter and travels to the monochromator assembly via a flight path to eliminate air scattering. The beam collimation in the scattering plane is limited by the size of the filament image on the anode and the horizontal slit S1 in front of the monochromator. Though the filament spot is .5 mm by 10 mm, viewed at 6° its effective size is only .5mm by 1mm. When the entrance slit separation is matched to the effective spot width (1mm), the collimation in the scattering plane is 3×10^{-3} radians HWHM. (This is for a 30 cm separation between the anode and the monochromator entrance slit.) For a perfect monochromator crystal, i.e. no mosaic, incoming rays will be reflected in an energy range limited by the collimation, $=3\times10^{-3}\times8{,}000/\tan\theta$ ev ~ 100 ev for copper K_α x-rays. This is adequate to reject most of the bremmstrahlung and the K_β although it is inadequate to separate out the $K_{\alpha1}$ radiation from the $K_{\alpha2}$ radiation since these lines are only 21 ev apart. The horizontal exit slit after the monochromator serves only to reduce the background reflections and is set such that it is marginally wider than the beam.

The reflectivity and the integrity of the monochromator crystals diminish with time from radiation induced surface oxidation. This effect is manifested by slight changes in the instrumental resolution

over the course of several months. Translation to a different crystal position or etching the entire crystal restores the crystal performance. Intense radiation is also capable of knocking out atoms from the crystal lattice to produce color centers. This effect is particularly pronounced for Lithium Fluoride crystals which turn yellow after only a few days exposure.

The next spectrometer element is the goniometer assembly. The goniometer, a Huber 404, has two concentric rotations stages that can be set to an accuracy of .0005°. These stages control the sample and the detector arm rotation. Adjustments are made such that the sample rotation is concentric with the goniometer axis via translation stages that sit on the goniometer. The entire goniometer assembly is positioned so that the x-ray beam passes through the goniometer's rotation axis. At the sample position the beam width is a few millimeters larger than the effective filament spot size since the $K_{\alpha 1}$ and $K_{\alpha 2}$ x-rays disperse. Vertical slits after the monochromator define the beam height.

The purpose of the analyzer is to resolve the angular distribution of x-rays scattered from the sample. The analyzer assembly consists of a slit before the crystal to reduce the background and a crystal mounted on a precision rotation stage attached to the goniometer arm. X-rays Bragg reflected from the analyzer are counted by a NaI scintillation detector. Since the sample acts as a point scattering source of nearly monochromatic x-rays the detector angle is a measure of the momentum transferred to the sample. In contrast to neutron scattering, where the analyzer can also measure the energy lost or gained by the sample, the x-ray analyzer primarily acts as a collimator.

The analyzer also serves a secondary role of reducing the dispersion from the finite width of the copper K_α lines.

The analyzer crystal is aligned such that it is parallel to the monochromator crystal at the zero angle position. With this configuration the dispersive nature of the monochromator crystal is exactly canceled by the dispersion of the analyzer at the arm zero position ($2\theta=0$) as shown in figure 4.1.3. The angular dispersion results from an incoming energy distribution and Bragg's law. If, on the other hand, the analyzer crystal reflects the main beam in the same direction as the monochromator crystal then the dispersions from each crystal add. This configuration is useful when the sample induced dispersion cancels the combined dispersion from the monochromator and analyzer crystals, this is labelled the W-configuration.

Bremsstrahlung with wavelength $\lambda/2$ is eliminated by the monochromator for Si(111) and Ge(111) monochromator crystals since the 222 reflection is not allowed. Photons with wavelength $\lambda/3$ are reflected by Ge(111) and Si(111) crystals but the detection system pulse height analyzer is sufficient to reject these events.

D) Spectrometer Resolution

The three dimensional resolution ellipse (section 1.2) results from the uncertainty in the magnitude and direction of $\vec{k}_i$ and $\vec{k}_f$. This is calculated explicitly by convoluting $\vec{k}_i$ with $\vec{k}_f$. In the scattering plane the resolution is primarily due to the Darwin widths of the monochromator and analyzer crystals with additional broadening due to the dispersive nature of the spectrometer. Out of the spectrometer/scattering plane the resolution is determined by the

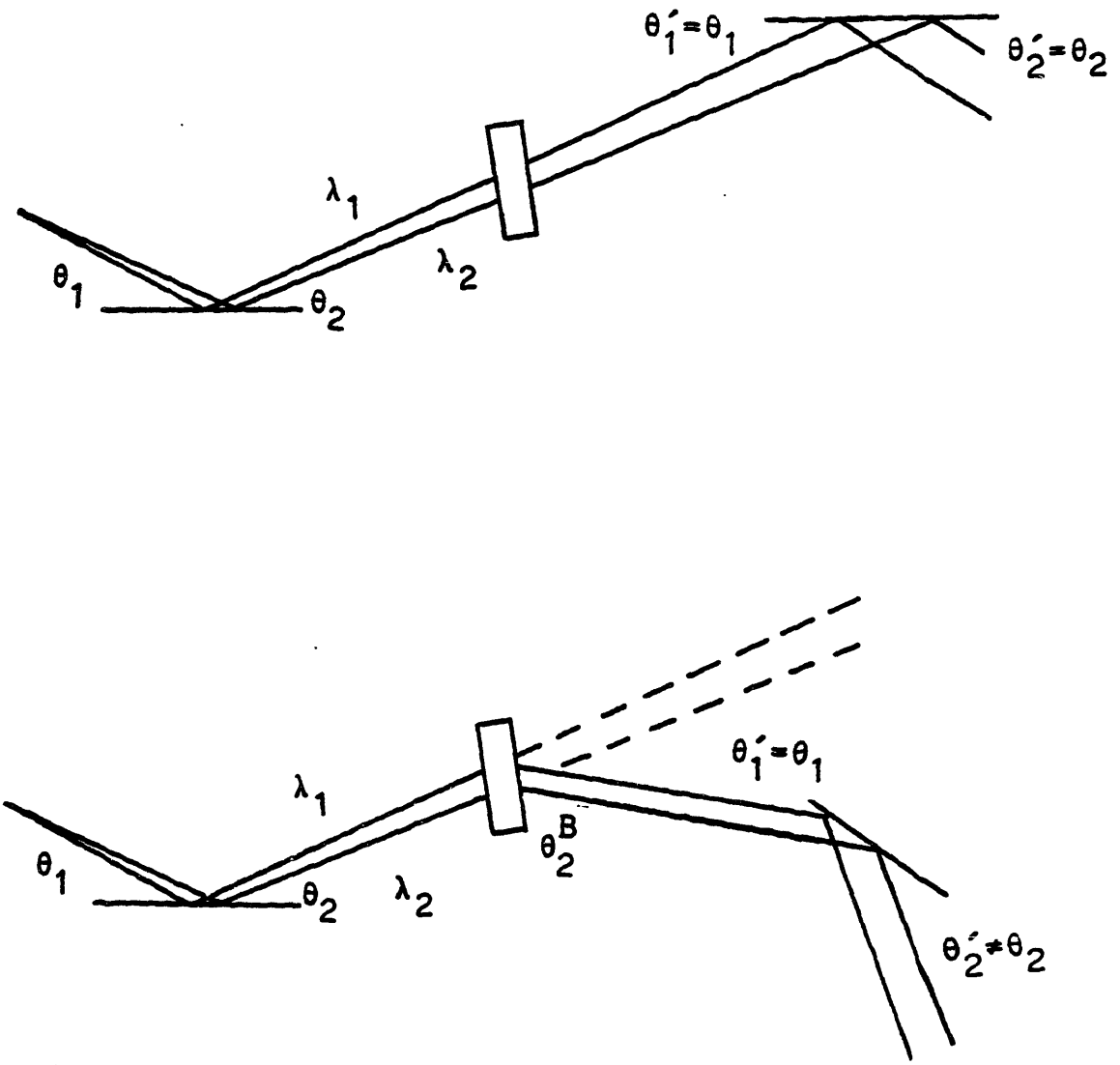

Figure 4.1.3

X-rays with wavelength λ_1 and λ_2 reflect off the monochromator crystal at angles θ_1 and θ_2.
Top: If the ray with wavelength λ_1 reflects from the analyzer at θ_1 then the ray with wavelength λ_2 will reflect at θ_2. This configuration is non-dispersive at $2\theta^B=0$
Bottom: The x-rays are scattered from the sample by $2\theta_1^B$ and $2\theta_2^B$ corresponding to wavelengths λ_1 and λ_2. If the ray with wavelength λ_1 reflects from the analyzer at θ_1 then the ray with energy λ_2 will no longer reflect at θ_2. This ray will reflect at $\approx\theta_2 + \tan(\theta_B)\ (\lambda_1-\lambda_2)/\lambda$ for small θ_B.

vertical slits before and after the sample and is independent of the choice of monochromator and analyzer crystals.

Ideally, the resolution is the convolution of the Bragg reflections from both crystals. The arm zero rocking curve measures the non-dispersive contribution to the longitudinal in-plane resolution. This results from the intrinsic Darwin widths of the perfect germanium or silicon monochromator and analyzer crystals. Because of the q^2 nature of the Darwin profile a Lorentzian provides a fair fit to the profile. Typical arm zero scans for silicon(111) and germanium(111) spectrometers are shown in figures 4.1.4 and 4.1.5. The widths of the profiles are .0035° and .0065° full-width-half-maximum(F.W.H.M.) respectively.

The arm zeros are fit to two functional forms: a simple Lorentzian and the sum of several Lorentzians. Figures 4.1.4 and 4.1.5 clearly show that a single Lorentzian given by

$$I(\theta) = \frac{I_0}{(\theta-\theta_0)^2+\delta\theta^2} \qquad 4.1.1$$

fails to fit the arm-zero scattering perfectly. Safinya improved the fit by adding correction term to the Lorentzian so that at intermediate θ the scattering falls off as q^4. The shape of the ideal Darwin profile has q^2 wings and the convolution of the two profiles should also have q^2 tails. It is the flat center region of the profile that differs from a Lorentzian. By adding several Lorentzians displaced in θ the theoretical profile is better approximated. The advantage of this scheme will become apparent when the convolution with the theoretical line-shape is performed (see Appendix 1).

The sum of three Lorentzians adequately describes the profile since the addition of more Lorentzians does not significantly improve the fit. For arbitrary Lorentzians this would require 9 parameters, however, only a separation parameter θ_s is statistically significant. The arm zero is fit to

$$I(\theta) \propto \left[\frac{1}{(\theta-\theta_0-\theta_s)^2+\delta\theta^2} + \frac{1}{(\theta-\theta_0)^2+\delta\theta^2} + \frac{1}{(\theta-\theta_0+\theta_s)^2+\delta\theta^2}\right] \qquad 4.1.2$$

and best fits to the data are plotted in figures 4.1.4 and 4.1.5 as solid lines. These fits have a goodness of fit parameter about ten times better than a fit to a single Lorentzian.

The spectrometer resolution function at non-zero angles contains two peaks corresponding to the two copper K_α lines. At the arm-zero it is impossible to distinguish these lines because there is no dispersion. However at 3°, a typical angle for the smectic A (001) reflection, the two peaks are separated by ≈0.007°. For a silicon spectrometer it is possible to resolve these lines since the 2θ resolution is 0.0035° F.W.H.M., however, for the germanium set-up the two peaks merge into a single peak since the 2θ resolution is 0.0065° F.W.H.M.. The intensity ratio between the two peaks is always close to the actual value of .43 and is measured for each line-up.

The resolution for each of the two copper K_α lines is calculated from the arm-zero fit and the intrinsic energy width of the lines. The energy broadening can be calculated by differentiating Bragg's law and gives,

$$\Delta\theta = \tan(\theta)\,\frac{\Delta E}{E} \qquad 4.1.3$$

where ΔE is the energy width of the line and E is the x-ray energy of

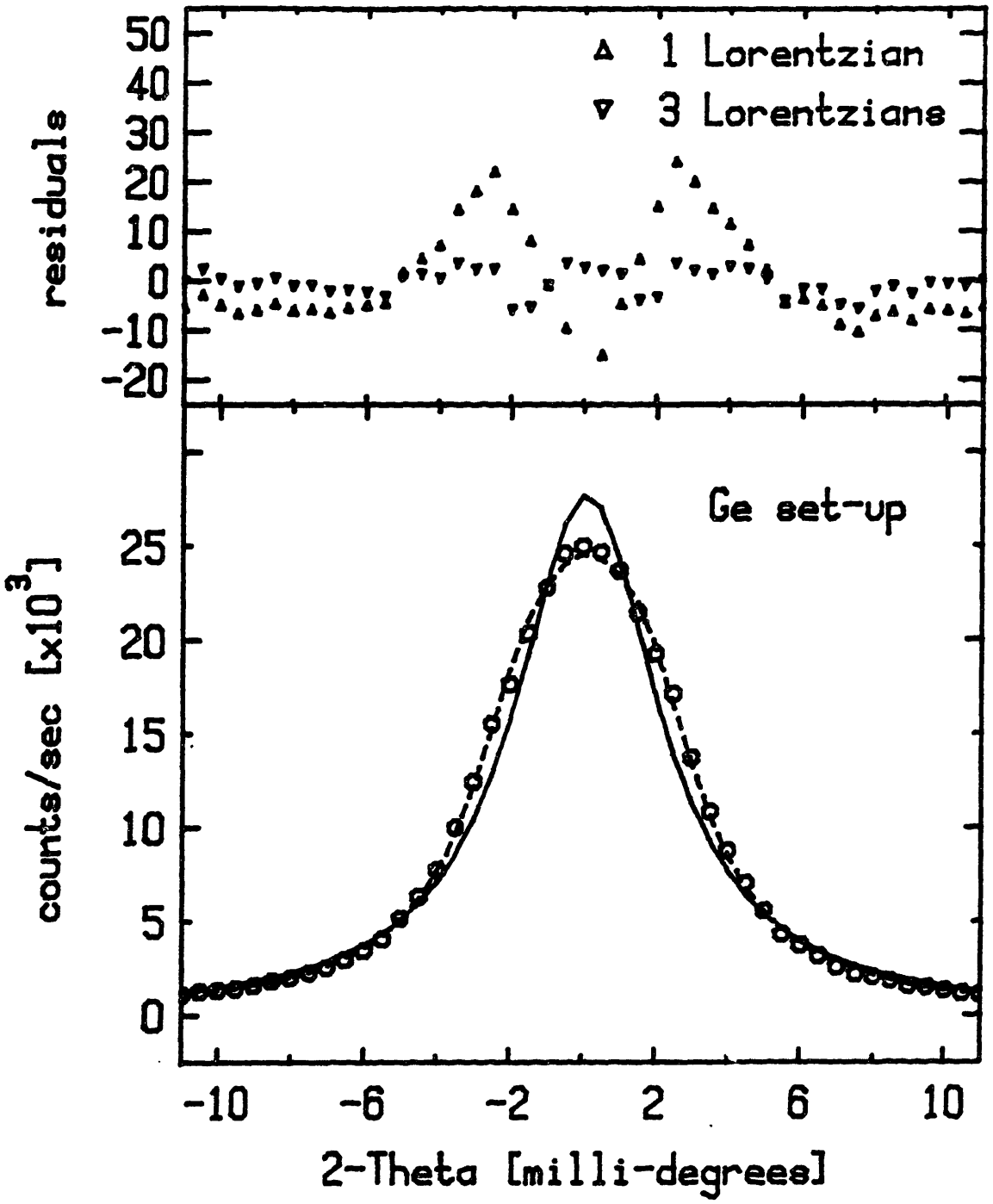

Figure 4.1.4

Arm-zero profile for a germanium(111) line-up with the open vertical set-up. The best fit to Eq 4.1.1 (solid line) gives $\delta\theta = 0.0024°$ with $\chi^2 = 65$. The best fit to Eq 4.1.2 (dashed line) gives $\delta\theta = 0.0019°$ and $\theta_s = 0.0011°$ with $\chi^2 = 5$.

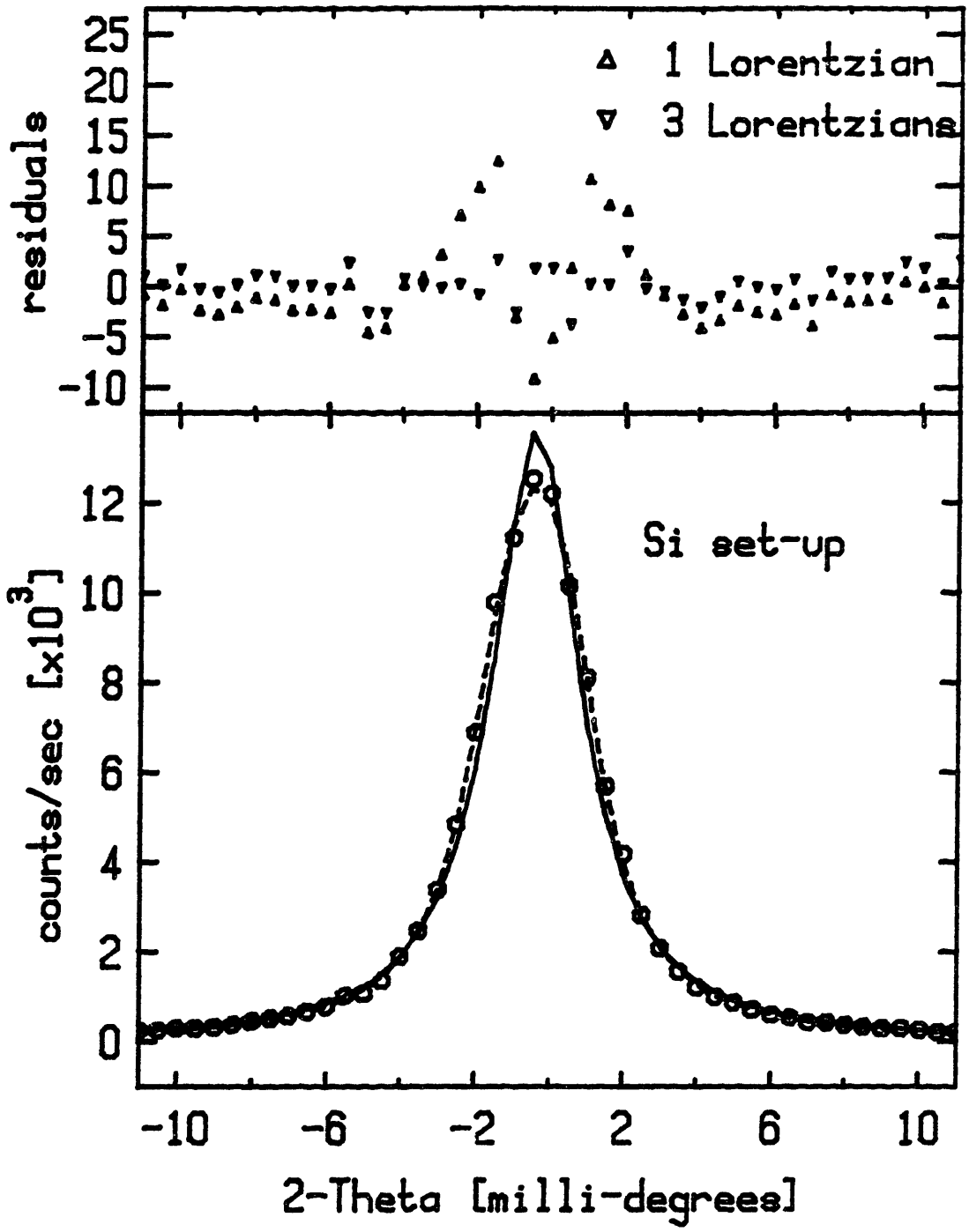

Figure 4.1.5

Arm-zero profile for a silicon(111) line-up with the open vertical set-up. The best fit to Eq 4.1.1 (solid line) gives $\delta\theta = 0.0014°$ with $\chi^2 = 12$. The best fit to Eq 4.1.2 (dashed line) gives $\delta\theta = 0.0012°$ and $\theta_s = 0.0008°$ with $\chi^2 = 12$.

the line. Since the energy distributions of the K_α lines are Lorentzian, the angular broadening must also be Lorentzian with the width given by Eq 4.1.3. The uncertainty in 2θ at the scattering position must be the convolution of the uncertainty in 2θ at the arm-zero and the dispersive contribution to the uncertainty in 2θ [see Appendix 1]. This amounts to a broadening in the 2θ resolution by $\approx 0.001°$ as shown in figure 4.1.6. The transverse in-plane resolution is smaller than the longitudinal in-plane resolution by a factor of $\sin\theta$, hence for all practical purposes a delta function description is adequate.

The resolution out of the scattering plane is the convolution of the incoming vertical distribution with the outgoing accepted distribution. The distribution of $\vec{k}_i$ in the vertical is limited by vertical slits after the monochromator which produces a square distribution function. For most of the experiments reported here the distribution of $\vec{k}_f$ is determined by the vertical acceptance of the detector ~ 1cm which has a square acceptance function (open vertical configuration). The vertical divergence of $\vec{k}_i$ is matched to the acceptance of $\vec{k}_f$ by adjusting the exit slits after the monochromator such that the detector is just fully illuminated at $2\theta=0$. Hence, the vertical resolution function should be modeled by a triangular function since it is the convolution of two square waves of equal width.

To measure the vertical resolution a perfect crystal is placed in the sample position. By rocking the crystal the intensity verses tilt angle is measured. The vertical component is calculated from geometry and Bragg's law. Figure 4.1.7 shows a typical measurement of the vertical resolution function. The vertical resolution may be

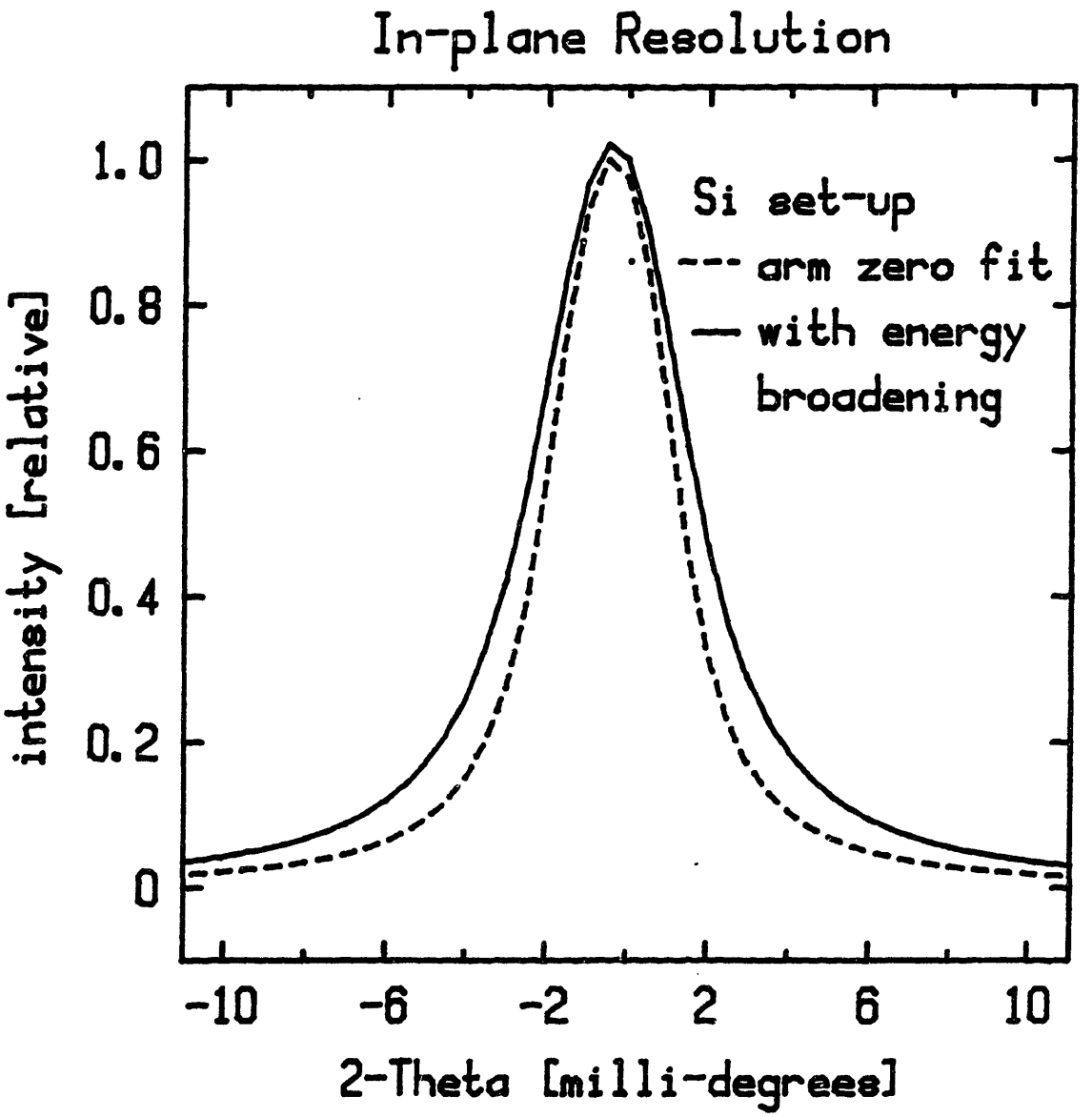

Figure 4.1.6

The dashed line is an arm-zero profile for a silicon line-up. The solid line is the calculated resolution at $2\theta = 3.0°$.

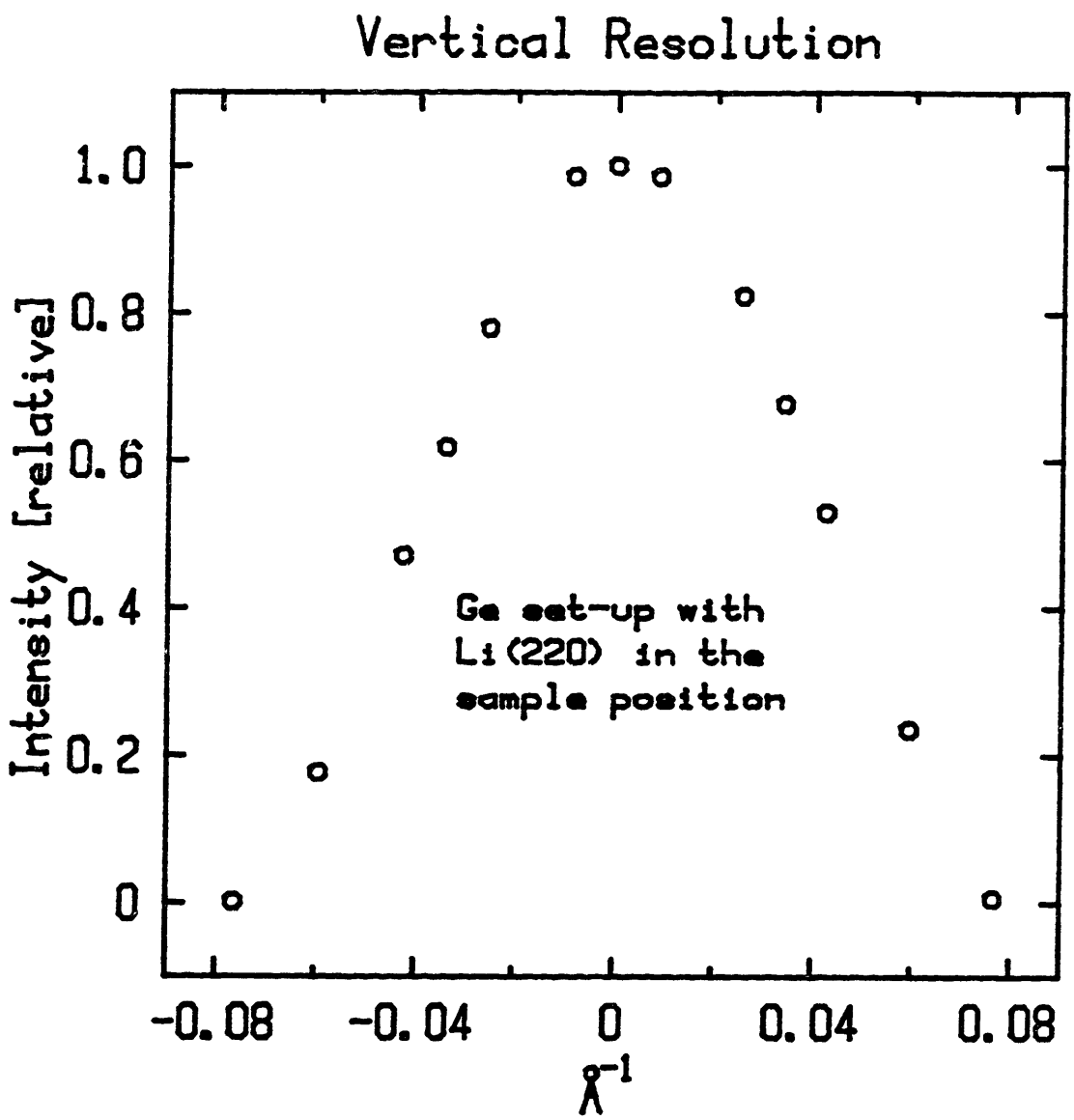

Figure 4.1.7

The vertical resolution function as measured by a LiF (220) crystal in the sample position.

equally well modeled by a triangular or a Gaussian function. For this configuration the vertical resolution is typically 0.05Å^{-1} H.W.H.M. which is much broader than the in-plane resolution.

To verify that the $N \rightarrow S_A$ line-shape does not depend on the vertical resolution several experiments were performed with better vertical resolution. Better resolution is obtained by placing Soller slits (parallel metal plates) before the analyzer. In a similar manner to the "open vertical" configuration, the divergence of the incoming beam is matched to the Soller slit acceptance with the vertical monochromator exit slits. This yields a vertical resolution of $.012\text{Å}^{-1}$ H.W.H.M., a factor of 4 better than the "open vertical configuration".

E) CONTROL ELECTRONICS

During the last several years of data acquisition the $N \rightarrow S_A$ scattering profile has been measured at over 1000 temperatures for the ~ 20 samples studied. Furthermore, for each profile the x-ray flux is counted in a period from one to several hundred seconds at 100 different goniometer angle settings. To accumulate this vast quantity of data nearly all aspects of the data collection and analysis have been highly automated. The back-bone behind this effort is a PDP 11/34 computer connected to a CAMAC crate for data acquisition and control.

Figure 4.1.8 shows the block diagram of the various electronic components utilized to collect data. The analyzer and sample angles are set by stepping motors connected to the goniometer through 10/1 gear reducers. A pulse train of length n is output by the pulse generator, where n is the number of steps necessary to reach the desired position. The pulse trains are connected to chopper type stepping motor drive

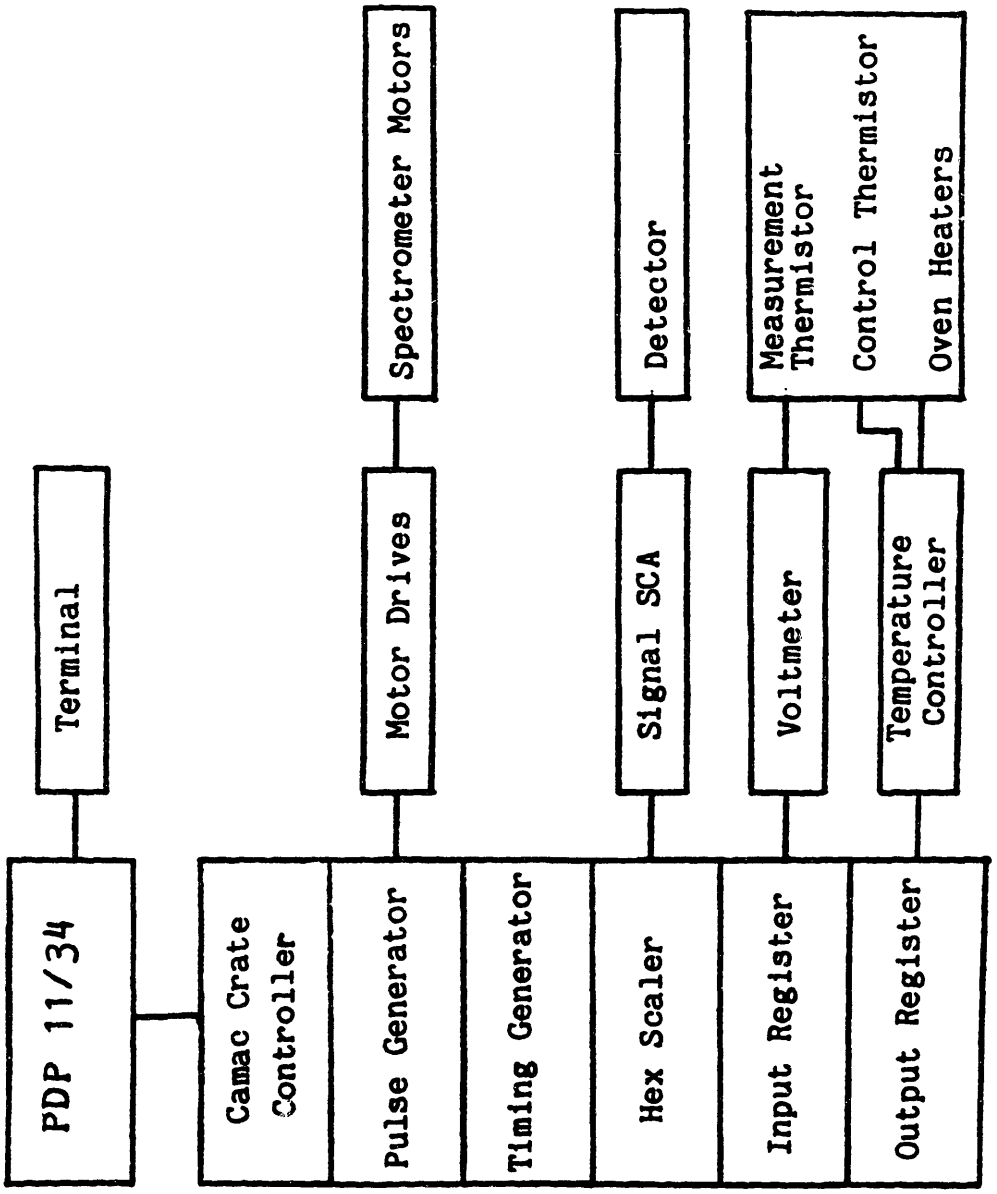

Figure 4.1.8

Block diagram of the data acquisition and control electronics.

units which provide uniform acceleration and deceleration and current to drive the motor coils. For each step received the goniometer angles move .0005°.

The counting circuit works as follows: X-rays strike the detector consisting of a NaI scintillator, a photomultiplier tube and a preamplifier. An electrical pulse is generated for each incident x-ray, with the pulse height proportional to the incident energy. A single channel analyzer (SCA) reduces the noise background to ~.2 counts per second. The output of the SCA goes into the hex scaler and is gated for a fixed period of time by the timing generator. One advantage of CAMAC is that interrupts are generated when a task is completed allowing the computer to run other processes in the interim.

4.2
Temperature Control, Alignment and Sample Preparation

A) Temperature Control

There are many constraints placed on the design of the oven used in these experiments. The oven must be as small as possible since the magnetic field is inversely proportional to the pole piece separation. To accomplish this and achieve excellent temperature control a custom made two stage oven was constructed as shown in figure 4.2.1. The primary advantage of this oven over an earlier design by Safinya is the ability to evacuate the oven or flow controlled amounts of N_2 to stabilize the transition temperatures. This oven was used for all measurements except the 40.7 and 9S5 experiments which used Safinya's oven.

The oven is constructed from two concentric brass cans, 1.0 and 1.5 inches in diameter that are 2.0 and 3.375 inches high. These cans are isolated from one another by 1/8 inch stainless steel tubes Two o-rings provide a vacuum seal between the outer can and the beryllium cylinder. An inner beryllium cylinder helps the inner oven maintain a constant temperature over its entire surface which tends to minimize surface cooling of the sample. The sample cell is attached to the bottom of the inner vessel via an aluminum support. Temperature gradients across the illuminated sample region must be considered to determine the temperature resolution of these measurements.

Vertical temperature gradients are most likely to influence the results since the beam is much larger and the oven less symmetric in this direction. Since the scattering at the q vector corresponding to the smectic A phase increases sharply at the $N \rightarrow S_A$ transition it provides

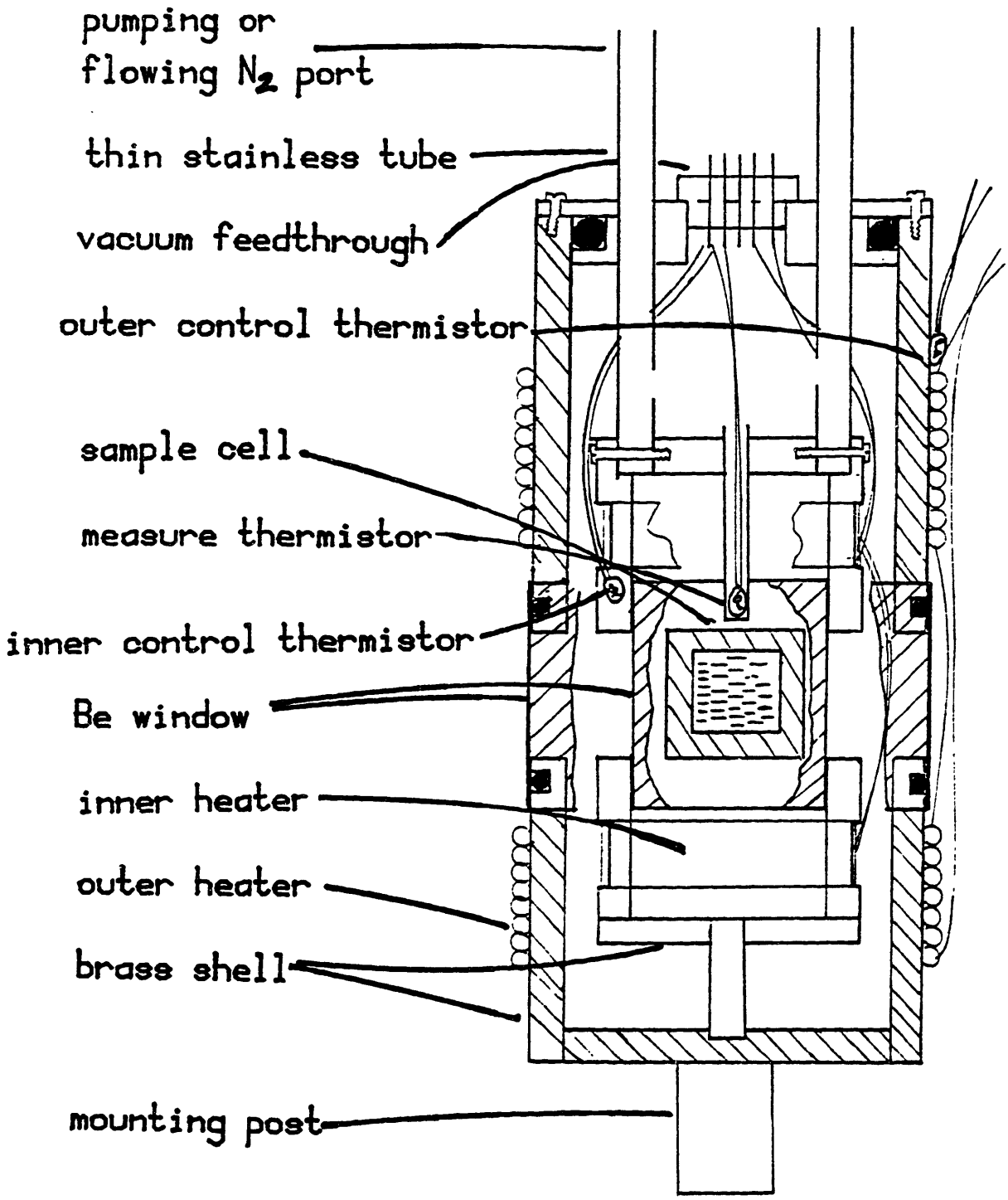

Figure 4.2.1

Sketch of two stage liquid crystal oven. The tubes at the top allow the oven evacuation or N_2 gas to flow. Two o-rings provide a vacuum seal between the outer can and the beryllium cylinder. (Kevin Evans-Lutterodt was instrumental in designing the oven.)

a probe of the local transition temperature. By adjusting the vertical exit slit after the monochromator different parts of the sample can be illuminated and the associated transition temperatures measured. Much to our surprise the transition temperature for a sample of 9CB differed by 0.020°C from the top to bottom of the sample. By using just the top or bottom inner heater the transition temperature gradient changed to either 0.010°C or to 0.030°C. If the T_c gradient results from a real temperature gradient then adjustment of the heater power would have a much more pronounced effect. Therefore, this 0.020°C gradient is due to an impurity gradients within the sample. Additional experiments on substances less susceptible to impurities allowed us to establish that the temperature gradient across the illuminated sample volume at 50°C is less than 0.001°C!

Both stages are temperature controlled by independent circuits. The heater coil power amplifier is controlled by the output voltage generated by a thermistor bridge with a filtered integrator circuit. This circuit adjusts the heater power until the error voltage generated by the bridge is nulled. The oven temperature is varied by manually changing the resistance on one leg of the bridge. Control about this set-point is obtained by a computer generated offset voltage added to the bridge error voltage. The circuit is balanced when the bridge produces an error voltage that cancels the offset voltage. To minimize the control temperature dependence on changes in the room temperature all components were selected to have small temperature coefficients.

The voltage produced by placing an ultra stable current source (1 part in 10^{-5}) in series with a calibrated glass encapsulated thermistor mounted a few millimeters from the sample measures the

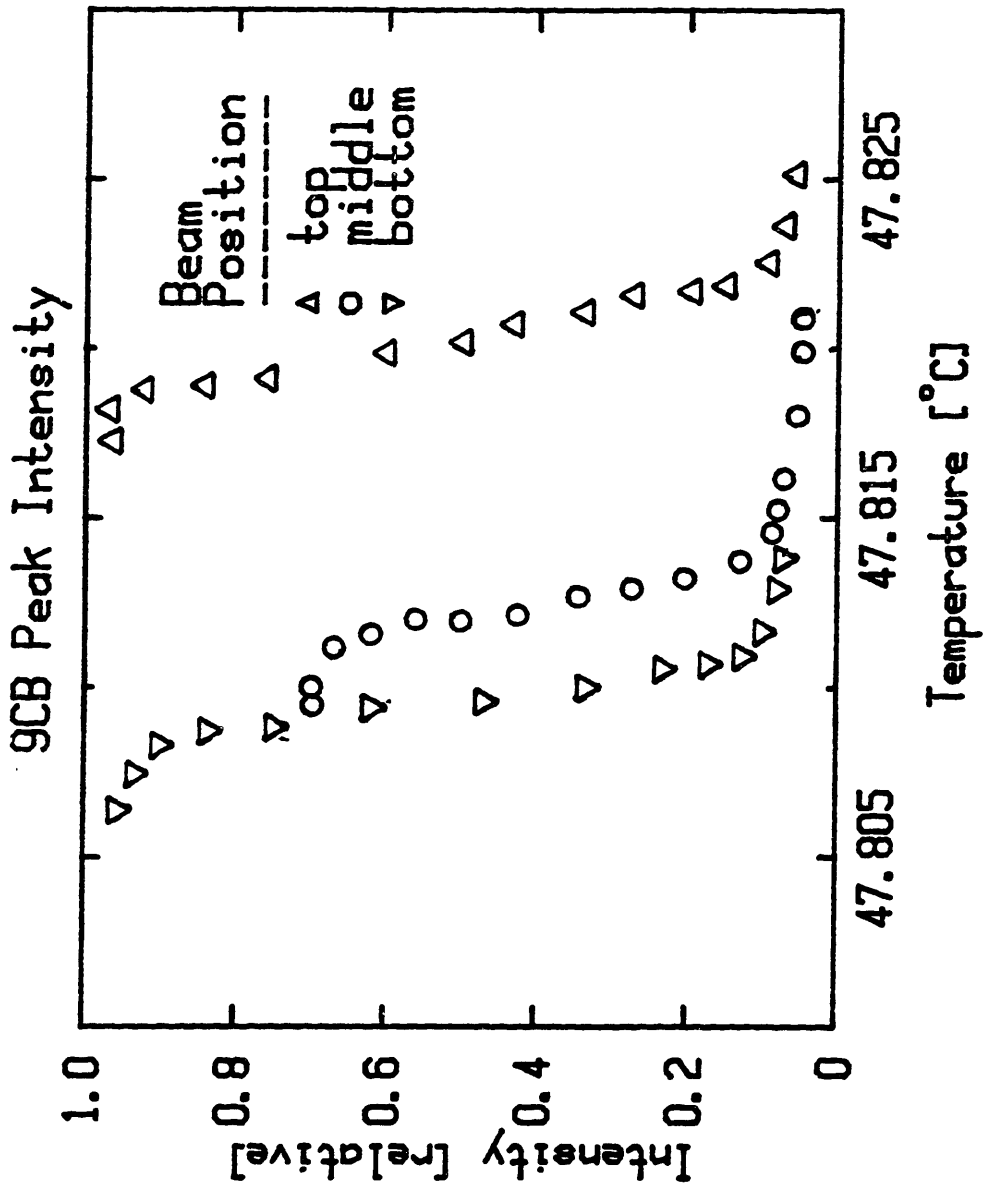

Figure 4.2.2

Peak intensity at the q vector corresponding to smectic layering for 9CB. Different parts of the sample were illuminated by adjusting the vertical exit slits of the monochromator. The transition temperature gradient results from an impurity gradient across the sample volume.

temperature. This voltage is measured with a 5 1/2 digit voltmeter producing 0.001°C resolution.

B) Sample Alignment

For all the experiments reported in this thesis, alignment is obtained by magnetically orienting the liquid crystal director. Both the electromagnet and the sample must rotate with the goniometer angle ϕ. A special design allows the beam to pass through the center of the pole pieces when the magnet is rotated by over 75°. The magnet, weighing ~1000 pounds, is suspended from the ceiling via a hoist, a precision swivel bearing and a leaf spring. Early experiments used a magnet capable of 4 kilogauss in a 1.6 inch gap. This was superseded by a custom made commercial magnet manufactured by ANAC Inc., figure 4.2.3, that produces a 7 kilogauss field in a 1.6 inch gap. Calibration curves for the ANAC magnet are shown in figure 4.2.4.

The performance of the photomultiplier tube is very sensitive to magnetic fields, especially the large field generated by the electromagnet. To minimize this effect the detector is surrounded by several layers of mu-metal. The susceptibility is checked by rotating the magnet, both on and off, with the detector positioned at $2\theta=0$. With proper shielding there is no difference and the only angular dependence is from the increase in the effective sample adsorption with angle.

The nematic director aligns along the magnetic field direction to reduce the diamagnetic free energy and should scale as the field squared. The diamagnetic susceptibility varies between compounds and is $-0.15\ cm^3mol^{-1}$ for most materials.[4] X-ray scattering techniques are not capable of measuring the alignment in the nematic phase since the

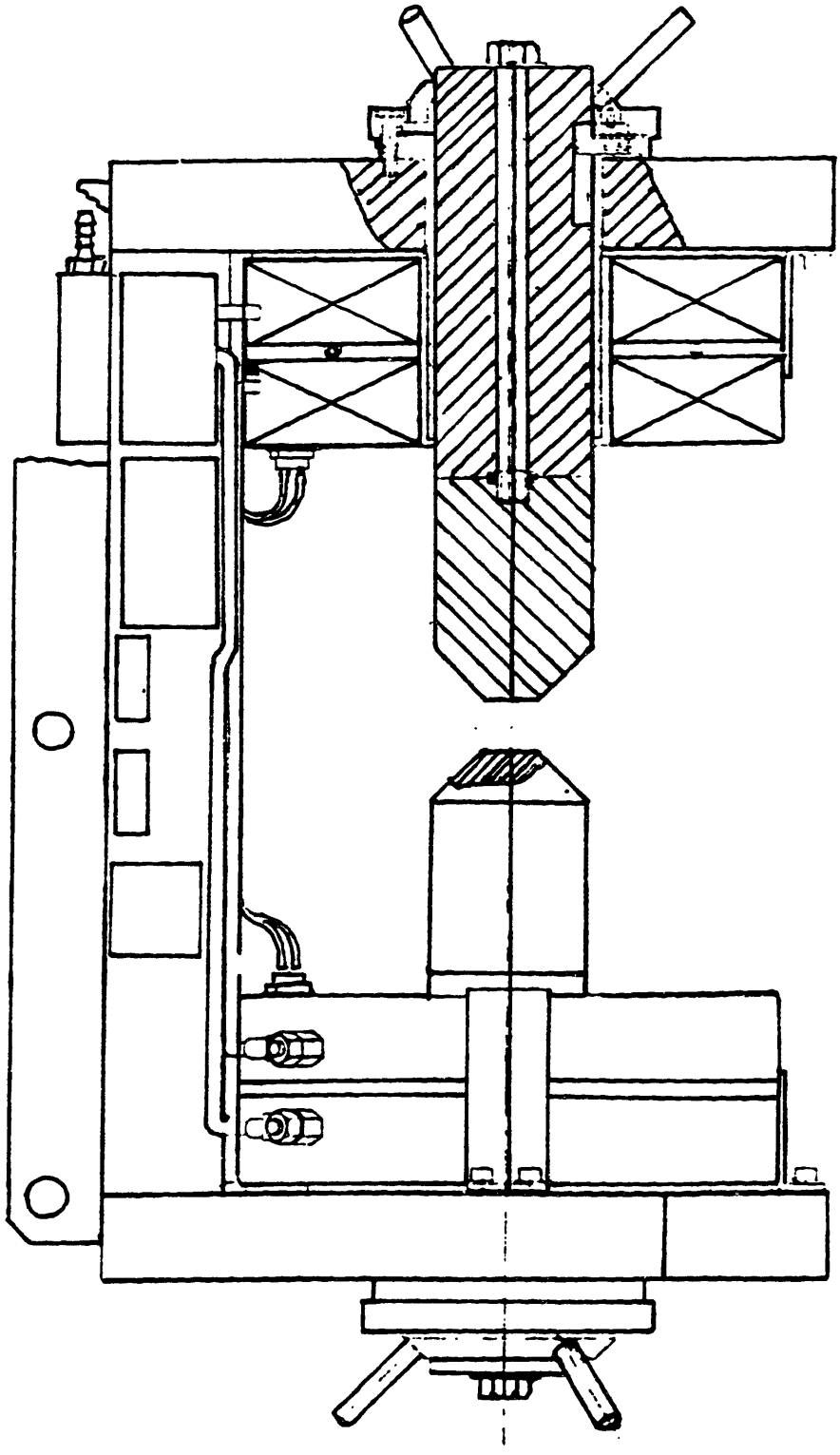

Figure 4.2.3

Side view of the ANAC electromagnet.

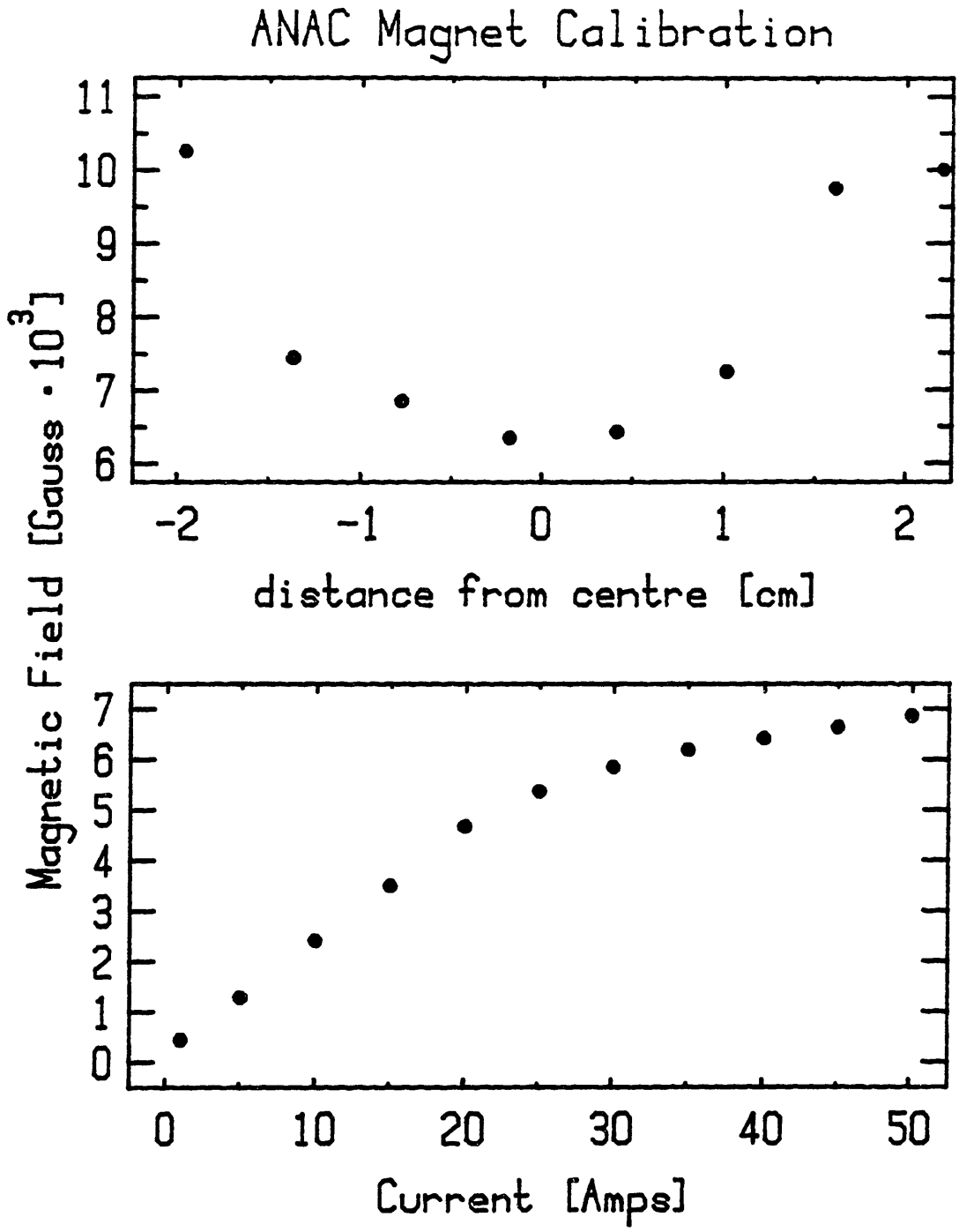

Figure 4.2.4

ANAC magnet calibration courtesy of Luz Martinez.
Top: Field as a function of longitudinal position.
Bottom: Magnetic field as a function of magnet current.

transverse order is limited by the finite size of smectic fluctuations. However in the smectic A phase the transverse width measures the layer distribution directly which is the sample mosaic.

The sample mosaicity depends on the strength and the homogeneity of the aligning magnetic field, the anchoring of the liquid crystal molecules to the wall of the sample cell and the particular compound. Materials with long nematic ranges such as 40.7 and $\overline{8}$S5 produced excellent alignment $\leq$0.05°H.W.H.M.. This might result from the nearby smectic C phase in both materials that allows the molecules to slide(tilt) easier with respect to one another or to a nearly saturated nematic order parameter. As the nematic phase decreases in a homologous series the mosaic worsens but is always better than 1.0°F.W.H.M.. Varying types of sample cells were used (see the next section) however no correlation was found between the mosaic and the sample cell walls. Misalignment between the layer direction preferred by the walls and the magnetic field often caused the peak position of the ϕ scan to shift and the width to increase as the temperature is lowered further into the smectic. The mosaic degraded the most for materials with the largest thermal coefficient of expansion since many more defects must be created for these materials as the temperature is lowered further into the nematic phase.

C) Sample Preparation and Cells

The materials studied in this thesis have been obtained from several sources. The nO.m samples (40.7 and 60.8) were purchased from CPAC Organix Inc.. A second sample of 40.7 was synthesized by John Goodby of Bell Labs. All of the $\bar{n}$S5 samples and the $\overline{6}$09 samples were

provides through the generosity of Mary Neubert and Dave Johnson of the Liquid Crystal Institute at Kent State University. Finally, the nCB samples were commercially prepared by British Drug House.

Impurities are an inherent feature of all liquid crystal systems although in most instances the most pronounced effects are to shift transition temperatures rather than altering the essential physics. These impurities may be neighboring homologs, adsorbed gasses, liquid crystal fragments, solvents, other chemical contaminants or just dust. Repeated recrystalization removes some of the contaminants, filtering removes dust, and pumping removes the adsorbed gasses, solvents and some of the fragments and other chemical contaminates. These shifts provide great difficulty in determining the critical behavior close to the transition when the drift exceeds 0.010°C per day. Furthermore, these drifts promote transition temperature gradients across the sample. Nevertheless, our results on 40.7 and 9CB indicate that the $N \rightarrow S_A$ critical behavior is independent of these features when corrections are made for the drifting T_{NA}.

To remove impurities many of the samples were heated to the nematic or isotropic phase under vacuum. Though this technique usually improves the transition temperatures by removing adsorbed gasses, the liquid crystals naturally drift downward as the gasses are readsorbed. Since these impurities are apparently benign, pumping on the samples provided needless complications if the sample is reexposed to air. To reduce the T_{NA} drift some of the measurements were performed in an evacuated oven while others were made with flowing N_2 or Argon at very slow rates through the oven. Both of these techniques were invaluable in stabilizing T_{NA}. A table summarizing the sample preparations is

presented in Appendix 2.

Several improvements were made to the liquid crystal sample cells over the period of these measurements however all the cells used beryllium windows. For most of the experiments the windows, 1/2" by 1/2" by 0.010", were attached to a machined aluminum cell with vacuum epoxy. To maximize the sample scattering, the thickness was closely matched to the x-ray adsorption length which varies between ~ 0.030" for the $\bar{n}$S5 compounds to ~ 0.100" for 40.7. The cross-sectional sample area was 0.35" by 0.35" with a typical volume of a few hundred micro-liters. As described by Safinya[2], these cells were filled through holes in the top while the liquid crystal remained in the isotropic phase.

Several sample cells were constructed that enabled the concentration to be varied by adding one of the liquid crystal components to the existing cell mixture. This wasn't possible in "Safinya's cell" since not all of the material added entered the sample volume; instead some of it collected near the fill holes, hence a precise calculation of the concentration was impossible. To minimize this uncertainty, a slot was machined between the two fill holes so that the new material could be added directly to the sample with a micro pipette. The concentration was calculated from the empty cell weight and the weight after adding liquid crystal. After a day of agitation the transition temperature gradient was always less than a few milli-degrees across the sample volume. The latter experiments utilized an all beryllium cell with a slotted top and sealed by an aluminum top with an indium o-ring. This sealed environment allowed the cell to be turned upside down during mixing and reduced the transition temperature drift. To neutralize the beryllium and epoxy surfaces some of the cells were

coated with a 1% solution of N,N-dimethyl-N-octadecyl-3-aminopropyltrimethoxysilyl chloride (DMOAP).[5] This did not reduce the transition temperature drift nor did it effect other aspects of the measurement. A summary of the sample cell configuration is presented in Appendix 2.

For samples with downward drifting transition temperatures the top of the cell always has a lower T_c than the bottom. The drift presumably corresponds to impurities diffusing through the open top since pumping on the oven reversed the gradient and caused T_c to drift upwards. Likewise, opening the evacuated oven to air caused both the gradient and drift direction to reverse. These effects are a manifestation of a small diffusion coefficient $10^6 cm^2 sec^{-1}$, hence the diffusion times are of order 10^6 seconds for a $1 cm^3$ sample.

REFERENCES

1. M. Kaplan, M.I.T Thesis(1980)

2. C. Safinya, M.I.T. Thesis(1981)

3. Encyclopedia of Physics, R.G. Lerner and G.L. Trigg editors, 1113, (Addison Wesley, Reading Mass, 1981).

4. A. Buka and W.H. de Jeu, J. Physics (Paris) 43 , 361(1982).

5. F.J. Kahn, Appl. Phys. Lett. 22 ,386(1973).

5.0
SUMMARY OF RESULTS

In this chapter high resolution x-ray scattering results on the smectic fluctuations in the nematic phase are presented. As described in the last chapter, the spectrometer resolution is primarily limited by the Darwin-widths of the perfect germanium/silicon monochromator and analyzer crystals. A summary of the exact spectrometer configuration for each experiment is shown in Appendix 2. The sample is contained in a beryllium window cell, contained in a computer controlled two-stage oven and aligned by an electromagnet.

For all of the scattering experiments, the scattering has been fit to

$$S(q_{\parallel},q_{\perp}) = \frac{\sigma_0}{1 + \xi_{\parallel}^2(q_{\parallel}-q_{\parallel}^0)^2 + \xi_{\perp}^2 q_{\perp}^2(1 + c\xi_{\perp}^2 q_{\perp}^2)} \qquad 5.0.1$$

convoluted with the appropriate resolution function. This line-shape is a Lorentzian with a fourth order correction in the transverse direction (LFC). The details of the convolution are given in Appendix 1. Some of the data have been fit to a Lorentzian raised to the power $1-\eta_{\perp}/2$ (LPC) along the transverse direction

$$S(q_{\parallel},q_{\perp}) = \frac{\sigma_0}{\xi_{\parallel}^2(q_{\parallel}-q_{\parallel}^0)^2 + (1 + \xi_{\perp}^2 q_{\perp}^2)^{1 - \eta_{\perp}/2}} \qquad 5.0.2$$

convoluted with the resolution function. Both forms evolve continuously from a pure Lorentzian , $c=0$ or $\eta_{\perp}=0$ to a Lorentzian squared, $c= 0.25$ or $\eta_{\perp}= -2$. In order to fit the data, c or $\eta_{\perp}$ must vary, hence the cross-section changes shape with temperature.

Experiments were performed with different values of the aligning field for some of the samples. Although the mosaic distribution in the smectic phase depends on the field strength, the critical behavior in the nematic phase does not. In the nematic phase, therefore, it is assumed that the nematic director is always well aligned, hence, it is not related to the mosaic in the smectic phase where wall effects are more dominant. Thus, no corrections have been made for the mosaic distribution.

This chapter is divided into three subsequent sections. In the first section results are presented for $\overline{6}09$ and 40.7. Both $\overline{6}09$ and 40.7 have long nematic ranges (≈25°C) and exhibit saturated second order transitions with very long correlation lengths. In section 5.2 the results for the $\bar{n}$S5 series are presented. Experiments were performed on the pure materials $\overline{9}$S5, $\overline{10}$S5, and $\overline{11}$S5 as well as mixtures $\overline{8.5}$S5, $\overline{9.75}$S5, $\overline{10.2}$S5 and $\overline{10.4}$S5 where the non-integer number gives the average chain length by weight. In section 5.3 results are presented for the pure materials 9CB and 8CB as well as for the mixtures 9.05CB, 9.09CB, 9.14CB, 9.20CB, and 9.28CB. We find that $\overline{10}$S5 and 9CB are very near their respective tricritical points. In Appendix 3 results in 60.8, which only has a 1.0°C nematic range, are presented.

5.1 Results in 40.7 and $\overline{6}09$; The Saturated Limit

40.7 Results

Extensive studies have been conducted on Shiff-base liquid crystal compounds because of their diverse phase behavior. Unfortunately, they tend to decompose when exposed to the moisture in air. These fragments, together with other impurities, renormalize the interactions resulting in lower transition temperatures. The transition temperature shifts much more rapidly in the nematic phase than in the smectic phases. Therefore, decomposition presents the greatest difficulty in measuring the $N \rightarrow S_A$ critical behavior close to the transition.

Studies were performed on two samples of 40.7. Sample 1 was prepared commercially (CPAC Organix), Sample 2 was synthesized by John Goodby at Bell Labs. In sample 1, before we took measures to reduce decomposition, the critical temperature drifted by over 0.1°C per day. To prevent further decomposition, we permanently sealed the sample cell with a low vapor pressure epoxy (Torr Seal). This reduced the drift of T_{NA} to 0.002°C per day. For sample 2, the oven with Kapton windows was modified to allow flowing argon (1 litre/hour); this also reduced the drift to 0.002°C per day. Because appropriate precautions were taken from the beginning, T_{NA} for this sample was 1.0°C higher than for sample 1. Nevertheless, our results, to be presented later in this section, indicate that the critical behavior is identical for both samples.

Using the silicon spectrometer set-up described in the last chapter, the wave vector dependent susceptibility of the smectic

fluctuations have been measured in 4O.7. These fluctuations are centered about the q vector for smectic layering $(0,0,q_{\parallel}^{o})$ where $q_{\parallel}^{o} = .2333Å^{-1}$ for sample 1 and $q_{\parallel}^{o} = 0.2339Å^{-1}$ for sample 2 as shown in figure 5.1.1. In order to map out the critical scattering longitudinal scans ($q_{\perp}=0$) and transverse scans ($q_{\parallel}=q_{\parallel}^{o}$; $q_{\perp}$varied) were taken for a series of reduced temperatures $t = T/T_{NA}-1$ equally distributed on a logarithmic scale.

The transition temperature, T_{NA}, could be determined by longitudinal and transverse scans through the $(0,0,q_{\parallel}^{o})$ peak in the immediate neighborhood of T_{NA}. As the transition temperature is approached from the nematic side both scans continuously narrow due to the diverging correlation lengths. The longitudinal width continues to narrow until at T_{NA} the width is comparable to the spectrometer resolution. As may be seen in figure 5.1.2, subtle changes in the longitudinal width manifest themselves in the depth of the dip between the $K_{\alpha 1}$ and $K_{\alpha 2}$ peaks. Since the integrated intensity of the $(0,0,q_{\parallel}^{o})$ peak increases dramatically at the transition, this provides a second measure of the transition temperature.

The behavior of the transverse width with temperature provides the most sensitive determination of T_{NA}. At the transition, the width of the transverse scan changes abruptly, by about a factor of five over a few millidegrees Centigrade. The width, which is controlled by the mosaic of the smectic layers, was better than 0.05°HWHM. The transition temperature, determined in this fashion, showed no hysteresis effects to within two millidegrees.

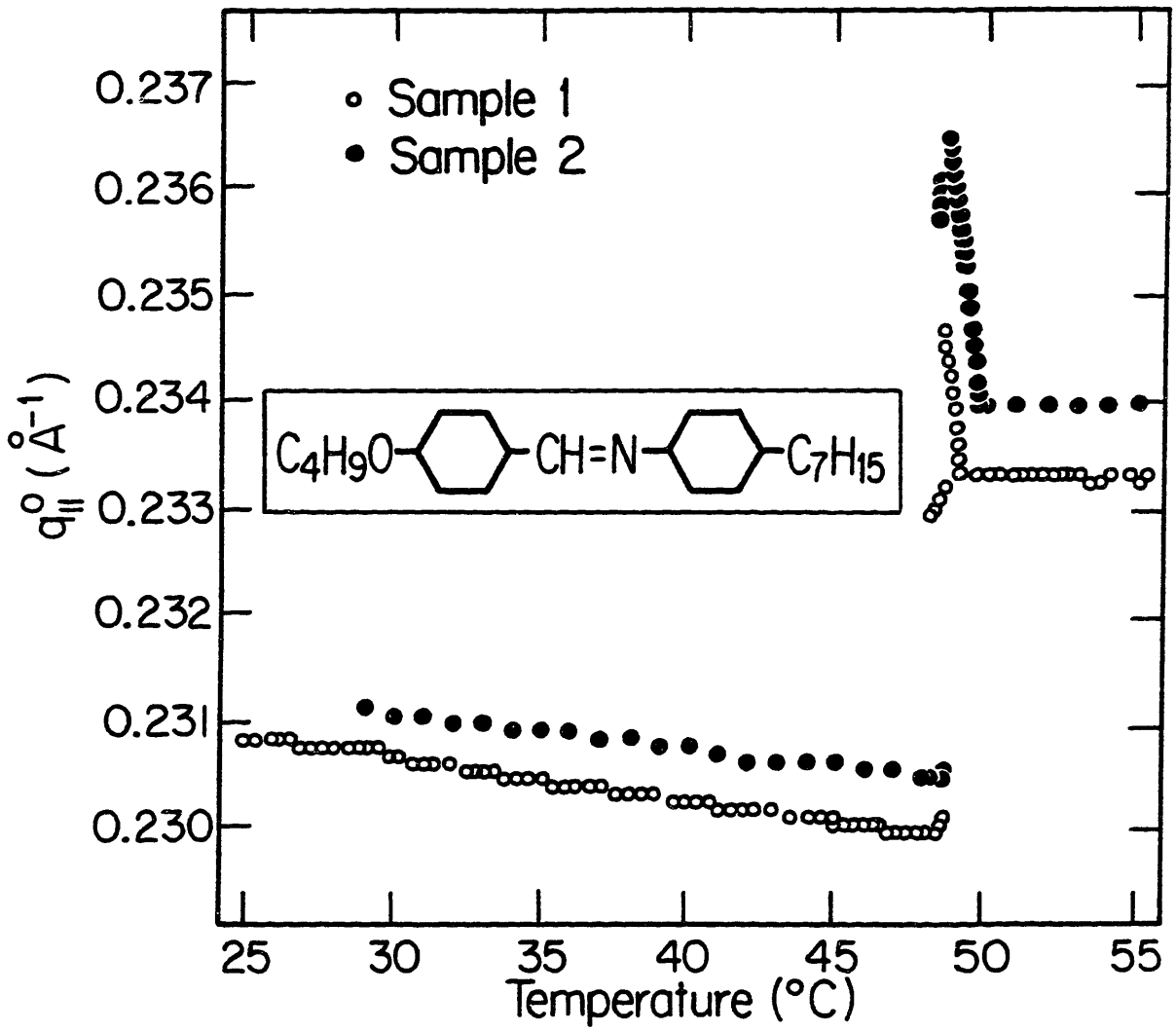

Figure 5.1.1

Smectic A q vector corresponding to smectic layering ($q_{\parallel}^{o}$) versus temperature in 40.7. The two samples are described in the text.

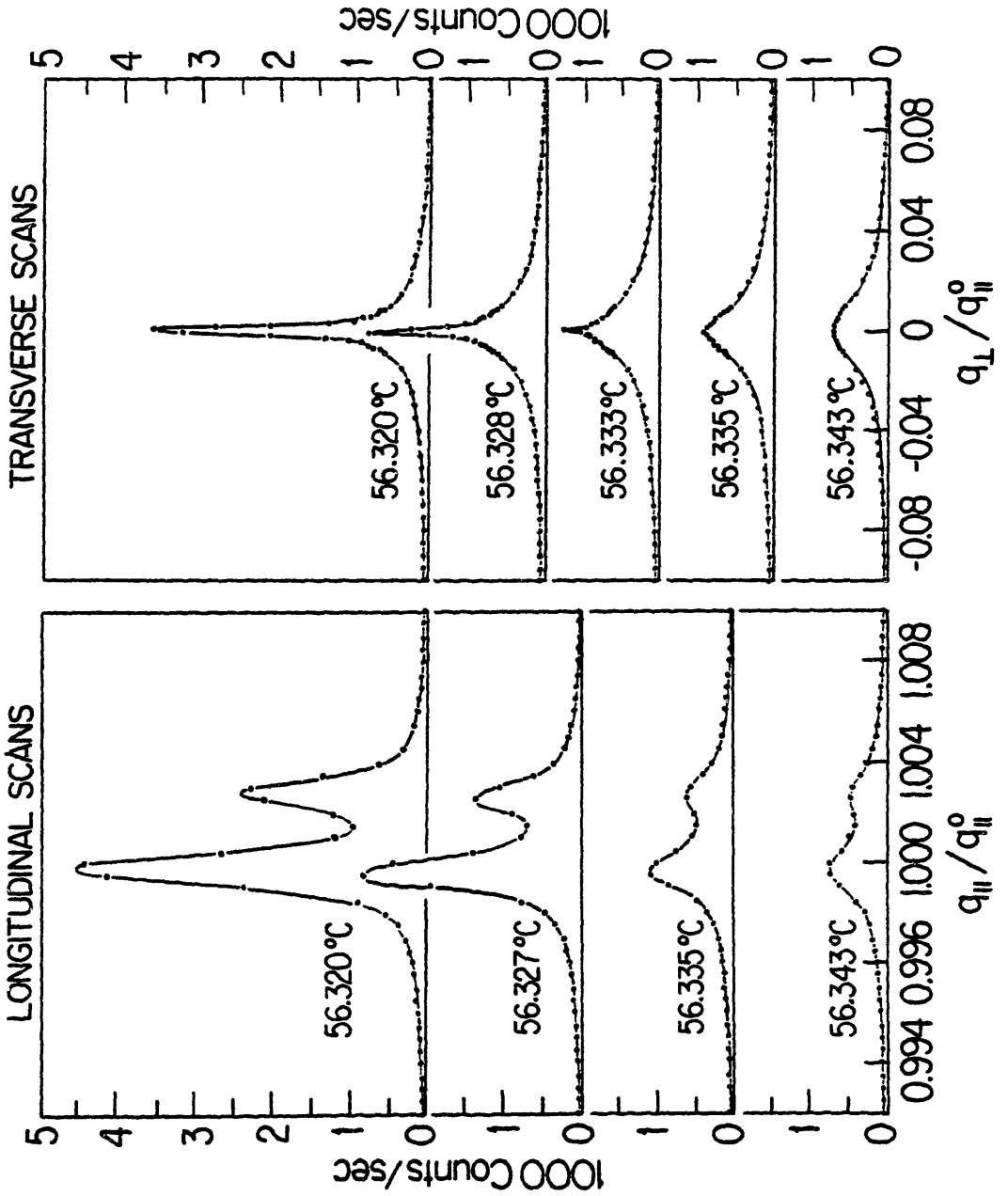

Figure 5.1.2

Longitudinal and transverse scans at a series of temperatures in the vicinity of the nematic to smectic A transition for sample 2 of 40.7. The transition temperature (T_{NA}) is 56.332 ± 0.003°C. The two peaks in the longitudinal scans correspond to $K_{\alpha 1}$ and $K_{\alpha 2}$ x-rays.

In figure 5.1.2 typical longitudinal and transverse scans, above and below the transitions, are shown for sample 2. The transition temperature is taken as 56.332 ± 0.003°C which clearly brackets both phases. The uncertainty in T_{NA} may include a small coexistence region or a transition temperature gradient across the illuminated sample region.

As mentioned earlier, steps were taken to reduce the drift in the transition temperatures. Since the shift was found to be linear with time the actual critical temperature could be interpolated accurately. The uncertainty in this correction always represents a negligible error in the reduced temperature. Impurities could have the effect of smoothing an otherwise first order transition into a continuous transition if the impurities are quenched. Since the smectic A phase is fluid within the plane it is likely that all the impurities would anneal.

At equally spaced reduced temperatures on a log scale, longitudinal and transverse scans are taken. In figure 5.1.3, top data panels, typical scans are shown at $t=7.3\times10^{-4}$. The scans through $q_{\parallel}^{o}$ are fit to a Lorentzian, modified by a fourth order term in the transverse direction, convoluted with the resolution function at each temperature (Appendix 1). A thorough discussion of the resolution function is given in chapter 4. The fitting routine adjusts the parameters to minimize the standard deviation between the model and the data. In this manner, the parameters σ_0, $\xi_{\parallel}$, $\xi_{\perp}$, c and the peak positions are obtained. It is important to note that $q_{\perp}$ is a vector with a component in and out of the scattering plane. As is evident from figure 5.1.3, the fit gives an excellent description of the critical

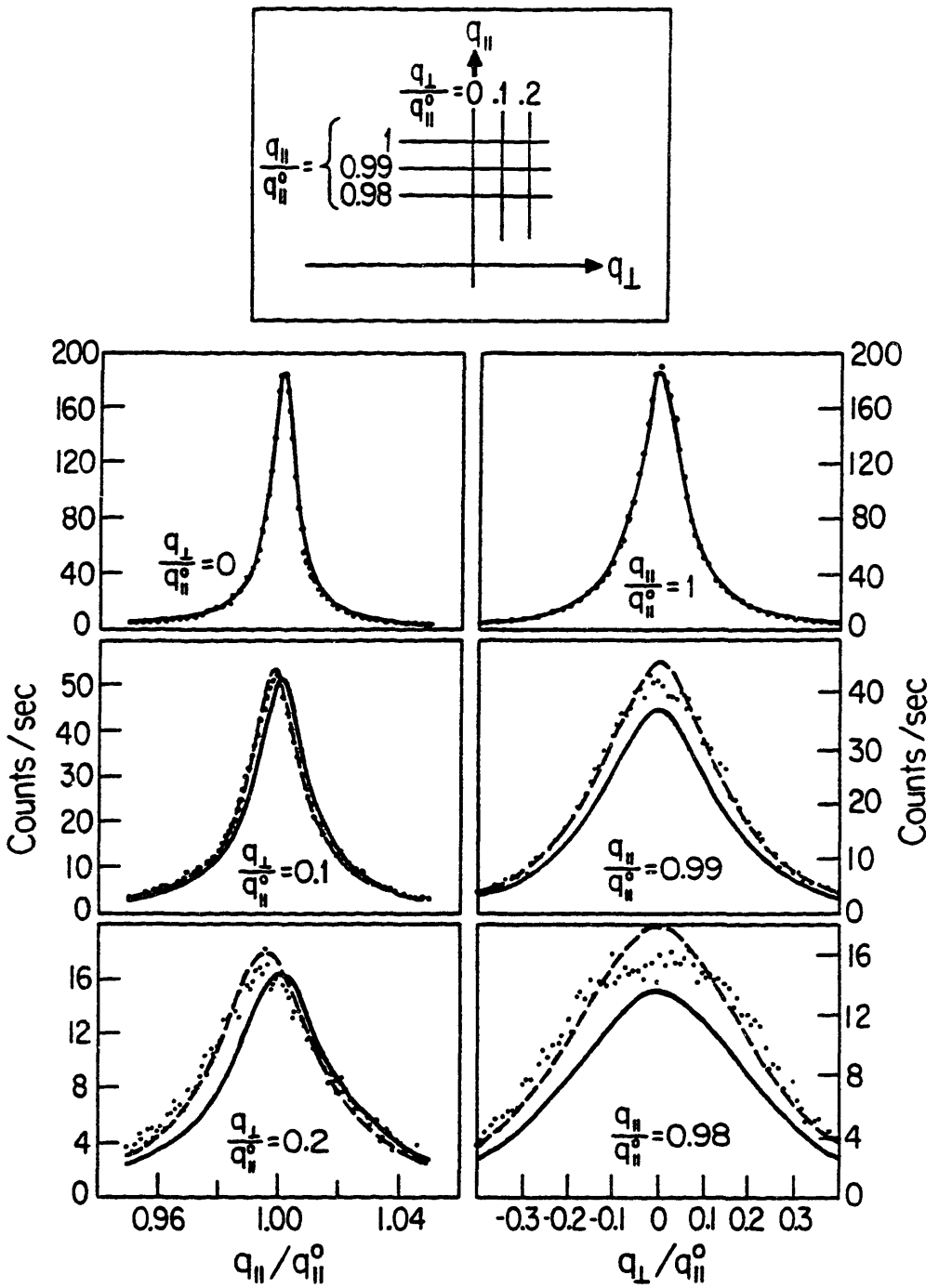

Figure 5.1.3

Longitudinal and transverse scans in the nematic phase of 40.7 at a reduced temperature of 7.3×10^{-4}. The solid line is the best fit for the scans $q_\perp/q_{\parallel}^o=0$ and $q_{\parallel}/q_{\parallel}^o=1$ (top data panels). The dashed lines involve slight adjustments of the peak position and amplitude to fit the wings of the scattering ellipse.

scattering with a goodness-of-fit parameter χ^2 typically around 2.

The scattering always falls off faster than a Lorentzian in the transverse direction, therefore, the fit always chooses c greater than zero. In figure 5.1.5 (bottom) the coefficient of the fourth order term is plotted as a function of reduced temperature. Close to the transition c is small indicating that a pure Lorentzian is adequate; however far from the transition c approaches 0.25 implying that a Lorentzian squared is a better description. There is no theory for this evolution from Lorentzian squared to Lorentzian profiles. Furthermore, the line-shape evolves so that the correlation length no longer represents the inverse half-width of the scattering cross-section.

Although Eq 5.0.1 provides an excellent description of the $N \rightarrow S_A$ cross-section when fit to the longitudinal and transverse scans through the $(0,0,q_{\parallel}^{o})$ peak, the universality of this form can not be ascertained from these scans alone. In order to probe this further, transverse scans through $(0,0,0.99q_{\parallel}^{o})$ and $(0,0,0.98q_{\parallel}^{o})$ and longitudinal scans through $(0.1q_{\parallel}^{o},0,q_{\parallel}^{o})$ and $(0.2q_{\parallel}^{o},0,q_{\parallel})$ were taken at several reduced temperatures. In figure 5.1.3 the results of these scans are shown at $t=7.3\times10^{-4}$. The solid lines are fits to Eq 5.1.1 using the parameters obtained from fitting the scans through $(0,0,q_{\parallel}^{o})$; the dashed lines involve slight adjustments of the intensity and peak position to optimize the fits. From these figures, it is apparent that the cross-section is nearly adequate to describe the complete critical scattering although cross terms, i.e. $(q_{\parallel}-q_{\parallel}^{o})^2\times q_{\perp}^{2}$, would clearly improve the fits to the wings of the scattering ellipse.

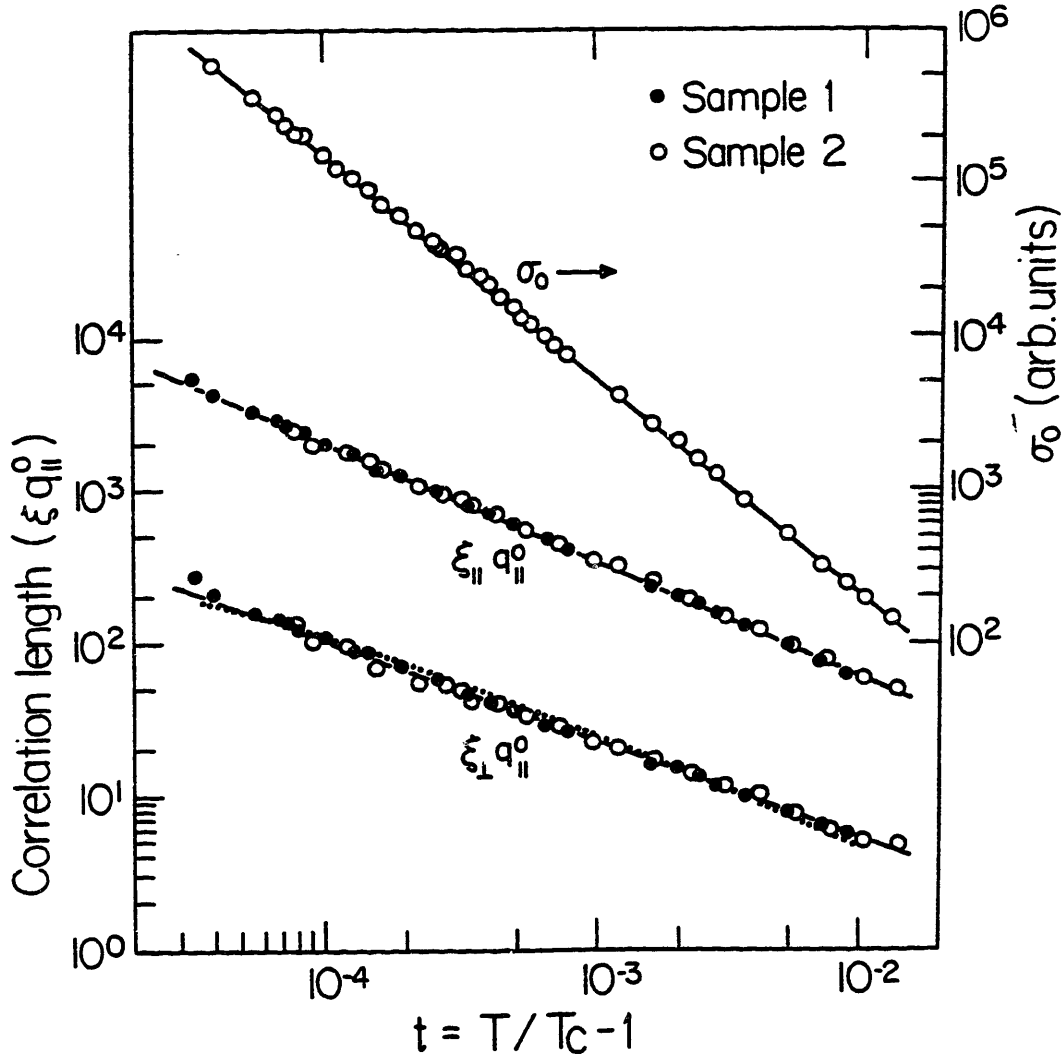

Figure 5.1.4

Susceptibility (σ_0) and the longitudinal and transverse correlation lengths versus reduced temperature in 40.7. The solid lines are single power law fits as described in the text. The dotted line is the Lubensky crossover form described in section 2.3.

The fitted parameters, σ_0, $\xi_{\parallel}$, and $\xi_{\perp}$ are plotted over the range $3\times10^{-5} < t < 2.5\times10^{-2}$ in figure 5.1.4 for both samples. Though the transition temperatures differ by 1.4°C for the two samples, there are no significant differences in the critical behavior. This important results supports the hypothesis that impurities are benign. From figure 5.1.4, it is also apparent that the parallel and perpendicular correlation lengths are diverging at slightly different rates. The ratio, $\xi_{\parallel}/\xi_{\perp}$, varies by a factor of two over the range measured, as shown in figure 5.1.5(top). Thus, as found previously in other materials, a single length scale is not adequate to describe the $N\rightarrow S_A$ transition in 40.7.

In figure 5.1.4 fits to simple power laws (solid lines)

$$\sigma_0 \propto t^{-1.45\pm0.03} \qquad 5.1.1a$$

$$\xi_{\parallel} q_{\parallel}^{o} = 1.55t^{-0.78\pm0.02} \qquad 5.1.1b$$

$$\xi_{\perp} q_{\parallel}^{o} = 0.25t^{-0.65\pm0.02} \qquad 5.1.1c$$

are shown, where $q_{\parallel}^{o}=0.2337\text{Å}^{-1}$. It is evident from these fits that mean-field theory $\nu_{\parallel}=\nu_{\perp}=0.50$, anisotropic dislocation behavior $\nu_{\parallel}=2\nu_{\perp}$, and non-transformed 3D XY behavior do not provide a suitable explanation of the critical fluctuations in the reduced temperature range $10^{-5}<t<10^{-2}$ in 40.7.

Lubensky and coworkers (section 2.3) have proposed that at the $N\rightarrow S_A$ transition the liquid crystal correlation lengths may exhibit crossover from 3D isotropic XY behavior $\nu_{\parallel}=\nu_{\perp}=\nu_{XY}$ to 3D anisotropic XY behavior $\nu_{\parallel}=2\nu_{\perp}=\nu_{XY}$. In an attempt to describe the measured data, the essential features of the crossover have been preserved with $\nu_{\parallel}$ fixed at 0.78 rather than at $\nu_{XY}=0.66$. This is necessary since $\xi_{\parallel}$ does not

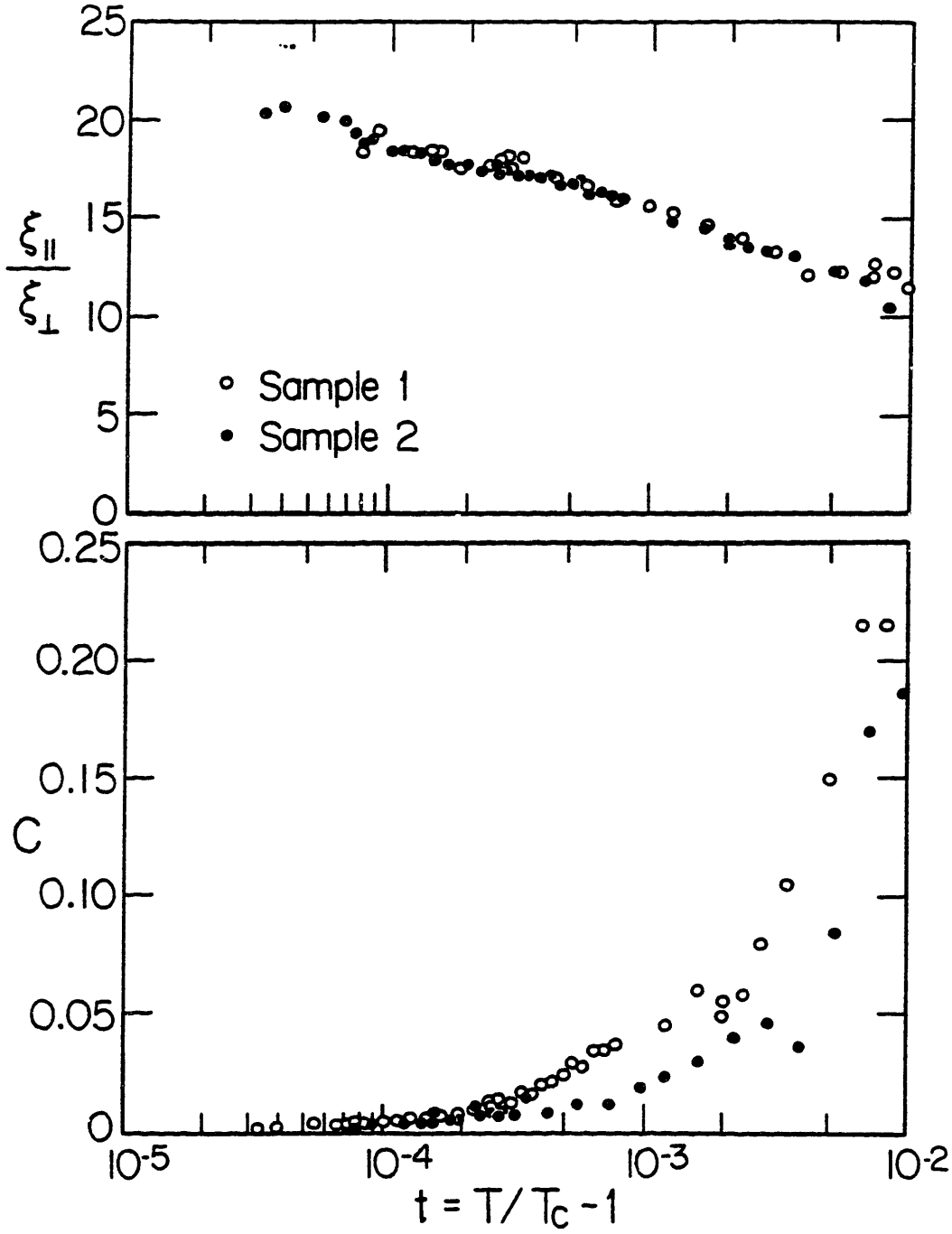

Figure 5.1.5

top: Ratio of correlation lengths $\xi_{\parallel}/\xi_{\perp}$ versus reduced temperature.
bottom: Fourth order coefficient c versus reduced temperature.

undergo a crossover according to the theory, however, $\xi_\perp$ should exhibit a crossover when the rescaled bend and splay elastic constants are equal, that is, when $K_1/K_3=S^2$ where S is the length anisotropy. The $\xi_\perp$ data have been fit to Eq 2.3.25 with S=7, $K_1=8\times10^{-7}$dynes, and $K_3=(K_BT/2\pi)q_{\parallel}^{0\,2}\xi_{\parallel}$. In figure 5.1.4 the best fit to the crossover form is shown as a dotted line and is slightly worse than the single power law fit. The theory, albeit with $\nu_{\parallel}=0.78$, predicts the right crossover temperature, however, the data are not sufficient to show uniqueness to the precise form for the crossover.

$\overline{6}09$ Results

These measurements in 40.7 as well as Safinya's measurements in $\overline{8}S5$ do not agree with the 3D XY values for γ and $\nu_{\parallel}$, whereas the earlier experiments in 40.8, CBOOA, 8CB and 8OCB seemed to. Furthermore, 40.7 and $\overline{8}S5$ have nearly identical nematic ranges and critical exponents with $\gamma=1.45$, $\nu_{\parallel}=0.78$, and $\nu_\perp=0.65$ in 40.7 and $\gamma=1.53$, $\nu_{\parallel}=0.83$, and $\nu_\perp=0.68$ in $\overline{8}S5$. This unusual behavior, in light of the earlier measurements, is probably due to the longer nematic range in these materials. To strengthen this hypothesis, the $N\rightarrow S_A$ critical behavior has been measured for 4-n-nonaphenyl-4′-n-hexaoxybenzoate $\overline{6}09$ which has a 26°C nematic range. As yet, there are no heat capacity measurements in $\overline{6}09$.

The $\overline{6}09$ sample was obtained from Kent State University and without further preparation it was placed into a silane treated aluminum cell with beryllium windows attached with epoxy. Temperature control,

~±0.001°C, was provided by the two stage oven with Be windows. Although $\overline{6}09$ is inherently very stable, flowing nitrogen gas was used to reduce the effects of impurities. Over the course of the experiment there was no noticeable drift in the transition temperature, furthermore, there was no apparent T_{NA} gradient across the illuminated sample. Most of the data were obtained using the silicon spectrometer set-up; however, the highest temperature points utilized the germanium set-up to reduce the counting time. The resolution in-plane is described by the sum of three Lorentzians for both the silicon and germanium set-ups as shown in figure 4.1.4 and figure 4.1.5, and the vertical resolution is triangular with $0.05A^{-1}$ HWHM. Alignment was obtained with the ANAC electromagnet which produces a 7 kiloGauss field at the sample position. In the smectic phase, the mosaic distribution was often less than 0.020° HWHM.

Smectic A ordering in $\overline{6}09$ occurs at $q_{11}^{o}=0.2038A^{-1}$ corresponding to a layer spacing of 30.83A. The transition temperature could be determined to within 0.001°C by rocking the sample at the 2θ angle corresponding to the $(0,0,q_{11}^{o})$ peak. As is apparent from figure 5.1.6, the shape of the rocking curve changes drastically in just 0.002°C from a spectrum which is flat over the scale .1° to a spectrum with ≈0.020° HWHM. Therefore, the transition temperature is taken to be 40.125±0.001°C. Further below the transition the intensity of the central peak continues to increase, albeit at a much slower rate.

Longitudinal and transverse scans are performed at equally spaced reduced temperatures on a logarithmic scale from $t= 2\times10^{-5}$ to 10^{-2} for the silicon set-up and from $t=2\times10^{-3}$ to 5×10^{-2} for the germanium line-up. In the longitudinal direction the data are always fit to a Lorentzian, however, in the transverse direction either a

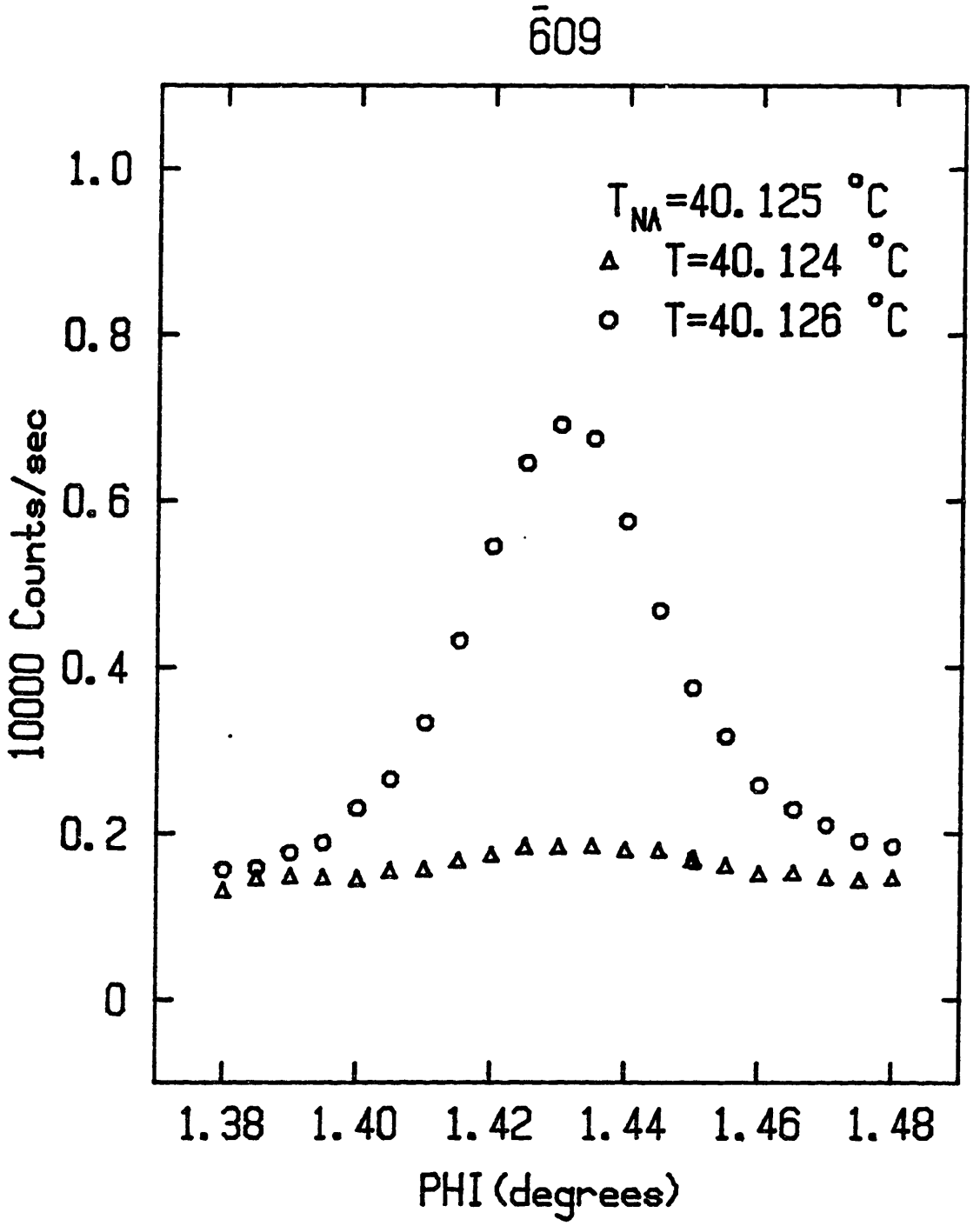

Figure 5.1.6

Rocking curves above and below the $N \rightarrow S_A$ transition in $\bar{6}09$.

Lorentzian with a fourth order correction (LFC), Eq 5.0.1, or a Lorentzian squared raised to the power $1-\eta_\perp/2$ (LPC), Eq 5.0.2, is used. As is the case with 40.7, a pure Lorentzian does not provide an adequate description of the data. The LFC cross-section provides a reasonable description of the data, however, there are still systematic deviations between the data and the line-shape in the transverse direction, especially for the temperature points closest to the transition. In figure 5.1.7 (top) the transverse scan and the LFC fit are shown at $T-T_{NA}=0.007°C$. At this temperature, the LFC fit gives $\xi_{\parallel}=7,300\pm600q_{\parallel}^{o}$, $\xi_\perp=347\pm50q_{\parallel}^{o}$, and $c=4\pm2\times10^{-4}$.

In figure 5.1.8 the fitted parameters $\xi_{\parallel}$, $\xi_\perp$, and σ_0 are plotted as a function of reduced temperature. A pure Lorentzian never describes the scattering since the data are never consistent with c=0. In figure 5.1.9 c is plotted as a function of reduced temperature on a log-log scale. Below $t=10^{-2}$ the fourth order term is allowed to float freely, however, above this reduced temperature c is fixed at 1/4. When c is allowed to grow much greater than 1/4, the correlation length deviates significantly from the inverse half width.

The parameters $\xi_{\parallel}$, $\xi_\perp$, and σ_0 derived from fits to the LFC line-shape have been fit to single power laws

$$\sigma_0 \propto t^{-1.45\pm0.03} \qquad 5.1.2a$$

$$\xi_{\parallel}q_{\parallel}^{o} = 2.10t^{-0.775\pm0.02} \qquad 5.1.2b$$

$$\xi_\perp q_{\parallel}^{o} = 0.26t^{-0.68\pm0.02} \qquad 5.1.2c$$

as shown in figure 5.1.8. The correlation lengths $\xi_{\parallel}$ and $\xi_\perp$ are about 10-20% larger in $\overline{6}09$ than in 40.7 though the nematic ranges are comparable. Although the data extends out to 5×10^{-2}, deviations from

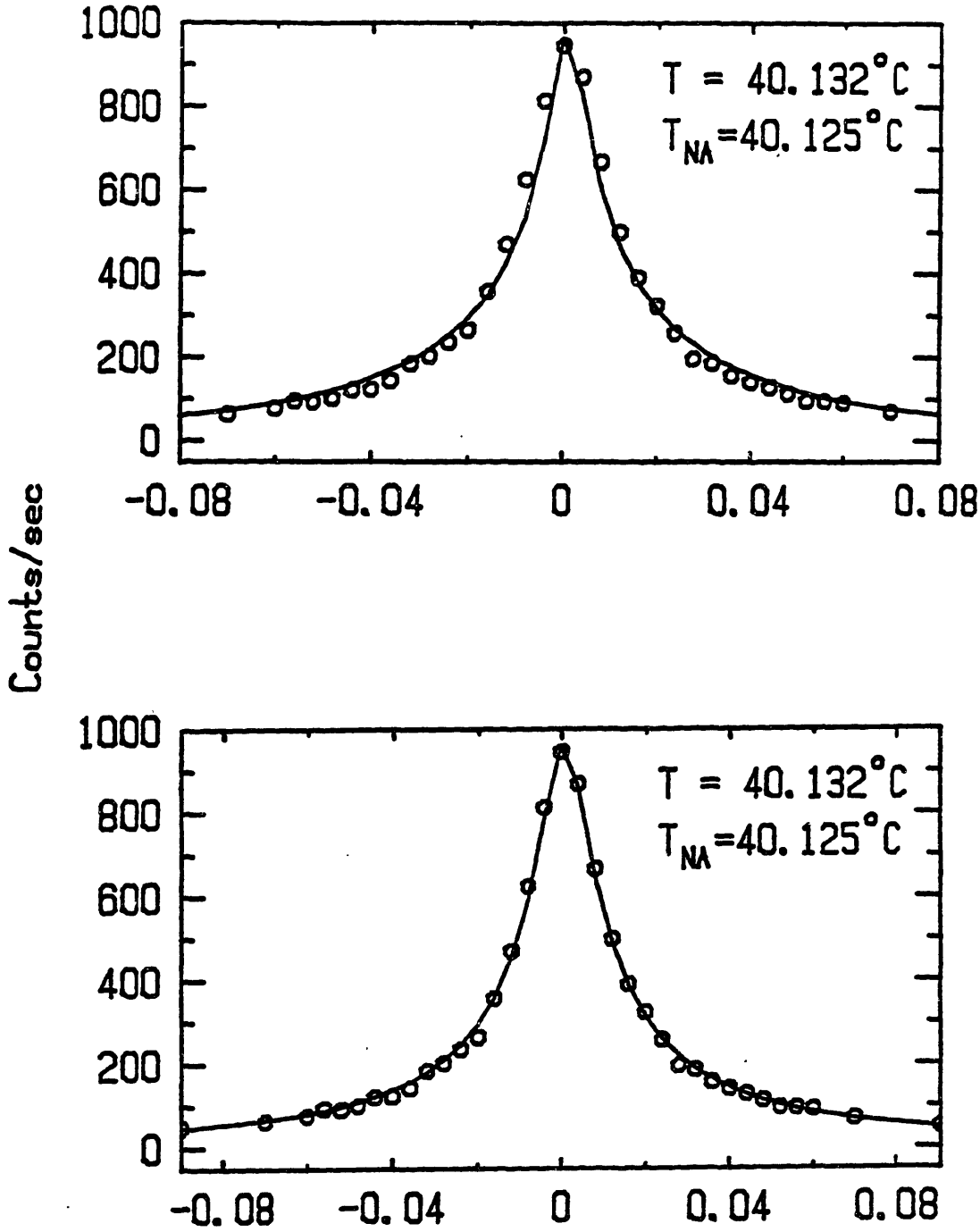

Figure 5.1.7

Transverse scans in $\bar{6}09$ at $T = T_{NA} + 0.007°C$.

Top: Solid line is the best fit to the LFC line-shape, Eq 5.0.1.

Bottom: Solid line is the best fit to the LPC line-shape, Eq 5.0.2.

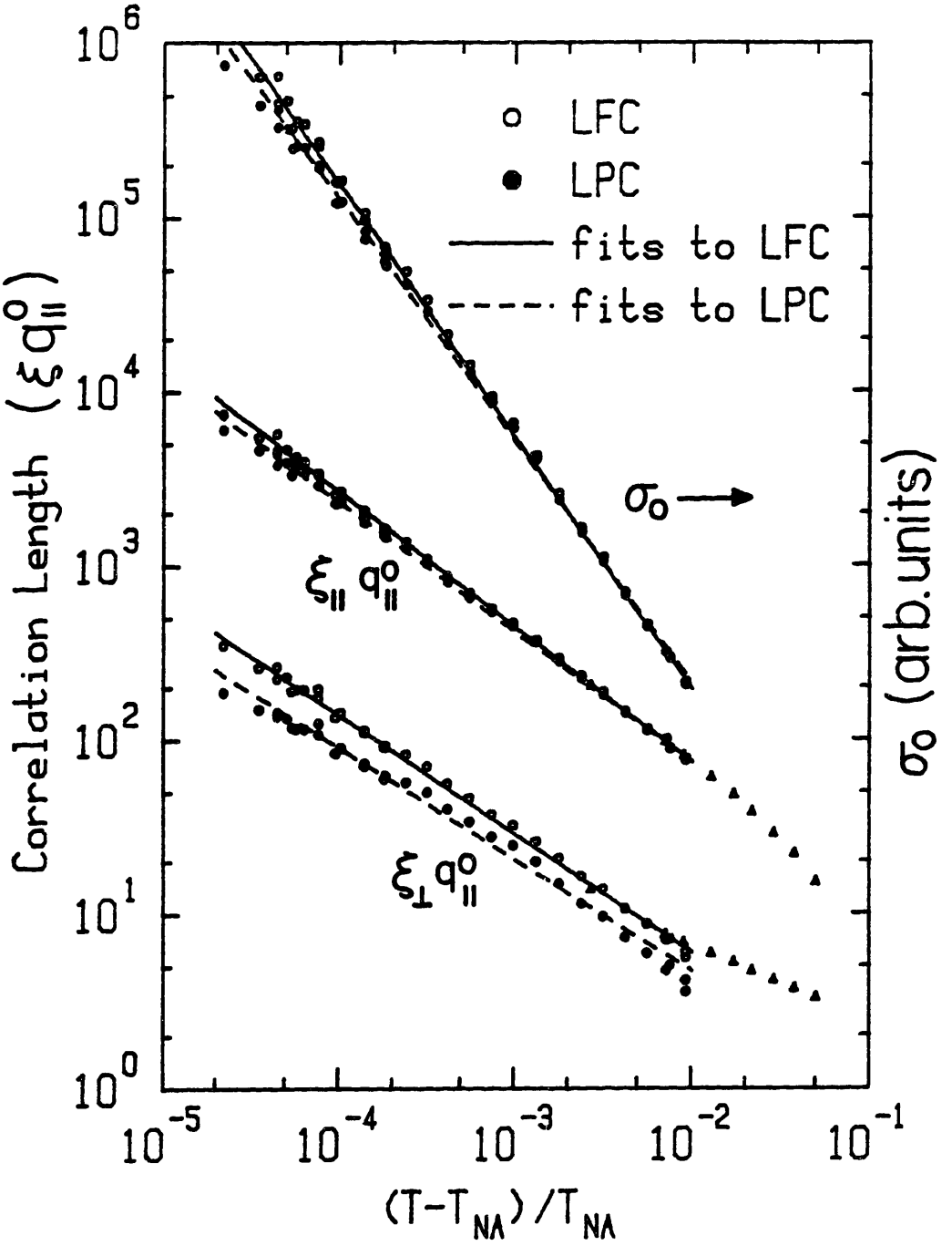

Figure 5.1.8

Fitted values of the correlation lengths $\xi_{\parallel}$ and $\xi_{\perp}$ and σ_0 to both the LFC and LPC line-shapes in $\overline{6}09$. The straight lines are fits to single power laws over the reduced temperature range $2\times10^{-5}<t<10^{-2}$.

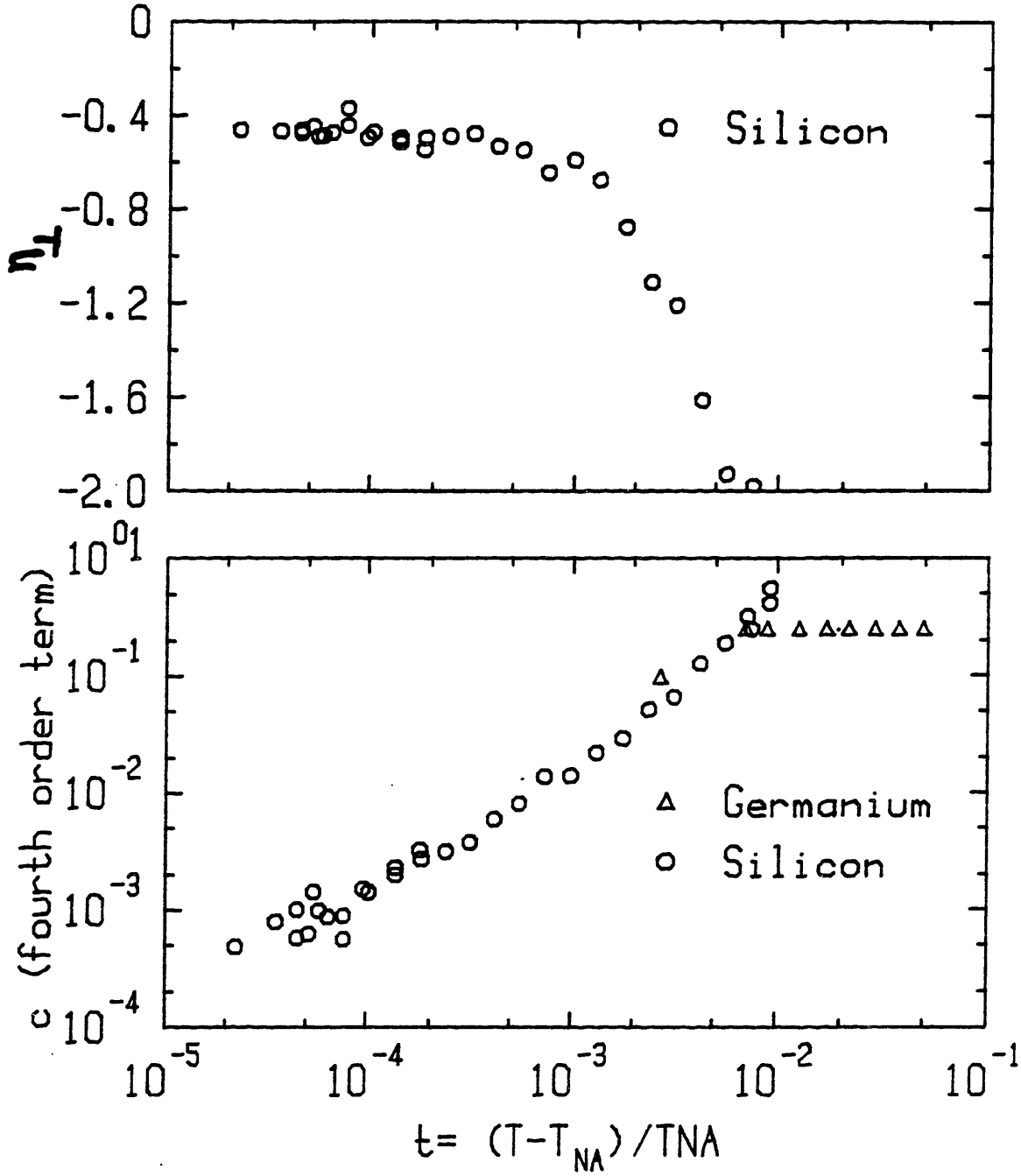

Figure 5.1.9

Top: $\eta_\perp$ (Eq 5.0.2) vs. t in $\bar{6}09$.
Bottom: Fourth order term c (Eq 5.0.1) vs. t in $\bar{6}09$.

single power law behavior are apparent beyond 10^{-2} at which point the line-shape has evolved to a Lorentzian squared. Since the asymptotic behavior is important, the fits have been restricted to the range $2\times10^{-5}<t<10^{-2}$. Allowing the transition temperature to float from the experimentally obtained value 40.125°C does not alter the exponents.

The scans with $t<10^{-2}$ have also been fit to the Lorentzian squared raised to the power $1-\eta_\perp/2$ (LPC) line-shape. On average, the χ^2 for these fits is better by a factor of two than fits to the LFC line-shape at most reduced temperatures. In figure 5.1.7 fits to the LPC and LFC line-shapes are shown at $T = T_{NA} + 0.007°C$. The LPC fit (bottom) clearly fits the transverse scan best and gives $\xi_{\parallel}=6000\pm300q_{\parallel}^{o}$, $\xi_\perp=186\pm20q_{\parallel}^{o}$, and $\eta_\perp=-0.45$. For $q_\perp>>1/\xi_\perp$ the correlation function falls off as $q_\perp^{2.45}$ even though the fit to the Lorentzian only required a small fourth order correction term! The correlation length $\xi_\perp$ is not the same for both functional forms, hence, it is not surprising that both fits give different results.

The parameters $\xi_{\parallel}$, $\xi_\perp$, and σ_0 obtained from fits to Eq 5.0.2 are shown as dashed lines in figure 5.1.8. Fits to single power laws for these parameters give

$$\sigma_0 \propto t^{-1.39\pm0.04} \qquad 5.1.3a$$

$$\xi_{\parallel}q_{\parallel}^{o} = 2.43t^{-0.745\pm0.02} \qquad 5.1.3b$$

$$\xi_\perp q_{\parallel}^{o} = 0.25t^{-0.64\pm0.03} \qquad 5.1.3c$$

where the transition temperature is chosen to be the same as the LFC fits. In comparison to the coefficients obtained from the LFC line-shape fits, the parameters obtained from the LPC fits deviate from a single power law, furthermore, these exponents are slightly lower. Over

the range $2\times10^{-5}<t<10^{-3}$ the parameter $\eta_\perp=-0.45\pm0.05$ whereas c varies by two orders of magnitude over the same range (figure 5.1.9). From $t=10^{-3}$ to $t=10^{-2}$ $\eta_\perp$ evolves from -0.45 to -2, hence, the line-shape evolves from $q_\perp^{-2.45}$ to $q_\perp^{-4}$ for large $q_\perp$.

From the anisotropic scaling relationship, $\gamma = \nu_{\parallel,\perp}(2-\eta_{\parallel,\perp})$, the line-shape exponent η is related to the critical exponents ν and γ. Using this relation and the critical exponents obtained from the LPC fits, $\eta_\parallel = 0.13+-0.15$ and $\eta_\perp = -0.17\pm0.15$ should describe the line-shapes. However, $\eta_\parallel=0$ always fits the longitudinal scan, whereas, $\eta_\perp= -0.45$ fits the transverse scan close to the transition. Thus, the anisotropic scaling relationship is not verified by Eq 5.0.2 although it does improve the fits to the transverse scan. Further theoretical effort is required to determine the proper form of the $N\rightarrow S_A$ cross-section which incorporates the evolution of the line-shape with temperature.

Both 40.7 and $\overline{6}09$ have the longest nematic ranges of all the materials studied with 26°C and 24°C ranges respectively. These materials exhibit saturated second order transitions with almost identical critical behavior. By saturated, we mean that the nematic order parameter is saturated at the transition. It is likely that experiments on nematogens with even greater nematic ranges will generate agreement with the measured critical exponents in 40.7 and $\overline{6}09$.

5.2
Results in $\bar{n}$S5 Samples

X-ray scattering experiments have been carried out in the 4-n-pentylphenyl-4-n-alkyloxybenzoate series ($\bar{n}$S5) including the pure materials $\overline{9}$S5, $\overline{10}$S5, and $\overline{11}$S5. In analogy to tricritical phenomena (section 2.1), the chain length n represents the nonordering field. By mixing neighboring homologs one can effectively vary n continuously where the average chain length is determined from the weight of the constituent materials. The mixtures $\overline{8.5}$S5, $\overline{9.75}$S5, $\overline{10.2}$S5, and $\overline{10.4}$S5 have been prepared.

The phase diagram for the $\bar{n}$S5 series is shown in figure 5.2.1. Over the range of chain lengths studied the N→I transition temperature is relatively constant although it is noticeably higher in $\overline{10}$S5. The N→I and I→S_A transitions are always first order as is the N→S_A transition if the nematic range is sufficiently short. In $\overline{12}$S5 there is no nematic phase, upon cooling from the isotropic phase a transition occurs directly into the smectic A phase. As the chain length is decreased the nematic phase emerges and increases in range as shown in figure 5.2.2. At about $\overline{10}$S5 the N→S_A transition crosses over from first order critical behavior to second order behavior. Eventually, at ~$\overline{7.5}$S5, the smectic A phase disappears and the nematic phase transforms to the smectic C phase upon cooling. Experiments on the N→S_A transition near the smectic A-smectic C-nematic multicritical point are reported in Safinya's Thesis.[1]

Though the exact details of the spectrometer set-up are described in chapter 4, a brief summary is provided for the reader. The in-plane resolution of ~5×10^{-4} or ~1×10^{-4} $Å^{-1}$ HWHM was achieved by

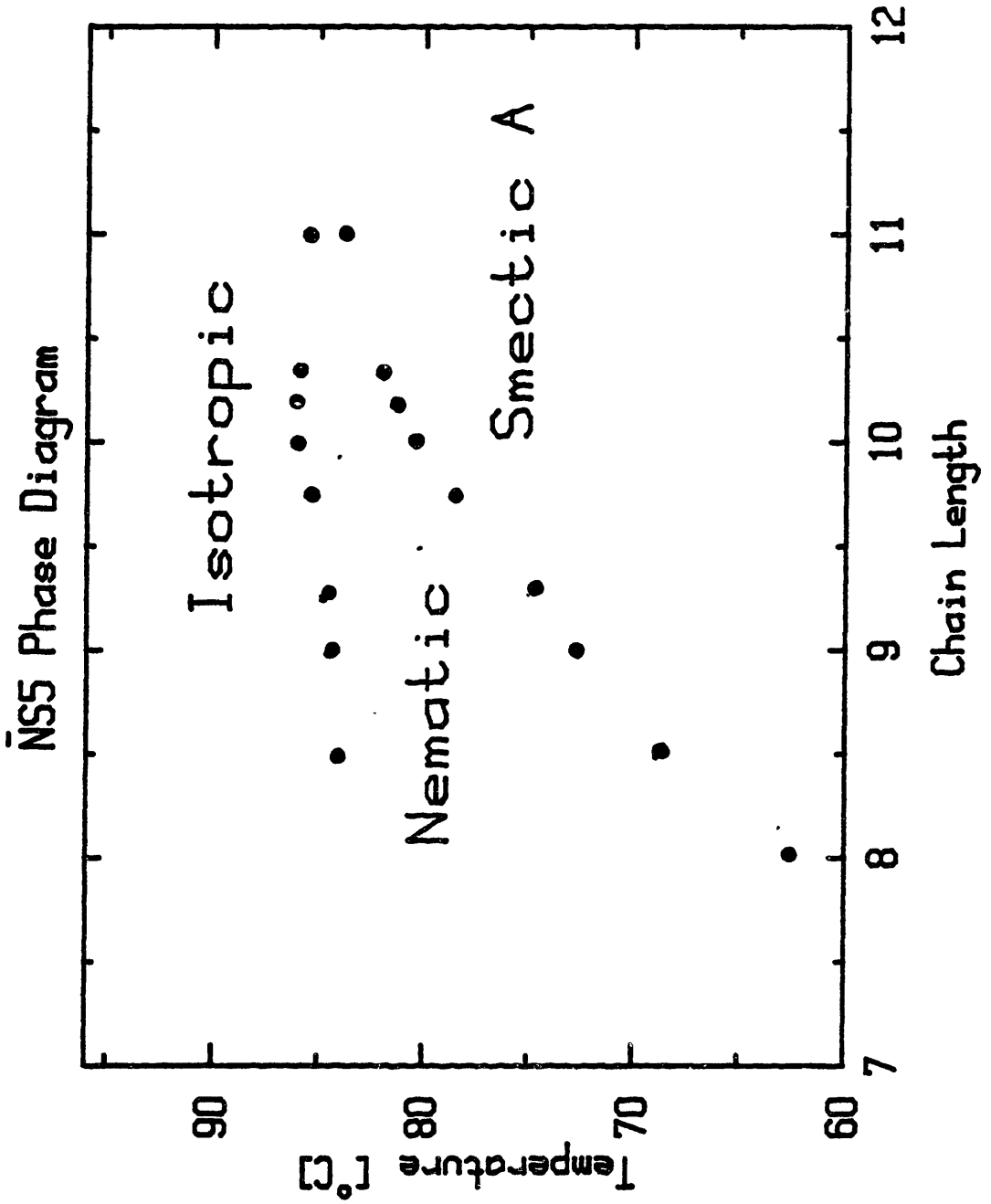

Figure 5.2.1

Phase diagram for the ñS5 series vs. chain length n. Non-integer chain length corresponds to mixtures as described in the text.

employing either perfect Si(111) or Ge(111) crystals as monochromators and analyzers. The precise in-plane resolution for each set-up was obtained by convoluting the direct beam profile with the appropriate energy broadening. The vertical resolution was set by matching the vertical divergence of the beam to the vertical acceptance of the detector which typically yielded a triangular function with a $0.05 \pm 0.005 A^{-1}$ HWHM.

Over the course of the measurements several improvements in the sample preparation and experimental set-up were made; these details are summarized in Appendix 2. All of the $\bar{n}$S5 material was obtained from Dave Johnson or Mary Neubert. Some of the material was pumped on in the nematic phase; however, the nematic to smectic A transition temperature drifted much more rapidly for these samples. After pumping, for instance, the $\overline{9}$S5 T_{NA} drifted at a rate of 0.004°C per hour and the $\overline{10}$S5 transition temperature drifted at 0.007°C per hour. This is somewhat unusual in that the $\bar{n}$S5 series is chemically very stable, furthermore, experiments in $\overline{8}$S5 by Safinya under similar conditions did not encounter such difficulty. A second sample of $\overline{10}$S5 was prepared via High Pressure Liquid Chromatography (HPLC) and never pumped on. This sample only drifted by 0.005°C per day under flowing nitrogen, a much more acceptable rate. These procedures contributed to reduced rates of the transition temperature drift; however, it is very plausible that compounds that are closer to the $N \rightarrow S_A$ tricritical point are more susceptible to impurity induced drifts. This is consistent with weak solution theory[2] which predicts that the coexistence region should be inversely proportional to the latent heat for first order transitions.

The layer spacing d is determined by measuring the q vector corresponding to smectic layering, $q_{11}^{o}=2\pi/d$ at the $N \rightarrow S_A$ transition. For $\overline{8}S5$ the layer spacing is ~28.3Å and increases linearly with chain length to ~31.3Å for $\overline{11}S5$ (see figure 5.2.2). Phase separation does not occur for the mixtures since the average layer separation varies linearly with chain length; furthermore, scattering occurs at only one q vector. The McMillan ratio (T_{NA}/T_{NI}) , see figure 5.2.2 (bottom panel), does not vary linearly with temperature as predicted by mean-field theory. There is no obvious explanation for this deviation, except perhaps the influence of the nearby smectic C phase.

In the smectic phase, the scattering profile is resolution limited in the longitudinal direction and mosaic limited in the transverse direction; therefore, quantitative analysis of the scattering line-shape is difficult. However, the integrated smectic intensity and the layering q vector, q_{11}^{o}, can be measured quite accurately in the smectic A phase. In figure 5.2.3 q_{11}^{o} is plotted as a function of temperature throughout the smectic A phase and into the smectic C phase. As the temperature is lowered from the nematic phase into the smectic A phase the q vector decreases; hence, the layers are getting thicker. This is somewhat unusual since most materials contract upon cooling. Since the total density decreases with temperature the molecules must move closer together in the plane of the layers. The coefficient of thermal expansion is largest near T_{NA}, suggesting that the layer spacing may have a critical contribution. In contrast, no noticeable change in q_{11}^{o} has been observed in 40.7 over the entire smectic A range.

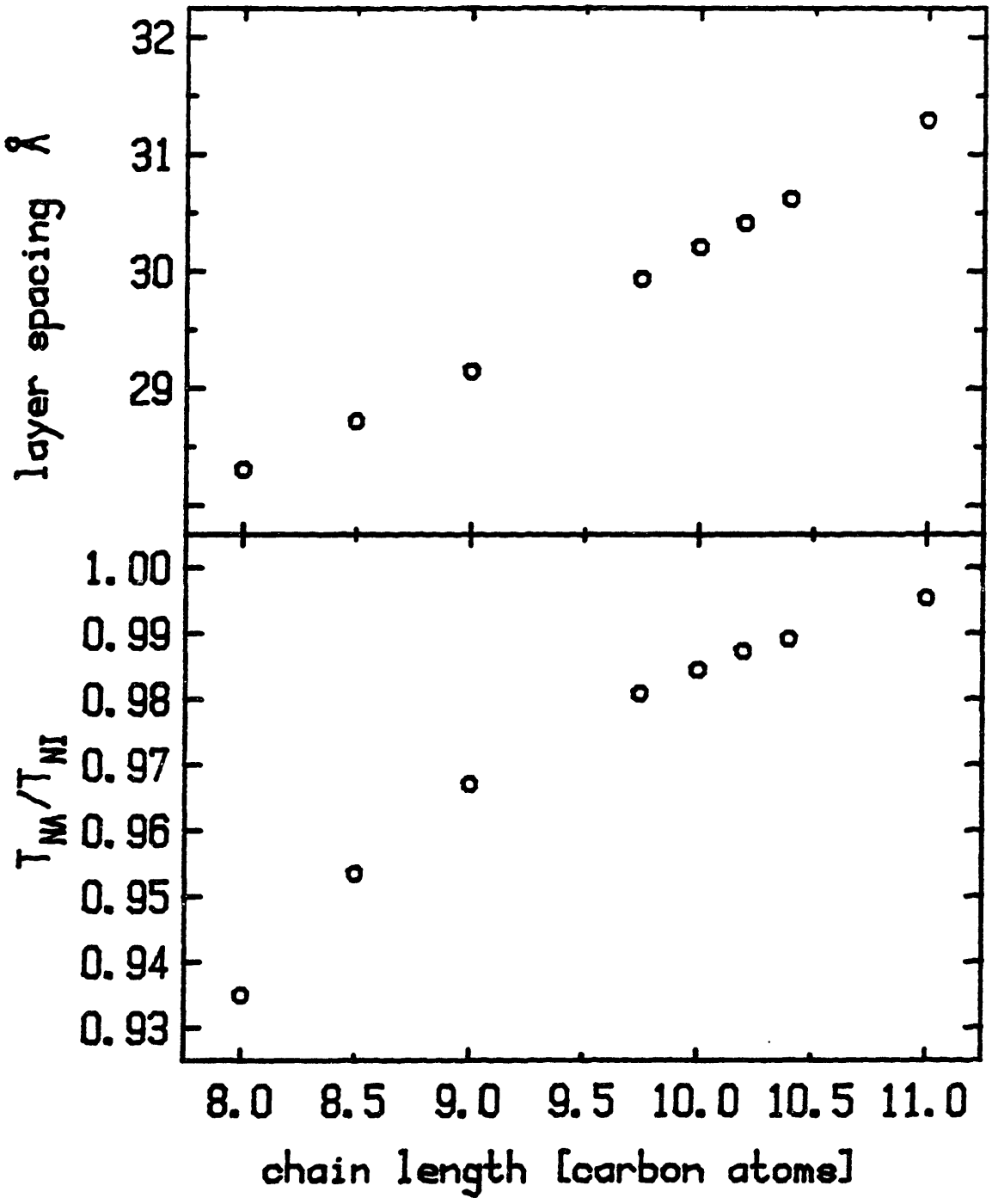

Figure 5.2.2

Top: Layer spacing vs. chain length in $\bar{n}$S5 samples. The layer spacing expands near the N→S_A transition and decreases in the smectic C phase.

Bottom: McMillan ratio (T_{NA}/T_{NI}) vs. chain length in $\bar{n}$S5 samples.

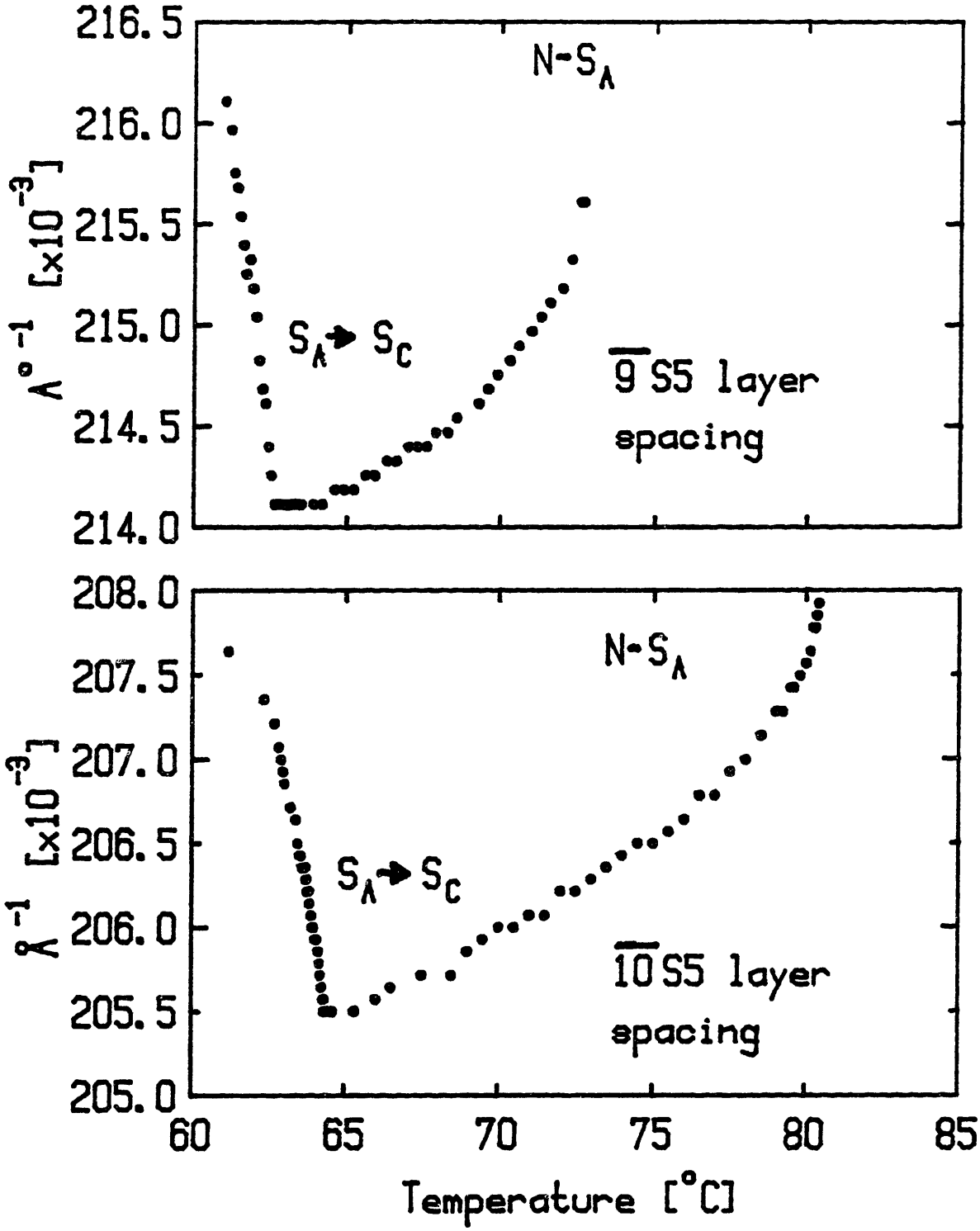

Figure 5.2.3

The smectic layering q vector, q_{11}^{o} vs. temperature in $\overline{9}$S5(top) and in $\overline{10}$S5(bottom).

The $N \rightarrow S_A$ transition temperature T_{NA} is determined from the x-ray scattering profile through $(0,0,q_{11}^{o})$. Above the transition the scattering is symmetric, at the transition the smectic peak emerges at q_{11}^{o} and continues to grow as the temperature is lowered further. In the longitudinal direction the peak is always resolution limited, however in the transverse direction the profile is determined by the angular distribution of the layers (mosaic) and is always asymmetric. The mosaic depends on the strength of the aligning field, wall effects and the inherent properties of the compound. Our findings show that the longer nematic range samples produce better quality crystals; for instance, the mosaic ranged from 0.1° HWHM for $\overline{8.5}$S5 to 0.9° for $\overline{11}$S5. At T_{NA} the nematic order parameter is more saturated for the long nematic range samples, concomitantly, the correlation lengths are larger than those in samples with shorter nematic ranges. Thus, smectic ordering is most developed at T_{NA} for materials with the longest nematic ranges before the mosaic distribution is locked in. The improved mosaic for samples with long nematic ranges may also result from the nearby smectic C phase. As the smectic C phase is approached, the free energy associated with neighboring molecules sliding with respect to one another decreases, therefore, it is expected that defects can anneal more readily.

In principle, if the smectic phase were to have long range order, the integrated intensity of the smectic scattering would scale as the average smectic order parameter squared $\langle\sigma^2\rangle$. Thus, the exponent β could be extracted from the data for second order transitions. However, because phase fluctuations destroy long-range order in the smectic A phase it is unclear how σ^2 should scale. For a first order transition,

with a coexistence region between the high and low temperature phases, the density of the two phases usually varies linearly within this region. For instance, the N→I transition in 60.8 exhibits this behavior as shown in Appendix 3. The smectic intensity varies linearly on the high temperature side of the N→S_A transition but is rounded on the low temperature side. As a result, it is difficult to determine the coexistence range precisely.

To measure the smectic integrated intensity, the smectic scattering from the $(0,0,q_{11}^{o})$ peak must be summed over. Since the sample mosaic width is always much less than the vertical resolution width, the spectrometer acts to integrate over the transverse out-of-plane direction. In the longitudinal direction, the smectic line-shape is resolution limited, therefore, this direction is also integrated over. There may be a slight correction due to the smectic A phase η line-shape; however, we believe that these corrections are negligible. In the transverse in-plane direction the sum must be performed explicitly since the mosaic distribution depends on temperature. This was accomplished by summing the intensity over ϕ at the 2θ position corresponding to q_{11}^{o} or by explicitly fitting the scattering to a sum of a Gaussian plus the N→S_A line-shape. This latter procedure will be discussed subsequently in the context of the $\overline{10.4}$S5 measurement. Both methods yield identical results.

The smectic integrated intensity is presented in figure 5.2.4 for $\overline{8.5}$S5, $\overline{10}$S5, $\overline{10.2}$S5, $\overline{10.4}$S5, and $\overline{11}$S5 as a function T_{NA}-T. As mentioned previously, T_{NA} is taken to be the temperature where the resolution limited smectic peak emerges in the transverse scan. The smectic integrated intensity has been normalized for all samples at

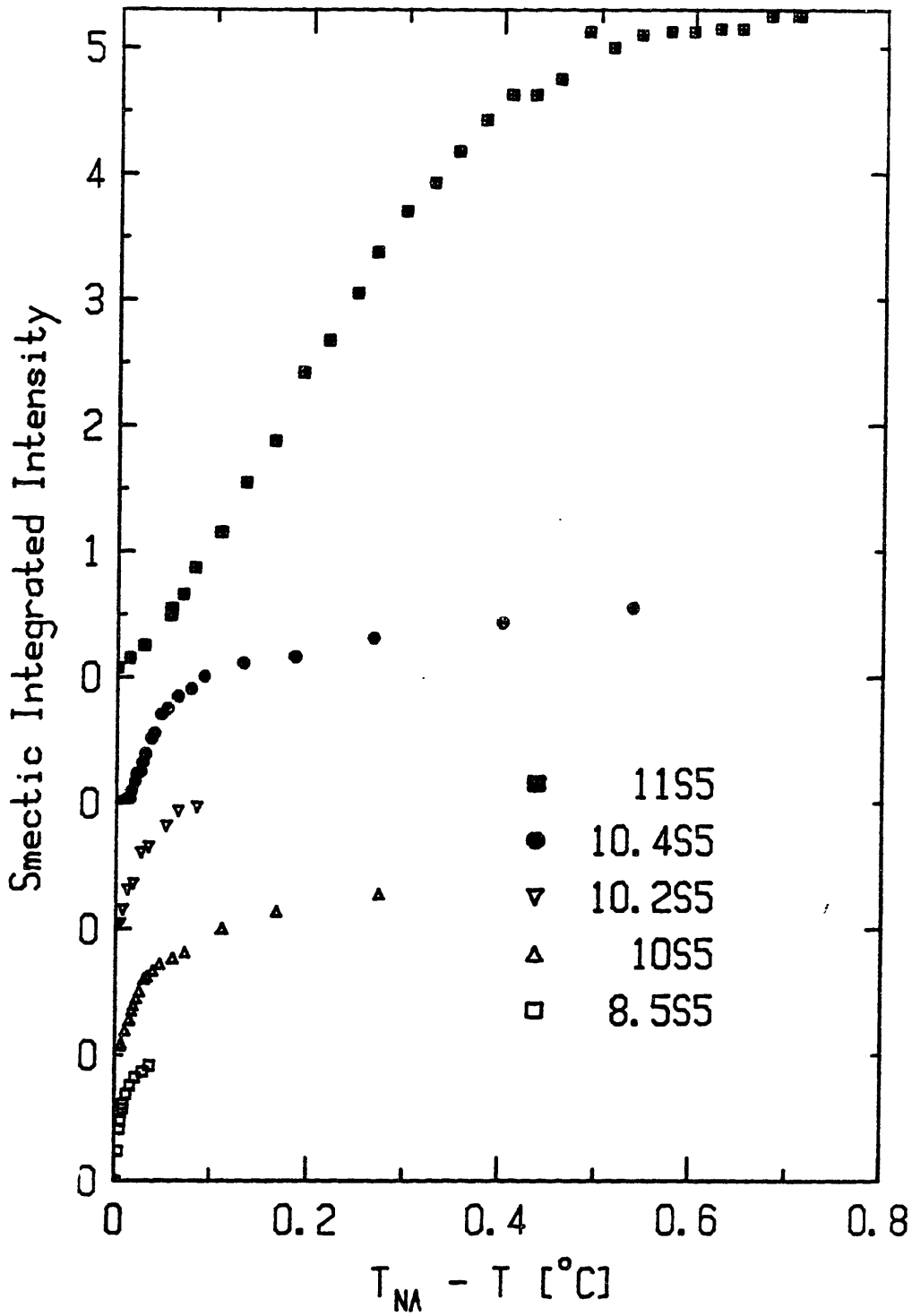

Figure 5.2.4

Smectic integrated intensity vs. T_{NA}-T.

$T=T_{NA}-0.1°C$. The intensity is reasonably well saturated at this temperature for all samples, except for $\overline{11}S5$ which doesn't saturate until $T=T_{NA}-0.50°C$. Furthermore, this sample displayed 0.020°C hysteresis between heating and cooling whereas the behavior for the other samples showed no hysteresis effects.

$N \rightarrow S_A$ Fits

Longitudinal scans ($q_\perp=0$, $q_{\parallel}$ varied) and transverse scans ($q_{\parallel}=q_{\parallel}^{o}$, $q_\perp$ varied) have been performed at equally spaced reduced temperatures $t=T_{NA}/T-1$ on a logarithmic scale in samples of $\overline{8.5}S5$, $\overline{9}S5$, $\overline{9.75}S5$, $\overline{10}S5$, $\overline{10.2}S5$, $\overline{10.4}S5$, and $\overline{11}S5$. At each reduced temperature, both scans are fit to a Lorentzian with a fourth order correction term (see Eq 5.01) convoluted with the appropriate resolution function (see Appendix 1). The fits are of comparable quality to those in $\overline{6}09$ and 40.7 with $\chi^2 \approx 2$.

Results of these fits a function of t are presented for the parameters $\xi_{\parallel}$ (figure 5.2.5), $\xi_\perp$ (figure 5.2.6), c_0 (figure 5.2.7), and c (figure 5.2.8). There is a dramatic evolution in the length scale as a function of chain length. At $t=2\times10^{-5}$, for instance, $\xi_{\parallel}(\overline{8}S5)/\xi_{\parallel}(\overline{10}S5)$ is ~ 14 whereas $\xi_\perp(\overline{8}S5)/\xi_\perp(\overline{10}S5)$ is ~ 7, therefore, the correlated smectic volume V_c differs by $\xi_\perp^2\xi_{\parallel}\approx750$. If two-scale universality holds, then the heat capacity ratio $C_p(\overline{8}S5)/C_p(\overline{10}S5)$ should equal V_c^{-1}. Therefore, at $t=2\times10^{-5}$ the heat capacity ratio should differ by nearly three orders of magnitude, a rather drastic effect. For concentrations which exhibit second order $N \rightarrow S_A$ transitions

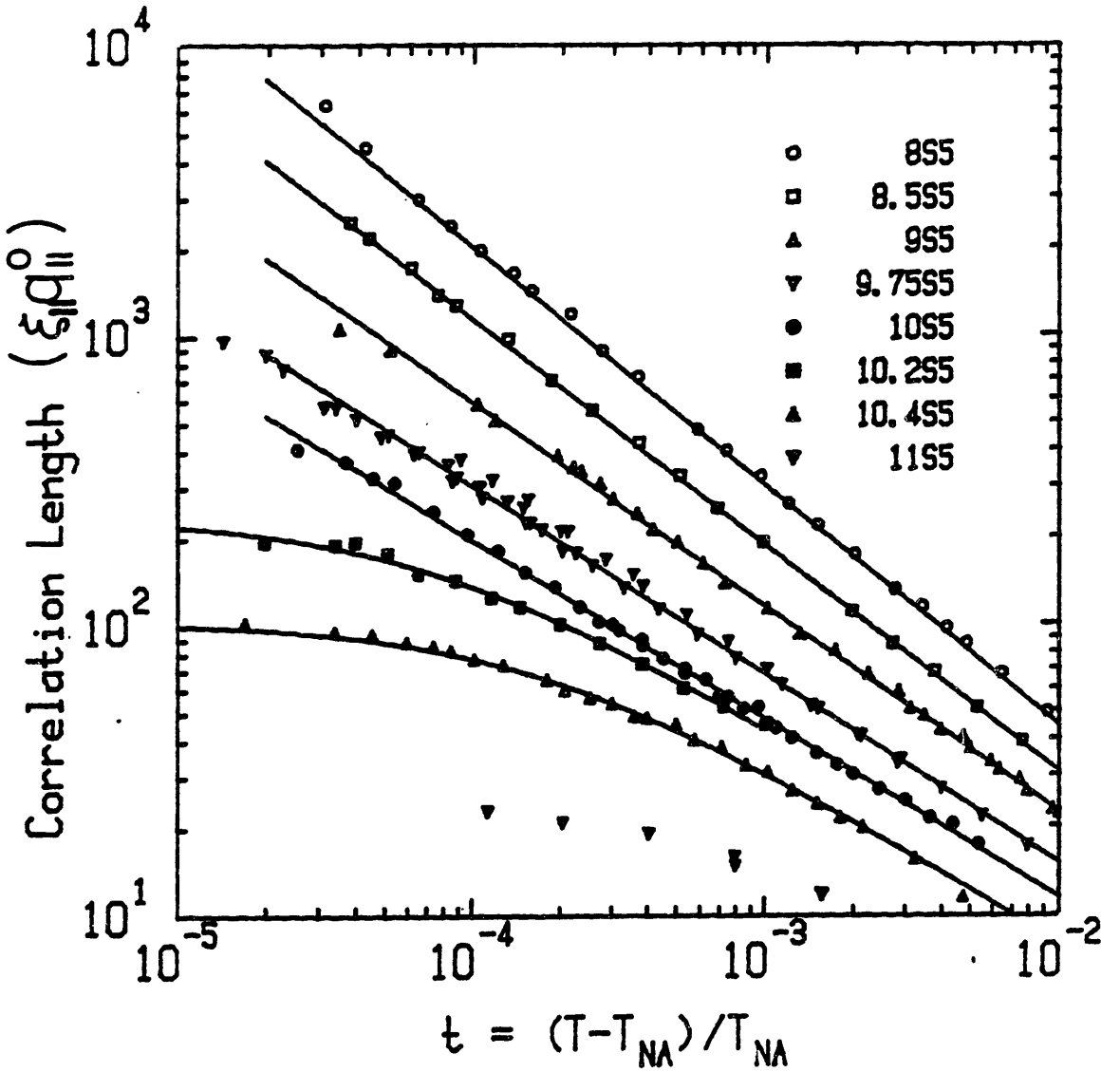

Figure 5.2.5

Longitudinal correlation lengths vs. reduced temperature in $\bar{n}$S5 samples. The solid lines are single power law fits. For first order transition ($\overline{10.2}$S5, $\overline{10.4}$S5, and $\overline{11}$S5) saturation occurs at small t, as a result, single power law fits give t′>0. The $\overline{8}$S5 data was taken by C.R. Safinya.

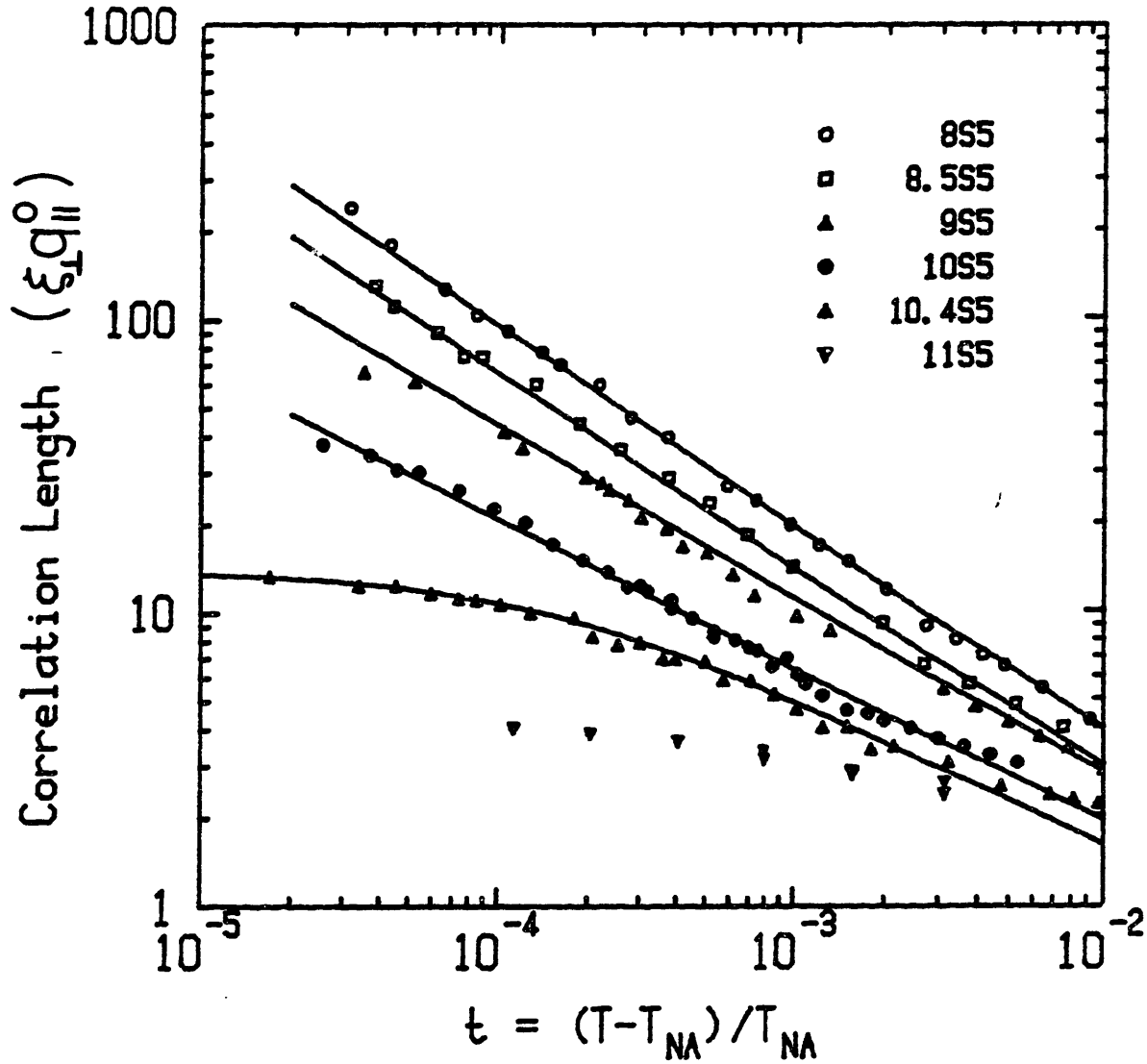

Figure 5.2.6

Transverse correlation lengths ($\xi_\perp$) vs. reduced temperature in $\bar{n}$S5 samples. The solid lines are single power law fits. For first order transition ($\overline{10.4}$S5 and $\overline{11}$S5) saturation occurs at small t, as a result, single power law fits give t′>0. The $\bar{8}$S5 data was taken by C.R. Safinya.

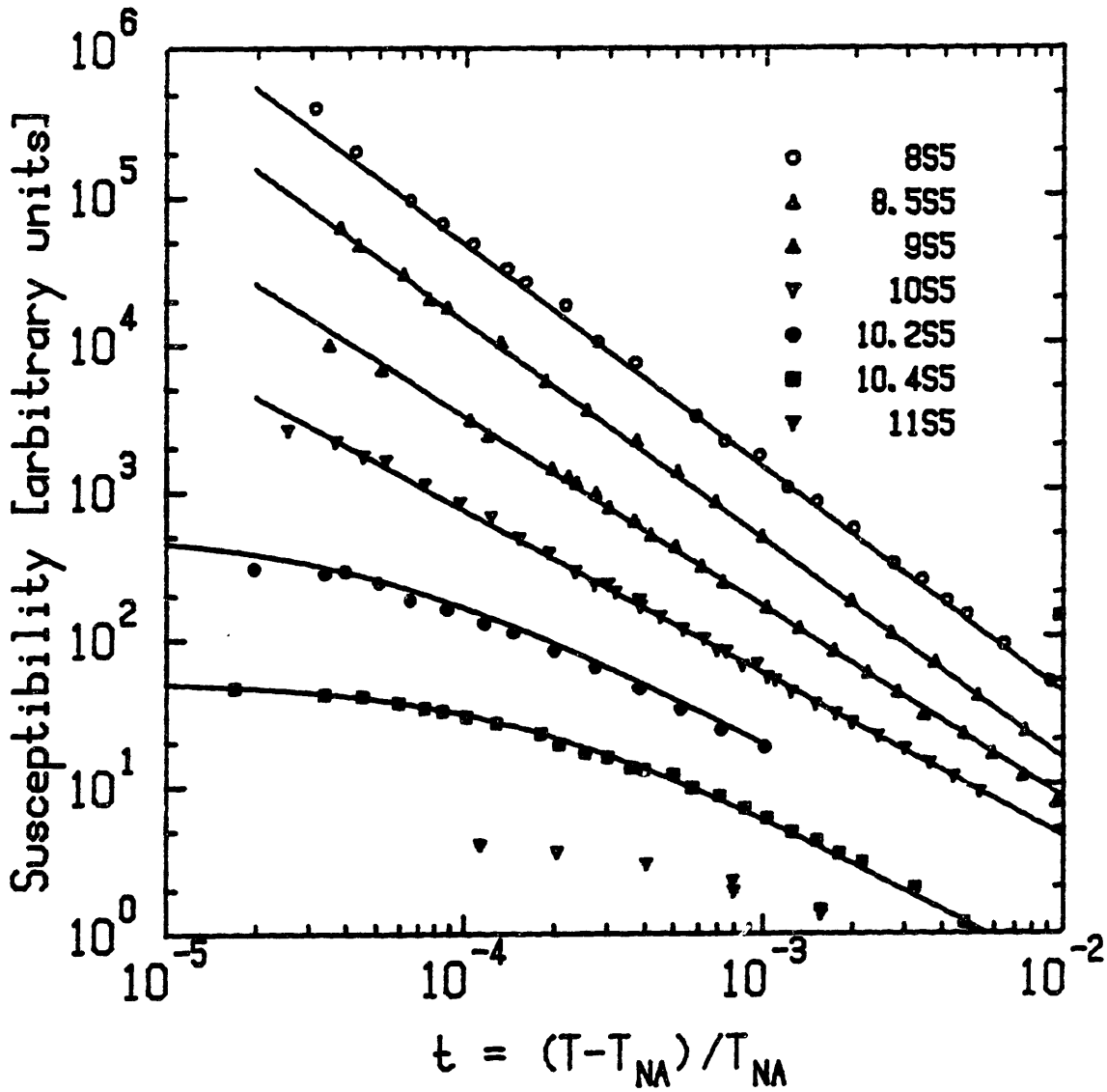

Figure 5.2.7

Susceptibility σ_0 vs. reduced temperature in $\bar{n}$S5 samples. The relative amplitudes have been adjusted for graphical purpose. The solid lines are single power law fits. For first order transition ($\overline{10.2}$S5, $\overline{10.4}$S5, and $\overline{11}$S5) saturation occurs at small t, as a result, single power law fits give t′>0. The $\overline{8}$S5 data was taken by C.R. Safinya.

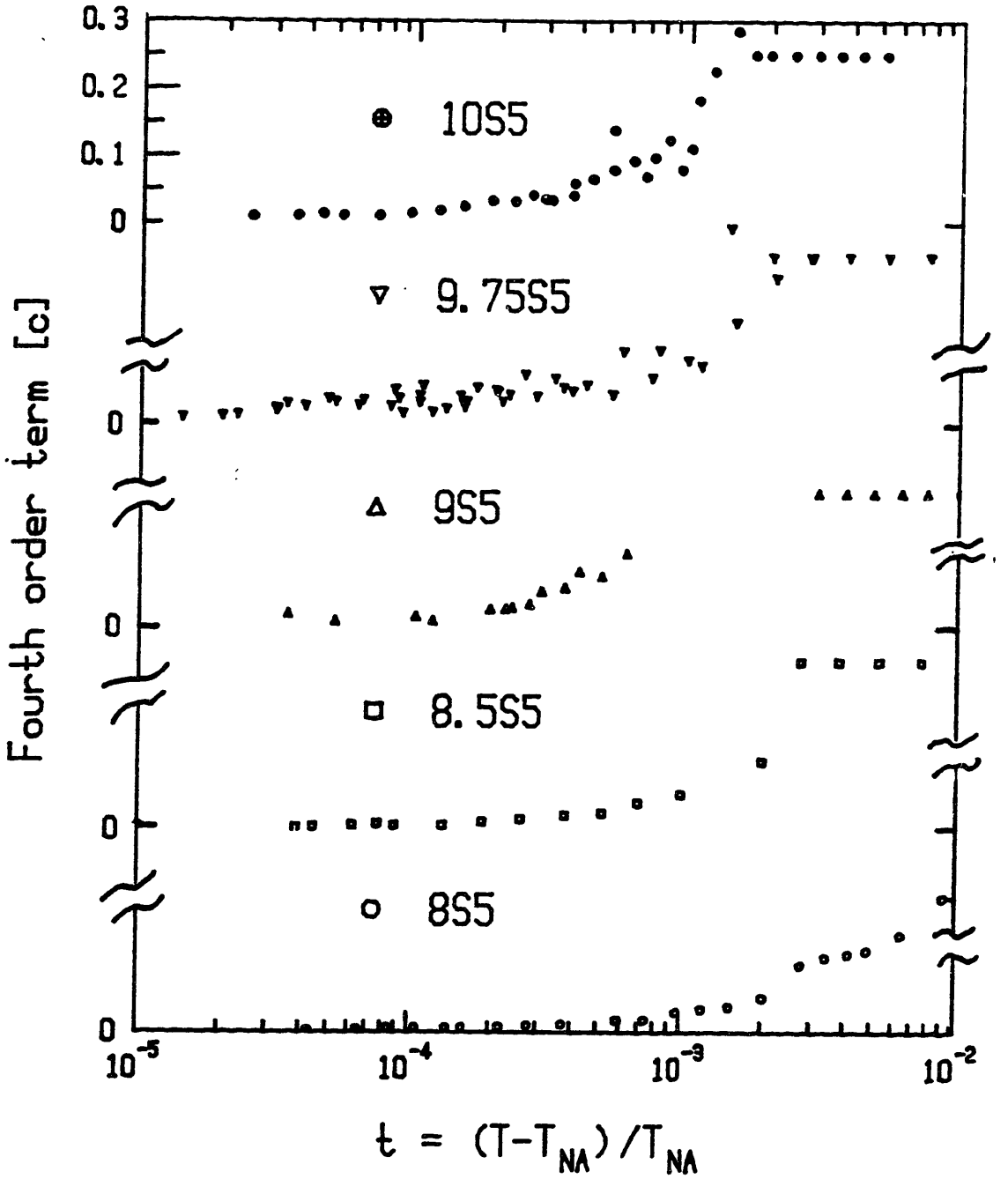

Figure 5.2.8

Fourth order coefficient (c) vs. reduced temperature in $\bar{n}$S5 samples. The $\bar{8}$S5 data was taken by C.R. Safinya.

($\overline{8.5}$S5, $\overline{9}$S5, $\overline{9.75}$S5, and $\overline{10}$S5) single power law behavior with t'=0 is exhibited by $\xi_{\parallel}$, $\xi_{\perp}$, σ_0 over the reduced temperature range -5×10^{-5} to -10^{-2}. However, if the transition is first order then T_{NA}, defined by the appearance of a resolution limited smectic peak, should be too high and accordingly the data should saturate at small reduced temperatures. Such an effect is indeed observed for $\overline{10.2}$S5 and $\overline{10.4}$S5 with $\xi_{\parallel}q_{\parallel}^{o}$ saturating at 220±40 and 100±20 respectively. The data strongly suggest that the tricritical point occurs very close to $\overline{10}$S5.

As mentioned previously, the data were obtained with both silicon(111) and germanium(111) spectrometer set-ups. Both configurations yield consistent results after deconvolution, as shown for $\overline{10}$S5 in figure 5.2.9. The uncertainty in $\xi_{\perp}$ is larger than in $\xi_{\parallel}$ because of the influence of the fourth order correction term in the transverse direction. The uncertainties in the other samples are comparable to those in $\overline{10}$S5.

The fitted line-shape parameters $\xi_{\parallel}$, $\xi_{\perp}$, and σ_0 have been fit to single power laws

$$\xi_{\parallel}q_{\parallel}^{o} = \xi_{\parallel}^{o}(t+t')^{-\nu_{\parallel}} \qquad 5.2.1a$$

$$\xi_{\perp}q_{\parallel}^{o} = \xi_{\perp}^{o}(t+t')^{-\nu_{\perp}} \qquad 5.2.1b$$

$$\sigma_0 = A(t+t')^{-\gamma} \qquad 5.2.1c$$

for each sample where t' measures the difference between T_{NA} and the temperature that gives the best fit to a single power law (This effectively permits the transition temperature to float). In table 5.2.1 the results of these fits are summarized. For $\overline{8.5}$S5, $\overline{9}$S5, $\overline{9.75}$S5, and $\overline{10}$S5 the fitted t' is less than 10^{-5} and setting t'=0 does not

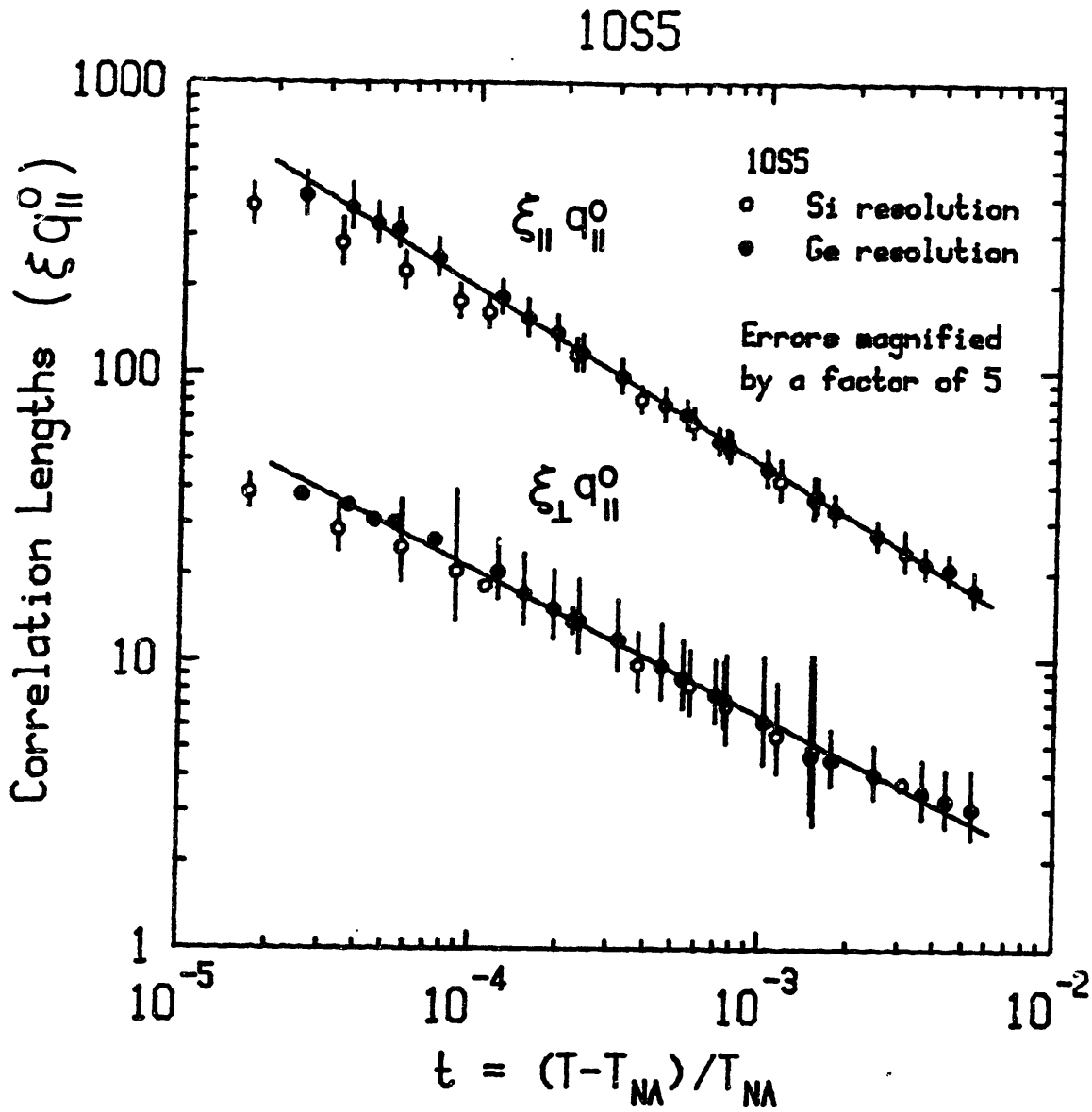

Figure 5.2.9

Correlation lengths $\xi_{\parallel}$ and $\xi_{\perp}$ in $\overline{10}S5$ obtained from the silicon and germanium set-ups (see chapter 4). The errors are one standard deviation errors, magnified by a factor of five, derived from the analysis of the scattering line-shape.

	T_{NA}/T_{NI}	γ	$\nu_{\parallel}$	$\nu_{\perp}$	$\xi_{\parallel}^{o}$	$\xi_{\perp}^{o}$	t'
$\overline{8}$S5	0.936	1.53	0.83	0.68	1.02	0.173	0.0
$\overline{8.5}$S5	0.954	1.48	0.78	0.66	0.86	0.142	0.0
$\overline{9}$S5	0.967	1.31	0.71	0.57	0.88	0.189	0.0
$\overline{9.75}$S5	0.981	1.22	0.66	0.53	0.71	0.205	0.0
$\overline{10}$S5	0.984	1.10	0.61	0.51	0.68	0.187	0.0
$\overline{10.2}$S5	0.987	(fixed at $\overline{10}$S5 values)			0.66	0.182	5.5×10^{-5}
$\overline{10.4}$S5	0.989	(fixed at $\overline{10}$S5 values)			0.50	0.156	1.1×10^{-4}

Table 5.2.1

Summary of single power law fits for the $\bar{n}$S5 system.

significantly alter the exponents. Therefore, t' has been fixed at zero for these samples. For first order transitions, such as in $\overline{10.2}$S5 and $\overline{10.4}$S5, a single power law with t'=0 is clearly inadequate. To fit these samples, the exponents γ, $\nu_{\parallel}$, and $\nu_{\perp}$ have been fixed at the $\overline{10}$S5 (tricritical) values which gives t' of 5.5×10^{-5} and 1.1×10^{-4} for $\overline{10.2}$S5 and $\overline{10.4}$S5 respectively.

Besides the dramatic evolution in the length scale with chain length, the critical exponents γ, $\nu_{\parallel}$, and $\nu_{\perp}$ also evolve, albeit at a more moderate rate. The critical exponents at the saturated nematic order parameter limit ($\overline{8}$S5 and at $\overline{8.5}$S5) and the tricritical limit ($\overline{10}$S5) do not agree with the theoretical predictions developed in chapter 2. At the tricritical point mean field theory predicts γ=1 and $\nu_{\parallel}$=1/2 whereas these measurements yield γ=1.10 and $\nu_{\parallel}$=0.61 in $\overline{10}$S5. In the saturated limit, the 3D XY model predicts γ=1.32 and $\nu_{\parallel}$=0.66, whereas, these measurements yield γ=1.48 and $\nu_{\parallel}$=0.78 in $\overline{8.5}$S5. On average, at both ends of the theoretical spectrum, the measured exponents are higher by 0.13 for γ and 0.11 for $\nu_{\parallel}$. Materials with intermediate nematic ranges, such as $\overline{9}$S5 , 40.8, 8OCB, and 8CB exhibit crossover behavior since the critical exponents are between the limiting values. It is very likely that the excellent single power law behavior is a manifestation of a very slow crossover, in this picture, these critical exponents would only represent effective exponents. As yet, there is no theory which explicitly predicts the behavior in the crossover regime between the saturated second order and the tricritical regimes.

At the tricritical point, the crossover exponent ϕ relates critical exponents along different field directions. As developed in section 1.3, the relationship $\nu_u = \phi\nu_t$ emerges from such an analysis where ν_t describes how ξ diverges with t whereas ν_u describes how the correlation length at the transition, ξ_s diverges with reduced concentration (this is the nonordering field). Since ξ_s has only been obtained for three first order samples ($\overline{10.2}S5$, $\overline{10.4}S5$, and $\overline{11}S5$) it is difficult to obtain ν_u reliably. However, it is possible to show consistency with the mean field crossover exponent ($\phi=2$). In figure 5.2.10 ξ_s ($\xi_{\parallel}$) is plotted vs. reduced concentration where n_t equals 10 ($\overline{10}S5$). The straight line is the best fit to $\xi_s \propto (n-n_t)^{-2\nu_t}$ where ν_t is fixed at the $\overline{10}S5$ value of 0.61. A more thorough analysis would also include the evolution in the length scale with concentration since it also effects ξ_s.

An essential feature of the $N \rightarrow S_A$ transition is that $\nu_{\perp}$ is smaller than $\nu_{\parallel}$, thus, there are two relevant length scales. Although both $\nu_{\parallel}$ and $\nu_{\perp}$ evolve with chain length, the difference $\nu_{\parallel}-\nu_{\perp}$ appears to remain at the constant value 0.14±0.02. The determination of $\nu_{\perp}$ is complicated by the evolution of the transverse line-shape with the fourth order correction term (see figure 5.2.8). This correction becomes increasingly significant at large t and for samples with short nematic ranges. It appears as if c is identical in different samples when $\xi_{\perp}$ is chosen to be the same. Therefore, the evolution in the line-shape depends on $\xi_{\perp}$ in a universal way for all samples.

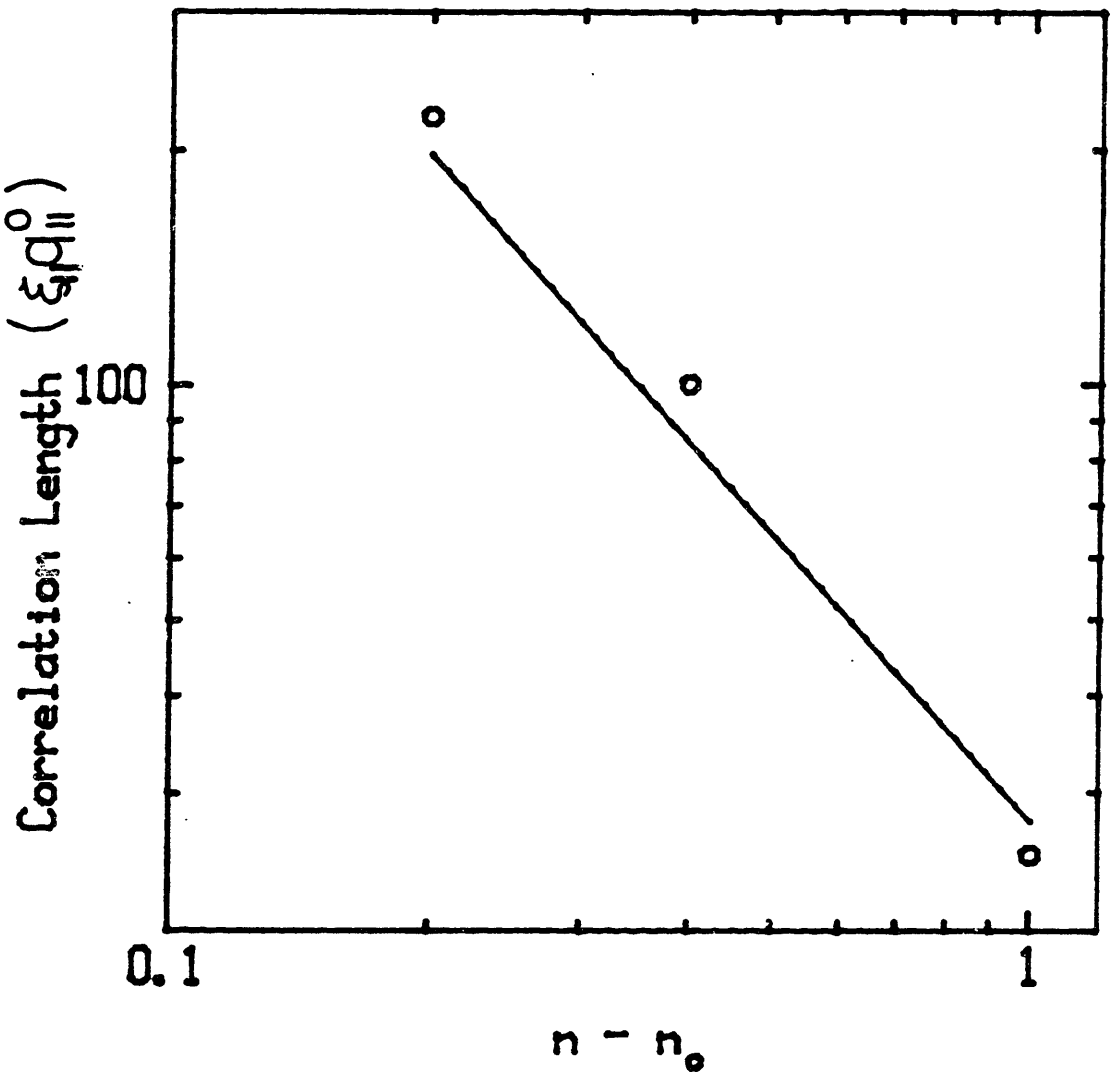

Figure 5.2.10
The saturated values of $\xi_{\parallel}$ at T_{NA} vs. reduced concentration where the tricritical concentration has been fixed at 10 (10S5). The straight line is the best fit with ϕ=2.

5.3
Results in nCB Samples

X-ray scattering experiments have been carried out in alkoxycyanobiphenyls (nCB), including the pure materials 8CB and 9CB. By mixing 10CB with 9CB the nematic range can be reduced from 2°C (9CB) to no nematic range at all. The mixtures 9.05CB, 9.09CB, 9.14CB, 9.20CB, and 9.28CB have been prepared where the effective chain length is determined from the weights of the constituent materials. The phase diagram for the 9CB/10CB mixtures is shown in figure 5.3.1.

A brief summary of the spectrometer set-up is provided here (see chapter 4 for more details). The in-plane resolution of $\sim 10^{-4}\text{Å}^{-1}$ is provided by germanium(111) analyzer and monochromator crystals. The vertical resolution $\sim 0.05 \pm 0.005\text{Å}^{-1}$ HWHM is achieved by matching the vertical divergence of the incoming beam with the vertical acceptance of the detector. Temperature control, provided by a two stage oven with beryllium windows, is stable to within 0.002°C per hour. A 7 kiloGauss field aligns the director along the field direction.

The 8CB, 9CB, and 10CB samples were obtained from BDH and used without further purification. As discussed in section 4.2, impurities caused the transition temperature T_{NA} in an open cell to drift downward. More importantly, T_{NA} was lower at the top of the cell than at the bottom by over 0.020°C. The drift and T_{NA} gradient are undoubtedly due to gases diffusing into the sample from the top of the cell. Flowing N_2 caused the direction of the T_{NA} gradient to change by removing some of the absorbed gasses from the exposed top part of the sample, but the magnitude of the gradient was unchanged. To minimize these impurity effects, measurements were carried out under vacuum and in an all

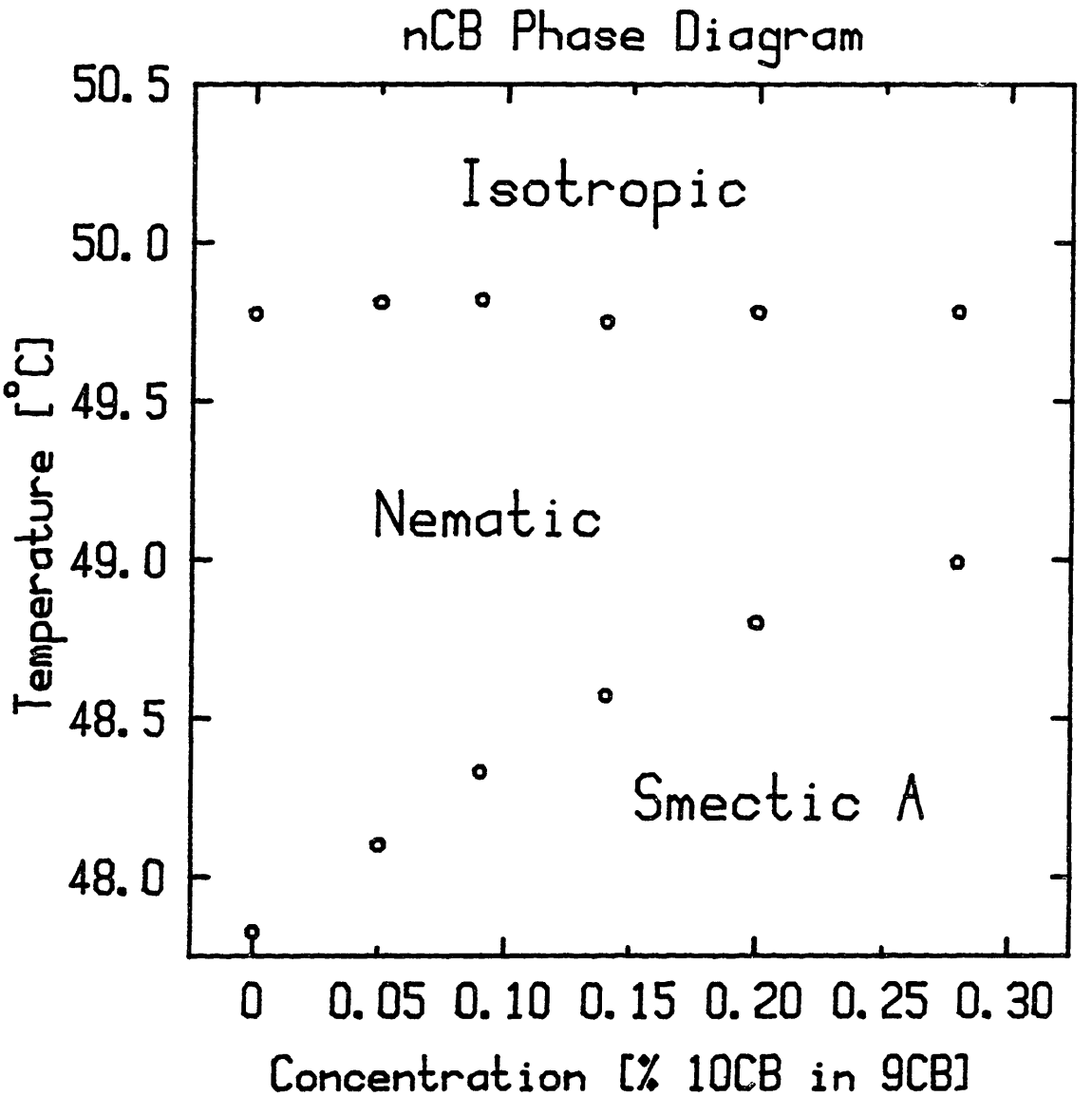

Figure 5.3.1

Phase Diagram for mixtures of 9CB and 10CB.

beryllium cell sealed with indium o-rings. To achieve a homogeneous sample, the entire oven was agitated in the isotropic phase before acquiring data rather than relying on diffusion to achieve equilibration. Using these techniques, the gradient across the illuminated sample was reduced to less than 0.003°C. Measurements carried out under vacuum in 9CB agree with data taken without any precautions outside of $t=10^{-4}$, although the transition temperature is 0.30°C lower in the latter case.

The layer spacing d is determined by measuring the q vector corresponding to smectic layering, $q_{11}^{o}=2\pi/d$ at the $N\rightarrow S_A$ transition. For 9CB the layer spacing is ~33.7A and increases linearly with increasing concentration of 10CB to ~34.2A for 9.28CB (see figure 5.3.2). Also, the McMillan ratio T_{NA}/T_{NI} (see figure 5.3.2 bottom panel) varies linearly with temperature from 0.994 for 9CB to 0.998 for 9.28CB.

The $N\rightarrow S_A$ transition temperature T_{NA} is determined from the x-ray scattering profile through $(0,0,q_{11}^{o})$. Above the transition the scattering is not resolution limited, however, at the transition a peak emerges which is resolution limited in the longitudinal direction and mosaic limited in the transverse direction. Since the mosaic is temperature independent (±10%), the peak intensity and the integrated intensity have the same temperature dependence. The mosaic increased with the 10CB concentration from 0.20°HWHM for 9CB to 0.50°HWHM for 9.28CB. In 9CB the intensity increases by over one and a half orders of magnitude in less than 0.002°C as shown in figure 4.2.2. Of course, this range depends on the impurity induced T_{NA} gradient across the illuminated sample volume as shown in figure 4.2.2. In contrast to $\overline{10}S5$, where the intensity saturates in 0.10°C, the behavior in 9CB is

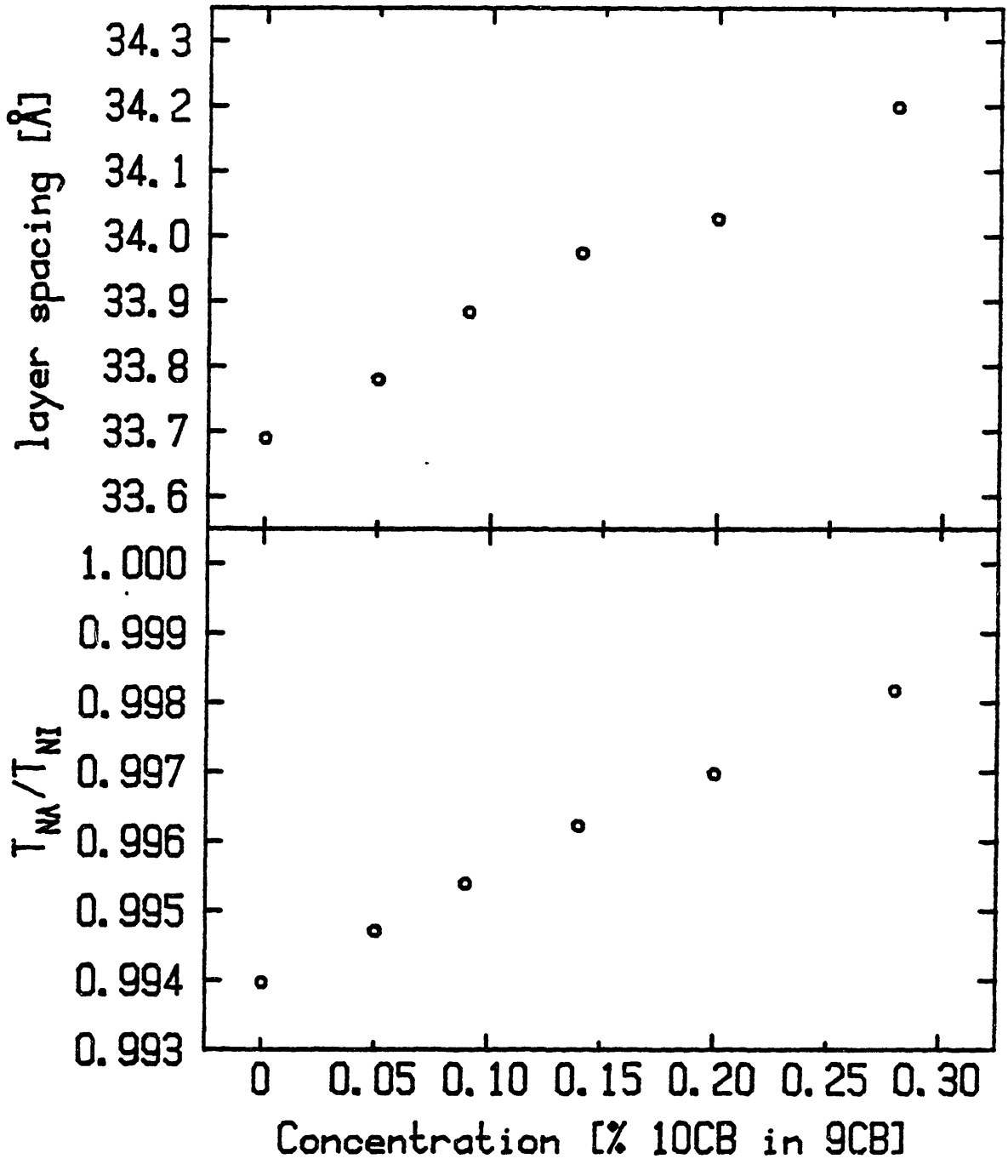

Figure 5.3.2

Top: Layer spacing vs. concentration for 9CB/10CB mixtures.

Bottom: McMillan ratio (T_{NA}/T_{NI}) vs. concentration for 9CB/10CB mixtures.

rather unusual.

For first order transitions, the peak intensity does not rise as sharp, furthermore, the behavior depends on the temperature slew rate. In 9CB, which is second order, T_{NA} determined by heating and cooling runs always agreed within a few millidegrees Centigrade at a slew rate of 0.050°C per hour. However, in 9.20CB there is a 0.020°C hysteresis at this same rate as shown in figure 5.3.3 (top). The precipitous change in the peak intensity in the bottom panel reflects a decrease in the mosaic width, perhaps due to a coexistence region between the two phase. Reducing the slew rate by an order of magnitude decreases the hysteresis to 0.005°C. In summary, for materials exhibiting a first order transition the smectic intensity displays hysteresis and longer equilibration times than for materials exhibiting second order transitions.

Longitudinal scans ($q_\perp$=0, $q_{\parallel}$ varied) and transverse scans ($q_{\parallel}=q_{\parallel}^{o}$, $q_\perp$varied) have been performed at equally spaced reduced temperatures on a logarithmic scale $t=T_{NA}/T-1$ in samples of 8CB, 9CB, 9.05CB, 9.09CB, 9.14CB, 9.20CB, and 9.28CB. In figure 5.3.4 scans are shown for 9CB at $t\sim2\times10^{-5}$. At each reduced temperature, both scans are fit to a Lorentzian with a fourth order correction term (LFC), Eq 5.0.1, or to a Lorentzian raised to the power $\eta_\perp$ (LPC). For both forms, the data have been convoluted with the appropriate resolution function (see Appendix 1). The fits are of comparable quality to fits in $\bar{6}09$, 40.7, and $\bar{n}S5$.

Close to the transition for the 9CB/10CB mixtures the best fit gives c = 0.05 whereas at large t it is necessary to restrict c to 0.25. The quality of the fits is insensitive to the choice of c though the

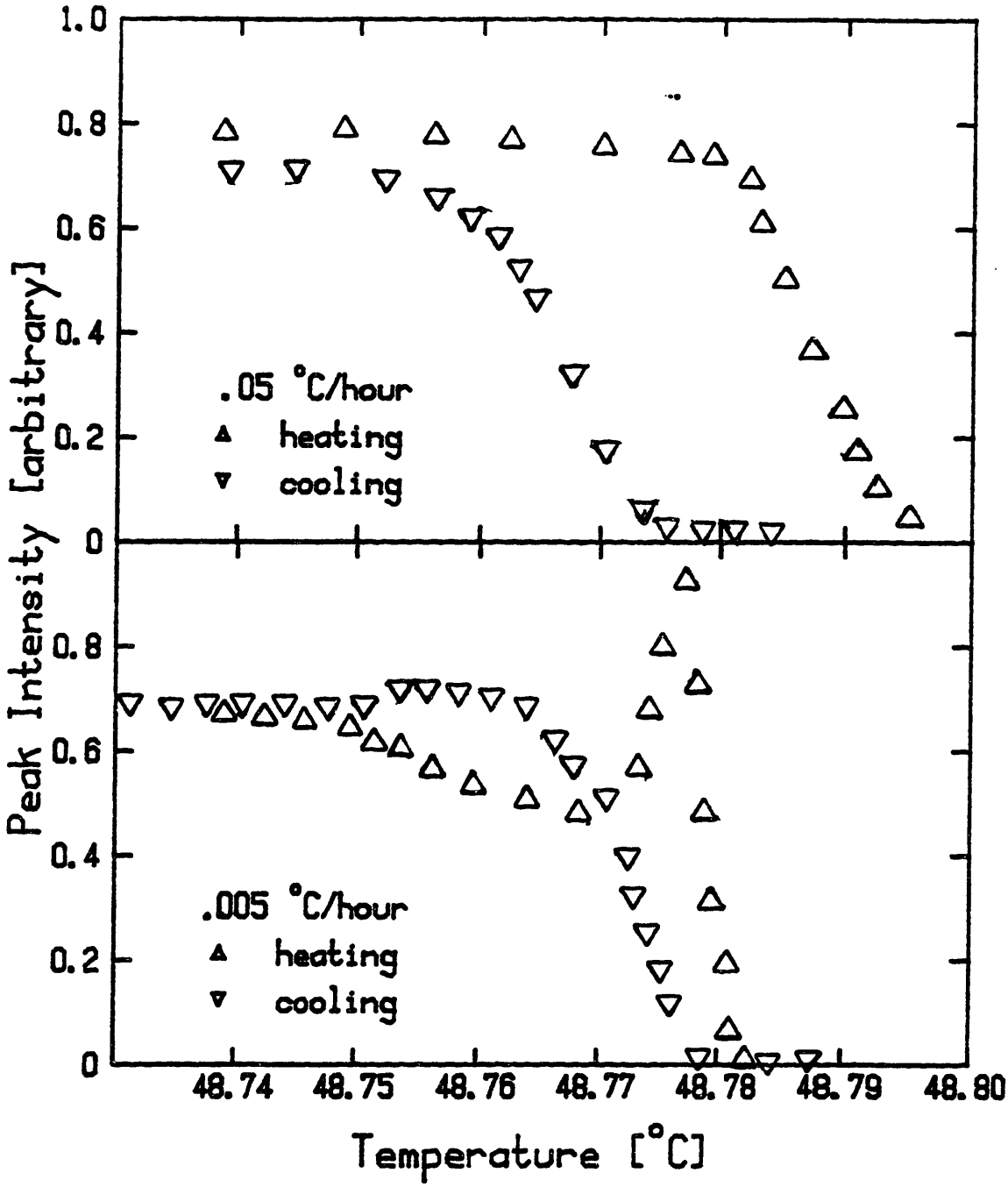

Figure 5.3.3

Peak intensity for 9.20CB at two different slew rates. The precipitous change in the peak intensity in the bottom panel reflects a decrease in the mosaic width, perhaps due to a coexistence region between the two phase.

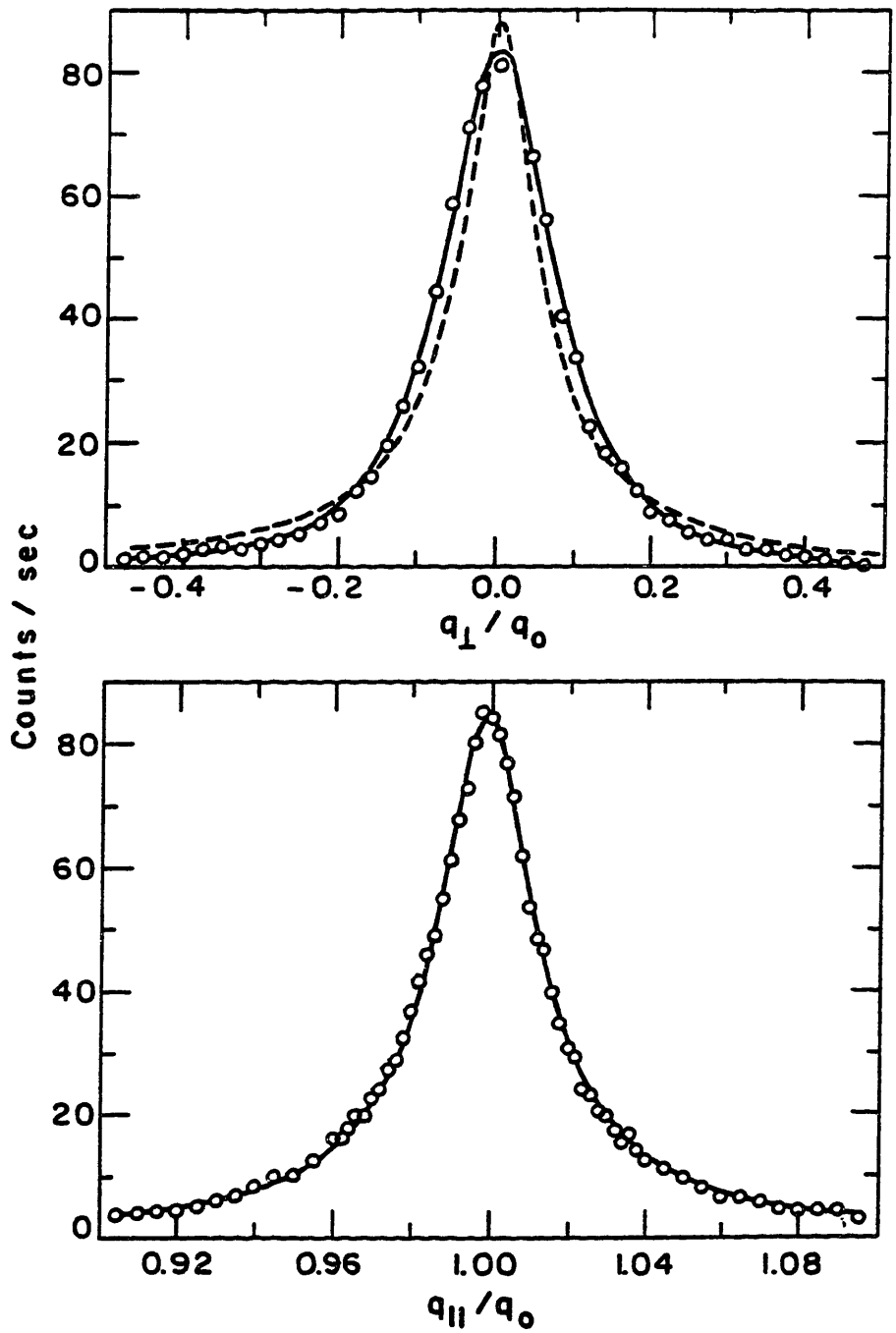

Figure 5.3.4

Transverse scan (top) and longitudinal scan (bottom) at $t \sim 2\times10^{-5}$ in 9CB. The dashed line is fit with c=0 (Lorentzian line-shape); the solid line is fit with c=0.25 (Lorentzian squared transverse line-shape).

correlation length $\xi_\perp$ depends strongly on the value of c at all temperatures. For instance, at $t=10^{-4}$ in 9CB the best fit gives c=0.16 and $\xi_\perp q_{\parallel}^{o}=19.2$, however, if c is fixed at 0.10 then $\xi_\perp q_{\parallel}^{o}=21.0$ and if c is fixed at 0.25 then $\xi_\perp q_{\parallel}^{o}=17.7$. Although $\xi_\perp$ varies by over 20%, the goodness of fit parameter $\chi^2=1.5\pm0.05$ for all three fits. Therefore, after convolution in the vertical, the profile shape is nearly identical for $0.10 < c < 0.25$. Measurements with better vertical resolution are necessary to determine the precise line-shape in the transverse direction.

In order to fit the data, c is held fixed at the same value for each sample. Results of these fits in 9CB to the LFC line-shape for $\xi_\parallel$ and $\xi_\perp$ are shown in figure 5.3.5 with c=0.10 (open circles) and c=0.25 (filled circles). It is apparent that the slopes do not depend on the choice of c, whereas the bare lengths do, especially $\xi_\perp^o$. The correlation lengths $\xi_\parallel$ and $\xi_\perp$ and the susceptibility σ_0 have been fit to single power laws

$$\xi_\parallel q_\parallel^{o} = \xi_\parallel^{o}(t+t')^{-\nu_\parallel} \qquad 5.3.1a$$

$$\xi_\perp q_\parallel^{o} = \xi_\parallel^{o}(t+t')^{-\nu_\perp} \qquad 5.3.1b$$

$$\sigma_0 = A(t+t')^{-\gamma} \qquad 5.3.1c$$

for each sample where t' measures the difference between T_{NA} and the temperature that gives the best fit to a single power law. As noted previously, this effectively permits the transition temperature to float. In 9CB the data are fit from 2×10^{-5} to 2×10^{-3}, giving $t'=10^{-5}\pm10^{-5}$. When c is held fixed at 0.10 or at 0.25, the critical exponents $\nu_\parallel=0.57$, $\nu_\perp=0.37$ and $\gamma=1.09$ obtained are identical although

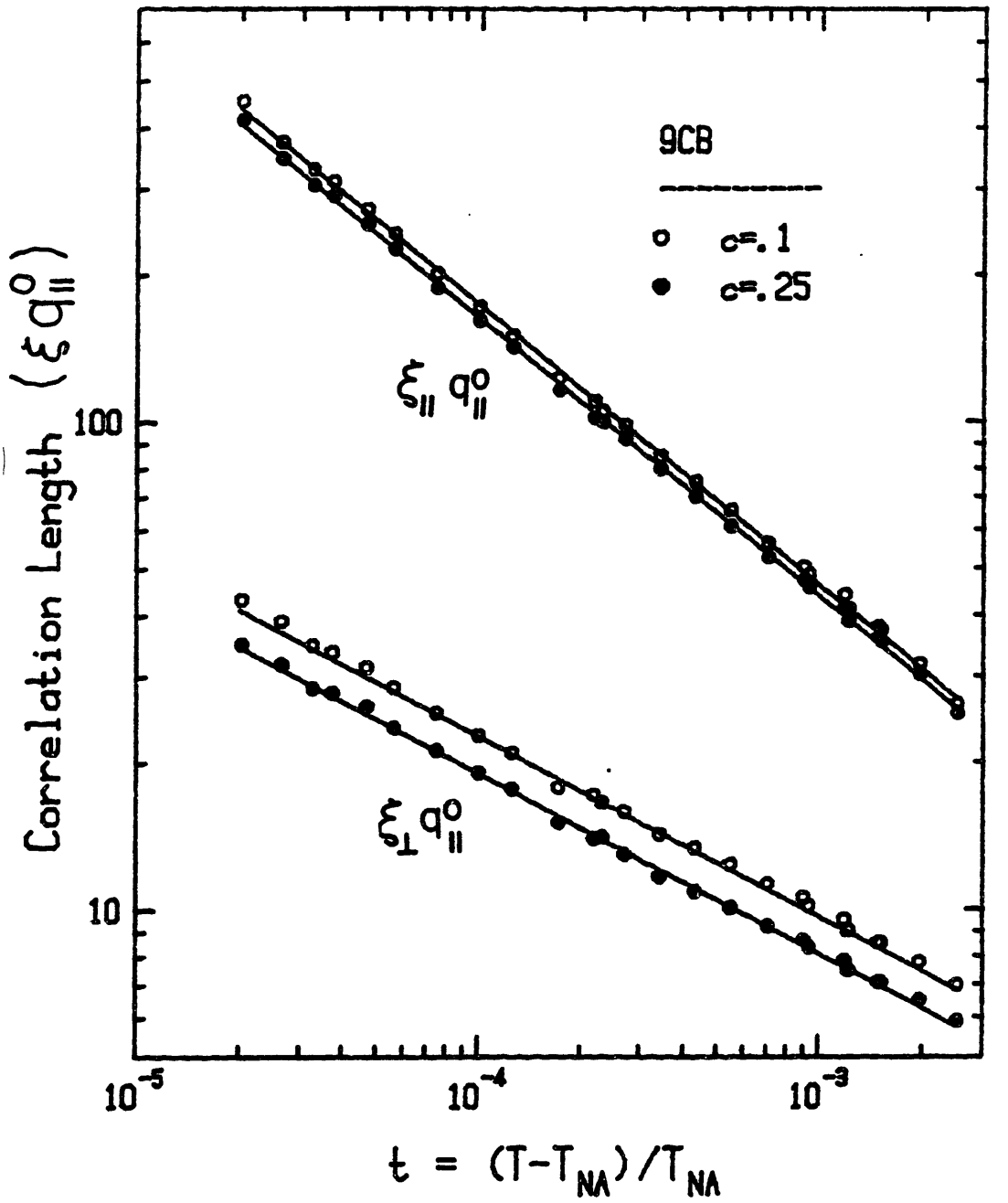

Figure 5.3.5

Correlation lengths $\xi_{\parallel}$ and $\xi_{\perp}$ vs. reduced temperature t in 9CB fit to a Lorentzian with a fourth order correction (Eq 5.0.1). with c=0.10 (filled circles) and c=0.25 (open circles). The straight lines are the results of power law fits as described in the text.

$\xi_\perp^0$ differs by ~ 20% (see figure 5.3.5). If c is allowed to float between 0.05 and 0.25, the best fit gives $\nu_{\parallel}$=0.59, $\nu_\perp$=0.43 and γ=1.13. The increase in $\nu_\perp$ is because of the additional 20% change in $\xi_\perp$ over the entire fitted range.

The data have also been fit to a Lorentzian raised to the power $1-\eta_\perp/2$ (Eq 5.0.2). When $\eta_\perp$ is allowed to float, the best fit gives $\eta_\perp$= -1 at small reduced temperatures crossing over to $\eta_\perp$= -2 far from the transition. The critical exponents obtained by fitting $\xi_{\parallel}$, $\xi_\perp$ and σ_0 to single power laws (Eq 5.3.1) are comparable to the LFC fits.

Measurement of the critical behavior in the nematic phase have also been carried out in the mixtures 9.05CB, 9.09CB, 9.14CB, 9.20CB, and 8CB. The data have been fit to the convolution of the LFC line-shape convoluted with the resolution function. The fourth order term has been fixed at 0.10 for all of the 9CB/10CB mixture fits because of the strong correlation between c and $\xi_\perp$ as discussed above in reference to the 9CB fits. This is not necessary in 8CB as $\xi_\perp$ evolves much more over the measured range. Results of these fits are shown for $\xi_{\parallel}$ (figure 5.3.6), $\xi_\perp$ (figure 5.3.7) and σ_0 (figure 5.3.8). As the nematic range is reduced by varying the average chain length, the correlation lengths decrease and the slopes evolve slightly. Subtle variations in these trends may result from slight variations in the background, vertical resolution and absorption corrections which are not properly accounted for in the fits.

For the samples which exhibit second order N→S_A transitions, 8CB, 9CB, 9.04CB, and 9.09CB, each of $\xi_{\parallel}$, $\xi_\perp$, and σ_0 exhibit single power laws with t'=0.0±10^{-5} over the temperature range ~2×10^{-5} to 2×10^{-3} with t' = 0. These results are summarized in table 5.3.1. As is

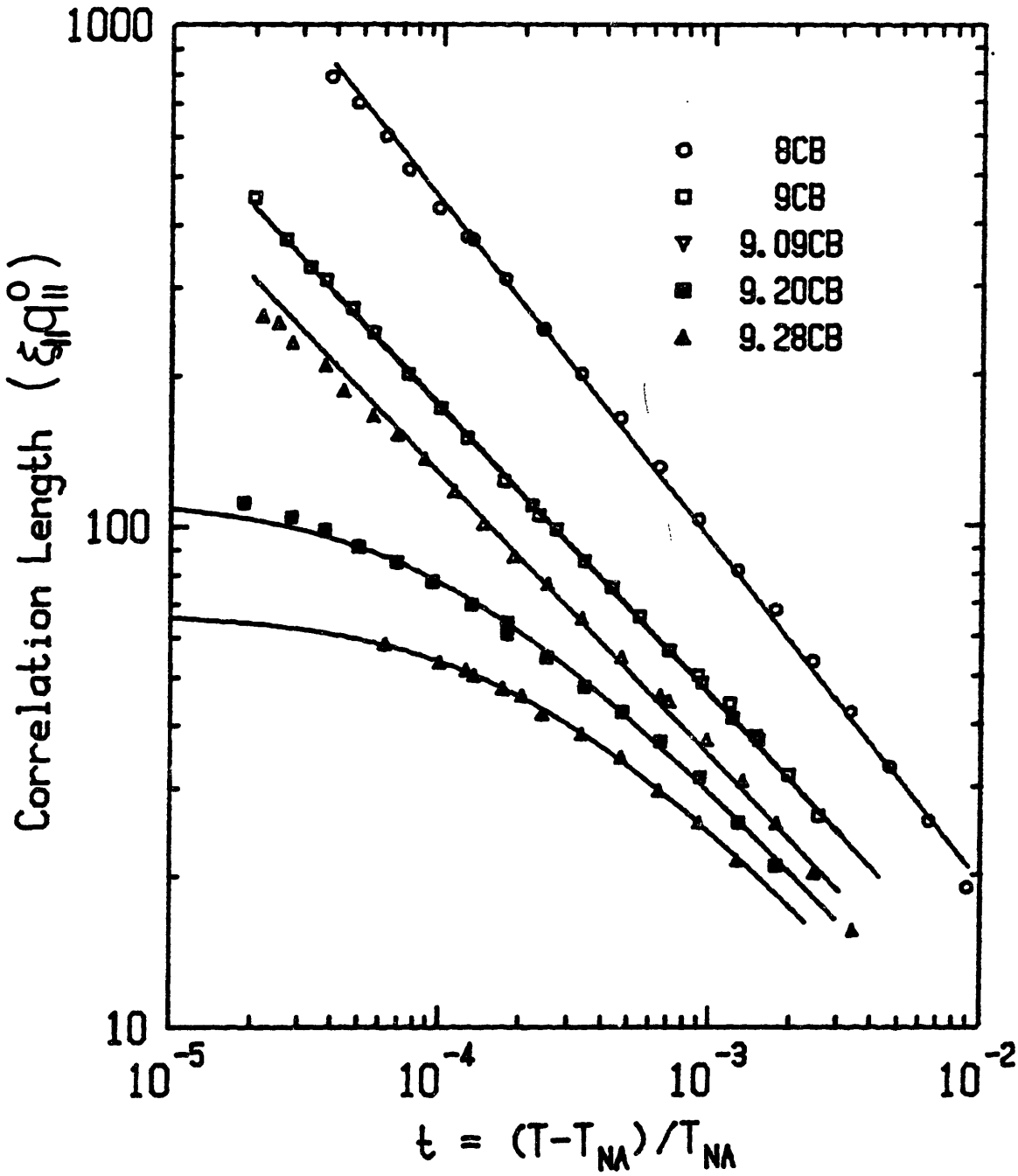

Figure 5.3.6

Longitudinal correlation lengths ($\xi_{\parallel}$) vs. reduced temperature (t) for nCB samples. The solid lines are single power law fits. For first order transitions (9.20CB and 9.28CB) saturation occurs at small t, therefore, the power law fit gives $t' \neq 0$.

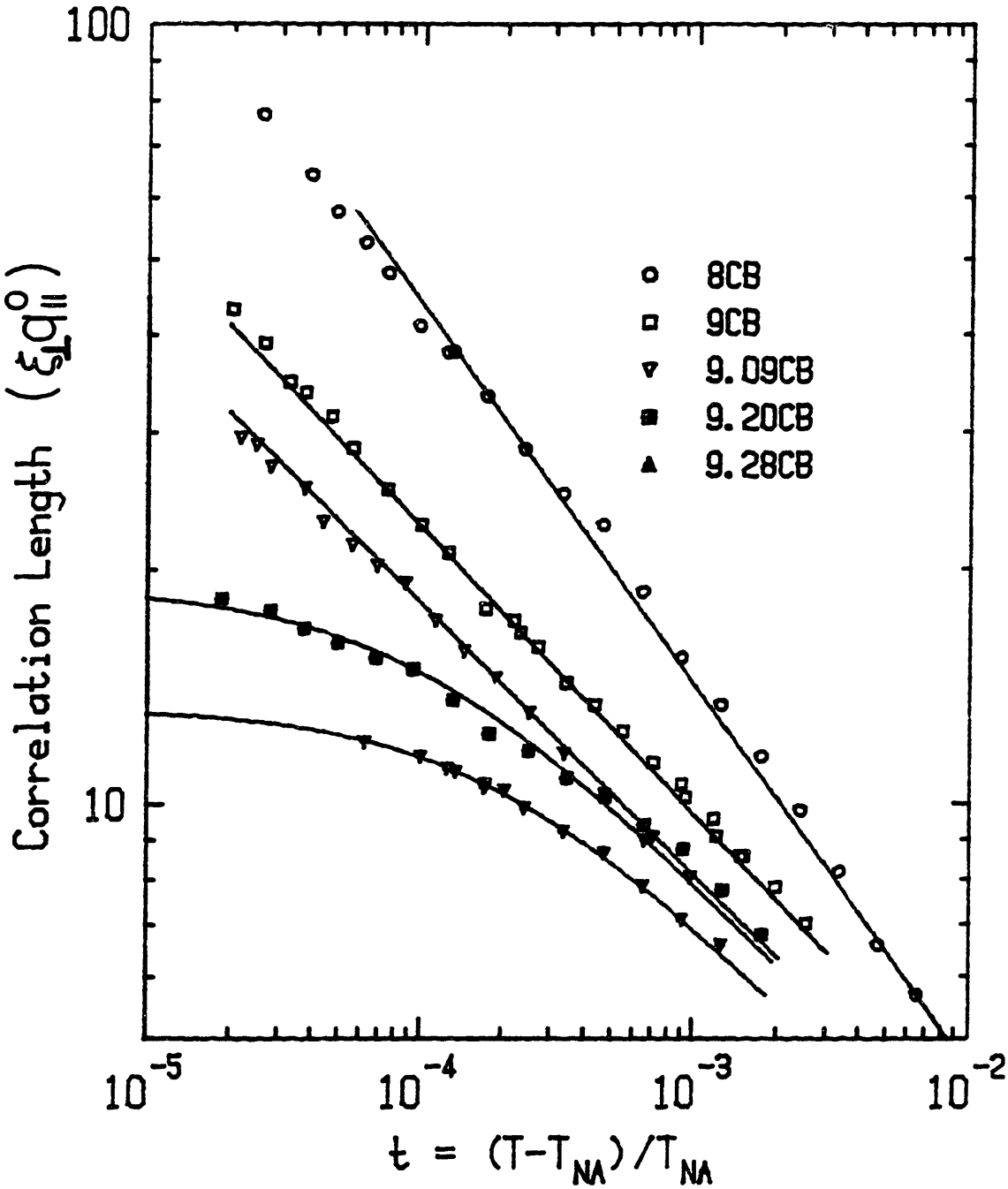

Figure 5.3.7

Transverse correlation lengths ($\xi_\perp$) vs. reduced temperature (t) for nCB samples The solid lines are single power law fits. For first order transitions (9.20CB and 9.28CB) saturation occurs at small t, therefore, the power law fit gives $t' \neq 0$.

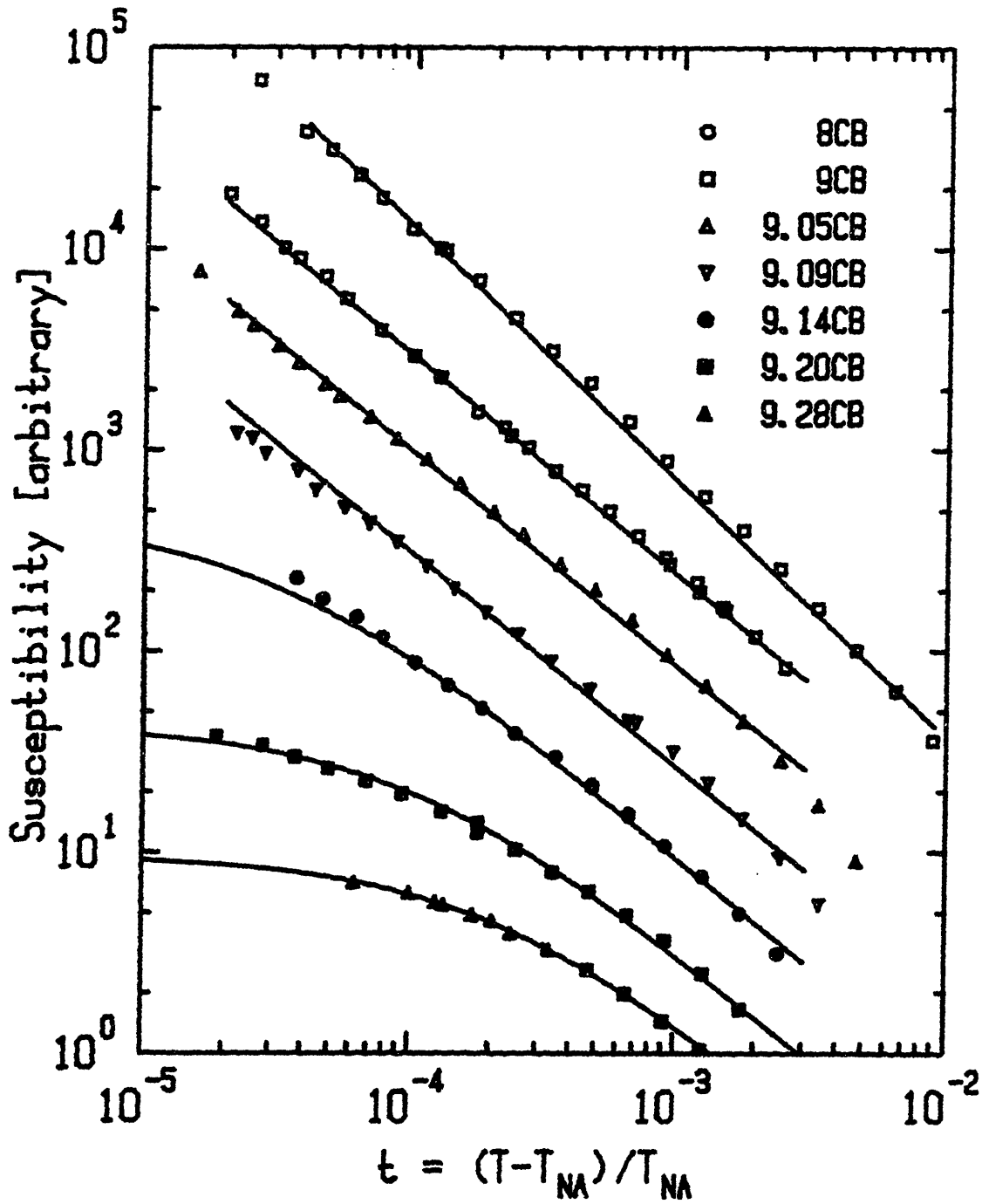

Figure 5.3.8

Susceptibility (σ_0) vs. reduced temperature (t) for nCB samples. The relative amplitudes have been adjusted for graphical purpose. The solid lines are single power law fits. For first order transitions (9.20CB and 9.28CB) saturation occurs at small t, therefore, the power law fit gives $t' \neq 0$.

evident from the table, the correlation length critical exponent anisotropy, $\nu_{\parallel}-\nu_{\perp}$, equals 0.20±0.02 whereas in all of the other systems studied the difference is less pronounced. The increased anisotropy primarily results from a smaller $\nu_{\perp}$ relative to other materials with comparable nematic ranges. This may be connected with the complications of the fourth order term in the fits.

For transitions which are clearly first order (9.14CB, 9.20CB, and 9.28CB) a single power law describes $\xi_{\parallel}$, $\xi_{\perp}$, and σ_0 provided that the transition temperature is allowed to float from the measured value. This is achieved by letting t' and the amplitudes float with γ, $\nu_{\parallel}$, and $\nu_{\perp}$ fixed at the 9CB (tricritical) values. These fits are shown in figures 5.3.6, 5.3.7, and 5.3.8 where $t'= 2\times10^{-5}$ (9.14CB), 10^{-4} (9.20CB), and 2×10^{-4} (9.28CB). If t' varies linearly with reduced chain length then the tricritical point occurs at 9.09CB; however, our data are also consistent with a quadratic dependence, in which case, the tricritical point occurs at 9CB. At the highest temperature points, especially in the shortest nematic range samples, there is a noticeable deviation from single power law behavior. This may be connected with the nearby isotropic phase which alters the $N\rightarrow S_A$ critical behavior.

To determine the sensitivity of the critical exponents to the form of the line-shape, the 8CB data have been fit to a Lorentzian raised to the power $1-\eta_{\perp}/2$ in the transverse direction (LPC) and to a Lorentzian with a fourth order correction (LFC). The correction terms $\eta_{\perp}$ and c are allowed to float for both forms. Over the entire range the LFC fits fits are better than the LFC fits as is the case in $\overline{6}09$ (see section 5.1). For all reduced temperatures $\xi_{\parallel}$(LFC) and $\xi_{\parallel}$(LPC) are almost identical, in fact, over the range $10^{-4}<t<10^{-2}$ the two

	T_{NA}/T_{NI}	γ	$\nu_{\parallel}$	$\nu_{\perp}$	$\xi_{\parallel}^{o}$	$\xi_{\perp}^{o}$	t'
8CB	0.979	1.31	0.70	0.49	0.75	0.48	0.0
9CB	0.994	1.09	0.57	0.37	0.87	0.75	0.0
9.04CB	0.995	1.07	0.54	0.38	1.02	0.59	0.0
9.09CB	0.995	1.07	0.56	0.35	0.71	0.72	0.0
9.14CB	0.996	(fixed at 9CB values)			0.65	0.58	2×10^{-5}
9.20CB	0.997	(fixed at 9CB values)			0.60	0.63	10^{-4}
9.28CB	0.998	(fixed at 9CB values)			0.53	0.57	2×10^{-4}

Table 5.3.1

Results to single power law fits for σ_0, $\xi_{\parallel}$, and $\xi_{\perp}$ in 8CB, 9CB and 9CB/10CB mixtures.

results are indistinguishable as shown in figure 5.3.9, thus, $\nu_{\parallel}$ must be the same. In the transverse direction the line-shapes differ and the fitted $\xi_{\perp}$ for the two forms do not agree, however, the slopes are identical. Therefore, the critical exponents do not depend on the precise choice of the line-shape. As is apparent from figure 5.3.10, $\eta_{\perp}$ is -1.2 over most of the measured range and eventually crosses over to -2 at $t \sim 10^{-2}$, whereas, c varies from 0.03 to 0.25. At about the same reduced temperature the correlation lengths start to diverge from single power law behavior, therefore, this might be connected with the evolution in the line-shape as measured with $\eta_{\perp}$ or c.

As mentioned previously (section 4.2), the mosaic in the smectic phase does depend on the aligning field. In the nematic phase, mosaic effects should be most pronounced close to the transition for the longest nematic range materials since $\xi_{\perp}$ is the largest for these samples. Such an effect would be manifested if $\xi_{\perp}$ depended on the field strength; however, no such behavior is observed in either 8CB or 9CB over the range $3\times10^{-5}<t<10^{-2}$. Therefore, the director must be well aligned in the nematic phase.

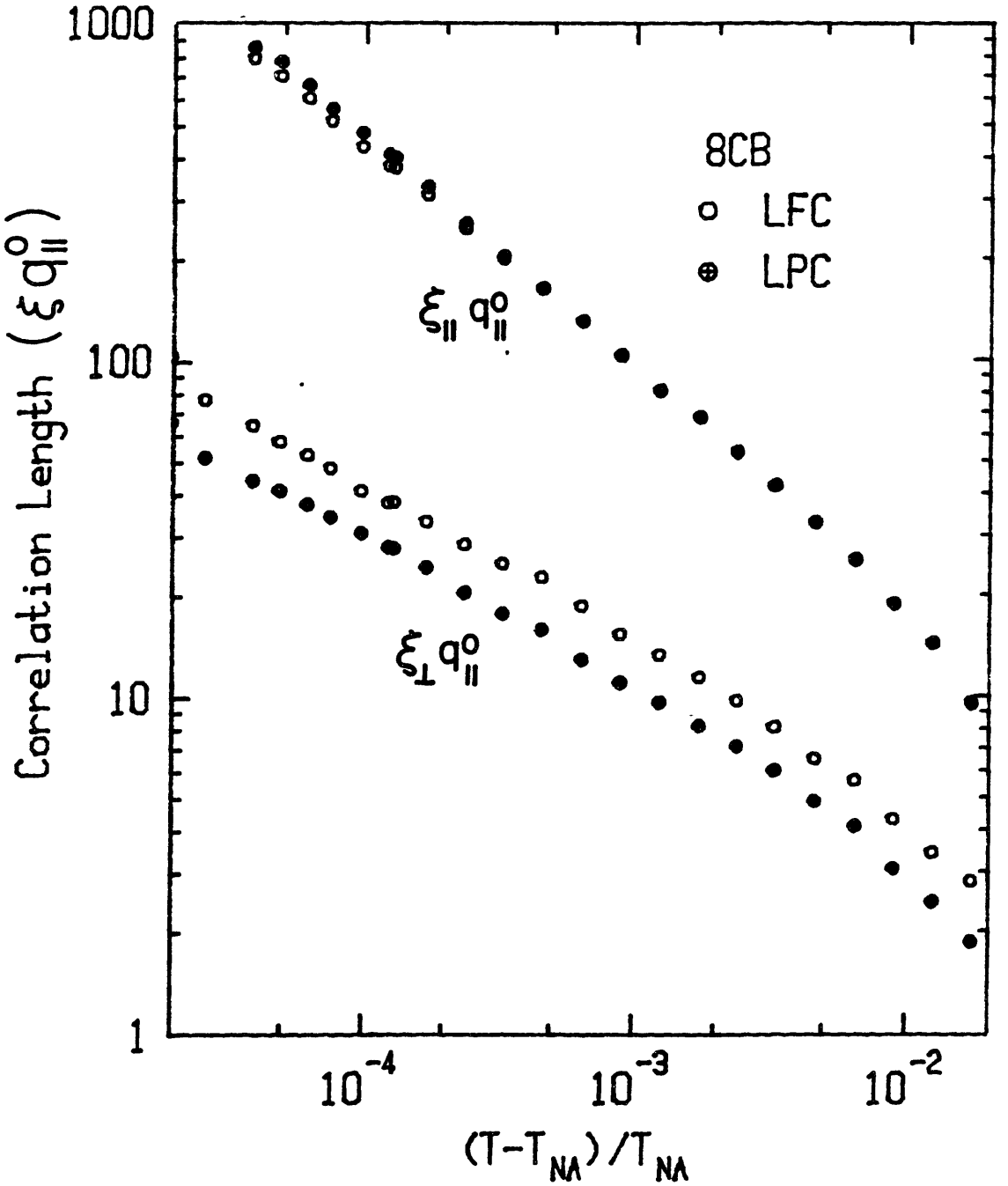

Figure 5.3.9

Fitted values of the correlation lengths $\xi_{\parallel}$ and $\xi_{\perp}$ to both the LFC and LPC line-shapes in 8CB. Over the range reduced temperature range $10^{-4}<t<10^{-2}$ $\xi_{\parallel}$ are identical for both fits.

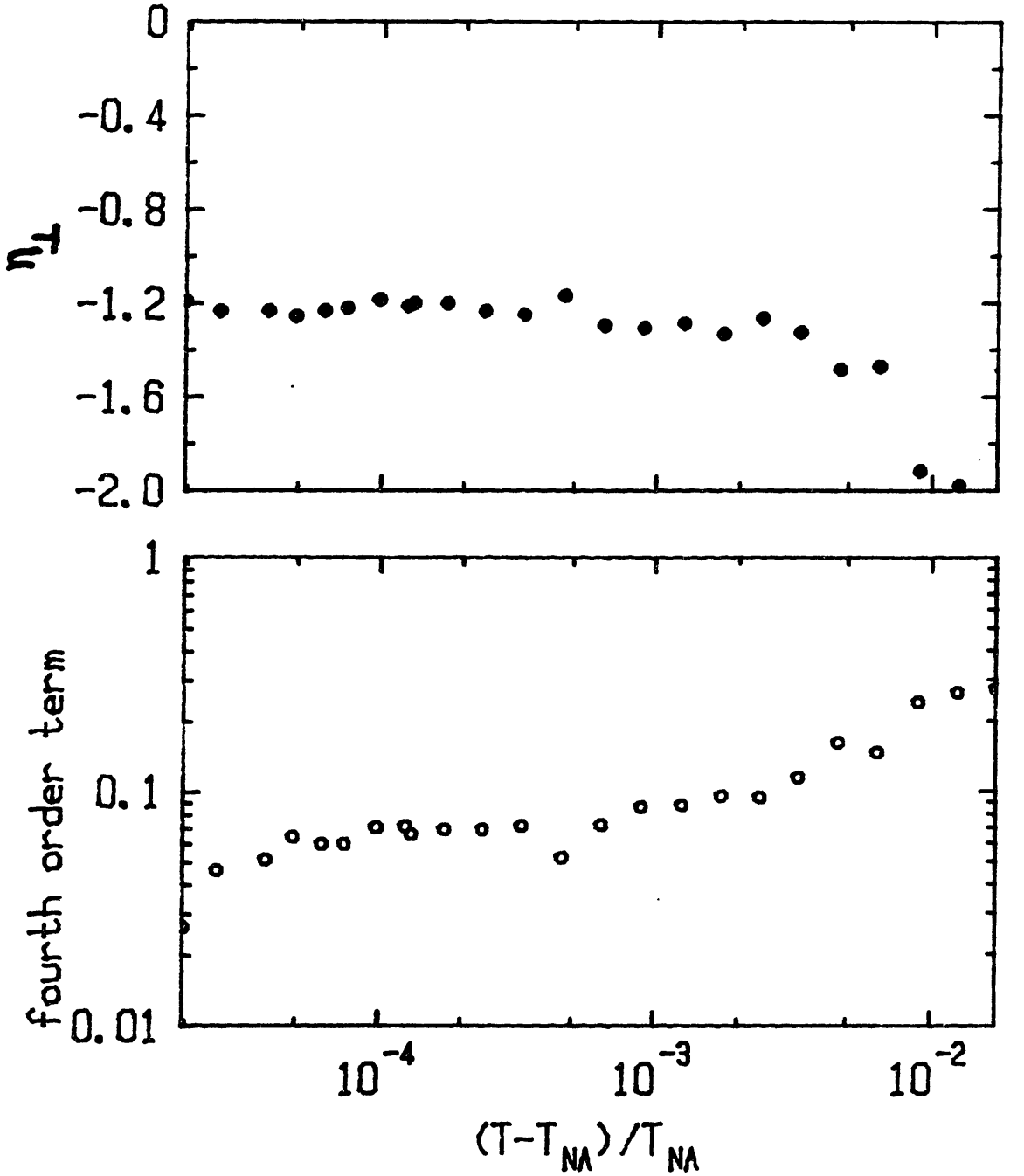

Figure 5.3.10

Top: $\eta_\perp$ (equation 5.0.2) vs. t in 8CB.
Bottom: c (equation 5.0.1) vs. t in 8CB.

REFERENCES

1. C. Safinya, M.I.T. Thesis(1981).

2. L.D. Landau and E.M. Lifshitz, Statistical Physics Part 1; Pergamon Press, Oxford(1980).

6.0
CONCLUDING REMARKS

The smectic fluctuations in the nematic phase have been characterized by measurements of the x-ray scattering profile at the (0,0,1) reflection. If the nematic order parameter is saturated, that is, there is a long nematic range, then critical behavior is observed; however, as the nematic range is reduced the coupling between S and ψ increases and a crossover to tricritical behavior is observed. This crossover occurs at T_{NA}/T_{NI}=0.984 for the $\bar{n}$S5 series and at T_{NA}/T_{NI}=0.994 for the nCB system. McMillan's mean field theory predicts T_{NA}/T_{NI}=0.88 at the tricritical point. As the nematic range is further decreased the $N \rightarrow S_A$ transition becomes first order.

The three materials with the longest nematic ranges studied, 40.7 (26°C), $\bar{6}$09 (24°C), and $\overline{8.5}$S5 (17°C) exhibit nearly identical critical behavior with averaged critical exponents γ=1.48 ± 0.03, $\nu_{\parallel}$=0.78 ± 0.03, and $\nu_{\perp}$=0.66 ± 0.04. These measurements provide an excellent test for the anisotropic hyperscaling relationship $2-\alpha=\nu_{\parallel}+2\nu_{\perp}$ which gives α=-0.10 ± 0.11. This agrees within the errors with α obtained from heat capacity measurements in 40.7 and $\bar{8}$S5 and the predictions of the 3D XY model (α~0). Although $\nu_{\perp}$ agrees with the 3D XY value (ν_{XY}=0.66 and γ_{XY}=1.32), both $\nu_{\parallel}$ and γ are larger than predicted. There is no theory which accounts for these differences. Additional measurements on materials with longer nematic ranges would be useful in determining whether the current results are indeed in the saturated nematic order parameter regime. Though several materials exhibit ~100°C nematic ranges, these same materials are complicated by the tendency to form a smectic phase at two q vectors.

As the nematic range is reduced, by increasing the chain length, the critical exponents $\nu_{\parallel}$, $\nu_{\perp}$, and γ decrease; in addition, the absolute lengths decrease. None of the current theories address this dramatic evolution of the length scale. At $\overline{10}$S5 and 9CB a crossover to tricritical behavior is observed, consistent with heat capacity results, with nearly identical critical behavior for both samples as shown in figure 6.0.1. Single power law fits give γ=1.10 ± 0.05, $\nu_{\parallel}$=0.59 ± 0.03, $\nu_{\perp}$=0.51±0.03($\overline{10}$S5), and $\nu_{\perp}=0.37^{+0.06}_{-0.03}$(9CB) while the tricritical mean field values are γ=1.0, ν=0.50, and α=0.50. These measured exponents, along with heat capacity results, α=0.45($\overline{10}$S5) and α=0.53(9CB) are consistent with the anisotropic hyperscaling relationship. Fluctuations on the high temperature side appear to be more pronounced at the N→S_A transition then at a Gaussian tricritical point since the measured heat capacity ratio A'/A is close to unity rather than 3.56 as predicted. One of the initial goals of this thesis was to measure the tricritical crossover exponent ϕ. This, however, was limited by the uncertainty in the tricritical concentration and by transition temperature gradients and drifts, which of course broaden the transition, thereby complicating the determination of the saturated values of ξ.

Materials with intermediate nematic ranges, such as 8CB and $\overline{9}$S5 exhibit single power laws for $\xi_{\parallel}$, $\xi_{\perp}$, and σ and satisfy the anisotropic hypersaling relationship. These samples should exhibit crossover between tricritical and critical behavior, however, it is very difficult to distinguish a slow crossover from single power laws. There are no specific theoretical predictions for the precise scaling crossover form.

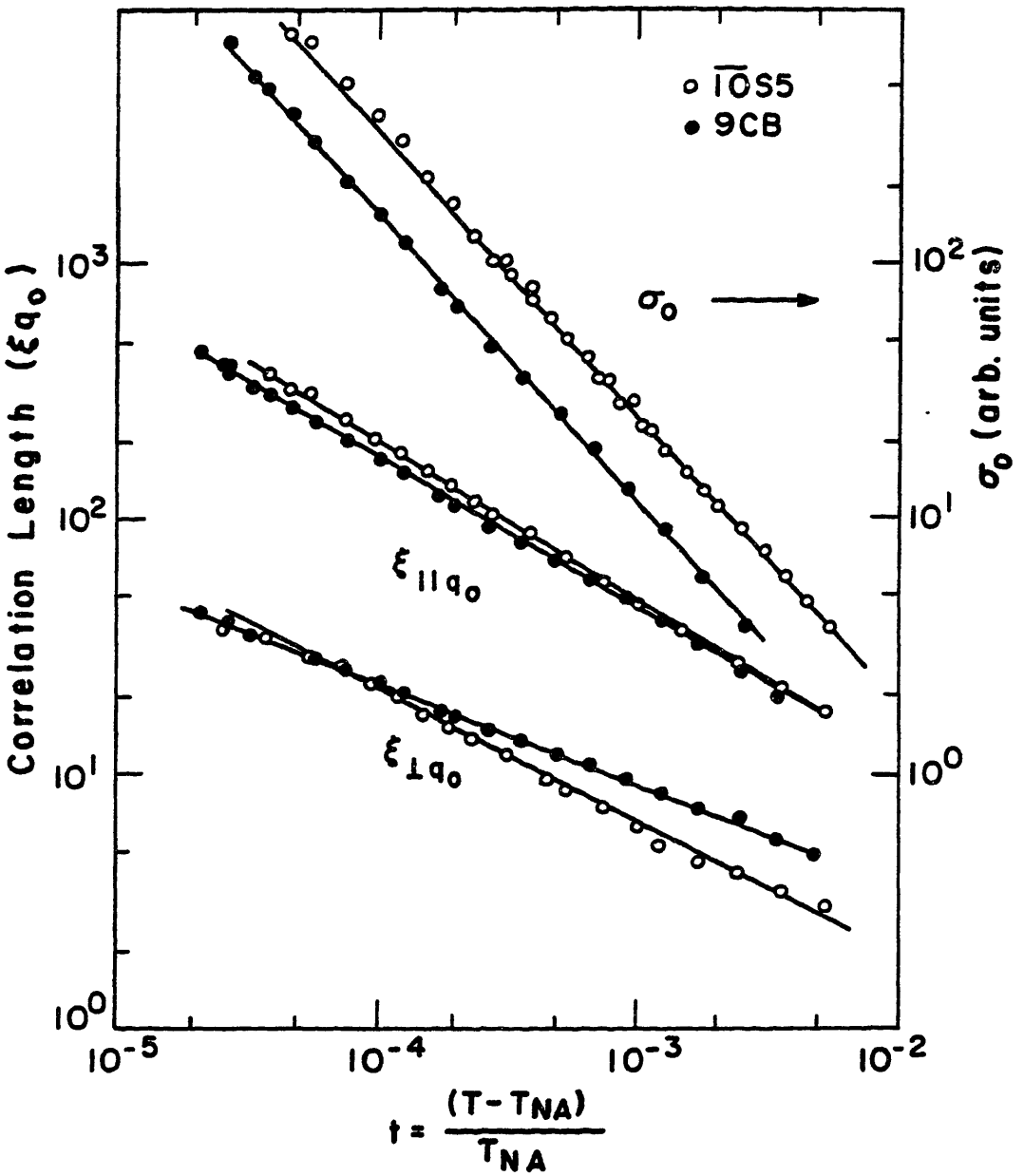

Figure 6.0.1

Longitudinal correlation length ($\xi_{\parallel}$), transverse correlation length ($\xi_{\perp}$), and susceptibility (σ_0) in 9CB and $\overline{10}$S5. The susceptibility has been adjusted for graphical purposes. The straight lines are power law fits as described in chapter 5.

The observed anisotropy in the critical exponents may be the result of divergent phase fluctuation characterizing the smectic A phase. To incorporate this feature, Lubensky and coworkers have transformed to a frame with well behaved fluctuations. In this frame the behavior is isotropic, but the transformation back to the physical frame introduces a crossover for $\nu_\perp$ from $\nu_{\parallel}$ to $\nu_{\parallel}/2$. This crossover adequately describes $\xi_\perp$, albeit with $\nu_{\parallel} \neq \nu_{XY}$, however, the appropriate hyperscaling relation is violated. Improved light scatting experiments might play an important role in determining whether the $N \rightarrow S_A$ transition is inherently isotropic since this theory predicts K_2, K_3, B, and D should scale as $t^{-\nu_{\parallel}}$. There are no quantitative predictions for $\xi_{\parallel}$ and $\xi_\perp$ in the dislocation model except $\nu_{\parallel} = 2\nu_\perp$ close to the transition.

The critical scattering is nearly Lorentzian, albeit anisotropic, with the profile widths inversely proportional to the correlation lengths $\xi_{\parallel}$ and $\xi_\perp$. Along the transverse direction the scattering always falls off faster than a Lorentzian, especially for large t and for samples with short nematic ranges. To incorporate this feature we have modified the Lorentzian to include either a $q_\perp^4$ term or a power law correction. For both cases the absolute value of $\xi_\perp$ varies with the profile shape but not the critical exponents. However, it is difficult to determine the exact line-shape after convolution in the vertical direction because the current experimental configuration effectively integrates over this component. To determine the precise scattering profile measurements must be performed with better vertical resolution ($\sim 0.005 \text{Å}^{-1}$). A comprehensive theory of the $N \rightarrow S_A$ transition must incorporate the non-Lorentzian scattering profile, perhaps through

the scaling relationship $\gamma=\nu(2-\eta)$ along both directions.

As yet, there are no detailed light scattering measurements in the neighborhood of the $N \rightarrow S_A$ tricritical point. Measurements of K_2 would be of particular interest in 9CB since anisotropic scaling predicts that K_2 should diverge with a critical exponent of $2\times0.37-0.57=0.17\pm0.12$, a rather small number. On the smectic side, the x-ray scattering saturates much more rapidly below the transition in 9CB than other materials studied. Therefore, one might expect anomalous behavior for B and D. Detailed measurements of the nematic order parameter at the tricritical point should help elucidate the coupling between S and ψ.

In summary, the critical exponents and correlation lengths evolve with the average chain length of the liquid crystal molecules. This appears to be consistent with a crossover from critical to tricritical behavior. At all concentrations the critical behavior is anisotropic, that is $\nu_{\parallel}\neq\nu_{\perp}$. There is no theory which properly explains the entire behavior of the $N \rightarrow S_A$ transition from the critical to tricritical region.

Appendix 1

Resolution Functions and convolutions with S(q)

As described in section 1.2, the resolution function can be separated into three orthogonal components the directions of which correspond to the principal axis of the spectrometer. Let us define x-y to be the spectrometer plane and z the direction normal to this plane. The scattering vector has two components, $q_{\parallel}$ and $q_{\perp}$, where we define $q_{\parallel}$ to lie along y and $q_{\perp}$ to lie in the x-z plane. To simplify the analysis, all q vectors are normalized at $q=q_{\parallel}^{o}$. The resolution function is given by

$$R^{n}(q)=R_{x}(q_{x})\ R_{y}^{n}(q_{y})\ R_{z}(q_{z}) \qquad \text{A.1}$$

where

$$R_{x} = \delta(q_{x}) \qquad \text{A.2}$$

$$R_{z} = \frac{1-|q_{z}|/\Delta}{2\Delta} \qquad \text{A.3}$$

and

$$R_{y}^{n}(q_{y})=E_{y}^{n}(q_{y})*A_{y}(q_{y}) \qquad \text{A.4}$$

where n=1,2 corresponding to copper $K_{\alpha 1}$ and $K_{\alpha 2}$. The dispersive element of the resolution E_{y}^{n} originates from the energy spectrum of the copper lines which is intrinsically Lorentzian. The arm zero profile A_{y} is non-dispersive and is either modeled by a pure Lorentzian or the sum of three Lorentzians.

The convolution of two Lorentzians is also a Lorentzian where the widths simply add. That is, if

$$f(x) = \frac{\pi/a}{a^2 + (x-x_a)^2} \qquad \text{A.5}$$

and

$$g(x) = \frac{\pi/b}{b^2 + (x-x_b)^2} \qquad \text{A.6}$$

are two normalized Lorentzians with widths a and b and peak positions x_a and x_b then the convolution is given by

$$h(x) = f(x)*g(x) = \frac{(a + b)/\pi}{(a + b)^2 + (x-x_a-x_b)^2} \qquad \text{A.7}$$

where h(x) is also a normalized Lorentzian with width (a + b) and peak position x_a+x_b.

To calculate the scattering intensity the line-shape must be convoluted with the resolution function

$$I(q) = S(q)*R(q) = \int d^3q' \; S(q-q')R(q') \qquad \text{A.8}$$

where S(q) is given by Eq 5.01 and Eq 5.02. Both reduce to

$$S(\vec{q}) = \frac{\sigma_0/\xi_{11}^{\;2}}{(q_y-q_{11}^{\;0})^2 + W(q_x,q_z)} \qquad \text{A.9}$$

where

$$W(q_x,q_z) = \frac{1 + (q_x^{\;2} + q_z^{\;2})\xi_\perp^2\{1 + c(q_x^{\;2} + q_z^{\;2})\xi_\perp^2\}}{\xi_{11}^2} \qquad \text{A.10}$$

for the Lorentzian with the fourth order correction and

$$W(q_x,q_z) = \frac{(1 + (q_x^{\;2} + q_z^{\;2})\xi_\perp^2)^{1-\eta_\perp/2}}{\xi_{11}^2} \qquad \text{A.11}$$

for the Lorentzian with a power law correction.

The convolution procedure is as follows. First, $R_y^n(q_y)$ is calculated for both $K_{\alpha 1}$ and $K_{\alpha 2}$. Specifically, E^n is convoluted with the arm-zero profile which is the sum of three Lorentzians. Because of

the two K_α peaks, $R_y(q_y)$ is characterized by six Lorentzians. These need only be calculated once since the resolution does not vary. Then, each Lorentzians is convoluted with S(q) to obtain the parameters for the new Lorentzians without explicitly evaluating S(q). The intergration over the vertical is performed by a variable step size algorithm developed by Mark Sutton. By adjusting the parameters, the fitting routine minimizes the χ^2 between the data and the line-shape. The C language line-shape subroutine is presented starting on the next page.

```
#include "/usr/gasfit/fitdefn.h"
#include "/usr/gasfit/fitext.h"
# define GAUSS .84932 /* converts half width to Gaussian width*/
# define PI 3.14159
# define NVERT 4. /* number of half widths in the vertical*/
# define IO fpar[0].p_b
# define ZPAR fpar[1].p_b
# define RATIO fpar[2].p_b
# define H1  fpar[3].p_b
# define H2 H1 *(1. + SALPHA)
# define DK (dp->d_k - fpar[4].p_b)
# define FOURTH fpar[5].p_b
# define QVERT fpar[6].p_b
# define RALPHA fpar[7].p_b
# define SALPHA fpar[8].p_b
# define RES fpar[9].p_b
# define ABS fpar[10].p_b
# define DELRES fpar[12].p_b
struct lorent {
        double wid;
        double pos;
        double norm;
        };
struct lorent armz;
struct lorent e1; /* alpha 1 energy broadening*/
struct lorent e2; /* alpha 2 energy broadening*/
struct lorent res1; /*armzero convoluted with e1*/
struct lorent res2; /*armzero convoluted with e2*/
struct lorent shape;
struct lorent shape1; /* linshape convoluted with the res1*/
struct lorent shape2; /* linshape convoluted with the res2*/
extern char *bufr;
struct initial initial[]{
        "peak amplitude",0,
        "longitudinal len",0,
        "ratio: of lengths",0,
        "long peak pos",0,
        "trans peak pos",0,
        "coeff: 4th order trm",0,
        "vertical(HWHM)",0,
        "ratio:alpha2 to1",0,
        "rel sep of alpha ",0,
        "resolution hwhm",0,
        "Absorption lengths",0,
        "Integration Error",0,
        "Res. displacement",0,
        };
int nmax 13;
double model(deriv)
int deriv;
{
        double vconv(),modl,cos(),exp(),varint();
        int err;
        if(fpar[7].p_fit == 1) resolution();
```

```
        modl=IO * varint(vconv,0.0,1.0,fpar[11].p_b,&err) ;
        dp->d_mmb =modl;
        dp->d_dmb =dp->d_y;
        return(modl);
}
double vconv(qv)
        double qv;
        {
        double gauss(),crossec(),triang(),square();
        return( triang(qv) * crossec(qv) );
        }
double gauss(qv)
double qv;
        {
        double tempv, exp(), sqrt();
        tempv = qv/( GAUSS * QVERT);
        tempv = sqrt(2. / PI ) * exp( -.5 * tempv * tempv) / (GAUSS * QVERT);
        return(tempv);
        }
double triang(qv)
double qv;
        {
        double tempv;
        if( qv > (2 * QVERT)) tempv =0;
        else tempv = ( 1. - .5 * qv / QVERT )/ QVERT;
        return(tempv);
        }
double square(qv)
double qv;
        {
        double tempv;
        if( qv > QVERT) tempv =0;
        else tempv = 1./ QVERT;
        return(tempv);
        }
double crossec(l)
        double l;
        {
        double zperp2 ,sqrt(),loreval(),summ;
        zperp2 = ZPAR * RATIO ;
        zperp2 = zperp2 * zperp2 * ( DK * DK  + l * l);
        shape.wid = sqrt(1. + zperp2 * (1. + FOURTH * zperp2))/ ZPAR ;
        if( DELRES <= 1e-5 || ZPAR <= .1/RES){
                if(ZPAR <= .2/SALPHA){
                        shape.norm = 1 +RALPHA;
                        shape.pos= ( H1 + RALPHA * H2)/(1. + RALPHA);
                        lorcon(&shape,&res1,&shape1);
                        summ = loreval( dp->d_h ,&shape1) ;
                        return(summ);
                        }
                else{
                        shape.norm = 1.;
                        shape.pos = H1  ;
                        lorcon(&shape,&res1,&shape1);
                        shape.pos = H2 ;
                        lorcon(&shape,&res2,&shape2);
```

```
                        summ = loreval( dp->d_h ,&shape1) + loreval( dp->d_h ,&shape2);
                        return(summ);
                        }
                }
        else{
                shape.norm = 1./3.;
                shape.pos = H1  + DELRES ;
                lorcon(&shape,&res1,&shape1);
                shape.pos = H2 + DELRES ;
                lorcon(&shape,&res2,&shape2);
                summ = loreval( dp->d_h ,&shape1) + loreval( dp->d_h ,&shape2);
                shape.pos = H1  - DELRES;
                lorcon(&shape,&res1,&shape1);
                shape.pos = H2 - DELRES ;
                lorcon(&shape,&res2,&shape2);
                summ = summ+loreval( dp->d_h ,&shape1)+loreval( dp->d_h ,&shape2);
                shape.pos = H1  ;
                lorcon(&shape,&res1,&shape1);
                shape.pos = H2 ;
                lorcon(&shape,&res2,&shape2);
                summ = summ+loreval( dp->d_h ,&shape1)+loreval( dp->d_h ,&shape2);
                return(summ);
                }
        }
double lpfact(ddp)
struct data *ddp;

{
        double vc,cosphi,exp(),cos();
        cosphi = cos(ddp->d_phi);
        vc = cosphi * exp(ABS*(1./cosphi -1.));
        ddp->d_y = vc * ddp->d_y ;
        ddp->d_w =/vc;
        if ( dp == data ){
                resolution();
                }
        return(1.);
}
double back()
{return (0.);}
resolution(){
        armz.wid= RES ;
        armz.pos=0;
        armz.norm = RES / PI ;
        e1.wid = 1.9e-4;
        e1.pos = 0;
        e1.norm = e1.wid/ ( PI * ( 1+ RALPHA ));
        e2.wid = 2.5e-4;
        e2.pos = 0;
        e2.norm = RALPHA * e2.wid / ( PI * ( 1+ RALPHA ));
        lorcon(&armz,&e1,&res1);
        lorcon(&armz,&e2,&res2);
}
lorcon(l1,l2,l3)
struct lorent *l1;
struct lorent *l2;
```

```
struct lorent *l3;
{
        l3->wid = l1->wid +l2->wid;
        l3->norm = PI * l1->norm * l2->norm *l3->wid;
        l3->norm = l3->norm/(l1->wid * l2->wid);
        l3->pos = l1->pos + l2->pos;
}
double loreval(qpos,l4)
struct lorent *l4;
double qpos;
        {
        qpos = l4->norm/(l4->wid * l4->wid + (qpos - l4->pos)*(qpos - l4->pos));
        return(qpos);
        }
lorprint(lorp,l5)
struct lorent *l5;
char *lorp;
{
        write(1,lorp,5);
        printf("  %f %f %f 0, l5->wid, l5->pos, l5->norm);
}
#define STAKSIZ 50              /*size of stack in varint().  Finest mesh will be
                                 *length of interval divided by 2**(STAKSIZ/2) */

/*
*Variable step size integration routine
*Works by comparing 2-point integration results with 3-point results
*If the error of the integral over the segment is greater
*than "abser" the interval is split into 2 and the test is repeated
*for each side, and so on recursively.
*varint() is very sensitive to high frequency fluctuations.  It is
*OK to have a sharp function only if it peaks at one of the end
*points or the middle.  Otherwise, varint should be called several
*times, with the integral broken up so the wavelength of fluctuations
*is larger than or on the order of the size of the segment

                func    function
                a       beginning point
                b       end point
                relerr  estimate of allowed per centage error
                err     pointer to return error message and number
                        of function calls made. (error if < 0 )

*/
double varint(func,leftpt,rightpt,relerr,err)
double (*func)(),leftpt,rightpt,relerr;
int *err;
{
        double int1, int2, h, fnew, bnew, sum, fa, fb, abser;
        int stakflo, fncalls;
        float stack[STAKSIZ];
        double fabs();
        register float *ptr;
        float *end;
        sum = 0.;
        stakflo = 0;
```

Portions of the text
on the following page(s)
are not legible in the
original.

```
        ptr = stack;
        end = &stack[STAKSIZ];
        if(rightpt == leftpt) {
                *err = 0;
                return(0.0);
                }
        fa = (*func) (leftpt);
        fb = (*func) (rightpt);
        fncalls = 2;
        abser = fabs(relerr * (fa + fb) * (rightpt - leftpt));
        while(1){
                /*calculate new width of integration, middle, value at middle*/
                h = (rightpt - leftpt) / 2.;
                bnew = leftpt + h;
                fnew = (*func)(bnew);
                fncalls++;
                int1 = (fa + fb) * h;
                int2 = int1 / 2. + fnew * h;
                /*compare results of 2-point and 3-point integration*/
                if((fabs(int1-int2) <= abser) || (ptr >= end)){
                        if(ptr >= end){
                                if(!stakflo)
                                printf("Ran out of stack space.  a = %f, b = %f0,leftpt,rightpt);
                                stakflo = 1;
                        }
                        /*this sub-integral is good enough*/
                        sum += int2;
                        if(ptr==stack) {
                                /*we have reached the top of the stack--integral done*/
                                /*left-hand endpoint is old right-hand endpoint
                                /*pull new right-hand endpoint off stack*/

                                *err = stakflo ? -fncalls : fncalls;
                                return (sum);
                                }

                        fa = fb;
                        leftpt = rightpt;
                        fb = *(--ptr);
                        rightpt = *(--ptr);
                }
                else{   /*Error too large.  Subdivide further*/
                        /*Stick right hand end point onto stack.  New right
                        *hand end point is old middle point*/
                        *(ptr++) = rightpt;
                        *(ptr++) = fb;
                        fb = fnew;
                        rightpt = bnew;
                }
        }
}
```

APPENDIX 2: Experimental Configuration

Sample	Date	Source	Preparation	Cell	Oven Windows	Gas/ vacuum	Field kGauss	q_{11} °A^{-1}	set-up	mosaic HWHM	T_{NA} °C	T_{NI} °C	T_{NA}(°K)/T_{NI}(°K)	drift °C/day
40.7	1/81	Organix	pumped	Be/Al	Kptn	air	4	0.2333	Si	0.05	54.93	83.0	0.921	0.002
40.7	10/81	Goodby	pumped	Kptn/Al	Kptn	Ar	4	0.2339	Si	0.05	56.33	83.0	0.925	0.002
609	4/83	Kent	none	Be/Al/Silane	Be	N_2	7	0.2038	Si &Ge	0.02	40.12	64.0	0.929	0.001
8.5S5	10/82	Kent	none	Be/Al/Silane	Be	N_2	2/4	0.2188	Si	0.10	68.50	85.1	0.954	0.005
9S5	12/81	Kent	pumped	Be/Al	Kptn	air	4	0.2156	Si	0.25	72.70	84.5	0.967	0.050
9.75S5	11/82	Kent	none	Be/Al/Silane	Be	N_2	4	0.2099	Ge & Si	0.35	78.72	85.60	0.981	0.005
10S5	8/82	Kent	none	Be/Al/Silane	Be	N_2	4	0.2080	Ge & Si	0.20	80.45	86.0	0.984	0.005
10.2S5	7/83	Kent	none	sealed Be	Be	air	7	0.2066	Ge	0.40	81.40	86.0	0.987	0.005
10.4S5	8/82	Kent	none	Be/Al	Be	N_2	4	0.2052	Ge	1.0	81.82	85.9	0.989	0.005
11S5	7/82	Kent	pumped	Be/Al/Silane	Be	N_2	4	0.2008	Ge	0.90	83.50	85.6	0.994	?
8CB	6/83	BDH	none	sealed Be	Be	air	1/7	0.1989	Ge	0.10	33.93	40.5	0.979	0.002
9CB	4/83	BDH	none	Be/Al	Be	vacuum	1/7	0.1865	Ge	0.20	47.82	49.8	0.994	0.010
9.05CB	5/83	BDH	none	Be/Al	Be	vacuum	7	0.1860	Ge	0.20	48.10	49.8	0.995	0.010
9.09CB	5/83	BDH	none	Be/Al	Be	vacuum	7	0.1854	Ge	0.30	48.33	49.8	0.995	0.010
9.14CB	5/83	BDH	none	Be/Al	Be	vacuum	7	0.1849	Ge	0.40	48.62	49.8	0.996	0.010
9.20CB	6/83	BDH	none	sealed Be	Be	air	7	0.1845	Ge	0.40	48.80	49.8	0.997	0.010
9.28CB	6/83	BDH	none	sealed Be	Be	air	7	0.1837	Ge	0.40	49.20	49.8	0.998	0.010
60.8	3/83	Organix	recryst	Be/Al/Silane	Be	N_2	7	0.2110	Ge	0.75	81.86	82.7	0.998	0.010

SYMBOLS:
Be-beryllium
Al-aluminum
Silane-silane coated
Kptn-Kapton
Si-silicon (111) spectrometer
Ge-germanium (111) spectrometer

Appendix 3

X-ray scattering measurements were performed in 60.8 to better our understanding of strongly first order $N \rightarrow S_A$ transitions. Of all the samples studied, 60.8 has the shortest nematic range 0.8°C with a corresponding McMillan ratio T_{NA}/T_{NI}=0.998. The 60.8 sample was obtained from Organix and recrystalized twice with light petrol(60-40). To minimize the transition temperature drifts, measurements were performed in the beryllium window oven under nitrogen gas. Initial measurements utilized the germanium set-up (chapter 4.1), however, the scattering was very weak since the scattering profile is broad, that is, the correlation lengths are small. To increase the counting rates, a LiF(220) analyzer crystal was used in place of the germanium analyzer, this degrades the resolution by an order of magnitude, however, the scattering remains broader than the resolution in the nematic phase.

In figure A3.1 (bottom) the $(0,0,q_{11}^{o})$ scattering intensities are shown from the isotropic phase through the nematic A phase to the smectic phase. The intensity only varies by a factor of ~ 2 over the entire nematic range. Heat capacity measurements (a.c.) in 60.8 are shown in the top panel of the same figure. The transition temperatures and the coexistence ranges agree absolutely. There is no indication of any precritical behavior at either the $N \rightarrow S_A$ or the $N \rightarrow I$ transitions.

In figure A3.2 the integrated $(0,0,q_{11}^{o})$ peak intensity is shown at the $N \rightarrow S_A$ transition. Note that the intensity does not increase linearly with temperature. In contrast, the peak intensity at the $N \rightarrow I$ transition, which is also first order, does have a simple linear relationship as shown in figure A3.3. This behavior is consistent with

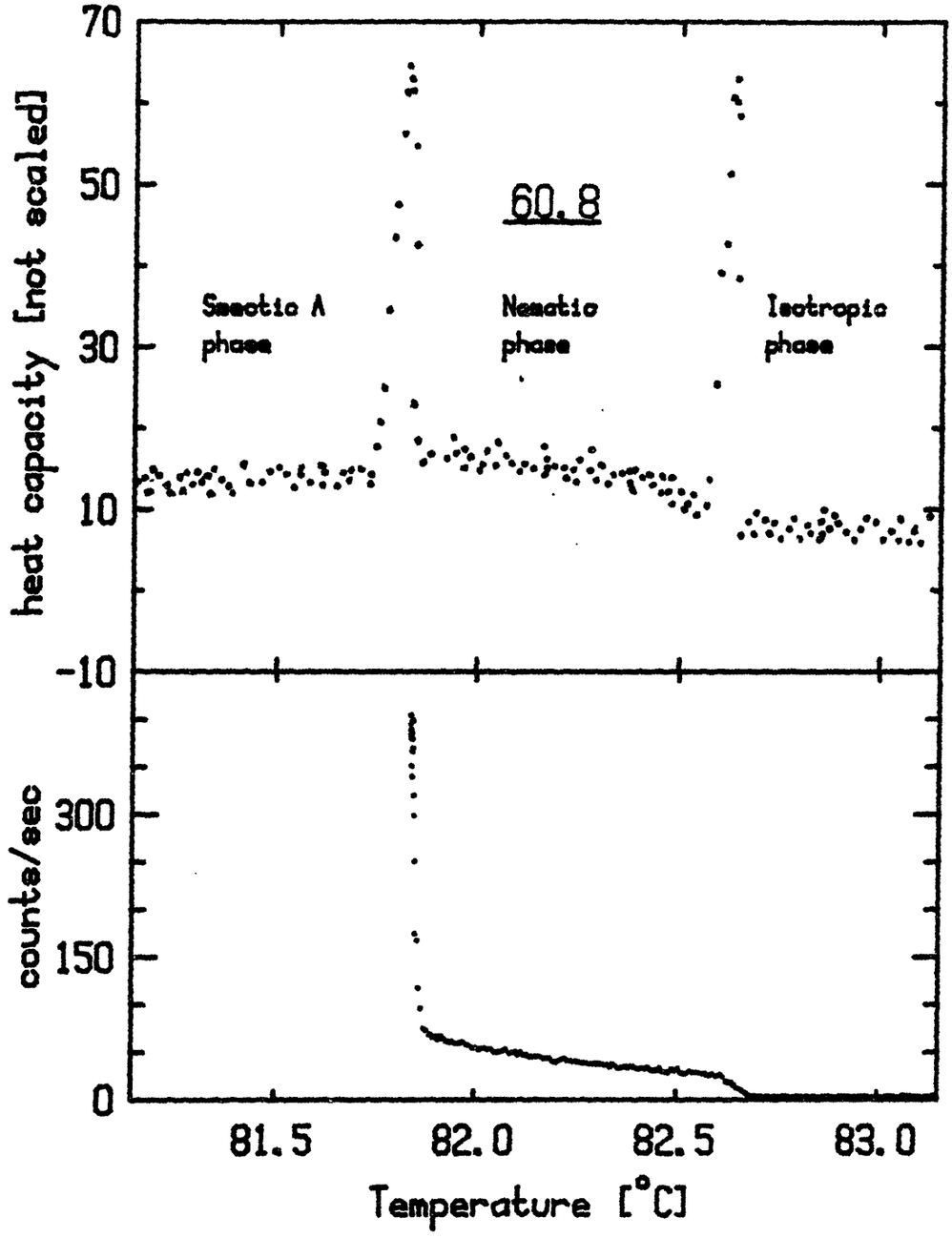

Figure A3.1

Top: Heat capacity results in 60.8.
Courtesy of C. Chiang and C.W. Garland.

Bottom: Peak x-ray scattering intensity at $(0,0,q_{11}^{o})$ in 60.8.

a coexistence region with a simple tradeoff between the nematic and isotropic phases.

The scattering line-shape evolves only slightly throughout the entire nematic phase in 60.8. In figure A3.4 typical longitudinal and transverse scans are shown at $T=T_{NA}+0.020°C$ and at $T=T_{NA}+0.32°C$. The line-shape widths only change by -50% for the two scans shown.

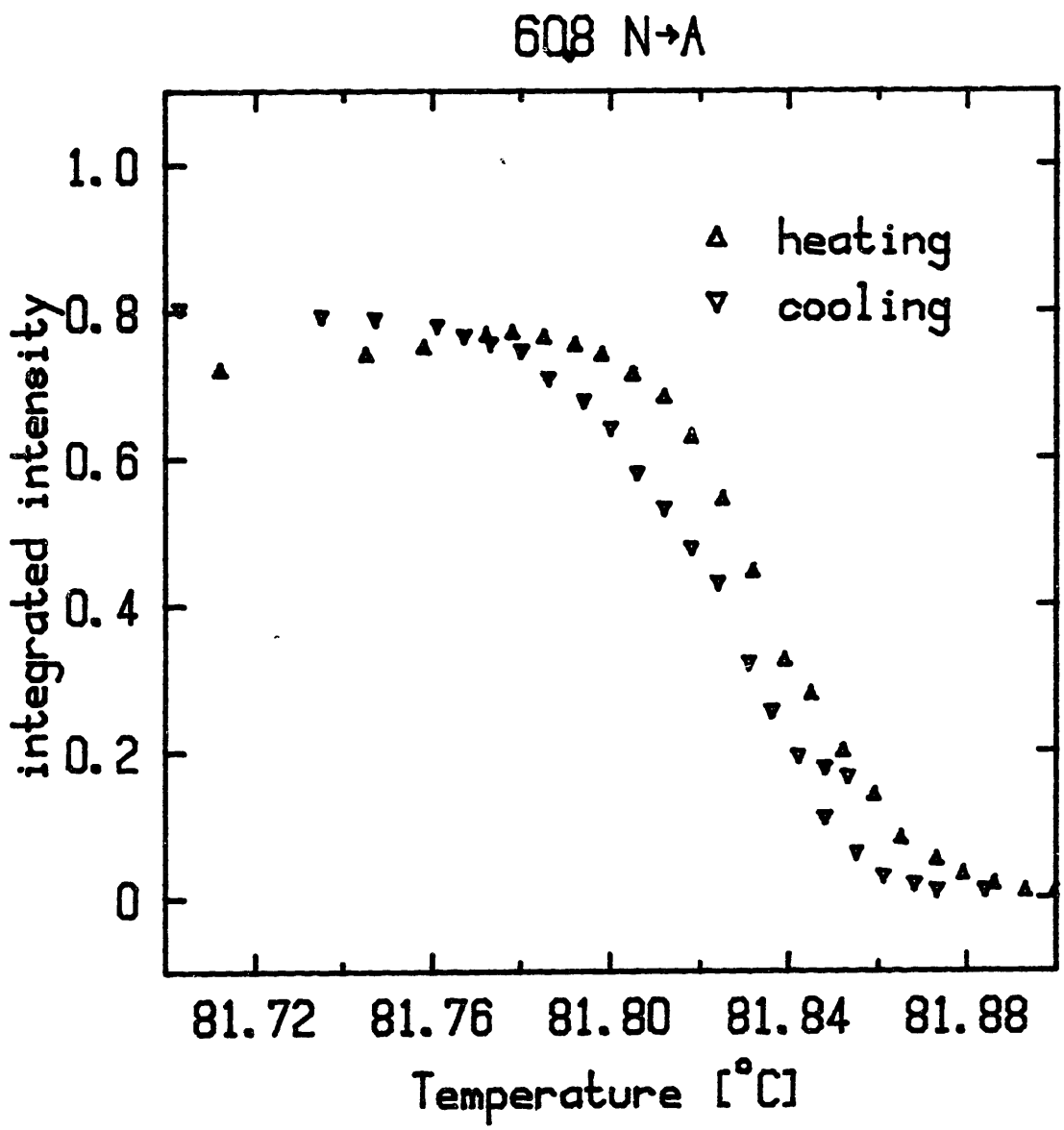

Figure A3.2

Integrated $(0,0,q_{11}^{o})$ intensity at the $N \rightarrow S_A$ transition in 60.8.

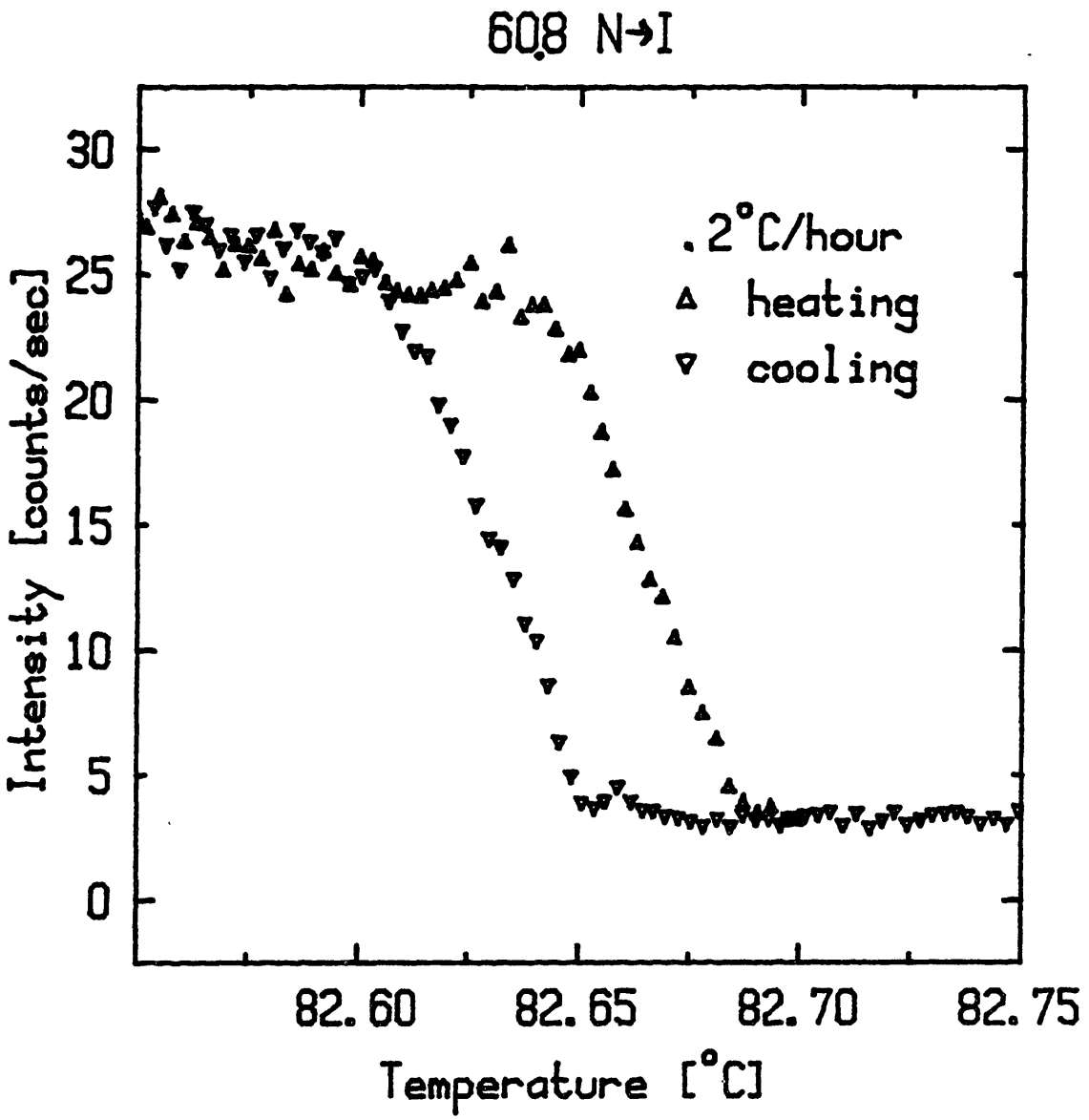

Figure A3.3

Peak intensity corresponding to the $(0,0,q_{11}^{o})$ position in 60.8.

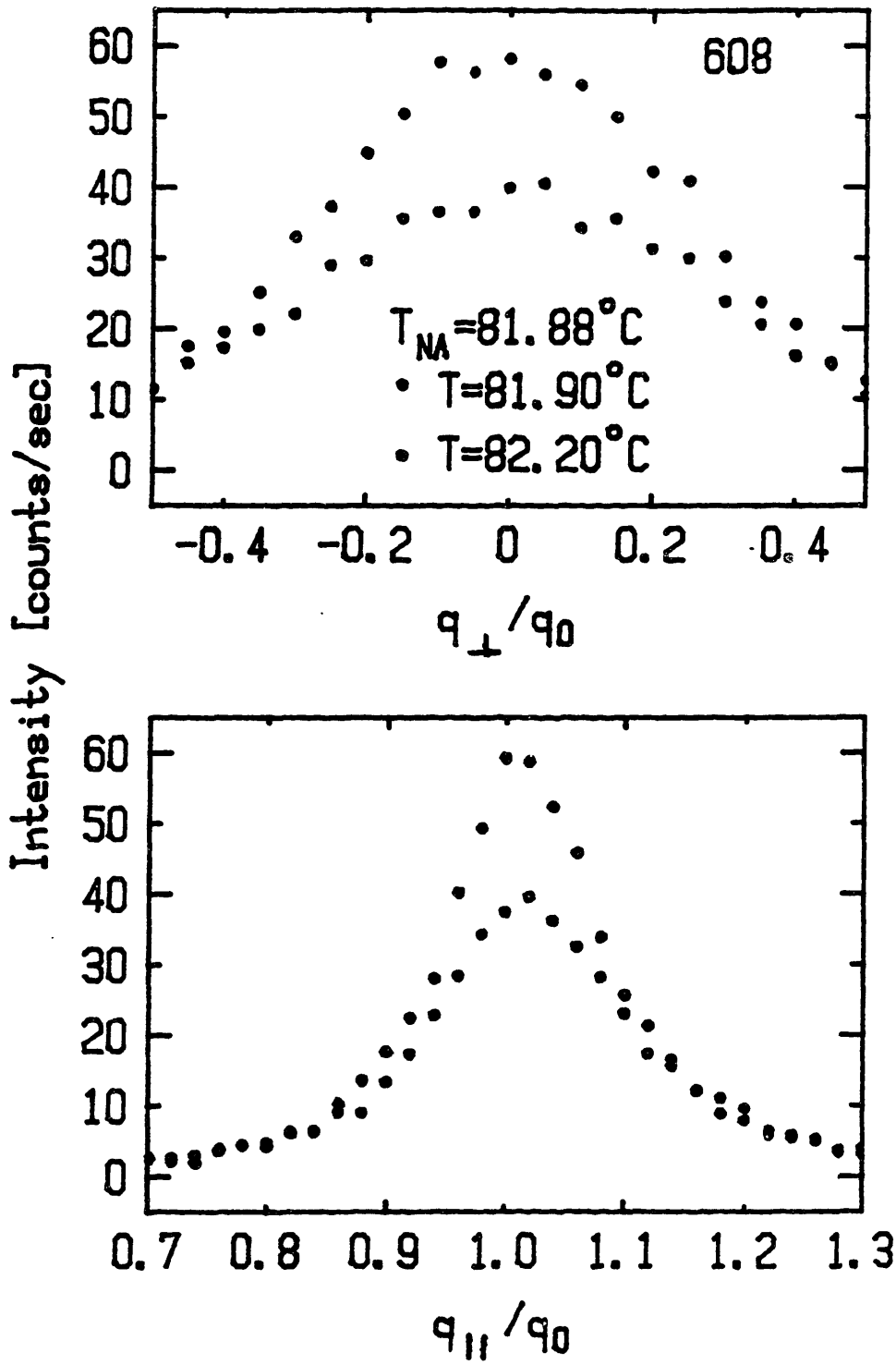

Figure A3.4

Transverse scans (top) and longitudinal scans (bottom) through $(0,0,q_{\parallel}^{\circ})$ in 60.8. Note that the profile only evolves slightly with temperature.

Appendix 4

Summary of Experimental Results

The following pages contain tables of the correlation lengths ($\xi_{\parallel}$ and $\xi_{\perp}$) the susceptibility (σ_0) and the fourth order correction term (c) obtained by fitting the data to Equation 5.0.1 convoluted with the resolution function. Each page contains the fits for one sample whereas each line of the table represents the parameters obtained by simultaneously fitting the longitudinal and transverse scans at a given temperature. The associated weights are the inverse of the one standard deviation errors.

40.7

T	T_{NA}	t	χ^2	σ_0	$\xi_{\parallel}$	$\xi_{\perp}$	c	$w(\sigma_0)$	$w(\xi_{\parallel})$	$w(\xi_{\perp})$	$w(c)$
56.4020	56.3500	1.5782e-04	-	2.52e+04	1.43e+03	7.12e+01	8.40e-03	7.27e-01	1.82e-02	2.32e-01	6.67e+02
56.4240	56.3500	2.2459e-04	-	1.45e+04	1.07e+03	5.51e+01	1.10e-02	1.53e-03	3.03e-02	3.61e-01	5.00e+02
56.4420	56.3500	2.7922e-04	-	1.16e+04	9.59e+02	5.27e+01	7.20e-03	2.07e-03	3.70e-02	4.09e-01	7.69e+02
56.4660	56.3500	3.5205e-04	-	7.96e+03	8.00e+02	4.24e+01	1.50e-02	2.82e-03	4.17e-02	4.51e-01	3.33e+02
56.7550	56.3550	1.2139e-03	-	1.58e+03	3.19e+02	2.09e+01	2.35e-02	2.35e-02	1.75e-01	1.36e+00	2.78e+02
56.8950	56.3550	1.6388e-03	-	1.02e+03	2.52e+02	1.71e+01	3.02e-02	4.22e-02	2.63e-01	1.96e+00	2.33e+02
57.0880	56.3550	2.2246e-03	-	6.30e+02	1.93e+02	1.38e+01	4.00e-02	6.19e-02	3.16e-01	1.95e+00	1.39e+02
57.3400	56.3550	2.9893e-03	-	4.01e+02	1.52e+02	1.14e+01	4.60e-02	9.87e-02	4.10e-01	2.26e+00	1.11e+02
57.6700	56.3550	3.9908e-03	-	2.64e+02	1.21e+02	1.00e+01	3.60e-02	1.44e-01	5.00e-01	2.45e+00	1.14e+02
58.1200	56.3550	5.3565e-03	-	1.60e+02	9.34e+01	7.62e+00	8.50e-02	2.32e-01	6.67e-01	2.97e+00	5.26e+01
56.4700	56.3650	3.1865e-04	-	1.06e+04	8.92e+02	4.93e+01	7.00e-03	2.47e-03	4.17e-02	4.51e-01	1.00e+03
56.5070	56.3650	4.3093e-04	-	6.83e+03	6.93e+02	4.05e+01	8.40e-03	4.17e-03	5.88e-02	5.93e-01	7.69e+02
56.5500	56.3650	5.6142e-04	-	4.50e+03	5.54e+02	3.32e+01	1.20e-02	6.53e-03	7.69e-02	7.50e-01	5.00e+02
56.6100	56.3650	7.4351e-04	-	3.15e+03	4.53e+02	2.85e+01	1.20e-02	1.10e-02	1.11e-01	9.80e-01	5.88e+02
56.6900	56.3650	9.8629e-04	-	1.95e+03	3.52e+02	2.25e+01	1.94e-02	1.93e-02	1.67e-01	1.36e+00	3.92e+02
58.7200	56.3500	7.1927e-03	-	9.66e+01	7.65e+01	6.04e+00	1.70e-01	3.40e-01	7.14e-01	3.40e+00	2.70e+01
59.5200	56.3500	9.6206e-03	-	6.06e+01	5.80e+01	5.07e+00	1.86e-01	4.23e-01	7.69e-01	2.99e+00	1.69e+01
60.6000	56.3500	1.2898e-02	-	4.09e+01	4.80e+01	4.70e+00	1.29e-01	1.44e-01	1.00e+00	3.63e+00	2.38e+01
61.9400	56.3500	1.6965e-02	-	2.54e+01	3.80e+01	3.72e+00	2.70e-01	1.01e+00	1.18e+00	3.51e+00	1.00e+01
64.0100	56.3500	2.3247e-02	-	1.44e+01	2.80e+01	2.97e-01	3.38e-01	1.38e+00	1.25e+00	3.84e+00	4.55e+00
56.3580	56.3320	7.8915e-05	-	8.83e+04	2.46e+03	1.34e+02	1.60e-03	1.81e-04	1.00e-02	9.87e-02	3.77e+03
56.3620	56.3320	9.1048e-05	-	5.64e+04	2.04e+03	1.05e+02	3.10e-03	3.09e-04	1.15e-02	1.24e-01	2.70e+03
56.3720	56.3320	1.2141e-04	-	4.21e+04	1.78e+03	9.68e+01	3.20e-03	5.78e-04	1.59e-02	1.64e-01	2.38e+03
56.3790	56.3320	1.4265e-04	-	3.60e+04	1.62e+03	8.75e+01	3.85e-03	6.78e-04	1.75e-02	2.89e-01	2.10e+03
56.3840	56.3330	1.5478e-04	-	3.20e+04	1.54e+03	8.35e+01	3.86e-03	6.73e-04	1.67e-02	1.83e-01	2.07e+03
56.3930	56.3330	1.8211e-04	-	2.44e+04	1.30e+03	7.42e+01	5.00e-03	9.86e-04	2.22e-02	2.29e-01	1.75e+03
56.3970	56.3330	1.9424e-04	-	2.27e+04	1.27e+03	7.17e+01	5.47e-03	1.08e-03	2.33e-02	4.88e-02	1.56e+03
56.4120	56.3340	2.3673e-04	-	1.71e+04	1.09e+03	6.14e+01	7.20e-03	1.53e-03	2.94e-02	2.92e-01	1.11e+03
56.4200	56.3340	2.6101e-04	-	1.49e+04	1.01e+03	5.64e+01	8.00e-03	2.02e-04	3.03e-03	5.06e-02	1.00e+03
56.4280	56.3340	2.8530e-04	-	1.25e+04	9.29e+02	5.30e+01	8.60e-03	2.04e-03	3.33e-02	3.47e-01	1.06e+03

T	T_{NA}	t	χ^2	σ_0	$\xi_{\parallel}$	$\xi_{\perp}$	c	$w(\sigma_0)$	$w(\xi_{\parallel})$	$w(\xi_{\perp})$	w(c)
55.5500	40.1100	4.9288e-02	4.13	1.09e+01	1.94e+09	1.26e+09	2.50e-01	5.94e-01	1.58e+00	3.68e+00	-
51.8890	40.1100	3.7601e-02	6.46	2.10e+01	6.08e+08	8.30e+08	2.50e-01	3.51e-01	1.21e+00	3.69e+00	-
49.1020	40.1100	2.8705e-02	7.85	3.61e+01	1.80e+09	1.37e+09	2.50e-01	2.51e-01	1.11e+00	4.03e+00	-
46.8890	40.1100	2.1640e-02	10.77	6.10e+01	9.59e+08	6.20e+07	2.50e-01	1.70e-01	9.48e-01	4.07e+00	-
45.4530	40.1100	1.7056e-02	10.99	9.45e+01	3.73e+08	5.97e+08	2.50e-01	1.34e-01	9.10e-01	4.39e+00	-
44.1010	40.1100	1.2740e-02	14.74	1.47e+02	2.53e+08	9.37e+08	2.50e-01	9.04e-02	7.50e-01	4.10e+00	-
42.9050	40.1100	8.9223e-03	14.02	2.51e+02	1.23e+08	1.12e+08	2.50e-01	6.60e-02	6.96e-01	4.38e+00	-
42.3050	40.1100	7.0070e-03	11.89	3.56e+02	4.41e+08	2.67e+08	2.50e-01	3.59e-02	4.64e-01	3.17e+00	-
40.9550	40.1100	2.6974e-03	6.65	1.39e+03	8.46e+08	1.00e+09	9.71e-02	1.12e-02	2.24e-01	1.48e+00	5.95e+01
40.1320	40.1250	2.2344e-05	10.30	2.35e+05	1.01e+09	1.68e+09	4.81e-04	1.59e-05	1.31e-03	1.96e-02	7.16e+03
40.1360	40.1250	3.5118e-05	7.56	1.27e+05	2.12e+09	1.68e+09	7.89e-04	3.71e-05	2.30e-03	3.32e-02	5.23e+03
40.1390	40.1250	4.4689e-05	6.83	8.94e+04	2.75e+08	2.12e+09	1.00e-03	5.65e-05	3.09e-03	4.11e-02	4.26e+03
40.1420	40.1250	5.4260e-05	6.75	6.49e+04	1.98e+09	1.47e+09	1.42e-03	8.27e-05	3.91e-03	5.14e-02	3.07e+03
40.1410	40.1250	5.1070e-05	10.45	9.30e+04	1.72e+09	4.00e+08	6.22e-04	5.64e-05	3.09e-03	4.20e-02	8.47e+03
40.1450	40.1250	6.3843e-05	9.16	6.82e+04	8.24e+08	1.83e+09	8.68e-04	8.67e-05	4.16e-03	5.58e-02	6.66e+03
40.1490	40.1250	7.6604e-05	7.32	5.09e+04	1.60e+09	1.56e+09	8.84e-04	1.36e-04	5.90e-03	7.16e-02	7.13e+03
40.1550	40.1250	9.5759e-05	6.37	3.13e+04	8.27e+08	1.97e+09	1.51e-03	2.36e-04	8.21e-03	9.87e-02	4.31e+03
40.1680	40.1250	1.3726e-04	4.78	2.10e+04	2.17e+08	1.89e+09	1.99e-03	4.05e-04	1.18e-02	1.35e-01	3.62e+03
40.1810	40.1250	1.7876e-04	5.19	1.34e+04	1.87e+09	2.00e+09	3.24e-03	6.01e-04	1.43e-02	1.60e-01	2.06e+03
40.2000	40.1250	2.3941e-04	3.56	9.68e+03	8.05e+07	1.95e+09	3.15e-03	9.78e-04	2.05e-02	2.09e-01	2.38e+03
40.2240	40.1250	3.1601e-04	2.92	6.62e+03	1.90e+09	1.95e+09	3.77e-03	1.57e-03	2.87e-02	2.70e-01	2.10e+03
40.2550	40.1250	4.1497e-04	2.21	4.21e+03	1.77e+09	4.46e+08	5.92e-03	2.80e-03	4.20e-02	3.86e-01	1.45e+03
40.2980	40.1250	5.5223e-04	1.82	2.82e+03	1.78e+09	1.55e+09	8.11e-03	4.57e-03	5.80e-02	5.08e-01	1.09e+03
40.3560	40.1250	7.3737e-04	1.85	1.86e+03	5.93e+08	1.30e+09	1.37e-02	6.75e-03	7.11e-02	6.08e-01	5.94e+02
40.4330	40.1250	9.8316e-04	1.81	1.31e+03	9.17e+08	1.02e+09	1.40e-02	9.48e-03	8.62e-02	6.87e-01	5.20e+02
40.5380	40.1250	1.3183e-03	1.87	8.50e+02	5.05e+08	1.76e+09	2.19e-02	1.40e-02	1.06e-01	8.00e-01	2.97e+02
40.1390	40.1250	4.4689e-05	11.40	1.28e+05	1.12e+09	1.01e+09	5.74e-04	3.96e-05	2.39e-03	3.53e-02	8.75e+03
40.1430	40.1250	5.7462e-05	9.98	7.08e+04	1.08e+09	8.45e+08	9.83e-04	7.91e-05	3.68e-03	5.27e-02	5.63e+03
40.1490	40.1250	7.6604e-05	6.60	5.39e+04	4.83e+08	1.51e+09	5.60e-04	1.27e-04	5.64e-03	6.47e-02	1.09e+04
40.1570	40.1250	1.0215e-04	6.92	3.22e+04	1.43e+09	2.51e+08	1.41e-03	2.25e-04	7.73e-03	9.23e-02	4.41e+03
40.1680	40.1250	1.3726e-04	5.14	1.90e+04	1.35e+09	2.07e+09	2.29e-03	4.30e-04	1.18e-02	1.35e-01	3.01e+03
40.1820	40.1250	1.8195e-04	4.18	1.28e+04	9.93e+08	1.90e+08	2.72e-03	6.90e-04	1.59e-02	1.74e-01	2.68e+03
40.6820	40.1250	1.7780e-03	2.64	5.16e+02	1.09e+09	1.65e+09	2.90e-02	3.28e-02	1.72e-01	1.22e+00	2.38e+02
40.8690	40.1250	2.3749e-03	2.19	3.30e+02	1.50e+08	5.01e+08	5.12e-02	5.38e-02	2.30e-01	1.53e+00	1.30e+02
41.1110	40.1250	3.1474e-03	2.27	2.23e+02	8.50e+08	1.70e+09	6.53e-02	7.40e-02	2.69e-01	1.64e+00	8.88e+01
41.4510	40.1250	4.2327e-03	2.13	1.40e+02	1.63e+09	1.01e+09	1.26e-01	1.12e-01	3.40e-01	1.85e+00	3.97e+01
41.8770	40.1250	5.5925e-03	1.90	9.16e+01	7.47e+08	1.82e+09	1.88e-01	1.92e-01	5.47e-01	3.64e+00	9.29e+01
42.4640	40.1250	7.4663e-03	1.70	5.87e+01	1.85e+09	1.67e+09	2.47e-01	2.37e-01	5.07e-01	2.16e+00	1.52e+01
43.0000	40.1250	9.1772e-03	1.19	4.28e+01	2.16e+08	1.88e+09	4.13e-01	3.47e-01	6.34e-01	2.45e+00	8.74e+00
42.3640	40.1250	7.1471e-03	10.68	6.32e+01	1.56e+09	9.16e+08	3.18e-01	1.13e-01	2.18e-01	1.04e+00	5.77e+00
43.0100	40.1250	9.2092e-03	8.59	4.15e+01	1.79e+09	1.50e+09	5.49e-01	1.77e-01	2.96e-01	1.15e+00	2.87e+00

8.5S5

T	T_{NA}	t	χ^2	o_o	$\xi_{\parallel}$	$\xi_{\perp}$	o	$w(o_o)$	$w(\xi_{\parallel})$	$w(\xi_{\perp})$	$w(o)$
69.1560	68.4910	1.9465E-3	0.93	1.64E2	1.12E2	9.23	1.02E-1	9.16E-2	4.31E-1	2.21	4.60E1
68.8250	68.4910	9.7763E-4	1.43	4.52E2	1.94E2	1.43E1	5.33E-2	3.23E-2	2.34E-1	1.56	1.05E2
68.7240	68.4910	6.8201E-4	1.95	7.76E2	2.54E2	1.84E1	4.10E-2	1.68E-2	1.56E-1	1.12	1.33E2
68.6650	68.4910	5.0932E-4	2.31	1.25E3	3.29E2	2.36E1	2.51E-2	9.78E-3	1.12E-1	8.58E-1	2.24E2
68.6180	68.4910	3.7173E-4	2.18	2.02E3	4.27E2	2.87E1	2.18E-2	6.33E-3	8.84E-2	7.51E-1	2.95E2
68.5840	68.4970	2.5464E-4	2.32	3.26E3	5.53E2	3.59E1	1.62E-2	3.00E-3	5.09E-2	4.55E-1	2.97E2
68.5600	68.4970	1.8439E-4	2.16	5.12E3	7.03E2	4.39E1	1.22E-2	1.98E-3	4.08E-2	3.93E-1	4.45E2
68.5420	68.4970	1.3171E-4	3.13	9.40E3	9.74E2	5.97E1	6.67E-3	8.89E-4	2.39E-2	2.44E-1	7.34E2
68.5270	68.4970	8.7806E-5	4.09	1.61E4	1.27E3	7.39E1	6.58E-3	4.45E-4	1.54E-2	1.68E-1	6.97E2
68.5230	68.4970	7.6105E-5	3.29	1.84E4	1.38E3	7.41E1	9.33E-3	5.10E-4	1.86E-2	2.19E-1	6.02E2
68.5180	68.4970	6.1456E-5	3.74	2.74E4	1.71E3	8.95E1	6.70E-3	3.01E-4	1.30E-2	1.62E-1	8.14E2
68.5120	68.4970	4.3903E-5	4.90	4.28E4	2.17E3	1.10E2	5.09E-3	1.69E-4	8.90E-3	1.16E-1	9.90E2
68.5100	68.4970	3.8052E-5	3.33	5.64E4	2.46E3	1.29E2	3.37E-3	9.22E-5	5.77E-3	7.24E-2	1.30E3
71.0450	68.4970	7.4580E-3	1.28	2.17E1	3.99E1	4.07	2.50E-1	5.47E-1	1.06	5.43	-
70.2750	68.4970	5.2042E-3	1.06	3.74E1	5.22E1	4.87	2.50E-1	4.44E-1	1.12	6.36	-
69.7640	68.4970	3.7085E-3	1.02	6.35E1	6.95E1	5.72	2.50E-1	3.56E-1	1.21	7.37	-
69.4130	68.4970	2.6811E-3	1.60	9.94E1	8.69E1	6.68	2.50E-1	1.92E-1	7.62E-1	5.32	-
72.0700	68.4970	1.0458E-2	1.14	1.32E1	3.05E1	3.45	2.50E-1	8.99E-1	1.37	6.17	-

$\overline{9S5}$

T	T_{NA}	t	χ^2	σ_0	$\xi_{\parallel}$	$\xi_{\perp}$	c	$w(\sigma_0)$	$w(\xi_{\parallel})$	$w(\xi_{\perp})$	w(c)
72.7120	72.6450	1.9376e-04	-	3.38e+03	3.85e+02	2.88e+01	2.70e-02	7.56e-03	1.00e-01	7.34e-01	5.00e+01
72.7230	72.6470	2.1977e-04	-	2.97e+03	3.52e+02	2.75e+01	2.80e-02	1.03e-02	1.30e-01	8.86e-01	2.78e+02
72.7300	72.6490	2.3424e-04	-	2.71e+03	3.40e+02	2.60e+01	3.00e-02	1.05e-02	1.25e-01	8.64e-01	2.50e+02
72.7450	72.6510	2.7184e-04	-	2.30e+03	3.08e+02	2.40e+01	3.50e-02	1.25e-02	1.43e-01	9.35e-01	2.00e+02
72.7570	72.6530	3.0076e-04	-	1.85e+03	2.73e+02	2.10e+01	5.35e-02	1.91e-02	2.00e-01	1.26e+00	1.43e+02
72.7820	72.6550	3.6726e-04	-	1.49e+03	2.43e+02	1.92e+01	5.90e-02	2.27e-02	2.13e-01	1.32e+00	1.28e+02
72.8000	72.6570	4.1354e-04	-	1.19e+03	2.14e+02	1.67e+01	8.30e-02	2.69e-02	2.33e-01	1.39e+00	8.33e+01
72.8330	72.6600	5.0026e-04	-	1.00e+03	1.94e+02	1.59e+01	7.60e-02	4.90e-02	4.00e-01	2.28e+00	1.33e+02
72.8740	72.6630	6.1015e-04	-	7.37e+02	1.64e+02	1.34e+01	1.10e-01	6.83e-02	5.00e-01	2.54e+00	8.33e+01
72.9500	72.7000	7.2286e-04	-	5.76e+02	1.40e+02	1.14e+01	1.70e-01	1.81e-02	5.00e-01	3.93e-01	5.00e+01
73.0500	72.7000	1.0120e-03	-	3.87e+02	1.14e+02	9.69e+00	2.00e-01	1.22e-01	6.67e-01	2.81e+00	1.00e+00
73.1500	72.7000	1.3012e-03	-	2.79e+02	9.34e+01	8.67e+00	2.00e-01	1.83e-01	9.09e-01	2.98e+00	1.00e+01
72.6510	72.6390	3.4706e-05	-	2.34e+04	1.05e+03	6.54e+01	2.00e-02	7.51e-04	2.50e-02	2.18e-01	2.00e+02
72.6580	72.6400	5.2048e-05	-	1.59e+04	8.93e+02	6.07e+01	9.00e-03	1.45e-03	3.70e-02	3.24e-01	7.69e+02
72.6780	72.6420	1.0412e-04	-	7.22e+03	5.78e+02	4.10e+01	1.60e-02	4.24e-03	7.69e-02	6.19e-01	3.85e+02
72.6840	72.6430	1.1857e-04	-	5.70e+03	5.09e+02	3.61e+01	1.00e-02	5.09e-03	8.33e-02	6.61e-01	3.33e+02
73.2200	72.6300	1.7063e-03	-	1.96e+02	8.20e+01	8.09e+00	2.00e-01	1.53e-01	6.25e-01	3.36e+00	1.00e+00
73.4000	72.6300	2.2269e-03	-	1.40e+02	6.80e+01	7.34e+00	2.00e-01	1.85e-01	6.67e-01	3.36e+00	1.00e+00
73.6000	72.6300	2.8053e-03	-	1.03e+02	5.92e+01	6.63e+00	2.00e-01	3.83e-01	7.14e-01	3.35e+00	1.00e+00
73.8000	72.6150	3.4272e-03	-	7.27e+01	4.89e+01	5.97e+00	2.00e-01	2.97e-01	7.69e-01	3.28e+00	1.00e+00
74.2200	72.6100	4.6564e-03	-	5.37e+01	4.15e+01	5.52e+00	2.00e-01	3.17e-01	7.14e-01	2.84e+00	1.00e+00
74.6100	72.6000	5.8135e-03	-	3.91e+01	3.41e+01	5.01e+00	2.00e-01	6.42e-01	1.25e+00	4.35e+00	1.00e+00
75.1200	72.6000	7.2885e-03	-	2.78e+01	2.95e+01	4.69e+00	2.00e-01	6.10e-01	1.00e+00	3.34e+00	1.00e+00
75.8800	72.6000	9.4866e-03	-	1.85e+01	2.33e+01	4.11e+00	2.00e-01	1.01e+00	1.43e+00	4.05e+00	1.00e+00
72.7120	72.6450	1.9376e-04	-	3.38e+03	3.85e+02	2.88e+01	2.70e-02	7.56e-03	1.00e-01	7.34e-01	5.00e+01
72.7230	72.6470	2.1977e-04	-	2.97e+03	3.52e+02	2.75e+01	2.80e-02	1.03e-02	1.30e-01	8.86e-01	2.78e+02
72.7300	72.6490	2.3424e-04	-	2.71e+03	3.40e+02	2.60e+01	3.00e-02	1.05e-02	1.25e-01	8.64e-01	2.50e+02
72.7450	72.6510	2.7184e-04	-	2.30e+03	3.08e+02	2.40e+01	3.50e-02	1.25e-02	1.43e-01	9.35e-01	2.00e+02
72.7570	72.6530	3.0076e-04	-	1.85e+03	2.73e+02	2.10e+01	5.35e-02	1.91e-02	2.00e-01	1.26e+00	1.43e+02
72.7820	72.6550	3.6726e-04	-	1.49e+03	2.43e+02	1.92e+01	5.90e-02	2.27e-02	2.13e-01	1.32e+00	1.28e+02
72.8000	72.6570	4.1354e-04	-	1.19e+03	2.14e+02	1.67e+01	8.30e-02	2.69e-02	2.33e-01	1.39e+00	8.33e+01
72.8330	72.6600	5.0026e-04	-	1.00e+03	1.94e+02	1.59e+01	7.60e-02	4.90e-02	4.00e-01	2.28e+00	1.33e+02
72.8740	72.6630	6.1015e-04	-	7.37e+02	1.64e+02	1.34e+01	1.10e-01	6.83e-02	5.00e-01	2.54e+00	8.33e+01
72.9500	72.7000	7.2286e-04	-	5.76e+02	1.40e+02	1.14e+01	1.70e-01	1.81e-02	5.00e-01	3.93e-01	5.00e+01
72.6510	72.6390	3.4706e-05	-	2.34e+04	1.05e+03	6.54e+01	2.00e-02	7.51e-04	2.50e-02	2.18e-01	2.00e+02
72.6580	72.6400	5.2048e-05	-	1.59e+04	8.93e+02	6.07e+01	9.00e-03	1.45e-03	3.70e-02	3.24e-01	7.69e+02
72.6780	72.6420	1.0412e-04	-	7.22e+03	5.78e+02	4.10e+01	1.60e-02	4.24e-03	7.69e-02	6.19e-01	3.85e+02
72.6840	72.6430	1.1857e-04	-	5.70e+03	5.09e+02	3.61e+01	1.00e-02	5.09e-03	8.33e-02	6.61e-01	3.33e+02
73.7700	72.4300	3.8775e-03	-	4.99e+01	4.38e+01	4.77e+00	2.00e-01	9.04e-01	2.00e+00	1.02e+01	1.00e+00
74.1400	72.4400	4.9191e-03	-	3.67e+01	3.77e+01	4.22e+00	2.00e-01	1.08e+00	1.85e+00	8.54e+00	1.00e+00
73.4800	72.4200	3.0674e-03	-	6.95e+01	5.17e+01	5.46e+00	2.00e-01	8.29e-01	2.00e+00	9.57e+00	1.00e+00
74.6000	72.4500	6.2211e-03	-	2.65e+01	3.19e+01	3.76e+00	2.00e-01	1.11e+00	1.67e+00	7.43e+00	1.00e+00
75.1300	72.4600	7.7255e-03	-	1.95e+01	2.69e+01	3.44e+00	2.00e-01	1.29e+00	1.75e+00	7.00e+00	1.00e+00
75.9250	72.4700	9.9965e-03	-	1.32e+01	[illegible]e+01	2.90e+00	2.00e-01	1.83e+00	2.00e+00	7.58e+00	1.00e+00

9.75S5

T	T_{NA}	t	χ^2	σ_0	$\xi_{\parallel}$	$\xi_{\perp}$	c	$w(\sigma_0)$	$w(\xi_{\parallel})$	$w(\xi_{\perp})$	w(c)
81.3900	78.6630	7.7513E-3	1.75	2.92E1	1.74E1	2.71	2.50E-1	4.13E-1	2.48	7.96	-
80.5690	78.6630	5.4176E-3	1.79	4.72E1	2.21E1	3.15	2.50E-1	3.28E-1	2.48	8.90	-
80.0320	78.6630	3.8913E-3	1.79	7.29E1	2.75E1	3.67	2.50E-1	2.59E-1	2.41	9.42	-
79.6680	78.6630	2.8566E-3	2.81	1.10E2	3.46E1	4.26	2.50E-1	1.61E-1	1.77	7.60	-
79.4000	78.6630	2.0949E-3	2.90	1.60E2	4.16E1	4.94	2.19E-1	1.07E-1	1.30	3.57	1.66E1
79.1900	78.6630	1.4980E-3	2.00	2.42E2	5.19E1	5.97	1.53E-1	8.37E-2	1.22	3.65	2.92E1
79.0600	78.6630	1.1284E-3	2.04	3.56E2	6.26E1	7.45	8.85E-2	6.09E-2	1.07	3.47	5.91E1
78.6890	78.6780	3.1270E-5	4.41	1.97E4	5.68E2	3.98E1	2.48E-2	3.57E-4	3.52E-2	2.92E-1	1.45E2
78.6890	78.6780	3.1270E-5	1.98	2.04E4	5.69E2	4.11E1	2.23E-2	5.22E-4	5.31E-2	4.29E-1	2.48E2
78.6920	78.6780	3.9792E-5	2.64	1.69E4	5.15E2	3.71E1	2.80E-2	5.49E-4	5.14E-2	4.07E-1	1.63E2
78.6960	78.6780	5.1155E-5	2.84	1.33E4	4.55E2	3.30E1	3.46E-2	6.72E-4	5.67E-2	4.34E-1	1.20E2
78.7010	78.6780	6.5359E-5	1.45	1.09E4	3.97E2	3.06E1	3.70E-2	1.15E-3	9.23E-2	6.52E-1	1.51E2
78.7070	78.6780	8.2425E-5	2.16	9.02E3	3.59E2	2.96E1	2.86E-2	1.12E-3	8.25E-2	5.46E-1	1.48E2
78.7150	78.6780	1.0515E-4	2.25	6.48E3	2.98E2	2.47E1	4.39E-2	1.51E-3	9.81E-2	6.11E-1	8.74E1
78.7300	78.6780	1.4781E-4	1.42	4.73E3	2.55E2	2.21E1	4.38E-2	2.49E-3	1.39E-1	8.14E-1	9.69E1
78.7480	78.6780	1.9896E-4	1.57	3.34E3	2.12E2	1.89E1	5.26E-2	3.18E-3	1.53E-1	8.31E-1	6.60E1
78.7100	78.6780	9.0947E-5	9.20	9.37E3	3.73E2	3.06E1	1.86E-2	1.27E-3	9.51E-2	6.58E-1	3.06E2
78.7190	78.6780	1.1654E-4	9.12	7.16E3	3.18E2	2.75E1	1.94E-2	1.65E-3	1.13E-1	7.25E-1	2.82E2
78.7320	78.6780	1.5349E-4	5.46	5.16E3	2.72E2	2.34E1	2.65E-2	2.87E-3	1.68E-1	1.05	2.51E2
78.7520	78.6780	2.1032E-4	3.77	3.33E3	2.11E2	1.92E1	3.58E-2	5.06E-3	2.51E-1	1.43	2.02E2
78.7780	78.6780	2.8423E-4	2.68	2.25E3	1.69E2	1.62E1	4.31E-2	8.31E-3	3.53E-1	1.83	1.77E2
78.8130	78.6780	3.8372E-4	2.21	1.52E3	1.37E2	1.36E1	5.16E-2	1.25E-2	4.52E-1	2.18	1.43E2
78.8660	78.6780	5.3434E-4	1.81	1.01E3	1.09E2	1.18E1	4.60E-2	2.01E-2	5.60E-1	2.35	1.37E2
78.9390	78.6780	7.4184E-4	1.41	6.58E2	8.82E1	9.55	7.11E-2	3.28E-2	7.45E-1	2.90	8.66E1
79.0320	78.6780	1.0062E-3	1.51	4.47E2	7.06E1	8.01	9.70E-2	4.35E-2	8.47E-1	2.93	5.22E1
78.7210	78.7180	8.5212E-6	3.50	8.68E4	1.34E3	8.61E1	7.09E-3	7.25E-5	1.23E-2	1.28E-1	6.16E2
78.7230	78.7180	1.4202E-5	2.73	4.73E4	9.54E2	6.47E1	1.11E-2	1.66E-4	2.22E-2	2.09E-1	4.36E2
78.7250	78.7180	1.9883E-5	3.26	3.68E4	8.59E2	5.75E1	1.30E-2	1.98E-4	2.30E-2	2.15E-1	3.30E2
78.7260	78.7180	2.2723E-5	2.61	3.04E4	7.64E2	5.29E1	1.50E-2	2.73E-4	2.98E-2	2.64E-1	3.13E2
78.7300	78.7180	3.4107E-5	2.57	1.73E4	5.64E2	3.85E1	3.21E-2	5.09E-4	4.42E-2	3.68E-1	1.37E2
78.7350	78.7180	4.8309E-5	2.17	1.14E4	4.47E2	3.22E1	3.94E-2	8.47E-4	6.20E-2	4.70E-1	1.11E2
78.7400	78.7180	6.2511E-5	1.86	9.30E3	3.91E2	3.08E1	3.03E-2	1.11E-3	7.66E-2	5.34E-1	1.47E2
78.7480	78.7180	8.5256E-5	1.83	6.16E3	3.16E2	2.48E1	5.31E-2	1.66E-3	9.57E-2	6.24E-1	7.63E1
78.7560	78.7180	1.0798E-4	1.37	4.81E3	2.76E2	2.20E1	5.93E-2	2.42E-3	1.26E-1	7.85E-1	7.34E1
78.7710	78.7180	1.5063E-4	2.11	3.47E3	2.26E2	2.10E1	3.52E-2	3.55E-3	1.60E-1	8.72E-1	1.33E2
79.6800	78.7000	2.7853E-3	1.23	1.40E1	3.37E1	4.42	2.50E-1	1.09	1.60	6.37	-
79.4150	78.7000	2.0321E-3	1.79	2.08E1	4.22E1	5.08	2.50E-1	7.15E-1	1.23	5.40	-
79.2000	78.7000	1.4210E-3	1.13	3.22E1	5.30E1	5.75	2.93E-1	4.81E-1	9.14E-1	2.55	1.11E1
78.9770	78.7000	7.8725E-4	1.50	6.21E1	7.73E1	8.57	1.12E-1	2.31E-1	5.98E-1	2.15	3.83E1
78.9050	78.7000	5.8262E-4	1.32	8.80E1	9.30E1	9.60	1.10E-1	1.96E-1	5.87E-1	2.29	4.81E1
78.8520	78.7000	4.3198E-4	1.53	1.29E2	1.14E2	1.19E1	6.03E-2	1.36E-1	4.84E-1	2.03	9.50E1
78.8160	78.7000	3.2968E-4	2.05	1.80E2	1.35E2	1.33E1	6.97E-2	9.14E-2	3.75E-1	1.66	7.99E1
78.7900	78.7000	2.5578E-4	1.71	2.49E2	1.61E2	1.51E1	7.55E-2	4.84E-2	2.26E-1	1.06	4.99E1
78.7710	78.7000	2.0179E-4	1.57	3.20E2	1.81E2	1.72E1	5.07E-2	4.15E-2	2.20E-1	1.08	8.57E1
78.7550	78.7000	1.5630E-4	1.49	4.71E2	2.26E2	2.08E1	3.60E-2	3.00E-2	1.85E-1	9.92E-1	1.38E2
78.8250	78.7000	3.5524E-4	1.34	2.26E2	1.50E2	1.48E1	5.63E-2	5.98E-2	2.74E-1	1.25	7.52E1
78.7990	78.7200	2.2452E-4	1.48	3.20E2	1.78E2	1.75E1	4.53E-2	4.25E-2	2.30E-1	1.10	9.95E1
78.7800	78.7200	1.7051E-4	1.90	4.22E2	2.14E2	1.84E1	5.63E-2	2.97E-2	1.74E-1	9.44E-1	7.65E1
78.7660	78.7200	1.3072E-4	2.02	6.61E2	2.68E2	2.45E1	2.48E-2	1.89E-2	1.36E-1	7.67E-1	1.88E2
78.7570	78.7200	1.0516E-4	1.58	9.18E2	3.01E2	2.54E1	3.45E-2	1.66E-2	1.37E-1	7.78E-1	1.30E2

105

T	T_{NA}	t	χ^2	σ_0	$\xi_{\parallel}$	$\xi_{\perp}$	c	$w(\sigma_0)$	$w(\xi_{\parallel})$	$w(\xi_{\perp})$	w(c)
81.0130	80.4000	1.7338E-3	0.00	8.91E1	3.32E1	4.52	2.50E-1	1.43E-1	1.31	5.08	-
81.0930	80.4000	1.9601E-3	0.00	7.75E1	3.08E1	4.28	2.50E-1	1.95E-1	1.69	6.36	-
81.2530	80.4000	2.4127E-3	0.00	6.35E1	2.73E1	4.04	2.50E-1	2.13E-1	1.70	5.99	-
81.4430	80.4000	2.9501E-3	0.00	5.18E1	2.50E1	3.71	2.50E-1	2.29E-1	1.64	5.67	-
81.6580	80.4000	3.5582E-3	0.00	4.15E1	2.18E1	3.49	2.50E-1	2.99E-1	1.97	6.29	-
81.9170	80.4000	4.2908E-3	0.00	3.34E1	2.07E1	3.28	2.50E-1	3.80E-1	2.13	6.79	-
82.2550	80.4000	5.2468E-3	0.00	2.64E1	1.76E1	3.07	2.50E-1	4.10E-1	2.15	6.13	-
80.9440	80.4200	1.4820E-3	0.00	1.04E2	3.64E1	4.64	2.85E-1	9.80E-2	8.73E-1	1.94	6.40
80.8540	80.4200	1.2275E-3	0.00	1.26E2	4.10E1	5.22	2.26E-1	9.80E-2	9.32E-1	2.24	1.06E1
80.7800	80.4200	1.0182E-3	0.00	1.58E2	4.62E1	6.14	1.11E-1	7.34E-2	7.71E-1	2.02	2.08E1
80.7160	80.4200	8.3719E-4	0.00	1.91E2	5.17E1	6.55	1.24E-1	6.39E-2	7.21E-1	2.00	2.11E1
80.6540	80.4200	6.9011E-4	0.00	2.41E2	5.74E1	7.61	6.95E-2	6.41E-2	8.53E-1	2.67	5.35E1
80.5300	80.4480	2.3190E-4	0.00	8.28E2	1.16E2	1.37E1	3.22E-2	1.39E-2	3.10E-1	1.28	1.24E2
80.5430	80.4480	2.6867E-4	0.00	6.74E2	1.03E2	1.22E1	4.18E-2	1.74E-2	3.60E-1	1.44	9.63E1
80.5600	80.4480	3.1674E-4	0.00	5.98E2	9.64E1	1.18E1	3.42E-2	2.01E-2	3.98E-1	1.54	1.15E2
80.5830	80.4480	3.8180E-4	0.00	4.81E2	8.54E1	1.03E1	5.90E-2	2.78E-2	4.86E-1	1.82	6.63E1
80.6060	80.4480	4.4685E-4	0.00	4.08E2	7.70E1	9.53	6.53E-2	3.07E-2	5.07E-1	1.80	5.39E1
80.6350	80.4480	5.2886E-4	0.00	3.37E2	7.10E1	8.63	7.89E-2	4.19E-2	6.24E-1	2.18	4.88E1
80.6680	80.4480	6.2218E-4	0.00	2.89E2	6.51E1	8.04	9.31E-2	4.50E-2	6.30E-1	2.09	3.68E1
80.7100	80.4480	7.4096E-4	0.00	2.37E2	5.67E1	7.40	9.77E-2	6.40E-2	8.49E-1	2.61	3.93E1
80.7800	80.4480	9.3892E-4	0.00	1.95E2	5.24E1	7.00	8.00E-2	7.34E-2	8.72E-1	2.63	4.18E1
80.8300	80.4480	1.0803E-3	0.00	1.51E2	4.44E1	5.72	1.83E-1	8.01E-2	8.76E-1	2.38	1.52E1
80.4580	80.4490	2.5460E-5	0.00	7.49E3	4.05E2	3.72E1	9.35E-3	1.39E-3	7.18E-2	4.32E-1	4.20E2
80.4620	80.4490	3.6766E-5	0.00	6.28E3	3.67E2	3.43E1	1.04E-2	1.62E-3	7.79E-2	4.52E-1	3.53E2
80.4650	80.4490	4.5246E-5	0.00	5.02E3	3.23E2	3.05E1	1.35E-2	2.24E-3	9.87E-2	5.50E-1	2.93E2
80.4680	80.4490	5.3747E-5	0.00	4.66E3	3.11E2	3.00E1	1.15E-2	2.50E-3	1.07E-1	5.87E-1	3.49E2
80.4750	80.4490	7.3532E-5	0.00	3.22E3	2.47E2	2.60E1	1.12E-2	3.75E-3	1.42E-1	6.95E-1	3.34E2
80.4830	80.4490	9.6166E-5	0.00	2.42E3	2.06E2	2.25E1	1.49E-2	4.84E-3	1.69E-1	8.56E-1	3.14E2
80.4920	80.4490	1.2160E-4	0.00	1.93E3	1.81E2	2.02E1	1.88E-2	6.84E-3	2.18E-1	1.06	2.71E2
80.5020	80.4490	1.4989E-4	0.00	1.40E3	1.53E2	1.70E1	2.48E-2	8.30E-3	2.29E-1	1.07	1.68E2
80.5160	80.4490	1.8948E-4	0.00	1.11E3	1.36E2	1.51E1	3.31E-2	1.11E-2	2.74E-1	1.24	1.30E2
80.5550	80.4490	2.9978E-4	0.00	6.76E2	1.01E2	1.23E1	3.56E-2	2.11E-2	4.33E-1	1.72	1.23E2
80.5830	80.4490	3.7897E-4	0.00	5.31E2	8.95E1	1.10E1	4.13E-2	2.32E-2	4.27E-1	1.62	8.69E1
80.6360	80.4490	5.2886E-4	0.00	3.34E2	6.87E1	8.23	1.38E-1	3.22E-2	4.89E-1	1.60	2.12E1
80.4910	80.4850	1.6957E-5	3.04	1.54E3	3.73E2	3.79E1	6.78E-3	7.41E-3	8.56E-2	4.89E-1	7.12E2
80.4970	80.4850	3.3936E-5	4.16	8.77E2	2.78E2	2.83E1	1.39E-2	1.10E-2	9.80E-2	5.23E-1	2.69E2
80.5050	80.4850	5.6546E-5	2.45	5.90E2	2.22E2	2.45E1	1.17E-2	2.11E-2	1.60E-1	7.77E-1	3.69E2
80.5160	80.4850	8.7656E-5	2.14	3.89E2	1.75E2	2.03E1	1.31E-2	3.38E-2	2.18E-1	9.68E-1	3.08E2
80.5240	80.4850	1.1029E-4	1.90	3.15E2	1.60E2	1.81E1	1.91E-2	4.31E-2	2.47E-1	1.09	2.18E2
80.5630	80.4850	2.2057E-4	1.63	1.68E2	1.15E2	1.37E1	2.73E-2	8.08E-2	3.49E-1	1.36	1.32E2
80.6160	80.4850	3.7043E-4	1.12	9.01E1	8.05E1	9.64	7.17E-2	1.79E-1	6.15E-1	2.21	6.59E1
80.6840	80.4850	5.6272E-4	1.39	6.14E1	6.63E1	8.17	8.56E-2	2.17E-1	6.23E-1	2.06	4.16E1
80.7510	80.4850	7.5218E-4	1.16	4.50E1	5.48E1	6.96	1.07E-1	3.08E-1	7.90E-1	2.37	3.12E1
80.8840	80.4850	1.1283E-3	1.87	2.87E1	4.20E1	5.50	1.99E-1	3.59E-1	7.61E-1	1.89	1.07E1
81.0200	80.4850	1.5128E-3	1.93	2.14E1	3.71E1	4.90	1.99E-1	5.03E-1	9.99E-1	3.97	-
81.5580	80.4850	3.0342E-3	1.47	1.01E1	2.38E1	3.75	1.99E-1	9.28E-1	1.37	4.43	-

10.2S5

T	T_{NA}	t	χ^2	σ_0	$\xi_{\parallel}$	$\xi_{\perp}$	c	$w(\sigma_0)$	$w(\xi_{\parallel})$	$w(\xi_{\perp})$	$w(c)$
81.4070	81.4000	1.9732E-5	4.86	5.97E2	1.94E2	1.82E1	9.58E-2	1.79E-2	1.61E-1	7.80E-1	3.5[illegible]E1
81.4120	81.4000	3.3849E-5	2.87	5.52E2	1.90E2	1.98E1	3.39E-2	2.54E-2	2.20E-1	1.07	1.45E2
81.4140	81.4000	3.9487E-5	3.03	5.74E2	1.94E2	2.12E1	2.15E-2	2.35E-2	2.07E-1	9.91E-1	2.19E2
81.4180	81.4000	5.0762E-5	2.51	4.79E2	1.77E2	1.93E1	2.81E-2	3.05E-2	2.48E-1	1.15	1.78E2
81.4230	81.4000	6.4857E-5	1.99	3.65E2	1.51E2	1.66E1	3.91E-2	4.48E-2	3.27E-1	1.43	1.35E2
81.4310	81.4000	8.7430E-5	2.18	3.15E2	1.43E2	1.59E1	3.20E-2	4.81E-2	3.22E-1	1.39	1.47E2
81.4410	81.4000	1.1564E-4	1.62	2.55E2	1.25E2	1.41E1	5.47E-2	6.72E-2	4.21E-1	1.67	9.55E1
81.4510	81.4000	1.4383E-4	1.55	2.21E2	1.16E2	1.37E1	4.04E-2	7.69E-2	4.49E-1	1.73	1.22E2
81.4700	81.4000	1.9743E-4	1.85	1.66E2	1.01E2	1.21E1	4.78E-2	9.64E-2	4.81E-1	1.87	1.14E2
81.4960	81.4000	2.7077E-4	1.26	1.28E2	8.69E1	1.10E1	4.66E-2	1.46E-1	6.57E-1	2.37	1.29E2
81.5350	81.4000	3.8077E-4	1.42	9.18E1	7.37E1	9.31	6.30E-2	1.81E-1	6.97E-1	2.40	7.93E1
81.5850	81.4000	5.2178E-4	1.71	6.67E1	6.09E1	8.39	6.30E-2	2.11E-1	7.21E-1	2.22	6.17E1
81.6530	81.4000	7.1358E-4	1.32	4.79E1	5.25E1	7.11	8.96E-2	3.07E-1	8.80E-1	2.60	4.30E1
81.7530	81.4000	9.9562E-4	2.01	3.67E1	4.55E1	6.78	5.90E-2	3.72E-1	9.46E-1	2.70	6.16E1

10.4S5

T	T_{NA}	t	χ^2	σ_0	$\xi_{\parallel}$	$\xi_{\perp}$	c	$w(\sigma_0)$	$w(\xi_{\parallel})$	$w(\xi_{\perp})$	w(c)
85.2400	81.8200	9.6346E-3	1.78	8.88	7.01	2.23	2.50E-1	8.26E-1	3.90	5.80	-
84.6600	81.8200	8.0007E-3	1.54	1.20E1	8.77	2.31	2.50E-1	7.75E-1	3.94	7.17	-
84.2000	81.8200	6.7048E-3	1.19	1.50E1	9.79	2.40	2.50E-1	7.88E-1	4.47	8.87	-
83.4700	81.8200	4.6483E-3	1.67	1.87E1	1.16E1	2.56	2.50E-1	5.86E-1	3.48	7.80	-
82.1230	81.8200	8.5360E-4	1.47	1.12E2	3.30E1	5.24	1.24E-1	1.31E-1	1.36	2.93	2.24E1
82.1800	81.8200	1.0142E-3	1.51	9.57E1	3.13E1	4.67	1.88E-1	1.45E-1	1.37	2.89	1.37E1
82.2560	81.8200	1.2283E-3	1.51	7.73E1	2.70E1	4.06	2.78E-1	2.12E-1	1.84	3.08	8.41
82.3490	81.8200	1.4903E-3	2.03	6.73E1	2.43E1	4.07	1.85E-1	2.19E-1	1.91	3.46	1.32E1
82.4500	81.8200	1.7748E-3	1.39	5.50E1	2.18E1	3.42	4.14E-1	3.01E-1	2.41	3.91	6.38
82.5730	81.8200	2.1213E-3	1.58	4.80E1	2.02E1	3.49	2.50E-1	3.50E-1	2.90	8.69	-
82.9500	81.8200	3.1834E-3	1.71	3.23E1	1.57E1	3.08	2.50E-1	4.10E-1	2.97	7.73	-
82.0700	81.8200	7.0428E-4	1.51	1.35E2	3.82E1	5.85	8.63E-2	1.27E-1	1.42	3.56	4.35E1
82.0220	81.8200	5.6907E-4	1.66	1.54E2	4.04E1	5.89	1.32E-1	1.12E-1	1.34	3.38	3.10E1
81.9950	81.8200	4.9301E-4	2.31	1.89E2	4.56E1	6.81	8.13E-2	8.03E-2	1.04	2.78	4.61E1
81.9600	81.8200	3.9440E-4	2.02	2.04E2	4.79E1	6.94	7.72E-2	8.20E-2	1.09	3.04	5.38E1
81.9470	81.8200	3.5777E-4	1.64	2.10E2	4.86E1	6.94	8.39E-2	8.92E-2	1.20	3.37	5.64E1
81.9260	81.8200	2.9862E-4	2.23	2.49E2	5.39E1	7.86	5.74E-2	6.60E-2	9.45E-1	2.75	7.40E1
81.9090	81.8200	2.5072E-4	1.95	2.66E2	5.63E1	7.74	7.53E-2	6.77E-2	9.89E-1	2.98	6.45E1
81.8930	81.8200	2.0565E-4	3.04	3.05E2	5.99E1	8.27	7.12E-2	4.85E-2	7.60E-1	2.32	5.83E1
81.8830	81.8200	1.7749E-4	2.49	3.59E2	6.50E1	9.58	3.38E-2	4.65E-2	7.87E-1	2.44	1.32E2
81.8650	81.8200	1.2677E-4	3.52	4.23E2	7.32E1	9.94	4.15E-2	3.42E-2	6.02E-1	2.03	1.02E2
81.8560	81.8200	1.0143E-4	3.08	4.68E2	7.66E1	1.06E1	3.62E-2	3.35E-2	6.21E-1	2.10	1.30E2
81.8500	81.8200	8.4511E-5	1.71	5.11E2	8.19E1	1.10E1	3.54E-2	3.27E-2	6.59E-1	2.40	1.60E2
81.8460	81.8200	7.3248E-5	2.13	5.37E2	8.47E1	1.11E1	4.28E-2	2.83E-2	5.77E-1	2.14	1.24E2
81.8410	81.8200	5.9170E-5	1.81	5.85E2	8.78E1	1.16E1	3.75E-2	2.85E-2	6.10E-1	2.27	1.57E2
81.8360	81.8200	4.5071E-5	1.95	6.44E2	9.32E1	1.23E1	2.87E-2	2.53E-2	5.61E-1	2.13	1.99E2
81.8320	81.8200	3.3809E-5	2.02	6.68E2	9.54E1	1.23E1	3.45E-2	2.43E-2	5.43E-1	2.09	1.70E2
81.8260	81.8200	1.6894E-5	2.40	7.36E2	1.02E2	1.32E1	2.51E-2	2.05E-2	4.72E-1	1.85	2.11E2

11S5

T	T_{NA}	t	χ^2	σ_0	$\xi_{\parallel}$	$\xi_{\perp}$	c	$w(\sigma_0)$	$w(\xi_{\parallel})$	$w(\xi_{\perp})$	$w(c)$
83.5600	83.5200	1.1215E-4	-	6.85E1	2.30E1	4.04	2.50E-1	1.43E-1	1.50	4.48	-
83.5920	83.5200	2.0188E-4	-	6.14E1	2.10E1	3.86	2.50E-1	1.64E-1	1.71	4.83	-
83.6630	83.5200	4.0095E-4	-	5.06E1	1.92E1	3.63	2.50E-1	1.80E-1	1.69	4.63	-
83.7980	83.5200	7.7943E-4	-	3.88E1	1.60E1	3.37	2.50E-1	2.49E-1	2.16	5.22	-
84.0700	83.5200	1.5421E-3	-	2.47E1	1.18E1	2.82	2.50E-1	3.35E-1	2.53	5.21	-
84.6220	83.5200	3.0897E-3	-	1.50E1	8.47	2.63	2.50E-1	6.32E-1	4.04	6.23	-
84.6200	83.5200	3.0841E-3	-	1.30E1	7.55	2.40	2.50E-1	5.33E-1	3.29	4.91	-
84.0700	83.5200	1.5421E-3	-	2.31E1	1.19E1	2.87	2.50E-1	3.59E-1	2.47	5.08	-
83.8000	83.5200	7.8506E-4	-	3.30E1	1.49E1	3.16	2.50E-1	3.06E-1	2.37	5.69	-

8CB

T	T_{NA}	t	χ^2	σ_0	$\xi_{\parallel}$	$\xi_{\perp}$	σ	$w(\sigma_0)$	$w(\xi_{\parallel})$	$w(\xi_{\perp})$	$w(\sigma)$
33.9350	33.9290	1.9541E-5	17.83	4.35E4	1.63E3	1.03E2	2.64E-2	1.39E-4	9.92E-3	9.56E-2	1.50E2
33.9370	33.9290	2.6050E-5	17.40	2.28E4	1.14E3	7.66E1	4.61E-2	2.78E-4	1.52E-2	1.31E-1	7.89E1
33.9410	33.9290	3.9081E-5	11.85	1.27E4	7.87E2	6.41E1	5.13E-2	7.91E-4	3.54E-2	2.48E-1	1.05E2
33.9440	33.9290	4.8845E-5	12.79	1.03E4	6.98E2	5.74E1	6.41E-2	9.43E-4	3.88E-2	2.63E-1	7.71E1
33.9480	33.9290	6.1877E-5	9.10	7.75E3	6.00E2	5.24E1	5.97E-2	1.47E-3	5.30E-2	3.38E-1	9.37E1
33.9520	33.9290	7.4895E-5	7.14	5.95E3	5.14E2	4.79E1	5.97E-2	2.18E-3	7.12E-2	4.17E-1	1.01E2
33.9590	33.9290	9.7691E-5	7.56	4.17E3	4.30E2	4.10E1	7.05E-2	3.00E-3	8.27E-2	4.54E-1	7.58E1
33.9670	33.9290	1.2374E-4	5.28	3.35E3	3.78E2	3.79E1	7.14E-2	4.48E-3	1.14E-1	5.85E-1	8.66E1
33.9690	33.9290	1.3026E-4	4.61	3.26E3	3.73E2	3.80E1	6.57E-2	4.93E-3	1.24E-1	6.30E-1	1.01E2
33.9820	33.9290	1.7259E-4	4.90	2.32E3	3.11E2	3.33E1	6.90E-2	6.62E-3	1.44E-1	6.77E-1	8.71E1
34.0020	33.9290	2.3772E-4	3.24	1.51E3	2.47E2	2.85E1	6.90E-2	1.22E-2	2.22E-1	9.45E-1	1.00E2
34.0300	33.9290	3.2890E-4	2.52	1.04E3	2.01E2	2.50E1	7.13E-2	1.94E-2	3.07E-1	1.18	1.04E2
34.0700	33.9290	4.5916E-4	2.87	7.18E2	1.64E2	2.28E1	5.22E-2	2.33E-2	2.94E-1	9.92E-1	1.18E2
34.1260	33.9290	6.4152E-4	2.39	4.62E2	1.31E2	1.87E1	7.20E-2	3.79E-2	3.88E-1	1.21	8.32E1
34.2030	33.9290	8.9227E-4	1.77	2.95E2	1.03E2	1.54E1	8.58E-2	6.53E-2	5.51E-1	1.55	7.14E1
34.3100	33.9290	1.2407E-3	1.65	1.96E2	8.16E1	1.34E1	8.75E-2	9.55E-2	6.83E-1	1.70	6.48E1
34.4600	33.9290	1.7292E-3	1.06	1.33E2	6.81E1	1.15E1	9.56E-2	1.63E-1	9.62E-1	2.26	6.57E1
34.6650	33.9290	2.3968E-3	1.78	8.56E1	5.38E1	9.81	9.46E-2	2.11E-1	1.03	2.34	5.99E1
34.9450	33.9290	3.3086E-3	1.51	5.46E1	4.25E1	8.18	1.15E-1	3.25E-1	1.29	2.64	4.46E1
35.3460	33.9290	4.6144E-3	1.53	3.37E1	3.30E1	6.59	1.62E-1	6.57E-1	2.10	3.83	3.60E1
35.9000	33.9290	6.4185E-3	1.44	2.12E1	2.58E1	5.69	1.47E-1	9.36E-1	2.45	4.02	3.38E1
36.6700	33.9290	8.9260E-3	1.35	1.20E1	1.90E1	4.36	2.41E-1	1.46	2.96	4.10	1.56E1
37.7500	33.9290	1.2443E-2	1.12	6.73	1.45E1	3.47	2.65E-1	2.12	3.32	4.24	1.09E1
39.2200	33.9290	1.7230E-2	1.04	3.40	9.69	2.86	2.76E-1	2.88	3.52	3.59	6.63

9CB

T	T_{NA}	t	χ^2	σ_0	$\xi_{\parallel}$	$\xi_{\perp}$	σ	$w(\sigma_0)$	$w(\xi_{\parallel})$	$w(\xi_{\perp})$	$w(\sigma)$
47.8015	47.7950	2.0253E-5	3.12	7.76E3	4.52E2	4.31E1	1.00E-1	1.49E-3	8.32E-2	4.83E-1	-
47.8035	47.7950	2.6494E-5	2.12	5.65E3	3.73E2	3.90E1	1.00E-1	2.44E-3	1.21E-1	6.35E-1	-
47.8055	47.7950	3.2722E-5	2.76	4.18E3	3.28E2	3.48E1	1.00E-1	3.03E-3	1.38E-1	6.54E-1	-
47.8070	47.7950	3.7393E-5	2.10	3.73E3	3.10E2	3.37E1	1.00E-1	3.50E-3	1.40E-1	6.96E-1	-
47.8100	47.7950	4.6747E-5	2.90	3.02E3	2.72E2	3.14E1	1.00E-1	3.86E-3	1.46E-1	6.90E-1	-
47.8130	47.7950	5.6089E-5	1.80	2.34E3	2.43E2	2.86E1	1.00E-1	5.66E-3	1.82E-1	8.45E-1	-
47.8190	47.7950	7.4786E-5	2.04	1.64E3	2.01E2	2.53E1	1.00E-1	1.06E-2	2.94E-1	1.26	-
47.8270	47.7950	9.9710E-5	1.56	1.22E3	1.72E2	2.28E1	1.00E-1	1.42E-2	3.41E-1	1.39	-
47.8350	47.7950	1.2463E-4	1.51	9.58E2	1.50E2	2.10E1	1.00E-1	1.74E-2	3.78E-1	1.44	-
47.8500	47.7950	1.7137E-4	1.40	6.44E2	1.23E2	1.78E1	1.00E-1	2.42E-2	4.37E-1	1.59	-
47.8690	47.7950	2.3057E-4	0.89	4.91E2	1.05E2	1.66E1	1.00E-1	3.58E-2	5.82E-1	1.93	-
47.8650	47.7950	2.1812E-4	3.53	5.40E2	1.10E2	1.72E1	1.00E-1	2.87E-2	4.70E-1	1.65	-
47.8810	47.7950	2.6797E-4	2.66	4.29E2	9.85E1	1.59E1	1.00E-1	3.97E-2	5.76E-1	1.96	-
47.9040	47.7950	3.3963E-4	3.66	3.28E2	8.51E1	1.43E1	1.00E-1	4.21E-2	5.44E-1	1.76	-
47.9330	47.7950	4.2998E-4	3.37	2.63E2	7.54E1	1.34E1	1.00E-1	5.19E-2	6.11E-1	1.86	-
47.9700	47.7950	5.4527E-4	3.92	2.07E2	6.59E1	1.24E1	1.00E-1	5.73E-2	6.10E-1	1.75	-
48.0200	47.7950	7.0106E-4	3.99	1.56E2	5.64E1	1.13E1	1.00E-1	6.95E-2	6.57E-1	1.77	-
48.0820	47.7950	8.9424E-4	5.76	1.22E2	5.04E1	1.06E1	1.00E-1	6.98E-2	5.74E-1	1.50	-
48.1710	47.7950	1.1716E-3	6.80	9.15E1	4.42E1	9.57	1.00E-1	7.98E-2	5.58E-1	1.41	-
48.2650	47.7950	1.4644E-3	6.80	6.87E1	3.81E1	8.58	1.00E-1	1.01E-1	6.19E-1	1.49	-
48.0920	47.7950	9.2539E-4	5.99	1.13E2	4.87E1	1.02E1	1.00E-1	1.03E-1	8.14E-1	2.12	-
48.1800	47.7950	1.1996E-3	6.29	8.24E1	4.14E1	9.09	1.00E-1	1.30E-1	8.81E-1	2.17	-
48.2750	47.7950	1.4956E-3	8.33	6.64E1	3.74E1	8.56	1.00E-1	1.32E-1	8.03E-1	1.89	-
48.4170	47.7950	1.9380E-3	5.71	4.94E1	3.19E1	7.82	1.00E-1	1.98E-1	1.05	2.30	-
48.6020	47.7950	2.5145E-3	5.26	3.45E1	2.64E1	7.02	1.00E-1	2.71E-1	1.22	2.44	-

9.05CB

T	T_{NA}	t	χ^2	σ_0	$\xi_{\parallel}$	$\xi_{\perp}$	c	$w(\sigma_0)$	$w(\xi_{\parallel})$	$w(\xi_{\perp})$	w(c)
48.1050	48.1000	1.5568E-5	9.03	4.77E3	4.43E2	4.05E1	1.00E-1	2.43E-3	8.23E-2	5.12E-1	-1.00
48.1070	48.1000	2.1790E-5	4.85	3.03E3	3.45E2	3.45E1	1.00E-1	1.07E-2	2.46E-1	2.23	-1.00
48.1080	48.1000	2.4913E-5	3.96	2.59E3	3.17E2	3.28E1	1.00E-1	6.63E-3	1.73E-1	9.41E-1	-1.00
48.1100	48.1000	3.1135E-5	2.73	2.05E3	2.76E2	3.02E1	1.00E-1	9.98E-3	2.38E-1	1.22	-1.00
48.1120	48.1000	3.7357E-5	3.06	1.68E3	2.49E2	2.82E1	1.00E-1	1.14E-2	2.48E-1	1.22	-1.00
48.1150	48.1000	4.6703E-5	3.41	1.32E3	2.19E2	2.58E1	1.00E-1	1.45E-2	2.80E-1	1.34	-1.00
48.1170	48.1000	5.2925E-5	3.58	1.15E3	2.08E2	2.44E1	1.00E-1	1.61E-2	2.87E-1	1.37	-1.00
48.1220	48.1000	6.8492E-5	3.02	9.10E2	1.83E2	2.25E1	1.00E-1	2.17E-2	3.49E-1	1.58	-1.00
48.1280	48.1000	8.7159E-5	2.30	7.06E2	1.59E2	2.06E1	1.00E-1	3.12E-2	4.52E-1	1.93	-1.00
48.1360	48.1000	1.1207E-4	1.66	5.60E2	1.41E2	1.90E1	1.00E-1	4.52E-2	5.90E-1	2.41	-1.00
48.1480	48.1000	1.4942E-4	2.12	4.24E2	1.21E2	1.70E1	1.00E-1	6.37E-2	7.91E-1	2.81	-1.00
48.1640	48.1000	1.9923E-4	1.49	3.07E2	1.02E2	1.51E1	1.00E-1	8.90E-2	8.74E-1	3.18	-1.00
48.1830	48.1000	2.5837E-4	1.50	2.38E2	8.96E1	1.39E1	1.00E-1	1.08E-1	9.48E-1	3.25	-1.00
48.2150	48.1000	3.5798E-4	1.23	1.69E2	7.54E1	1.22E1	1.00E-1	1.56E-1	1.16	3.80	-1.00
48.2560	48.1000	4.8561E-4	5.40	1.26E2	6.62E1	1.10E1	1.00E-1	1.30E-1	8.22E-1	2.66	-1.00
48.3150	48.1000	6.6926E-4	3.72	8.92E1	5.59E1	9.75	1.00E-1	2.03E-1	1.08	3.34	-1.00
48.3930	48.1000	9.1207E-4	3.97	6.02E1	4.56E1	8.43	1.00E-1	2.65E-1	1.18	3.40	-1.00
48.5100	48.1000	1.2763E-3	3.97	4.20E1	3.85E1	7.44	1.00E-1	3.39E-1	1.25	3.44	-1.00
48.6650	48.1000	1.7588E-3	3.85	2.80E1	3.15E1	6.50	1.00E-1	4.52E-1	1.37	3.51	-1.00
48.8830	48.1000	2.4374E-3	3.36	1.78E1	2.55E1	5.52	1.00E-1	6.44E-1	1.56	3.74	-1.00
49.1780	48.1000	3.3557E-3	4.85	1.07E1	2.04E1	4.64	1.00E-1	8.16E-1	1.49	3.36	-1.00
49.5970	48.1000	4.6599E-3	4.45	5.66	1.61E1	3.79	1.00E-1	9.58E-1	1.20	2.62	-1.00

9.09CB

T	T_{NA}	t	χ^2	σ_0	$\xi_{\parallel}$	$\xi_{\perp}$	σ	$w(\sigma_0)$	$w(\xi_{\parallel})$	$w(\xi_{\perp})$	$w(\sigma)$
49.4100	48.3250	3.3751E-3	1.46	1.10E1	1.56E1	4.32	1.00E-1	1.58	3.94	7.43	-
49.1050	48.3250	2.4263E-3	1.67	1.87E1	2.03E1	5.28	1.00E-1	1.09	3.45	7.04	-
48.8880	48.3250	1.7513E-3	1.37	2.93E1	2.55E1	6.23	1.00E-1	8.95E-1	3.49	7.66	-
48.7450	48.3250	1.3065E-3	1.68	4.41E1	3.10E1	7.13	1.00E-1	4.32E-1	2.07	4.86	-
48.6350	48.3250	9.6430E-4	1.26	6.31E1	3.74E1	8.05	1.00E-1	3.88E-1	2.18	5.51	-
48.5500	48.3250	6.9989E-4	1.85	8.82E1	4.46E1	9.07	1.00E-1	3.10E-1	2.03	5.39	-
48.5350	48.3250	6.5324E-4	1.37	9.05E1	4.58E1	8.99	1.00E-1	3.07E-1	1.97	5.42	-
48.4750	48.3250	4.6659E-4	2.33	1.29E2	5.46E1	1.03E1	1.00E-1	1.77E-1	1.34	3.88	-
48.4320	48.3250	3.3284E-4	1.22	1.78E2	6.53E1	1.16E1	1.00E-1	1.60E-1	1.46	4.34	-
48.4050	48.3250	2.4885E-4	1.51	2.42E2	7.65E1	1.31E1	1.00E-1	1.10E-1	1.15	3.55	-
48.3850	48.3250	1.8663E-4	1.46	3.11E2	8.69E1	1.45E1	1.00E-1	9.15E-2	1.07	3.43	-
48.3360	48.3290	2.1774E-5	1.86	2.41E3	2.62E2	2.95E1	1.00E-1	8.46E-3	2.53E-1	1.25	-
48.3370	48.3290	2.4895E-5	2.11	2.28E3	2.54E2	2.89E1	1.00E-1	8.38E-3	2.45E-1	1.20	-
48.3380	48.3290	2.8004E-5	1.52	1.91E3	2.32E2	2.71E1	1.00E-1	1.15E-2	3.09E-1	1.47	-
48.3410	48.3290	3.7331E-5	1.97	1.58E3	2.09E2	2.54E1	1.00E-1	1.19E-2	2.96E-1	1.35	-
48.3430	48.3290	4.3549E-5	3.76	1.26E3	1.86E2	2.30E1	1.00E-1	1.28E-2	2.80E-1	1.27	-
48.3470	48.3290	5.5996E-5	3.52	1.03E3	1.66E2	2.15E1	1.00E-1	1.60E-2	3.21E-1	1.38	-
48.3510	48.3290	6.8444E-5	3.33	8.64E2	1.52E2	2.02E1	1.00E-1	2.75E-2	5.04E-1	2.06	-
48.3570	48.3290	8.7097E-5	3.96	7.00E2	1.36E2	1.92E1	1.00E-1	2.89E-2	4.79E-1	1.84	-
48.3650	48.3290	1.1199E-4	2.96	5.28E2	1.17E2	1.72E1	1.00E-1	4.28E-2	6.29E-1	2.30	-
48.3750	48.3290	1.4309E-4	1.86	4.09E2	1.01E2	1.57E1	1.00E-1	6.71E-2	8.87E-1	3.06	-

9.14CB

T	T_{NA}	t	χ^2	σ_0	$\xi_{\parallel}$	$\xi_{\perp}$	c	$w(\sigma_0)$	$w(\xi_{\parallel})$	$w(\xi_{\perp})$	w(c)
48.5780	48.5660	3.7291E-5	2.84	9.19E2	1.73E2	2.26E1	1.00E-1	1.78E-2	3.06E-1	1.30	-
48.5810	48.5660	4.6623E-5	2.23	7.23E2	1.53E2	2.06E1	1.00E-1	2.49E-2	3.81E-1	1.57	-
48.5860	48.5660	6.2156E-5	2.36	5.91E2	1.40E2	1.94E1	1.00E-1	4.10E-2	5.61E-1	2.19	-
48.5910	48.5660	7.7701E-5	2.09	4.69E2	1.22E2	1.83E1	1.00E-1	4.83E-2	5.95E-1	2.13	-
48.5990	48.5660	1.0257E-4	1.63	3.51E2	1.05E2	1.60E1	1.00E-1	7.70E-2	8.40E-1	2.96	-
48.6100	48.5660	1.3676E-4	1.54	2.71E2	9.27E1	1.45E1	1.00E-1	9.75E-2	9.40E-1	3.20	-
48.6250	48.5660	1.8339E-4	1.26	2.07E2	7.90E1	1.32E1	1.00E-1	1.34E-1	1.16	3.68	-
48.6450	48.5660	2.4555E-4	1.18	1.55E2	6.77E1	1.20E1	1.00E-1	1.71E-1	1.31	3.90	-
48.6780	48.5660	3.4813E-4	1.44	1.19E2	6.01E1	1.10E1	1.00E-1	2.16E-1	1.39	4.13	-
48.7200	48.5660	4.7868E-4	1.40	8.66E1	5.09E1	9.73	1.00E-1	2.84E-1	1.57	4.44	-
48.7780	48.5660	6.5896E-4	1.86	6.22E1	4.29E1	8.58	1.00E-1	2.97E-1	1.43	3.80	-
48.7790	48.6250	4.7859E-4	1.42	8.35E1	4.99E1	1.00E1	1.00E-1	2.75E-1	1.66	4.49	-
48.8360	48.6250	6.5573E-4	1.06	6.05E1	4.25E1	9.03	1.00E-1	3.85E-1	2.09	5.40	-
48.9160	48.6250	9.0436E-4	1.45	4.31E1	3.58E1	8.03	1.00E-1	4.27E-1	1.98	4.82	-
49.0270	48.6250	1.2493E-3	1.92	3.03E1	3.01E1	7.00	1.00E-1	4.85E-1	1.90	4.41	-
49.1800	48.6250	1.7248E-3	1.27	1.98E1	2.43E1	6.16	1.00E-1	7.89E-1	2.59	5.47	-
49.3950	48.6250	2.3930E-3	1.83	1.25E1	1.93E1	5.09	1.00E-1	9.08E-1	2.43	4.86	-

9.20CB

T	T_{NA}	t	χ^2	σ_0	$\xi_{\parallel}$	$\xi_{\perp}$	c	$w(\sigma_{\epsilon\ \parallel})$	$w(\xi_{\parallel})$	$w(\xi_{\perp})$	w(c)
48.8060	48.8000	1.8638E-5	5.66	3.74E2	1.11E2	1.83E1	1.00E-1	3.37E-2	3.80E-1	1.26	-
48.8090	48.8000	2.7951E-5	5.28	3.39E2	1.04E2	1.77E1	1.00E-1	3.81E-2	4.16E-1	1.34	-
48.8120	48.8000	3.7276E-5	4.81	2.96E2	9.81E1	1.68E1	1.00E-1	4.45E-2	4.50E-1	1.44	-
48.8160	48.8000	4.9705E-5	4.79	2.60E2	9.09E1	1.61E1	1.00E-1	4.90E-2	4.70E-1	1.45	-
48.8220	48.8000	6.8332E-5	4.89	2.26E2	8.46E1	1.54E1	1.00E-1	5.88E-2	5.61E-1	1.58	-
48.8300	48.8000	9.3190E-5	4.44	1.95E2	7.74E1	1.49E1	1.00E-1	6.34E-2	5.40E-1	1.53	-
48.8420	48.8000	1.3045E-4	4.02	1.59E2	6.97E1	1.36E1	1.00E-1	7.90E-2	6.11E-1	1.70	-
48.8570	48.8000	1.7704E-4	4.47	1.40E2	6.41E1	1.37E1	1.00E-1	7.98E-2	5.40E-1	1.42	-
48.8570	48.8000	1.7704E-4	8.59	1.25E2	6.09E1	1.23E1	1.00E-1	1.48E-1	1.00	2.68	-
48.8800	48.8000	2.4849E-4	7.68	1.03E2	5.46E1	1.17E1	1.00E-1	1.78E-1	1.10	2.78	-
48.9100	48.8000	3.4167E-4	5.69	7.96E1	4.78E1	1.08E1	1.00E-1	2.45E-1	1.35	3.20	-
48.9520	48.8000	4.7212E-4	4.33	6.37E1	4.25E1	1.02E1	1.00E-1	3.13E-1	1.53	3.42	-
49.0100	48.8000	6.5227E-4	4.81	4.84E1	3.71E1	9.40	1.00E-1	3.60E-1	1.54	3.26	-
49.0920	48.8000	9.0697E-4	4.38	3.64E1	3.15E1	8.75	1.00E-1	4.35E-1	1.65	3.18	-
49.2050	48.8000	1.2580E-3	3.48	2.49E1	2.56E1	7.75	1.00E-1	6.25E-1	2.03	3.56	-
49.3610	48.8000	1.7425E-3	3.32	1.65E1	2.10E1	6.80	1.00E-1	8.11E-1	2.17	3.52	-

9.28CB

T	T_{NA}	t	χ^2	σ_0	$\xi_{\parallel}$	$\xi_{\perp}$	c	$w(\sigma_0)$	$w(\xi_{\parallel})$	$w(\xi_{\perp})$	$w(c)$
49.5960	49.1950	1.2440E-3	1.82	1.56E1	2.15E1	6.59	1.00E-1	6.69E-1	1.68	2.89	-
49.4840	49.1950	8.9656E-4	1.71	2.17E1	2.56E1	7.10	1.00E-1	5.84E-1	1.70	3.24	-
49.4030	49.1950	6.4527E-4	2.32	2.96E1	2.96E1	7.85	1.00E-1	4.13E-1	1.41	2.83	-
49.3450	49.1950	4.6534E-4	2.33	3.89E1	3.45E1	8.64	1.00E-1	3.39E-1	1.30	2.77	-
49.3020	49.1950	3.3194E-4	2.34	4.89E1	3.84E1	9.22	1.00E-1	2.93E-1	1.26	2.82	-
49.2720	49.1950	2.3887E-4	3.12	5.91E1	4.21E1	9.88	1.00E-1	2.22E-1	1.05	2.41	-
49.2500	49.1950	1.7063E-4	2.58	7.29E1	4.74E1	1.05E1	1.00E-1	2.10E-1	1.08	2.65	-
49.2350	49.1950	1.2409E-4	2.76	8.46E1	5.16E1	1.11E1	1.00E-1	1.47E-1	8.21E-1	2.08	-
49.2600	49.1950	2.0164E-4	1.77	6.84E1	4.58E1	1.04E1	1.00E-1	2.13E-1	1.10	2.61	-
49.2500	49.1950	1.7063E-4	2.00	7.33E1	4.73E1	1.06E1	1.00E-1	1.93E-1	1.04	2.49	-
49.2380	49.1950	1.3340E-4	1.75	8.23E1	5.03E1	1.10E1	1.00E-1	1.89E-1	1.06	2.62	-
49.2270	49.1950	9.9277E-5	1.98	9.38E1	5.34E1	1.15E1	1.00E-1	1.64E-1	9.94E-1	2.49	-
49.2150	49.1950	6.2047E-5	2.46	1.06E2	5.81E1	1.20E1	1.00E-1	1.35E-1	8.54E-1	2.23	-